

Translational Physiologically-based Pharmacokinetic (PBPK) Modeling and Simulation to Support Drug Development and Pharmacotherapy

Dissertation

Zur Erlangung des Grades
des Doktors der Naturwissenschaften
der Naturwissenschaftlich-Technischen Fakultät
der Universität des Saarlandes

von
Daniel Andreas Moj

Saarbrücken
2018

Die vorliegende Arbeit wurde von Januar 2013 bis Februar 2018 unter Anleitung von Herrn Professor Dr. Thorsten Lehr in der Fachrichtung Klinische Pharmazie der Naturwissenschaftlich-Technischen Fakultät der Universität des Saarlandes angefertigt

Tag des Kolloquiums: 07.05.2018

Dekan: Prof. Dr. Guido Kickelbick

Vorsitzender: Prof. Dr. Marc Schneider

Berichterstatter: Prof. Dr. Thorsten Lehr

Prof. Dr. Markus R. Meyer

Akad. Beisitzer: Dr. Sonja Keßler

Included Project Publications

- I. Physiologically-based pharmacokinetic (PBPK) analysis of zoxtarelin doxorubicin drug-drug interaction potential - integrating preclinical, phase I and phase II data. Hanke N, Teifel M, Moj D, Wojtyniak JG, Britz H, Aicher B, Sindermann H, Ammer N, Lehr T. *Cancer Chemother Pharmacol.* 2018. Feb;81(2):291-304.
- II. Clarithromycin, midazolam, and digoxin: Application of PBPK modeling to gain new insights into drug-drug interactions and co-medication regimens. Moj D, Hanke N, Britz H, Frechen S, Kanacher T, Wendl T, Haefeli WE, Lehr T. *AAPS J.* 2017 Jan;19(1):298-312.
- III. A physiologically-based pharmacokinetic and pharmacodynamic (PBPK/PD) model of the histone deacetylase (HDAC) inhibitor vorinostat for pediatric and adult patients and its application for dose specification. Moj D, Britz H, Burhenne J, Stewart CF, Egerer G, Haefeli WE, Lehr T. *Cancer Chemother Pharmacol.* 2017 Nov;80(5):1013-1026.
- IV. The feasibility of physiologically-based pharmacokinetic modeling in forensic medicine illustrated by the example of morphine. Schaefer N, Moj D, Lehr T, Schmidt PH, Ramsthaler F. *Int J Legal Med* 2018. Mar;132(2):415-424.

Contribution Report

The author would like to declare his contributions to the publications of the projects I-IV included in this thesis.

- I. The author contributed to project I by helping to generate manuscript figures, by reviewing the relevant Matlab® code and finally by reviewing the manuscript during manuscript development, before submission and during the peer-review process.
- II. The author performed all major working steps that resulted in the publication of project II. The author gathered all relevant information from the literature and the collaboration partners, performed the entire modeling and simulation work, analyzed the modeling and simulation results, conceptualized and wrote the manuscript.
- III. The author performed all major working steps that resulted in the publication of project III. The author gathered all relevant information from the literature and the collaboration partners, performed the entire modeling and simulation work, analyzed the modeling and simulation results, conceptualized and wrote the manuscript.
- IV. The author performed the entire modeling and simulation work, analyzed the modeling and simulation results, revised the initial manuscript and supported the manuscript submission during the peer-review process.

Table of Contents

Included Project Publications	i
Contribution Report	ii
A. List of Tables	v
B. List of Figures	vi
C. List of Abbreviations	vii
D. Graphical Abstract	x
1 Introduction	1
1.1 Drug Development & Pharmacotherapy	1
1.2 Pharmacometrics (PMx), Quantitative Systems Pharmacology (QSP) & Physiologically-based Pharmacokinetics (PBPK)	2
1.3 PBPK in Drug Development.....	4
1.4 PBPK in Pharmacotherapy.....	5
1.5 PBPK & Drug-Drug-Interactions (DDI).....	7
1.5.1 DDI Assessment and Authority Perspective	7
1.5.2 DDI Management	8
1.6 PBPK & Pharmacodynamics (PD)	8
1.7 Current Obstacles in PBPK Research.....	9
2 Aims and Objectives of Projects I-IV	11
3 Methods	14
3.1 PBPK Model Structure	14
3.2 PBPK Implementation of Metabolism and Transport	20
3.3 Generic PBPK Modeling and Simulation Strategy	23
3.4 Used Software.....	24
4 Results	26
4.1 Project I: Physiologically-based pharmacokinetic (PBPK) analysis of zoqtarelin doxorubicin drug-drug interaction potential - integrating preclinical, phase I and phase II data.....	26

TABLE OF CONTENTS

4.2	Project II: Clarithromycin, midazolam, and digoxin: Application of PBPK modeling to gain new insights into drug-drug interactions and co-medication regimens	41
4.3	Project III: A physiologically-based pharmacokinetic and pharmacodynamic (PBPK/PD) model of the histone deacetylase (HDAC) inhibitor vorinostat for pediatric and adult patients and its application for dose specification.....	57
4.4	Project IV: The feasibility of physiologically-based pharmacokinetic modeling in forensic medicine illustrated by the example of morphine.	72
5	Conclusions	83
6	Summary	87
7	Zusammenfassung	88
8	Bibliography	89
9	Supporting Information	102
9.1	Supporting Information of Project I.....	102
9.2	Supporting Information of Project II	168
9.3	Supporting Information of Project III	181
10	Appendix	200
10.1	Original Publications.....	200
10.2	Conference Abstracts.....	200
10.3	Oral Presentation	201
10.4	Book Chapter	202
11	Acknowledgments	203

A. List of Tables

Table	Title	Page
1	Organ-specific expression ($\text{EXPR}_{\text{P,organ}}$) of CYP3A4 and P-gp	23

B. List of Figures

Figure	Title	Page
1	Schematic of a blood-flow limited PBPK model	14
2	Schematic of a permeability-limited PBPK organ model of the heart	19
3	Schematic of a permeability-limited PBPK organ model of the liver	22
4	A general PBPK modeling strategy for an orally formulated drug	25

C. List of Abbreviations

Abbreviation	Definition
ADME	Absorption, distribution, metabolism and excretion
AUC	Area under the curve
[AP-] _{BC}	Acidic phospholipids concentration in blood cells
[AP-] _T	Acidic phospholipids concentration in tissue
[PR] _P	Binding protein concentration in plasma
[PR] _T	Binding protein concentration in tissue
AAG	Alpha-1-acid glycoprotein
Ab _{CYP3A4}	Microsomal abundance of CYP3A4
Av _{rbc}	Surface/volume ratio of red blood cells
B:P	Blood to plasma concentration ratio
BC	Blood cells
BSA	Body surface area
C _A	Arterial drug concentration
C _{cell}	Intracellular drug concentration
C _{CYP3A4,liver}	Absolute CYP3A4 protein concentration in the liver
C _{int}	Interstitial drug concentration
CL _{hep}	Hepatic clearance
CL _{int}	Intrinsic clearance
CL _{kid}	Renal clearance
CO	Cardiac output
C _{P,organ}	Organ-specific intracellular protein concentration
C _{pls}	Plasma drug concentration
C _{rbc}	Red blood cell drug concentration
C _T	Tissue drug concentration
C _{UT,ss}	Tissue drug concentration at steady-state
C _{UP,ss}	Plasma unbound drug concentration at steady-state
C _{vt}	Venous drug concentration in tissue
C _{vuT}	Venous unbound drug concentration in tissue
CYP2C19	Cytochrome P450 2C19
CYP2C9	Cytochrome P450 2C9
CYP3A4	Cytochrome P450 3A4
CYP3A7	Cytochrome P450 3A7
DDI	Drug-drug-interactions
DGI	Drug-gene-interactions

continued...

C. LIST OF ABBREVIATIONS

Abbreviation	Definition
e.g.	Exempli gratia
EMA	European Medicines Agency
EXPR _{P,organ}	Protein expression level in a specific organ
FDA	US Food and Drug Administration
f _{EW}	Fractional tissue volume of extracellular water
f _{IW}	Fractional tissue volume of intracellular water
f _{IW,BC}	Fractional tissue volume of intracellular water in blood cells
f _{IW,P}	Fractional tissue volume of intracellular water in plasma
f _{NL}	Fractional tissue volume of neutral lipids
f _{NL,BC}	Fractional tissue volume of neutral lipids in blood cells
f _{NL,P}	Fractional tissue volume of neutral lipids in plasma
f _{NP}	Fractional tissue volume of neutral phospholipids
f _{NP,BC}	Fractional tissue volume of neutral phospholipids in blood cells
f _{NP,P}	Fractional tissue volume of neutral phospholipids in plasma
fu	Fraction unbound
f _{vas}	Vascular fraction of the red blood cells
GFR	Glomerular filtration rate
HCT	Hematocrit
HDAC	Histone deacetylase
HSA	Human serum albumin
i.e.	Id est
IND	Investigational new drug
iv	Intravenous
K _a	Association constant
K _{int,rbc}	Drug partition coefficient between plasma and interstitial space
K _M	Michaelis-Menten constant
K _{pu}	Tissue to plasma partition coefficient
K _{pu_{BC}}	Blood cell to plasma water partition coefficient
K _{rbc}	Drug partition coefficient between red blood cells and plasma
K _{water,cell}	Drug partition coefficient between intracellular space and water
K _{water,int}	Drug partition coefficient between interstitial space and water
LogMA	Membrane affinity
LogP	N-octanole to water partition coefficient
mg	Miligram
mL	Milliliter
MPPGL	Microsomal protein per gram of liver
MW	Molecular weight

...continued...

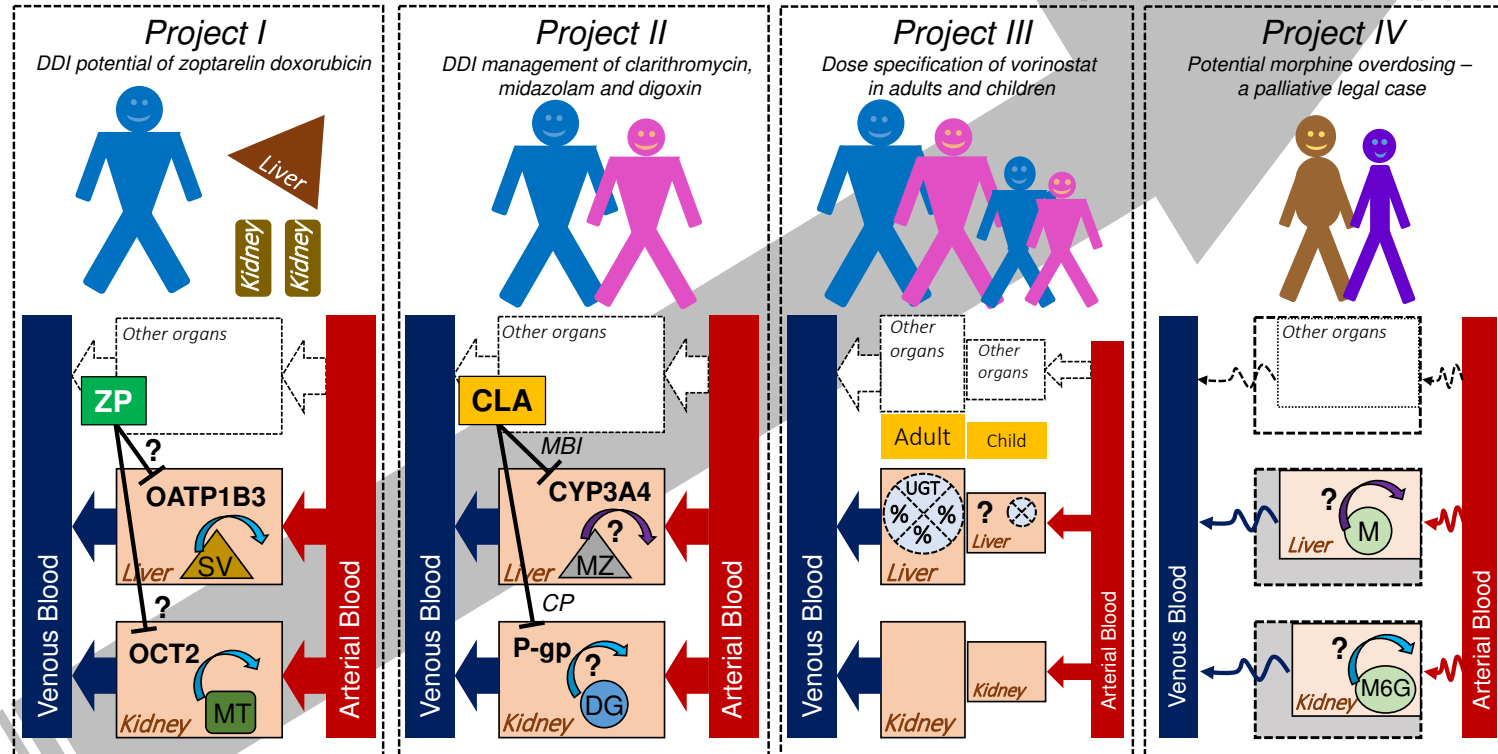
Abbreviation	Definition
MW _{Eff}	Effective molecular weight
OATP	Organic anion-transporting polypeptide
OATP1B3	Organic anion-transporting polypeptide 1B3
OCT2	Organic cation transporter 2
P	Partition coefficient of the unionized drug
PA	Permeability-surface area product
PBPK	Physiologically-based pharmacokinetics
PD	Pharmacodynamics
P _D	Drug cellular permeability
P _{endothelial}	Drug cellular permeability from plasma to interstitial space
P-gp	P-glycoprotein
pH	Potential for hydrogen
pH _{BC}	Blood cell pH
pH _{IW}	Intracellular water pH
pH _P	Plasma pH
PK	Pharmacokinetics
pKa	Acid dissociation constant
PMR	Postmortem redistribution
PMx	Pharmacometrics
po	Per os
P _{pls,rbc}	Drug cellular permeability from plasma to red blood cells
QSP	Quantitative systems pharmacology
Q _T	Tissue blood flow
RF	Reference concentration
SA _{int}	Surface area between plasma and interstitial space
SA _{rbc}	Surface area between red blood cells and plasma
TDM	Therapeutic drug monitoring
T _{int,cell}	Passive drug transport from interstitial to intracellular space
T _{pls,int}	Passive drug transport from plasma to interstitial space
T _{pls,rbc}	Passive drug transport from plasma to red blood cells
UGT1A9	UDP-glucuronosyltransferase 1A9
UGT2B7	UDP-glucuronosyltransferase 2B7
V	Volume
V _{max}	Maximum reaction velocity
V _{rbc,organ}	Red blood cell volume in an organ
V _T	Tissue volume
WT _{liver}	Liver weight

...end

D. Graphical Abstract

Translational PBPK modeling from...

... to pharmacotherapy



Graphical Abstract.
 CLA clarithromycin, CP competitive inhibition, CYP3A4 cytochrome P450 (CYP) 3A4, DG digoxin, M morphine, MBI mechanism-based inhibition, M6G morphine-6-glucuronide, MT metformin, MZ midazolam, OATP1B3 organic anion-transporting polypeptide 1B3, OCT2 organic cation transporter 2, P-gp P-glycoprotein, SV simvastatin, ZP zoptarelin doxorubicin

1 Introduction

1.1 Drug Development & Pharmacotherapy

The existing drug development process¹ is regulated by authorities like the US Food and Drug Administration (FDA) or the European Medicines Agency (EMA) and it ensures that safe and effective medications are made available to the public in an ethically rigorous manner. However, the drug development process is hampered by its duration and its costs. The average time for a new molecular entity to successfully enter the drug market is 13.5 years at costs of 1,778 million US Dollars². These costs have been steadily increasing over the last decades³. This poses not only a threat to pharmaceutical companies which have to make risky decisions during drug development but also to patients for whom safe and effective pharmacotherapy is not available yet.

Pharmacotherapy (therapy using pharmaceutical drugs) poses further challenges to medical professionals as well as patients. All patients have individual anatomical and physiological properties such as age and genetics and they can be in different disease states with varying co-medications. These factors, among various others, can positively or negatively impact a drug's pharmacokinetics (PK) and pharmacodynamics (PD) and thus pharmacotherapy. However, the drug development process can only cover a small fraction of the population during the clinical research phases. Hence, the drug therapy is not equally safe and effective for all patients treated with the dosing regimens approved by the authorities for a new drug, as not all possible patient properties are equally accounted for by these dosing regimens that were determined during the clinical study phases.

A sophisticated solution to reduce the time drug development takes as well as its costs and to improve pharmacotherapy is the development and application of mathematical modeling and simulation.

1.2 Pharmacometrics (PMx), Quantitative Systems Pharmacology (QSP) & Physiologically-based Pharmacokinetics (PBPK)

Mathematical models are often used to describe real-life measurements and to predict non-measured values by simulation of “what-if” scenarios. This approach is common practice in natural sciences, engineering and many industries like aerospace or automotive.

Pharmacometrics (PMx - equivalent to “population pharmacokinetics” or “POP-PK”) is the science of mathematically and statistically quantifying disease, drug and clinical trial characteristics such as dose, biomarkers, endpoints and study design⁴. Since the pioneering development of key concepts of PK and PD in the 1950s⁵, PMx has evolved from a scientific curiosity in literature and academia⁶⁻¹⁰ to a vital part of regulatory guidelines¹¹⁻¹⁸ that has been identified as a strategic component for the Critical Path Initiative¹⁹ with the aim of improving decision making in drug development and pharma-cotherapy.

In the past, PMx activities have helped to increase the drug research and development efficiency²⁰⁻²³ by enabling approval of unstudied dosing regimens, providing confirmatory evidence of effectiveness and deriving model-based primary study endpoints²⁴. Furthermore, PMx helped to increase the mechanistic understanding of drugs^{25,26}, determine first-in-human doses^{27,28}, optimize study designs^{21,29-31}, characterize risks and benefits from early clinical responses³²⁻³⁶, select dose schedules and label recommendations³⁷⁻³⁹ and to differentiate between comparator and standard of care drugs⁴⁰⁻⁴³.

Next to PMx, Quantitative Systems Pharmacology (QSP) has emerged as an innovative tool lately⁴⁴. QSP aims at joining physiologically-based pharmacokinetics (PBPK) with in vitro-in vivo correlation of absorption, distribution, metabolism and excretion (ADME) data⁴⁵, often enhanced by complex systems biology models and methodology.

PBPK modeling and simulation is one of the main pillars of the modeling and simulation (r)evolution in the pharmaceutical sciences^{46,47}. PBPK models were first conceptualized as soon as 1937 by the Swedish physiologist Torsten Teorell^{48,49} who many now attribute as being the father of modern PK^{50,51}. However, computing capacity has only started in the 1960s and 1970s to become powerful enough to cope with the mathematical equation systems of PBPK models⁵².

PBPK models consist of multiple compartments which are based on real tissue characteristics such as volume, surface area and protein expression. The tissue compartments are mechanistically connected via tissue blood flows to simulate *in vivo* ADME^{47,53}. PBPK models can be developed in varying degrees of complexity as minimal^{54,55}, whole-body^{56,57}, and as whole-body models incorporating even more complex systems biology models^{44,58,59}. In minimal PBPK models, organ tissues that show similar PK behavior are ‘lumped’ together^{60–62} to reduce model complexity while considering available physiological, anatomical and ADME information and the questions to be answered by the model^{63–67}. Next to these drug-independent physiological and anatomical parameters, PBPK models build upon drug-dependent parameters such as logP, pKa, molecular weight and drug-biological parameters such as unbound drug fraction in plasma (fu), metabolism data, drug transporter data and pharmacogenetics.

PBPK modeling was initially applied in the field of toxicology and toxicokinetics^{68–70} where it is still used today⁷¹. As computing capacity has grown and new *in silico* and *in vitro* methodologies emerged, PBPK modeling and simulation has expanded to various clinically relevant fields during drug development and pharmacotherapy. PBPK has already made contributions in the prediction and assessment of (i) drug-drug- and drug-gene-interactions (DDI^{72–75} and DGI^{76–79}) via metabolic enzymes and drug transporters and (ii) the PK of special populations, such as pediatric^{80–82}, geriatric^{83,84} and pregnant individuals^{85,86} or patients with differing degrees of hepatic^{87,88} or renal^{89,90} impairment.

1.3 PBPK in Drug Development

During drug discovery, PBPK modeling and simulation can be applied in the lead optimization or candidate drug selection by providing human PK predictions⁹¹. The prediction of high necessary drug doses or the need for multiple drug administrations per day might already discourage the further development of a candidate drug. At this stage, the PBPK model is informed by drug-dependent parameters such as logP, pKa or molecular weight.

In preclinical development, the ADME of the candidate drug is assessed by metabolism and transporter assays, as well as by PK studies in animal species such as mice, rats, rabbits, dogs and monkeys⁹²⁻⁹⁴. Here, basic information on relevant drug metabolizing enzymes (e.g. cytochrome P-450 (CYP), UDP-glucuronosyltransferase (UGT)), drug transporters (e.g. P-glycoprotein (P-gp), organic anion-polypeptide transporters (OATP)), drug permeability, distribution and excretion is obtained. At this stage the PBPK model gains information on important drug-biological properties. PBPK modeling now has the capacity to inform clinical trials and to simulate DDIs. In case enough safety margin can be predicted in worst-case simulation scenarios, clinical DDI trials can be waived¹⁵.

In clinical development the so far developed PBPK model can be applied to predict clinical phase I safety trials in healthy volunteers. In vivo concentration-time profiles and excretion data of the investigational new drug (IND) can then help to improve the PBPK model performance for the prediction of clinical phase II trials which assess the drug efficacy in patients. Clinical phase III trials that provide a more thorough understanding of the effectiveness of the drug, the benefits and the range of possible adverse reactions are in many cases also accompanied by PBPK modeling exercises. Fully developed PBPK models can be used as part of the regulatory submission to support the market access.

With increasing information during the drug development, the confidence in the PBPK modeling predictions is increasing. This pushes the candidate drug development process forward by enabling the prediction of the drug PK in special populations (e.g. children) at strategically important milestones.

After drug approval by the authorities and market access, PBPK models can be regularly updated to accommodate emerging new scientific information on the drug. After the replacement of the drug by more efficacious and/or safer competitors, the obsolete drug can still be a valuable part of a PBPK model repository⁹⁵, for instance, to simulate DDI scenarios in order to predict the effect of the obsolete co-administered drugs on newly developed medications and vice versa.

At every stage in the development of a drug, PBPK modeling and simulation helps to combine all available drug-dependent and drug-biological in silico, in vitro and in vivo information to help answer complex questions in order to move drug candidates from their discovery to the market and beyond.

1.4 PBPK in Pharmacotherapy

PBPK models and hence the simulations which are based on them are *ab initio* blind for human age, meaning that the models initially do not take into account anatomical or physiological changes, i.e. maturation in the young or functional decline in the elderly. In general, human life can be categorized into several age groups, each showing physiological and anatomical properties which are specific to the respective age group. Commonly, infancy (0-2 years), childhood (2-12 years), adolescence (12-18 years), adulthood (20-65 years), the elderly life stage (>65 years) and death are differentiated.

Age-dependent anthropometric measures such as body height/weight but also organ/tissue weights and volumes as well as varying degrees of organ functions can be implemented into PBPK models to simulate age-specific PK from birth to the elderly. As already ascertained in the literature: neonates, infants, children and adolescents are

1. INTRODUCTION

not small adults^{96–99} but demonstrate particular anatomical and physiological properties which have the potential to alter the PK of drugs when compared to adults and elderly patients^{100–103}. Next to height and body weight¹⁰⁴, the body composition¹⁰⁵, the cardiac output^{106,107} as well as blood flows^{108–111} are altered in pediatric patients. Absorption of drugs might be different in children by a relatively elevated intra-gastric pH due to reduced acid output and decreased volume of gastric secretion^{112–114}, immature conjugation and transport of bile salts^{115,116} and immature intestinal motor activity¹¹⁷. Maturation of drug transporters^{118–120}, e.g. P-gp and OATP, might impact the absorption, distribution and elimination of drugs that are substrates of these transporters. Reduced alpha-1-acid glycoprotein (AAG) and human serum albumin (HSA)^{121,122} quantities can increase the free fraction of drugs in pediatric patients and thereby can alter their distribution and elimination. Delayed maturation of most drug-metabolizing phase I and II enzymes such as CYP 2C9^{123–125}, CYP2C19^{123,124}, CYP3A4^{126–129}, UGT 1A9¹³⁰ and UGT2B7^{130–132} can increase or decrease the metabolic clearance and hence decrease or increase the exposure of substrates, respectively. Finally, the glomerular filtration rate (GFR) follows a particular age-dependent maturation with increasing GFR from birth to adulthood¹³³.

While pediatric patients mostly show immature physiological systems (an exception is CYP3A7^{126,128}) which develop towards the adult functionality, elderly patients in many aspects show declining physiological functioning. Elderly patients show a loss of muscle mass but a relative increase in fat mass^{134–136}, a decrease in liver^{137–139} and kidney weight^{140,141}, a reduction in cardiac index¹⁴², which relates the cardiac output (CO) to the body surface area (BSA), and reduced kidney blood flow¹⁴³. All of these parameters have the capacity to influence the PK of drugs in the elderly.

In summary, PBPK modeling and simulation can be used to describe and predict the PK of drugs at all stages of human life by implementing human anatomical and physiological data (drug-independent parameters) and can thereby help to personalize drug treatments for more effective and safer pharmacotherapies.

1.5 PBPK & Drug-Drug-Interactions (DDI)

While steady scientific progress has been accomplished in various areas of PBPK research, most contributions have been made in the area of DDI modeling, shown by its over-proportional use in DDI simulations for regulatory submissions¹⁴⁴⁻¹⁴⁶.

1.5.1 DDI Assessment and Authority Perspective

In a DDI scenario, the co-administered “perpetrator” drug causes an altered systemic and/or local exposure of the “victim drug” which may lead to increased rates of undesirable effects due to sub- or supra-therapeutic “victim” drug concentrations. This is especially important when the PK interaction is large enough in magnitude to produce a clinically relevant change on the PD of the “victim” drug, the “victim” exhibits a narrow therapeutic index and the variability in the PK of the victim is small enough for the DDI to be identifiable¹⁴⁷. As DDIs can negatively impact pharmacotherapy, it is important to assess and quantify potential DDIs during drug development and beyond market access to provide guidance to medical professionals and drug regulatory authorities on how to treat clinically relevant DDIs during drug therapy.

The FDA and EMA provide a systematic, risk-based approach for the assessment of the DDI potential of IND¹⁴⁻¹⁶. During this assessment there are three major tasks: 1. To identify the primary routes of the IND’s elimination; 2. To derive the contribution of enzymes and transporters to the IND’s disposition; 3. To characterize the impact of the IND on enzymes and transporters. By translating these in vitro observations into in vivo

1. INTRODUCTION

predictions, the PBPK modeling approach is in some cases able to replace clinical in vivo studies as stated recently in an updated FDA guideline on DDIs¹⁵.

1.5.2 DDI Management

The number of patients taking more than one drug at a time has increased over the last decade^{148,149}. Hence, the risk of unanticipated, unrecognized, or mismanaged DDIs is increasing, which is an important cause of morbidity and mortality¹⁵⁰. Therefore, the FDA recommends developing DDI management strategies when a clinically significant DDI has been identified¹⁴.

These DDI management strategies may include the contraindication and avoidance of the concomitant use, the temporary discontinuation and/or dosage modifications of the interacting drugs, including staggered drug administration and specific monitoring strategies (e.g. therapeutic drug monitoring (TDM)).

Especially in the case of successfully marketed drugs, PBPK modeling and simulation might either help to catch up on DDI studies which have not been performed in vivo in the past or help to reassess already conducted in vivo DDI studies. Hence, formerly contraindicated drugs might be eligible for concomitant use with dose modifications based on PBPK simulations. In that sense, PBPK modeling and simulation can become a valuable tool for DDI management strategies.

1.6 PBPK & Pharmacodynamics (PD)

While the PK relates the drug administration to drug concentrations within the body over time, the PD relates the response (desired and undesired) to drug concentrations.

In PBPK models, organs can be explicitly represented with intracellular, interstitial, plasma and red blood cell compartments of these organs. Hence, on- and off-target tissue exposure to drugs can be directly quantified. Furthermore, drug targets like enzymes or other proteins can be distributed in the PBPK model in a tissue-specific manner using

in vitro and in vivo mRNA and/or protein quantification data^{151–153}. Subsequently, PBPK/PD models enable the simulation of tissue-specific PD at the actual site of drug action. In the literature, PBPK/PD models have been successfully applied to model the effect of antibiotics on bacterial growth in the lung¹⁵⁴ or to investigate dosing schedules for a switch of medication from warfarin to rivaroxaban¹⁵⁵.

PBPK/PD models can offer a unique method to assess and optimize drug treatments taking advantage of the high spatial resolution (tissue representation) of PBPK models.

1.7 Current Obstacles in PBPK Research

Although there have been successes in PBPK modeling and simulation research over the years, there are critical issues that prevent the PBPK approach from being used at its full potential.

Firstly, the DDI potential analysis of drug transporter substrates during drug development is a field with a high research demand. Due to the complex model development and data integration process, many reliable victim drug models to assess the impact of potential perpetrator drugs in coupled PBPK models are not available in the literature. Hence, it is crucial to develop these victim drug models but also to find a scientifically sound “work-around” to analyze the general DDI potential of perpetrators in case PBPK models of victim drugs are missing.

Secondly, a vividly investigated topic is the implementation of enzyme and transporter inhibition models into PBPK models and their application in DDI simulation scenarios. Some perpetrator and victim drugs, which are often used in in vitro DDI screenings heavily depend on tissue-specific (e.g. intestine, liver, kidney) metabolism and transport. A major hurdle preventing easily accessible and usable DDI models is to combine these drugs in DDI models while accounting for tissue-specific inhibition, tissue-specific protein abundances and half-lives and to simultaneously reflect the literature information on the

1. INTRODUCTION

PK of these drugs. Furthermore, questions on how these DDI models could be applied in DDI management and assessment scenarios remain.

Thirdly, to apply PBPK models for dose specification in pediatric patients, maturation functions, describing the expression of enzymes and transporters over time, must be available and implemented in pediatric PBPK models. It is only recently that expression data of some neglected metabolic enzymes, such as UGT2B17, has become available. Hence, pediatric PBPK models and simulations for UGT2B17 substrates are needed for the design of future pediatric clinical trials.

Fourthly, there is a need to develop the existing PBPK software further. Many complex induction or inhibition processes of proteins, mediated by drugs, have not yet been implemented into these software packages and can therefore not be accounted for in the model simulations. Equally missing are integrated PD models to simultaneously account for plasma drug concentrations together with safety and efficacy biomarkers in the target tissues.

Finally, as described in the introduction, PBPK modeling has been applied in several patient populations. So far, these applications have been limited to model simulations for living patients. As of now, PBPK research tries to push this boundary forward to describe and predict the PK of drugs shortly before and after death. Here, PBPK models could be applied in the guidance of palliative drug dosing and in cases of legal medicine.

2 Aims and Objectives of Projects I-IV

The aim of this thesis was to overcome some of the major obstacles in current PBPK research, to innovate state-of-the-art PBPK modeling and simulation techniques and to generate new explanations and hypotheses for future research. The thesis' aim was realized within the scope of the following projects:

Project I: DDI potential of zoptarelin doxorubicin

The aim of project I was to support the drug development of the new chemotherapeutic drug zoptarelin doxorubicin by evaluating its DDI potential using the PBPK approach. The specific objectives of project I were (i) to establish the first whole-body PBPK model of zoptarelin doxorubicin and its active metabolite doxorubicin, (ii) to apply the zoptarelin doxorubicin model for a general assessment of the DDI potential with OATP1B3 and OCT2 victim drugs and (iii) to predict the magnitude of zoptarelin doxorubicin DDIs with simvastatin and metformin in worst-case scenarios.

Project II: DDI management of clarithromycin, midazolam and digoxin

The aim of project II was to support drug development by providing PBPK models of clarithromycin, midazolam and digoxin and to support pharmacotherapy by providing dosing rationales for midazolam and digoxin during co-medication with clarithromycin. Furthermore, the aim was to develop the existing PBPK software further by implementing a mechanism-based inhibition (MBI) model for CYP3A4 and clarithromycin. The specific objectives of project II were (i) to develop fully mechanistic PBPK models for the single compounds clarithromycin, midazolam and digoxin, (ii) to couple the clarithromycin and midazolam PBPK models to predict the metabolic DDI (via CYP3A4) of these drugs and (iii) to couple the clarithromycin and digoxin PBPK models to predict the transporter-based DDI (via P-gp) of these two drugs.

2. AIMS AND OBJECTIVES OF PROJECTS I-IV

Project III: Dose specification of vorinostat in adults and children

The aim of project III was to support pharmacotherapy by specifying pediatric vorinostat doses and thereby enabling a rational pediatric pharmacotherapy and by specifying potentially safer and more effective adult dosing regimens than the approved vorinostat dosage. Furthermore, the aim was to develop the existing PBPK software further by implementing a functional relationship between PD biomarkers and vorinostat plasma concentrations. The specific objectives of project III were (i) to build and evaluate an adult whole-body PBPK model of the chemotherapeutic agent vorinostat being able to describe and predict the PK of varying doses of intravenously and orally administered vorinostat, (ii) to develop and evaluate a pediatric PBPK model for vorinostat and estimate vorinostat doses for children between 0 and 17 years, (iii) to build and evaluate a PBPK/PD model incorporating the vorinostat-mediated histone deacetylase activity inhibition and a thrombocytopenia model, (iv) to identify potentially effective vorinostat dosing regimens while considering HDAC activity and the number of circulating thrombocytes and (v) to perform a parameter sensitivity analysis for the developed whole-body PBPK model.

Project IV: Potential morphine overdosing - a palliative legal case

The aim of project IV was to support pharmacotherapy by simulating the morphine and morphine-6-glucuronide PK shortly before a patient's death by implementing palliative medical information using the PBPK approach. The specific objective of project IV was to examine a potential overdosing of morphine in a palliative care patient (i) by suggesting which dosing unit ("mg" or "mL") appeared more likely as no dosing units were reported in clinical documentation, (ii) by assessing whether the analytically determined

morphine concentrations could be explained by the clinically documented morphine administration and (iii) by exploring potential physiological and mechanistic reasons that could explain the documented morphine concentrations.

3 Methods

3.1 PBPK Model Structure

PBPK models consist of multiple organs which are connected via the circulating blood system. A schematic representation of a simple blood-flow limited PBPK model following intravenous dosing is shown in Figure 1.

In the case of a blood-flow limited PK, the ADME processes are rate-limited by the arterial and venous blood flow. The rate of change of drug in the non-eliminating tissues can then be calculated using (1),

$$V_T * \frac{dC_T}{dt} = Q_T * C_A - Q_T * C_{vT} \quad (1)$$

where Q is the blood flow [L/h], C is concentration [mg/L], V is volume [L], T is tissue, A is arterial, V is venous, C_{vT} is $C_T/(K_{pu}/B:P)$ with K_{pu} denoting the tissue to plasma partition coefficient and $B:P$ the blood to plasma ratio.

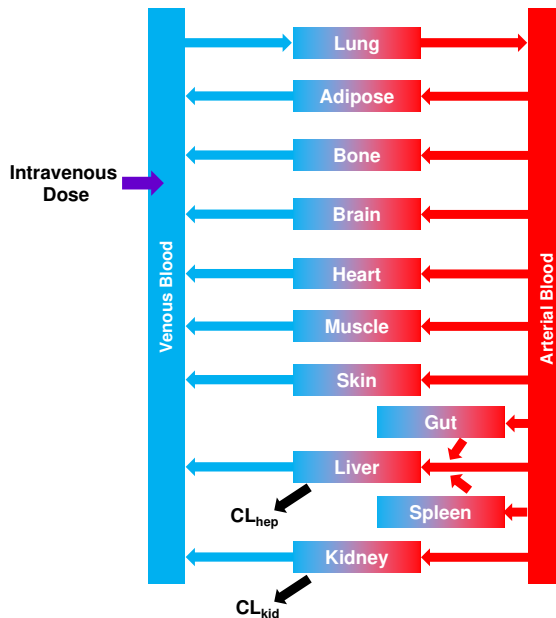


Figure 1 Schematic of a blood-flow limited PBPK model. The red and blue arrows indicate the arterial and venous blood flows, respectively. CL_{hep} hepatic clearance, CL_{kid} renal clearance.

In eliminating tissues such as the liver or the kidney, the unbound drug concentration ($C_{v_{uT}}$) drives the clearance rate as stated in (2),

$$V_T * \frac{dC_T}{dt} = Q_T * C_A - Q_T * C_{v_T} - CL_{int} * C_{v_{uT}} \quad (2)$$

where CL_{int} is the intrinsic clearance of the drug [L/h] and u denotes “unbound”. The intrinsic clearance is a measure of the intrinsic ability of a drug to be metabolized by enzymes which is independent on extrinsic factors like the blood flow.

K_{pu} s are a crucial part of PBPK models which influence the tissue concentrations of drugs in addition to the blood flow and the B:P. Among various approaches for the prediction of K_{pu} values^{156–161}, the method by Rodgers and co-workers is the most popular one. Derivations of the following equations from this approach are available in the literature^{156,157}.

In general, the K_{pu} for any tissue can be experimentally determined using (3),

$$K_{pu} = \frac{C_{u_{T,ss}}}{C_{u_{p,ss}}} \quad (3)$$

where $C_{u_{T,ss}}$ is the steady-state concentration of the drug [mg/L] in a tissue outside of the blood perfusing it and the $C_{u_{p,ss}}$ is the corresponding unbound concentration [mg/L] in plasma.

For diprotic moderate-to-strong bases ($pK_a \geq 7$) electrostatic interactions with tissue acidic phospholipids, drug partitioning into neutral phospholipids and drug dissolution in tissue water can be considered by the estimation of the K_{pu} . Assuming that drugs distribute by passive diffusion with the blood flow, electrostatic interactions predominate and non-saturating conditions prevail in the tissues, the K_{pu} can be calculated with (4),

3. METHODS

$$K_{pu} = \frac{C_T}{Cu_p} = \left[f_{EW} + \left(\frac{1+10^{pK_a2-pH_{IW}}+10^{pK_a1+pK_a2-2pH_{IW}}}{1+10^{pK_a2-pH_p}+10^{pK_a1+pK_a2-2pH_p}} \right) * f_{IW} \right. \\ \left. + \left(\frac{(P*f_{NL} + ((0.3*P+0.7)*f_{NP}))}{1+10^{pK_a2-pH_p}+10^{pK_a1+pK_a2-2pH_p}} \right) \right. \\ \left. + \left(\frac{(K_a*[AP^-]_T * (10^{pK_a2-pH_{IW}}+10^{pK_a1+pK_a2-2pH_{IW}}))}{1+10^{pK_a2-pH_p}+10^{pK_a1+pK_a2-2pH_p}} \right) \right] \quad (4)$$

where C_T is $C_{T,ss}$ [mg/L], Cu_p,ss is Cu_p [mg/L], f_{EW} is the fractional tissue volume of extracellular water, pH_{IW} is the pH of intracellular tissue water, pH_p is the pH of plasma, f_{NL} is the fractional tissue volume of neutral lipids, f_{NP} is the fractional tissue volume of neutral phospholipids, P is the partition coefficient of the unionized drug and K_a is the association constant [M^{-1}] of basic compounds with acidic phospholipids (AP^-). P is the n-octanol to water partition coefficient for all tissues except adipose where it represents the vegetable oil to water partition coefficient. For monoprotic bases the term $\left(\frac{1+10^{pK_a2-pH_{IW}}+10^{pK_a1+pK_a2-2pH_{IW}}}{1+10^{pK_a2-pH_p}+10^{pK_a1+pK_a2-2pH_p}} \right)$ can be reduced to $\left(\frac{1+10^{pK_a-pH_p}}{1+10^{pK_a-pH_p}} \right)$.

As K_a is not readily available one can rearrange equation (4) and apply it to acidic phospholipids containing blood cells (BC) by defining that the extracellular space of blood cells is 0. Additionally, the blood cell to plasma water concentration ratio ($K_{pu,BC}$) can be experimentally determined from the B:P, the fraction of drug unbound in plasma or the hematocrit. Equation (5) gives the calculation of $K_{a,BC}$ for a diprotic base,

$$K_{a,BC} = \left(K_{pu,BC} - \left(\frac{1+10^{pK_a2-pH_{BC}}+10^{pK_a1+pK_a2-2pH_{BC}}}{1+10^{pK_a2-pH_p}+10^{pK_a1+pK_a2-2pH_p}} * f_{IW,BC} \right) \right. \\ \left. - \left(\frac{(P*f_{NL,BC} + (0.3P+0.7)*f_{NP,BC})}{1+10^{pK_a2-pH_p}+10^{pK_a1+pK_a2-2pH_p}} \right) \right) \\ * \left(\frac{1+10^{pK_a2-pH_p}+10^{pK_a1+pK_a2-2pH_p}}{[AP^-]_{BC} * 10^{pK_a2-pH_{BC}}+10^{pK_a1+pK_a2-2pH_{BC}}} \right) \quad (5)$$

where pH_{BC} and pH_p are the pH values in blood cells and plasma, respectively. The parameter $f_{IW,BC}$ denotes the fractional tissue volume of neutral lipids in blood cells, $f_{NL,BC}$

denotes the fractional tissue volume of intracellular water in blood cells and $f_{NP,BC}$ denotes the fractional tissue volume of neutral phospholipids in blood cells.

In a generalized form, (4) can be simplified to (6),

$$K_{pu} = \left[f_{EW} + \left(\frac{1+X}{1+Y} * f_{IW} \right) + \left(\frac{(P*f_{NL} + ((0.3*P+0.7)*f_{NP}))}{1+Y} \right) + \left(\frac{(Ka*[AP]_T*X)}{1+Y} \right) \right] \quad (6)$$

and (5) can be simplified to (7),

$$K_a = \left(K_{pu,BC} - \left(\frac{1+Z}{1+Y} * f_{IW,BC} \right) \right) - \left(\frac{(P*f_{NL,BC} + (0.3P+0.7)*f_{NP,BC})}{1+Y} \right) * \left(\frac{1+Y}{[AP]_{BC}*Z} \right) \quad (7)$$

where X, Y and Z can be replaced by (8-10) for di-basic zwitterions and by (11-13) for di-acidic zwitterions. For very weak monoprotic bases X = 1+10^{pKa-pH_{IW}} and Y = 1+10^{pka-pH_P}; for monoprotic acids X = 1+10^{pH_{IW}-pKa} and Y = 1+10^{pH_P-pKa}. For neutral drugs X and Y equal 1.

$$X = 10^{pH_{IW}-pK_a_{ACID}} + 10^{pK_a^2_{BASE}-pH_{IW}} + 10^{pK_a^1_{BASE}+pK_a^2_{BASE}-2pH_{IW}} \quad (8)$$

$$Y = 10^{pH_P-pK_a_{ACID}} + 10^{pK_a^2_{BASE}-pH_P} + 10^{pK_a^1_{BASE}+pK_a^2_{BASE}-2pH_P} \quad (9)$$

$$Z = 10^{pH_{BC}-pK_a_{ACID}} + 10^{pK_a^2_{BASE}-pH_{BC}} + 10^{pK_a^1_{BASE}+pK_a^2_{BASE}-2pH_{BC}} \quad (10)$$

$$X = 10^{pK_a^1_{ACID}-pH_{IW}} + 10^{2pH_{IW}-pK_a^1_{ACID}-pK_a^2_{ACID}} + 10^{pK_a^1_{BASE}+pH_{IW}} \quad (11)$$

3. METHODS

$$Y = 10^{pK_{a1,ACID} - pH_P} + 10^{2pH_P - pK_{a1,ACID} - pK_{a2,ACID}} + 10^{pK_{a,BASE} + pH_P} \quad (12)$$

$$Z = 10^{pK_{a1,ACID} - pH_{BC}} + 10^{2pH_{BC} - pK_{a1,ACID} - pK_{a2,ACID}} + 10^{pK_{a,BASE} + pH_{BC}} \quad (13)$$

In case of a di-acidic zwitterion that has one or more basic pKa values < 7, equation (14) should be used,

$$K_{pu} = \frac{X * f_{IW}}{Y} + f_{EW} + \left(\frac{P * f_{NL} + (0.3P + 0.7) * f_{NP}}{Y} \right) + \left[\left(\frac{1}{f_u} - 1 - \left(\frac{P * f_{NL} + (0.3P + 0.7) * f_{NP,P}}{Y} \right) \right) * \frac{[PR]_T}{[PR]_P} \right] \quad (14)$$

where the aforementioned replacement of Y applies and $[PR]_P$ and $[PR]_T$ refer to the binding protein concentration in either the plasma ($[PR]_P$) or the tissue ($[PR]_T$).

In contrast to blood-flow limited PBPK models, permeability-limited PBPK models sub-divide the PBPK organs into further physiological distribution spaces such as the plasma, red blood cells, interstitial and intracellular volumes. A schematic of a permeability-limited PBPK model is presented in Figure 2. Further sub-compartments are available for instance in the kidney which has an additional urine compartment to represent the amount of drug excreted into urine.

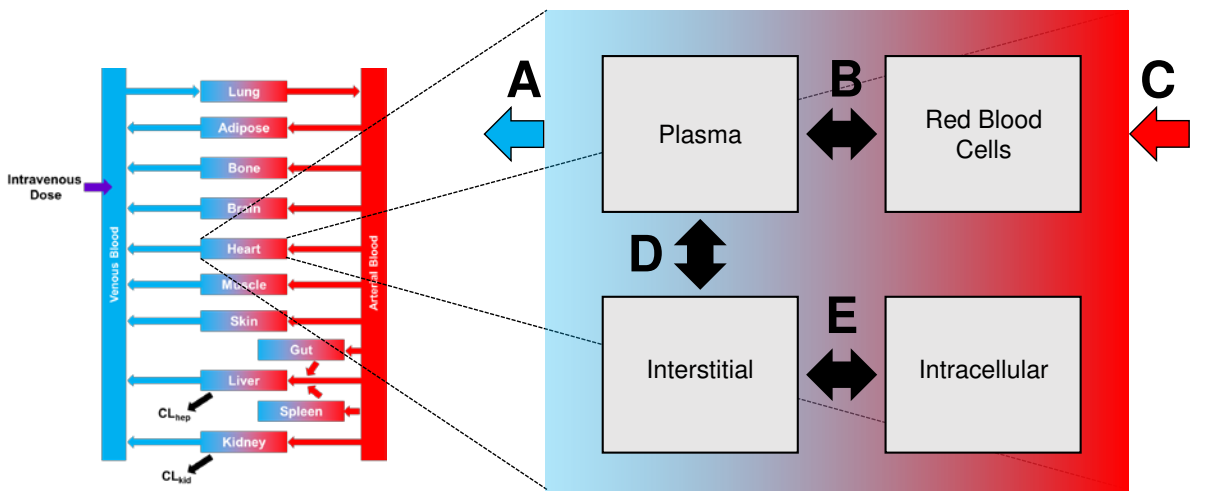


Figure 2 Schematic of a permeability-limited PBPK organ model of the heart. **A** blood flow from the heart to the venous blood compartment, **B** passive drug transport between plasma and red blood cells, **C** blood flow from the arterial blood compartment to the heart, **D** passive drug transport between plasma and interstitial space, **E** passive drug transport between interstitial and intracellular space.

The passive drug transport from plasma to red blood cell ($T_{pls,rbc}$) [$\mu\text{mol}/\text{min}$] (Figure 2 B) is calculated using (15),

$$T_{pls,rbc} = SA_{rbc} * fu * P_{pls,rbc} * (C_{pls} - \frac{C_{rbc}}{K_{rbc}}) \quad (15)$$

where SA_{rbc} is the surface area between red blood cells and plasma [dm^2], fu is fraction unbound, $P_{pls,rbc}$ is the cellular permeability from plasma to red blood cell cells and vice versa [dm/min], C_{pls} is the drug plasma concentration [$\mu\text{mol}/\text{L}$], C_{rbc} is the drug red blood cell concentration [$\mu\text{mol}/\text{L}$] and K_{rbc} denotes the drug partition coefficient between blood cells and plasma .

In this context SA_{rbc} is estimated using (16),

$$SA_{rbc} = HCT * A_{V_{rbc}} * 0.6 * V_{rbc,organ} * f_{vas} \quad (16)$$

where HCT is the hematocrit, $A_{V_{BC}}$ is the surface/volume ratio of red blood cells [$1/\text{dm}$], $V_{rbc,organ}$ is the red blood cell volume in the respective organ [L] and f_{vas} is the vascular fraction of the red blood cells.

3. METHODS

The main parameter driving the sub-compartmental distribution is the drug permeability (P_D) [dm/min] which is calculated using (17),

$$P_D = \left(\frac{MW_{Eff} * 10^9}{336} \right)^{-6} * \frac{10^{Log_{MA}}}{5} * 10^{-5} \quad (17)$$

where MW_{Eff} is the effective molecular weight [g/mol], which takes into account the small contribution of halogens to the molecular volume in relation to their weight and Log_{MA} is the membrane affinity which might be replaced by the LogP values.

The passive drug transport between plasma and interstitial space ($T_{pls,int}$) [$\mu\text{mol}/\text{min}$] (Figure 2 D) is described using equation (18),

$$T_{pls,int} = SA_{int} * fu * P_{endothelial} * (C_{pls} - \frac{C_{int}}{K_{int,rbc}}) \quad (18)$$

where SA_{int} is the surface area between plasma and interstitial volume [dm^2], fu is fraction unbound, $P_{endothelial}$ is the cellular permeability from plasma to interstitial space and vice versa [dm/min], C_{pls} is the drug plasma concentration [$\mu\text{mol}/\text{L}$, C_{int} is the interstitial drug concentration [$\mu\text{mol}/\text{L}$] and $K_{int,rbc}$ denotes the drug partition coefficient between plasma and interstitial space.

Finally, the passive distribution between interstitial and intracellular space ($T_{int,cell}$) [$\mu\text{mol}/\text{min}$] is described by (19),

$$T_{int,cell} = K_{water,int} * PA_{int,cell} * C_{int} - K_{water,cell} * PA_{cell,int} * C_{cell} \quad (19)$$

where $K_{water,int}$ and $K_{water,cell}$ denote the drug partition coefficient interstitial to water and intracellular to water, respectively. PA is the product of P times SA [dm^2/min] and C denotes the interstitial (C_{int}) or intracellular (C_{cell}) drug concentration.

3.2 PBPK Implementation of Metabolism and Transport

Many drugs do not only show passive absorption, distribution and excretion as presented in the blood-flow limited and permeability-limited PBPK models before, they are often actively transported (e.g. substrate of P-gp) and/or metabolized (e.g. substrate of

CYP3A). Drug transporters as well as metabolizing enzymes show an organ-specific distribution and they act in specific sub-compartments of organs. Hence, permeability-limited PBPK models are often better suited for the description of active processes than blood-flow limited models. Figure 3 presents a schematic of a permeability-limited PBPK model with active P-gp-mediated drug transport and CYP3A-mediated drug metabolism.

The organ-specific protein expression can be calculated relatively to the expression in the organ with the highest protein concentration (e.g. P-gp, CYP3A), which is the reference concentration (RF) [$\mu\text{mol/L}$]. The RF corresponds to an expression level of 100%. The organ-specific protein concentrations are then calculated using (20),

$$C_{P,\text{organ}} = RF * \text{EXPR}_{P,\text{organ}} \quad (20)$$

where $C_{P,\text{organ}}$ is the organ-specific protein concentration [$\mu\text{mol/L}$] and $\text{EXPR}_{P,\text{organ}}$ [%] is the expression level of the respective protein in the specific organ. Database comprising whole genome expression arrays from ArrayExpress¹⁶², RT-PCR derived gene expression estimates from the literature^{152,153} and expressed sequence tags (EST) from UniGene¹⁶³ are available^{151,163}. Table 1 summarizes $\text{EXPR}_{P,\text{organ}}$ for CYP3A4 and P-gp for selected organs.

3. METHODS

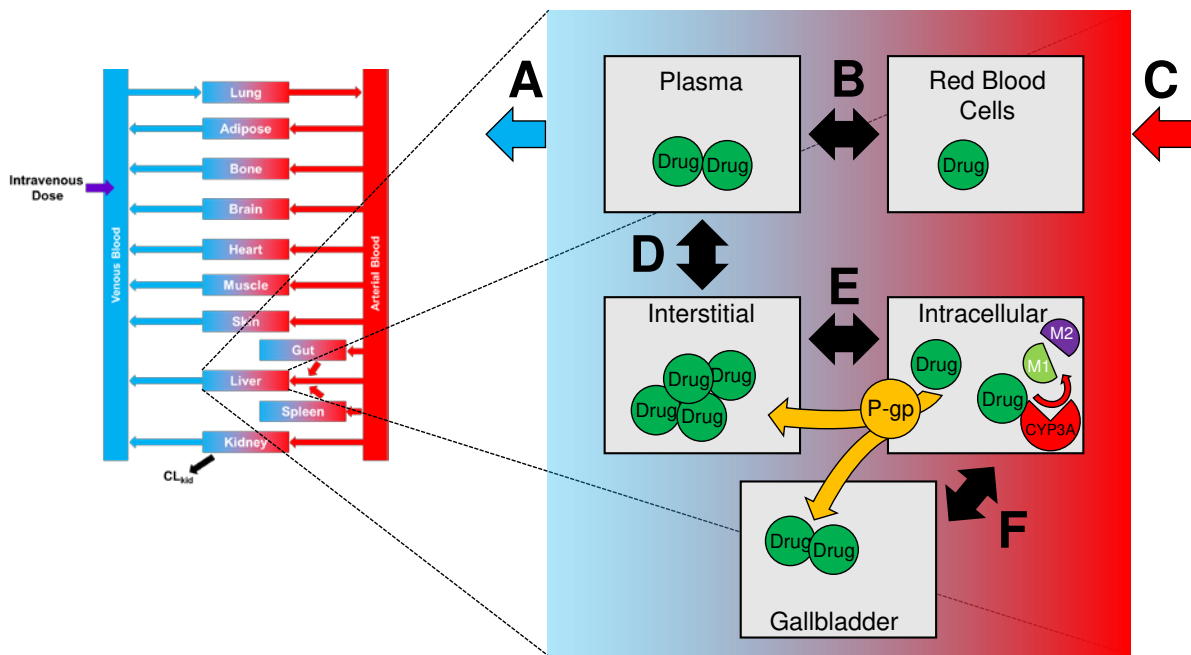


Figure 3 Schematic of a permeability-limited PBPK organ model of the liver. **A** blood flow from the heart to the venous blood compartment, **B** passive drug transport between plasma and red blood cells, **C** blood flow from the arterial blood compartment to the heart, **D** passive drug transport between plasma and interstitial space, **E** passive drug transport between interstitial and intracellular space and **F** passive drug transport between intracellular space and the gallbladder. In the intracellular compartment in yellow: active P-gp-mediated drug transport from the intracellular space to the interstitial space and the gallbladder, in red: active CYP3A-mediated drug metabolism to its metabolites M1 and M2.

The absolute protein concentration of CYP3A4 in the liver ($C_{\text{CYP3A4,liver}}$ [$\mu\text{mol/L}$]) can be calculated using (21),

$$C_{\text{CYP3A4,liver}} = \text{MPPGL} * \text{WT}_{\text{liver}} * \text{Ab}_{\text{CYP3A4}} \quad (21)$$

where MPPGL is the amount of microsomal protein per gram of liver [mg/g], $\text{Ab}_{\text{CYP3A4}}$ is the CYP3A4 microsomal abundance [pmol/mg] and WT_{liver} is the liver weight [kg] assuming the tissue density of the liver to be 1 g/ml.

Table 1 Organ-specific expression (EXPR_{P,organ}) of CYP3A4 and P-gp

Organ	Array [%]	RT-PCR [%]	EST [%]
CYP3A4			
Bone	4.75	-	-
Brain	3.66	0.42	1.23
Fat	-	-	-
Kidney	3.65	0.54	2.87
Liver	100.00	100.00	100.00
Lung	3.67	0.04	-
Muscle	3.14	-	0.80
Small Intestine	39.99	7.28	40.05
P-gp			
Bone	8.85	3.42	-
Brain	30.56	10.73	5.16
Fat	-	-	-
Kidney	66.24	100.00	2.49
Liver	27.28	27.03	5.27
Lung	14.45	9.27	-
Muscle	6.48	1.81	1.05
Small Intestine	100.00	39.60	100.00

CYP3A4 cytochrome P450 3A4, P-gp P-glycoprotein, RT-PCR reverse transcription polymerase chain reaction, EST expressed sequence tags

3.3 Generic PBPK Modeling and Simulation Strategy

The PBPK modeling approach uses “bottom-up” information meaning that the model is built by mechanistically connecting many different sources of information like drug-dependent, drug-independent and drug-biological parameters, to predict concentration-time profiles of a drug without prior provision of in vivo concentration-time profiles. However, these models need to be compared and assessed against in vivo profiles as soon as these are available. Potential deviations between predictions and observations often lead to parameter optimizations, in order to match the predicted to the observed data as closely as possible. This means that the model is also based on “top-down” information

3. METHODS

(concentration-time profiles). Hence, a general PBPK modeling and simulation strategy in most cases relies on a combination of “bottom-up” and “top-down” information. Figure 4 summarizes the modeling and simulation steps for building a PBPK model after administration of an orally formulated drug.

Although there seems to be a clear disconnect between intravenous and oral solution and oral formulation model building, in many cases a separation of these modeling steps is not possible and hence intravenous and oral *in vivo* data is often combined to optimize parameters simultaneously. Due to the diverse nature of informing data of the PBPK models and the wide range of physicochemical and ADME characteristics of compounds, deviations from this general modeling strategy are often demanded and indicated.

3.4 Used Software

All PBPK modeling and simulation work was accomplished using PK-Sim® (5.3.2 and higher) and MoBi® (3.3.2 and higher) provided by Bayer Technology Services, Leverkusen, Germany. All statistical analyses and graphics were compiled using Matlab and its Statistics Toolbox 2013b (32-Bit, The MathWorks, Inc., Natick, Massachusetts, United States). Parameter sensitivity analyses were performed using the model export function of MoBi in combination with Matlab.

Whenever necessary, data, such as concentration-time profiles, were digitized using GetData Graph Digitizer 2.25.0.32¹⁶⁴.

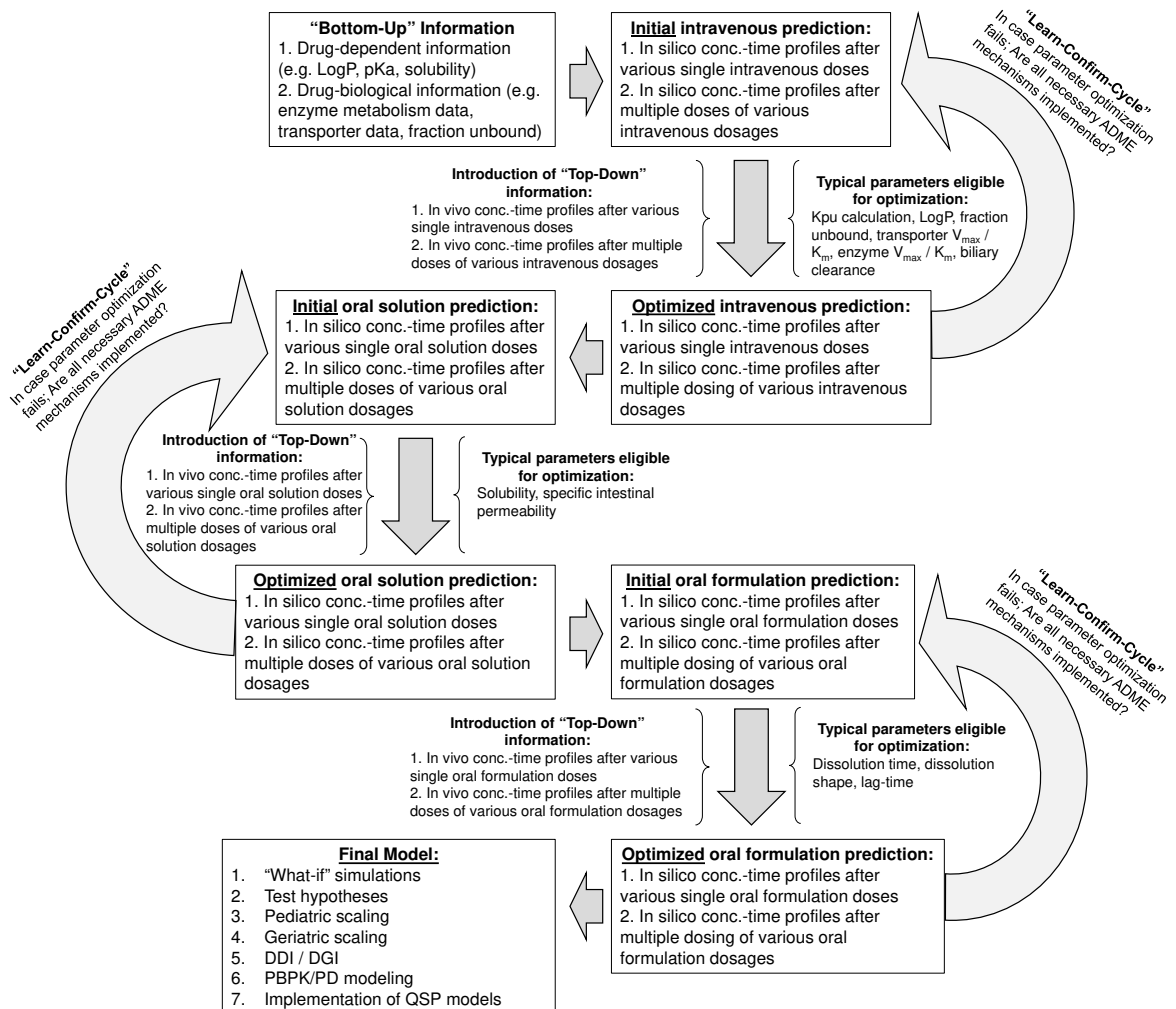


Figure 4 A general PBPK modeling strategy for an orally formulated drug. LogP n-octanol to water partition coefficient, pKa acid dissociation constant, V_{max} maximum reaction velocity, K_M Michaelis-Menten constant, ADME absorption, distribution, metabolism and excretion, DDI drug-drug-interaction, DGI drug-gene-interaction, PBPK physiologically-based pharmacokinetics, PD pharmacodynamics, QSP quantitative systems pharmacology. “Learn-Confirm-Cycle” adopted from Sheiner¹⁶⁵.

4 Results

4.1 Project I:

Physiologically-based pharmacokinetic (PBPK) analysis of zoptarelin doxorubicin drug-drug interaction potential - integrating preclinical, phase I and phase II data.

A physiologically based pharmacokinetic (PBPK) parent-metabolite model of the chemotherapeutic zoxtarelin doxorubicin—integration of in vitro results, Phase I and Phase II data and model application for drug–drug interaction potential analysis

Nina Hanke¹ · Michael Teifel² · Daniel Moj¹ · Jan-Georg Wojtyniak¹ · Hannah Britz¹ · Babette Aicher² · Herbert Sindermann² · Nicola Ammer² · Thorsten Lehr¹

Received: 1 September 2017 / Accepted: 28 November 2017
© Springer-Verlag GmbH Germany, part of Springer Nature 2017

Abstract

Purpose Zoxtarelin doxorubicin is a fusion molecule of the chemotherapeutic doxorubicin and a luteinizing hormone-releasing hormone receptor (LHRHR) agonist, designed for drug targeting to LHRHR positive tumors. The aim of this study was to establish a physiologically based pharmacokinetic (PBPK) parent-metabolite model of zoxtarelin doxorubicin and to apply it for drug–drug interaction (DDI) potential analysis.

Methods The PBPK model was built in a two-step procedure. First, a model for doxorubicin was developed, using clinical data of a doxorubicin study arm. Second, a parent-metabolite model for zoxtarelin doxorubicin was built, using clinical data of three different zoxtarelin doxorubicin studies with a dosing range of 10–267 mg/m², integrating the established doxorubicin model. DDI parameters determined in vitro were implemented to predict the impact of zoxtarelin doxorubicin on possible victim drugs.

Results In vitro, zoxtarelin doxorubicin inhibits the drug transporters organic anion-transporting polypeptide 1B3 (OATP1B3) and organic cation transporter 2 (OCT2). The model was applied to evaluate the in vivo inhibition of these transporters in a generic manner, predicting worst-case scenario decreases of 0.5% for OATP1B3 and of 2.5% for OCT2 transport rates. Specific DDI simulations using PBPK models of simvastatin (OATP1B3 substrate) and metformin (OCT2 substrate) predict no significant changes of the plasma concentrations of these two victim drugs during co-administration.

Conclusions The first whole-body PBPK model of zoxtarelin doxorubicin and its active metabolite doxorubicin has been successfully established. Zoxtarelin doxorubicin shows no potential for DDIs via OATP1B3 and OCT2.

Keywords AEZS-108 · AN-152 · Doxorubicin · PBPK modeling · Drug–drug interaction · Targeted chemotherapy

Introduction

Zoxtarelin doxorubicin (also known as AEZS-108, AN-152 and ZEN-008) is a fusion molecule of the chemotherapeutic doxorubicin and an LHRHR agonist [1]. The DNA intercalating agent doxorubicin is chemically linked to the carrier molecule D-Lys6-LHRH, which enables specific binding and selective uptake of zoxtarelin doxorubicin by tumors expressing receptors for LHRH (“drug targeting”), followed by the intracellular release of the active component doxorubicin. The rationale for the synthesis and development of this hybrid molecule is to increase the cytotoxic specificity, while decreasing the general toxicity when compared to doxorubicin alone.

Electronic supplementary material The online version of this article (<https://doi.org/10.1007/s00280-017-3495-2>) contains supplementary material, which is available to authorized users.

✉ Thorsten Lehr
thorsten.lehr@mx.uni-saarland.de

¹ Clinical Pharmacy, Saarland University, Campus C2 2,
66123 Saarbruecken, Germany

² Aeterna Zentaris GmbH, Weismuellerstr. 50,
60314 Frankfurt, Germany

In vitro, zoptarelin doxorubicin has shown stronger anti-proliferative effects in human LHRHR positive ovarian and endometrial cancer cells compared to doxorubicin [2], as well as higher cytotoxic potency in LHRHR expressing human oral and laryngeal carcinoma cells [3]. In nude mice bearing subcutaneous human LHRHR positive endometrial and ovarian tumors, equimolar doses of zoptarelin doxorubicin were significantly more effective in tumor growth inhibition compared to doxorubicin. Furthermore, in the high-dose study arm, seven of the ten mice treated with doxorubicin died, while all ten mice treated with zoptarelin doxorubicin survived [4]. Growth of subcutaneous human urinary bladder cell tumors in nude mice was more potently inhibited by zoptarelin doxorubicin compared to doxorubicin [5].

In clinical Phase I and Phase II studies, zoptarelin doxorubicin has shown therapeutic activity in patients with LHRHR positive ovarian and endometrial cancer [6, 7]. The PK properties of zoptarelin doxorubicin have been assessed in the first-in-human, dose escalation Phase I study in patients. Plasma half-life and clearance were calculated to be approximately 2 h and 1 L/(min*m²), with the reservation that in this early study the measured plasma concentrations showed a high variability [8]. Due to the size and hydrophilicity of zoptarelin doxorubicin (decapeptide coupled via a glutaryl linker to doxorubicin), passive distribution into tissues is limited, but cellular entry is expected to be facilitated by target binding to LHRHR, followed by internalization of the drug–receptor complex and intracellular cleavage to release the doxorubicin moiety within the target cells. In aqueous solution and in blood plasma, zoptarelin doxorubicin is subject to spontaneous and carboxylesterase-mediated hydrolysis into doxorubicin and probably D-Lys6-LHRH-glutarate. Metabolite profiles in liver microsomal incubations suggest a minor role of oxidative metabolism compared to hydrolysis.

Doxorubicin PK studies in patients show that doxorubicin follows a multiphasic disposition after intravenous infusion. The initial distribution half-life of approximately 5 min indicates rapid tissue uptake, while a terminal half-life of 20–48 h reflects slow elimination from tissues. Steady-state distribution volumes exceed 20–30 L/kg revealing extensive drug uptake into tissues. Plasma clearance is in the range of 8–20 mL/min/kg and is governed by metabolism and biliary excretion [9–11].

To evaluate the zoptarelin doxorubicin DDI potential in vitro, a DDI screening on cytochrome P450 (CYP) enzymes and recommended drug transporters has been performed. In these assays, zoptarelin doxorubicin showed no inhibition or induction of CYP enzymes, but in the transporter studies, zoptarelin doxorubicin inhibited OATP1B3 and OCT2 with IC₅₀ values of 16.5 and 3.26 μmol/L, respectively. Doxorubicin itself and D-Lys6-LHRH-glutarate inhibited OATP1B3 with IC₅₀ values > 100 μmol/L

and OCT2 with IC₅₀ values > 200 μmol/L. Based on these results, in vivo interactions with drugs that are substrates of OATP1B3 (e.g. simvastatin) or OCT2 (e.g. metformin) could not be ruled out. As these victim drugs are widely used, their co-administration with zoptarelin doxorubicin would be very likely, creating a need to investigate the impact of these potential DDIs. However, clinical DDI studies involving DNA intercalating agents are, for ethical reasons, difficult to conduct. PBPK modeling offers an excellent alternative to dedicated clinical DDI studies and is recommended and supported by the FDA (US Food and Drug Administration) and EMA (European Medicines Agency) to predict the magnitude of in vivo DDIs from in vitro results [12, 13].

The objectives of this modeling investigation were (1) to establish the first whole-body PBPK model of zoptarelin doxorubicin and its active metabolite doxorubicin, (2) to apply the zoptarelin doxorubicin model for a general assessment of the DDI potential with OATP1B3 and OCT2 victim drugs and (3) to predict the magnitude of zoptarelin doxorubicin DDIs with simvastatin and metformin in worst-case scenarios.

Materials and methods

Clinical studies used

The results of three different clinical studies with PK blood sampling were available for model development (Table 1). Study 1 (ZEN-008-Z023) is a Phase I first-in-human sequential group dose escalation and PK study, performed in 17 female patients with LHRHR positive tumors. Zoptarelin doxorubicin was administered as a 2-h intravenous infusion, once every 21 days, in doses of 10, 20, 40, 80, 160 or 267 mg/m² [8]. Data of two patients were excluded due to bioanalytical issues. Study 2 (AEZS-108-046) is a combined Phase I/II study, with PK sampling performed in a sub-set of 14 male or female patients with locally advanced unresectable or metastatic LHRHR positive urothelial carcinoma who failed platinum-based chemotherapy. Zoptarelin doxorubicin was administered as a 2-h infusion every 21 days in doses of 160, 210 or 267 mg/m² (results not published, yet). Data of four patients were excluded because of sample hemolysis. Study 3 (AEZS-108-053) is a Phase I cardiac safety and PK study comparing zoptarelin doxorubicin and doxorubicin therapy in 21 and 11 female patients, respectively, with locally advanced recurrent or metastatic cancer. Zoptarelin doxorubicin was administered as a 2-h infusion of 267 mg/m². Doxorubicin was administered as a 1-h infusion of 60 mg/m² (results not published, yet). Data of two patients were excluded due to sampling issues. Details on the patient demographics of these studies (age, weight, body surface area) are listed in Table 1.

Table 1 Studies used for zoxtarelin doxorubicin PBPK model development and evaluation

Dose (mg/m ²)	Administration	n	Women (%)	Age (years)	Weight (kg)	BSA (m ²)	Dataset	Study references
Doxorubicin								
36	iv (96 h), SD	7	50 ^a	30.0 ^a	64.0 ^a	1.73 ^a	Training	[15]
30	iv (bolus), QD	7	50 ^a	30.0 ^a	64.0 ^a	1.73 ^a	Training	[16]
60 ^a	iv (1 h), SD ^a	3 ^a	100 ^a	71.0 (67–74) ^a	67.0 (58–84) ^a	1.64 (1.57–1.77) ^a	Training	[18]
60	iv (1 h), SD	9	100	59.9 (44–74)	64.1 (41–84)	1.63 (1.28–1.81)	Training	Study 3 (AEZS-108-053)
Zoxtarelin doxorubicin								
10	iv (2 h), SD	1	100	58.0	84.0	1.89	Training	Study 1 (ZEN-008-Z023)
20	iv (2 h), SD	1	100	48.0	65.0	1.70	Training	Study 1 (ZEN-008-Z023)
40	iv (2 h), SD	1	100	69.0	145.0	2.48	Training	Study 1 (ZEN-008-Z023)
80	iv (2 h), SD	1	100	44.0	55.0	1.63	Training	Study 1 (ZEN-008-Z023)
160	iv (2 h), SD	6	100	59.3 (55–69)	83.2 (58–107)	1.89 (1.60–2.12)	Test	Study 1 (ZEN-008-Z023)
267	iv (2 h), SD	5	100	48.8 (31–63)	66.9 (59–85)	1.73 (1.64–1.89)	Test	Study 1 (ZEN-008-Z023)
160	iv (2 h), SD	3	0	64.0 (63–65)	78.3 (69–90)	1.97 (1.84–2.07)	Test	Study 2 (AEZS-108-046)
210	iv (2 h), SD	3	29	66.0 (55–83)	89.6 (64–121)	2.02 (1.71–2.38)	Test	Study 2 (AEZS-108-046)
267	iv (2 h), SD	4	25	69.0 (62–87)	70.0 (52–86)	1.81 (1.51–1.98)	Test	Study 2 (AEZS-108-046)
267	iv (2 h), SD	21	100	61.6 (46–78)	71.4 (45–108)	1.73 (1.35–2.13)	Training	Study 3 (AEZS-108-053)

Values given for age, weight and BSA are arithmetic means, minima and maxima

^aAssumed, BSA: body surface area, iv: intravenous, n: number of individuals studied, QD: once daily, SD: single dose, test: test dataset (model evaluation), training: training dataset (model development and parameter optimization)

To supplement the measurements of the doxorubicin arm of Study 3, published human *in vivo* data of doxorubicin in plasma, white blood cells, urine and feces were added, to build the “training dataset” for the development and parameter optimization of the doxorubicin model. As training data for zoxtarelin doxorubicin model development and parameter optimization, the four lowest dose applications of Study 1 (10, 20, 40, 80 mg/m²) plus the measurements of Study 3 (267 mg/m², highest clinical dose) were chosen. Evaluation of the zoxtarelin doxorubicin model was carried out with the clinical data of the remaining dosing groups of Study 1 as well as the complete clinical Study 2 as the “test dataset”.

Software

PBPK modeling was performed with PK-Sim® and MoBi® (Open Systems Pharmacology Suite, Version 7.0.0, Bayer AG, Leverkusen, Germany). Parameter optimization was accomplished using the Monte Carlo algorithm of the “Parameter Identification Toolbox” in MATLAB® (Version R2013b, The MathWorks, Inc., Natick, MA, USA). Sensitivity analysis was performed within PK-Sim®. Graphics and PK parameter analyses were compiled with MATLAB® R2013b.

Doxorubicin model development

Model development was started with the establishment of a model of the active metabolite doxorubicin. To limit the

parameters to be optimized during model development, the minimal number of processes necessary was implemented into the model. For the doxorubicin model these are (1) doxorubicin binding to DNA, (2) an unspecific metabolic hepatic clearance and (3) an unspecific elimination to bile. Glomerular filtration and enterohepatic cycling were enabled, as they are active under physiological conditions. A diagram of the PBPK model structure is given in Zoxtarelin Doxorubicin Supplementary Fig. 1.

To model the binding of doxorubicin to DNA as the cause of the extensive distribution into and slow elimination from body tissues, a binding partner was implemented into the DNA-rich organs, with published values for K_d and k_{off} [14]. In the literature, there are reports of doxorubicin concentration measurements in plasma and white blood cells [15, 16] that were utilized to inform the distribution (cellular permeability, see below) and DNA binding processes. As there is no white blood cell (WBC) compartment in PK-Sim, the red blood cell (RBC) compartment was used as a substitute to represent the nucleated white blood cells. The volume of this red blood cell compartment is larger than the physiological volume of the white blood cells; therefore, a relative concentration of DNA binding sites (that are absent in the anucleate RBCs) was implemented into the RBC compartment and estimated. The DNA binding site reference concentration (concentration in the tissue with the highest concentration of binding sites) was also optimized.

To account for hepatic metabolism to doxorubicinol and other metabolites, an unspecific metabolic first-order clearance was implemented into the liver and optimized.

To model biliary excretion, an unspecific first-order transport from liver to bile was implemented and estimated. As the lipophilicity of doxorubicin is very low ($\log P = 1.27$), calculated passive cellular permeability is low. However, doxorubicin has been reported to be a substrate of diverse transporters, including the human isoforms of OATP1A and OATP1B [17]. To accurately describe the available clinical data, passive cellular permeability was increased, to compensate for active transport processes that have not been implemented into the model.

To obtain values for the parameters that could not be adequately informed from literature or in-house preclinical studies, optimization was performed by simultaneously fitting the model to the data of the doxorubicin arm of Study 3 (9 patients), measured doxorubicin plasma and white blood cell intracellular concentration–time profiles of Speth et al. [15, 16] (two studies with mean values of 7 patients each) and published fraction of doxorubicin dose administered excreted unchanged to urine and feces information [18].

Zoptarelin doxorubicin model development

The final doxorubicin model was then used in the establishment of the zoptarelin doxorubicin model, together with clinically observed plasma concentration–time profiles of zoptarelin doxorubicin and doxorubicin following intravenous administration of zoptarelin doxorubicin. The following processes were implemented into the zoptarelin doxorubicin model: (1) zoptarelin doxorubicin binding to the LHRHR target, (2) internalization of zoptarelin doxorubicin by LHRHR and (3) hydrolysis of zoptarelin doxorubicin to release the active doxorubicin moiety within blood plasma as well as intracellularly. A diagram of the PBPK model structure is given in Zoptarelin Doxorubicin Supplementary Fig. 1.

To model the binding of zoptarelin doxorubicin to its target LHRHR, this receptor was implemented and values for K_d , k_{off} as well as the LHRHR reference concentration were estimated. Expression of LHRHR is described in the literature to occur in non-malignant pituitary, ovary, testis, prostate and breast cells, as well as in cancer cells of diverse origin [19, 20]. In the model, LHRHR was implemented into the gonadal compartment (approximate organ volume of 0.013 L). To compensate for the missing pituitary, prostate, breast and, most notably, cancer cell expression, as these tissues are not represented in standard PK-Sim individuals, LHRHR expression was further added at a 50% expression level to the lung compartment (approximate organ volume of 1 L). The lung was chosen as a well perfused organ with no special pharmacokinetic function in this analysis (as would

have been the case with liver or kidney). Implementation of zoptarelin doxorubicin binding to LHRHR into the model clearly improved the shape of the simulated zoptarelin doxorubicin plasma concentration–time curves.

Internalization of zoptarelin doxorubicin was implemented as a cellular uptake facilitated by LHRHR (into gonads and lung), followed by intracellular hydrolysis to release the doxorubicin moiety. As K_M value of this uptake process an IC_{50} value of 7.45 nmol/L was used, measured in a radio ligand displacement assay with very low concentrations of the radiolabeled ligand [21]. Therefore, it was assumed that $IC_{50} = K_i$ and this value was used as K_M value for the internalization process. A very similar IC_{50} value of 10 nmol/L has been described in the literature for the binding of the endogenous agonist LHRH to LHRHR [22]. The internalization turnover number was estimated.

To model the hydrolysis of zoptarelin doxorubicin to D-Lys6-LHRH-glutarate and doxorubicin, a hydrolytic clearance was implemented into blood plasma, gonads and lung. The hydrolysis rate in plasma was optimized, informed by the measured concentrations of zoptarelin doxorubicin being hydrolyzed and of doxorubicin resulting from this hydrolysis. The hydrolysis rate in gonads and lung was assumed to be the same as in plasma.

Parameter optimization was performed by simultaneously fitting the model to measured zoptarelin doxorubicin and doxorubicin plasma concentration–time profiles after administration of zoptarelin doxorubicin obtained in Study 1 (10, 20, 40, 80 mg/m²) and Study 3 (267 mg/m²).

Virtual population characteristics

To predict the variability of the simulated plasma concentration–time profiles, virtual populations of 100 individuals were generated according to the population demographics of each respective dosing group of the Studies 1, 2 and 3. The ICRP (International Commission on Radiological Protection) database in PK-Sim [23] was used for generation of virtual Caucasian populations. In the generated virtual populations, age, height, weight, corresponding organ volumes, tissue compositions, blood flow rates, etc. are varied by an implemented algorithm within the limits of the ICRP database. In addition, the zoptarelin doxorubicin hydrolysis rate, the reference concentrations of the binding partners LHRHR and DNA, as well as the doxorubicin hepatic and biliary clearance rates were set to be log-normally distributed with variabilities of 25%CV (relative standard deviation). To create a virtual population for the DDI predictions, reflecting an even larger demographic variability and representing the target cancer patient population, preliminary demographics of a large clinical Phase III study (Study 4, AEZS-108-050 [24]) were used.

Model evaluation

Model performance was evaluated by comparison of the predicted concentration–time profiles of the virtual populations to the plasma concentrations observed in the clinical studies, which had not been used during parameter optimization (test dataset). All population predictions compared to observed plasma concentration–time profiles are documented in the “Results” section or in the supplementary material, together with predicted compared to observed AUC_{last} and C_{max} values of all studies. Furthermore, the biological plausibility of optimized parameters was checked and sensitivity analyses were conducted for the doxorubicin and zoptarelin doxorubicin models.

Sensitivity of the final models to single parameters (local sensitivity analysis) was investigated, measured as changes of the AUC extrapolated to infinity (AUC_{inf}) of a simulation of the highest applied dose. All parameters relevant to the respective model were included into the analysis, optimized parameters as well as parameters fixed to literature values. Parameters were defined as relevant if they have been optimized (see Zoptarelin Doxorubicin Supplementary Tables 4 and 5), if they might have a strong influence due to calculation methods used in the model (lipophilicity, fraction unbound), if they are related to optimized parameters (doxorubicin-DNA K_d , doxorubicin-DNA k_{off} , doxorubicin blood/plasma ratio) or if they had significant impact in former models (solubility, intestinal permeability, EHC continuous fraction, cellular permeability, blood/plasma ratio, GFR fraction). A sensitivity value of -1.0 signifies that a 10% increase of the examined parameter causes a 10% decrease of the simulated AUC_{inf} .

General assessment of the zoptarelin doxorubicin DDI potential

To obtain a general statement on the DDI potential of zoptarelin doxorubicin, the final model was applied to predict the *in vivo* inhibition of OATP1B3 and OCT2 in a generic manner (independent of the victim drug affected by this inhibition), by calculating the relative change of these transporters’ K_M values due to inhibition by zoptarelin doxorubicin.

Assuming a competitive inhibition and Michaelis–Menten kinetics, we expect a change in the K_M value of the transport of the affected victim drugs, but not of the maximal transport rate, as competitive inhibition can be overcome by high victim drug concentrations. Therefore, the inhibition is characterized by the relative change of K_M according to Eq. 2:

K_M apparent, victim drug ($\mu\text{mol/L}$)

$$= K_M \text{ victim drug} * \left(1 + \frac{\text{inhibitor concentration}}{\text{inhibitor } K_i} \right) \quad (1)$$

K_M apparent, victim drug (%)

$$= 100\% * \left(1 + \frac{\text{inhibitor concentration}}{\text{inhibitor } K_i} \right) \quad (2)$$

Simulations to assess the DDI potential of zoptarelin doxorubicin were performed for the highest clinical dose of 267 mg/m^2 zoptarelin doxorubicin as intravenous infusion over 2 h. OATP1B3 is predominantly expressed at the basolateral membranes of hepatocytes located around the central vein, facilitating the uptake of organic anions for hepatic clearance [25]. To estimate the effect of zoptarelin doxorubicin on OATP1B3, predicted population interstitial unbound concentrations of zoptarelin doxorubicin in the liver were used as input for Eq. 2. OCT2 is mainly expressed at the basolateral membrane of renal tubule cells, facilitating the uptake of organic cations from the blood for subsequent renal secretion [26]. To estimate the impact of zoptarelin doxorubicin on OCT2, predicted population interstitial unbound concentrations of zoptarelin doxorubicin in the kidney were employed.

The zoptarelin doxorubicin K_i values for inhibition of OATP1B3 and OCT2 were calculated from IC_{50} values determined *in vitro* (16.5 and $3.26 \mu\text{mol/L}$), the substrate concentrations applied in these assays ($0.05 \mu\text{mol/L}$ estradiol-17beta-glucuronide and $10.0 \mu\text{mol/L}$ metformin) and the OATP1B3 and OCT2 transport K_M values for these substrates (15.8 [27] and $990.0 \mu\text{mol/L}$ [28]), according to the Cheng-Prusoff equation for competitive inhibition [29]:

$$K_i = \frac{IC_{50}}{1 + \text{substrate concentration}/K_M} \quad (3)$$

K_i values for pure competitive inhibition are independent of the affected victim substrate, the substrate concentration and the assay conditions [30]. Therefore, the relative changes of K_M calculated from Eq. 2 are in theory applicable to all putative zoptarelin doxorubicin victim drugs transported by OATP1B3 and OCT2.

Specific assessment of the zoptarelin doxorubicin DDI potential

To evaluate the *in vivo* interaction potential of zoptarelin doxorubicin with actual OATP1B3 and OCT2 victim drugs, the model was coupled to PBPK models of simvastatin and metformin (for details on the simvastatin and metformin PBPK models see the Simvastatin and Metformin Supplemantaries). Simvastatin acid, the pharmacologically active metabolite of the prodrug simvastatin, is recommended by the FDA as a victim drug for the clinical investigation of OATP1B1/1B3 DDIs [31]. Metformin is recommended by the FDA as well-established substrate of the cationic

transport system for the use in clinical studies of DDIs involving OCT2/MATE [31].

Simvastatin is administered in the form of the inactive lactone that is hydrolyzed after ingestion to the active simvastatin acid. Only the acid form is transported by OATP1B1 and OATP1B3 from blood plasma into hepatocytes. The model applied for DDI prediction is a whole-body parent-metabolite PBPK model of simvastatin lactone and simvastatin acid. Because of the overlapping substrate specificities of OATP1B1 and OATP1B3, it is difficult to pinpoint the exact contribution of each isoform to simvastatin acid transport [32]. As the goal of this analysis was to assess worst-case scenarios, a combined OATP1B1/3 transport was modeled and this whole transport was inhibited with the zoptarelin doxorubicin K_i determined for OATP1B3, even though OATP1B1 was not affected in vitro. This approach results in an overprediction of the impact of OATP1B3 inhibition, but avoids underprediction of the DDI potential due to misspecification of the OATP1B3 contribution.

As worst-case co-administration scenarios, simultaneous administrations of 267 mg/m^2 zoptarelin doxorubicin with 80 mg simvastatin (once daily, day 5) or 1000 mg metformin (three times daily, day 5) were simulated, and victim drug plasma concentrations with and without co-administration of zoptarelin doxorubicin were assessed in population predictions. Different time intervals between the start of zoptarelin doxorubicin infusion and the day 5 morning dose of the victim drugs were simulated, to find the administration schemes resulting in highest drug–drug interaction impact for worst-case scenario assessment.

Results

A comprehensive parent-metabolite PBPK model for the prediction of zoptarelin doxorubicin and doxorubicin concentrations following different intravenous doses of zoptarelin doxorubicin has been successfully developed.

A schematic representation of the parent-metabolite model structure is shown in Zoptarelin Doxorubicin Supplementary Fig. 1. All drug-dependent parameters of the final model, taken from literature or preclinical studies as well as all optimized parameter values, are given in Zoptarelin Doxorubicin Supplementary Table 4. All system-dependent parameters of the final model, particularly expression levels of the implemented binding partners in the different tissues with their geometric standard deviations of lognormal distribution in virtual populations, are given in Zoptarelin Doxorubicin Supplementary Table 5. No other system-dependent parameters were changed or adjusted.

PBPK model development and performance

The established doxorubicin and zoptarelin doxorubicin PBPK models show excellent descriptive and predictive performance.

The data used for doxorubicin model development consisted of individual plasma concentration–time profiles following application of 60 mg/m^2 of doxorubicin to a total of nine patients. These measurements were supplemented by literature data of white blood cell concentrations and excretion to urine and feces information (Table 1). Predicted and observed doxorubicin plasma concentrations of Study 3 as well as fractions excreted to urine and feces following administration of doxorubicin are presented in Zoptarelin Doxorubicin Supplementary Fig. 2 (training dataset). Predicted and observed doxorubicin plasma and white blood cell concentrations following administration of doxorubicin as published by Speth et al. are shown in Zoptarelin Doxorubicin Supplementary Fig. 3 (training dataset). These concentrations were fitted with lower weight compared to the measurements of Study 3, given the age of the data and the assumption underlying the blood cell concentrations that 10^9 cells equal a volume of 1 mL , knowing that white blood cells are very diverse in size and shape. Prediction of the doxorubicin concentrations resulting from administration of zoptarelin doxorubicin is presented in Figs. 1 and 2 as well as in Zoptarelin Doxorubicin Supplementary Figs. 4 and 5.

The data used for zoptarelin doxorubicin model establishment included individual plasma concentration–time profiles collected in three clinical trials, following application of seven different doses of zoptarelin doxorubicin in a range of $10\text{--}267 \text{ mg/m}^2$. Plasma concentrations of zoptarelin doxorubicin and doxorubicin were collected in a total of 46 patients (Table 1). Model performance of the final zoptarelin doxorubicin model is demonstrated in Fig. 1 and Zoptarelin Doxorubicin Supplementary Fig. 4 for the studies used during parameter optimization (training dataset) and in Fig. 2 and Zoptarelin Doxorubicin Supplementary Fig. 5 for the independent clinical data (test dataset).

As can be seen in Fig. 1, the inter-individual variability of the measured concentrations is wider for zoptarelin doxorubicin than for doxorubicin. This is unexpected, as the variability of its main ADME mechanism, namely the hydrolysis of zoptarelin doxorubicin to doxorubicin, affects both analytes. The more pronounced variability of the parent compound concentrations in blood plasma, where zoptarelin doxorubicin and doxorubicin are sampled, might result from its very low permeability compared to doxorubicin, which extensively distributes into body tissues [11]. The predicted variability in the population simulations is also wider for zoptarelin doxorubicin.

Furthermore, the variance of the measured concentrations in the very first clinical Study 1 is higher than in the

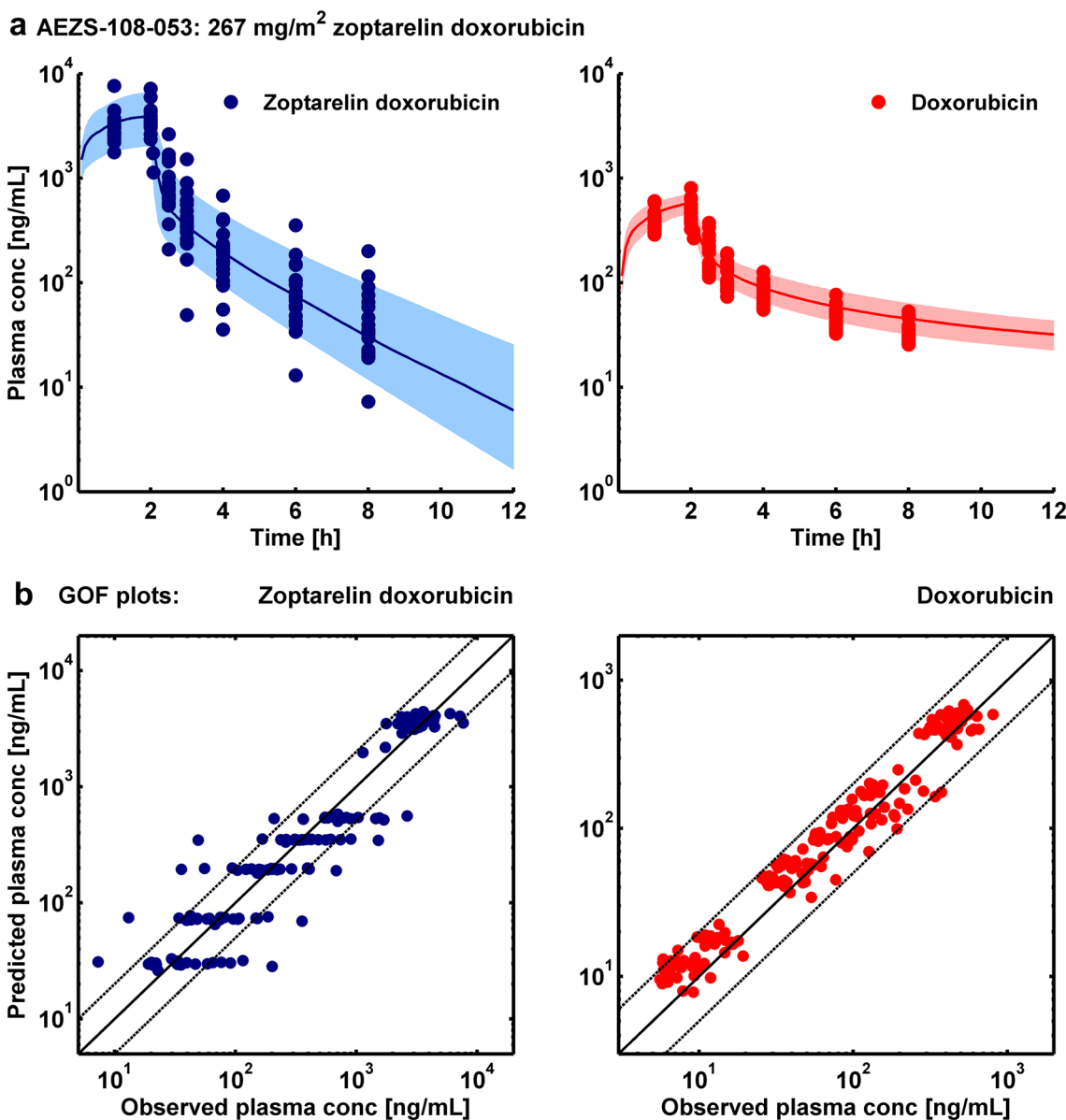


Fig. 1 Training dataset: **a** Population simulations (semilog scale) compared to observed data of zoptarelin doxorubicin (blue) and doxorubicin plasma concentrations (red) following intravenous administration of 267 mg/m² zoptarelin doxorubicin. Clinical data (Study 3, $n=21$) are shown as dots. Population simulation medians are shown as lines; the shaded areas depict the 5th–95th percentile popula-

tion prediction intervals. **b** Goodness of fit (GOF) plots (log scale) demonstrating the correlation of individual predicted with observed zoptarelin doxorubicin (blue) and doxorubicin plasma concentrations (red) of the study shown above. The solid lines represent the line of unity; the dashed lines indicate twofold deviation

following trials (see Zoptarelin Doxorubicin Supplementary Fig. 5, test dataset). This high variability might be the result of errors in sampling time or of hydrolytic cleavage of zoptarelin doxorubicin prior to freezing of some of the blood samples [8]. These issues could be resolved and, therefore, did not affect later measurements.

Precision of model parameter estimates is shown in the tables listing the drug-dependent and system-dependent

zoptarelin doxorubicin PBPK model parameters (Zoptarelin Doxorubicin Supplementary Tables 4 and 5).

Using the final model, pharmacokinetic parameters (AUC_{last} and C_{max}) of all dosing groups have been calculated from population simulations as mean values with standard deviation and compared to observed values (see Zoptarelin Doxorubicin Supplementary Tables 1 and 2). Prediction errors for AUC_{last} and C_{max} values are also

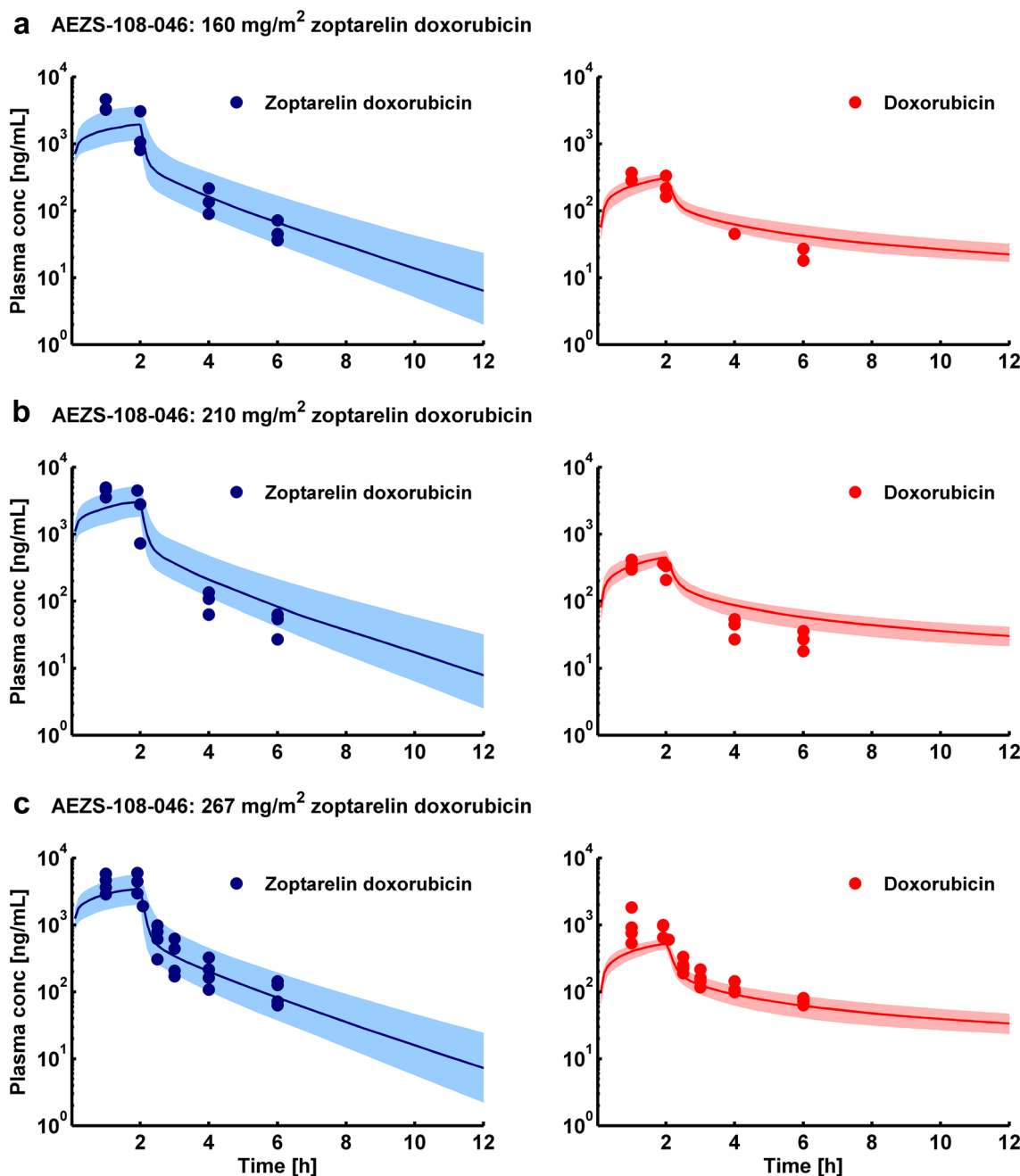


Fig. 2 Test dataset: Population simulations (semilog scale) compared to observed data of zoptarelin doxorubicin (blue) and doxorubicin plasma concentrations (red) following intravenous administration of 160, 210 or 267 mg/m² zoptarelin doxorubicin. Clinical data (Study

2, $n=3$, $n=3$ and $n=4$) are shown as dots. Population simulation medians are shown as lines; the shaded areas depict the 5th–95th percentile population prediction intervals

given in Zoptarelin Doxorubicin Supplementary Tables 1 and 2. Plots of predicted versus observed AUC_{last} and C_{max} values with twofold prediction success limits are shown in Zoptarelin Doxorubicin Supplementary Fig. 6.

PBPK model sensitivity analysis

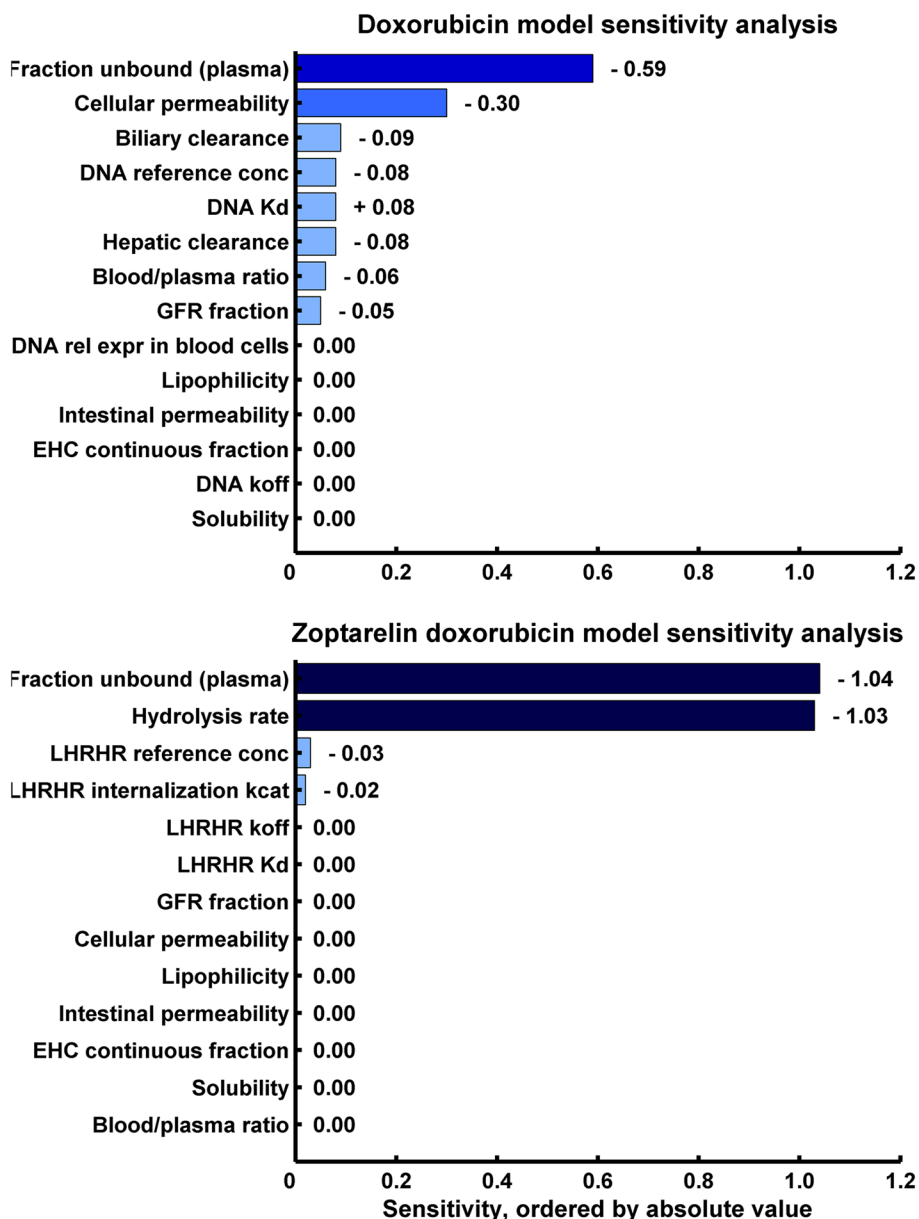
Sensitivity analyses were conducted for the doxorubicin and the zoptarelin doxorubicin model, with simulations of

single intravenous administrations of 60 mg/m^2 doxorubicin (1-h infusion) and of 267 mg/m^2 zoptarelin doxorubicin (2-h infusion), respectively. The investigated model parameters and results are listed in Fig. 3. The doxorubicin model is sensitive to the values of fraction unbound in plasma (sensitivity value of -0.6) and cellular permeability (sensitivity value of -0.3). The zoptarelin doxorubicin model is sensitive to the values of fraction unbound in plasma (sensitivity value of -1.0) and zoptarelin doxorubicin hydrolysis rate (sensitivity value of -1.0).

General assessment of the zoptarelin doxorubicin DDI potential

To obtain a general assessment of the in vivo DDI potential of zoptarelin doxorubicin via OATP1B3 and OCT2, independently of the substrate affected by this inhibition, the relative changes of the apparent K_M values for these two transporters were calculated according to Eq. 2. As input inhibitor concentrations, predicted population interstitial unbound concentrations of zoptarelin doxorubicin in the liver and the kidney, respectively, were used (267 mg/m^2 zoptarelin doxorubicin, 2-h infusion). Zoptarelin doxorubicin K_i values were calculated to be $16.45 \mu\text{mol/L}$ for

Fig. 3 Doxorubicin and zoptarelin doxorubicin model sensitivity analysis results. Conc: concentration, EHC: enterohepatic circulation, GFR: glomerular filtration rate, k_{cat} : catalytic rate constant, K_d : dissociation constant, k_{off} : dissociation rate constant, LHRHR: luteinizing hormone-releasing hormone receptor, rel expr: relative expression, normalized to tissue with highest expression



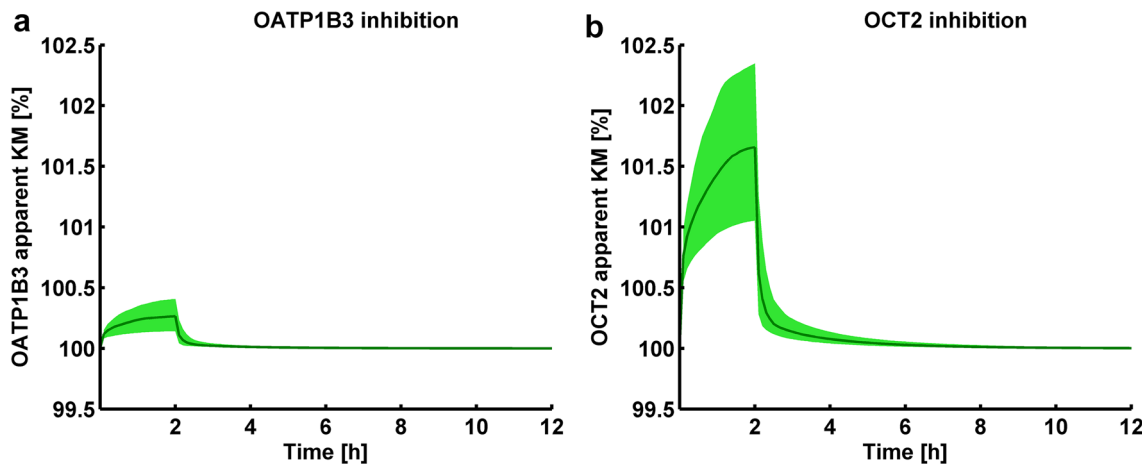


Fig. 4 Zoptarelin doxorubicin DDI potential: Maximum impact of zoptarelin doxorubicin on OATP1B3 and OCT2. **a** Relative change of OATP1B3 apparent K_M during inhibition by 267 mg/m² zoptarelin doxorubicin. **b** Relative change of OCT2 apparent K_M during inhibi-

tion by 267 mg/m² zoptarelin doxorubicin. Population simulation medians are shown as lines; the shaded areas depict the 5th–95th percentile population prediction intervals

OATP1B3 and 3.23 μmol/L for OCT2 (see “Materials and methods”). The resulting relative changes of apparent K_M values amount to less than 0.5% for OATP1B3 and to less than 2.5% for OCT2, as illustrated in Fig. 4.

To rate the impact of a 2.5% change in K_M , the relation of initial reaction velocity v_0 and K_M can be applied:

$$v_0 = \frac{V_{\max} * \text{substrate concentration}}{K_M + \text{substrate concentration}} \quad (4)$$

For substrate concentrations significantly below K_M and unchanged maximal reaction velocity V_{\max} (competitive inhibition assumed), a 2.5% increase of K_M results in a 2.5% decrease of initial reaction velocity. For higher substrate concentrations, the influence of increased K_M will be even smaller.

DDI potential of zoptarelin doxorubicin with simvastatin and metformin

For specific DDI predictions with simvastatin and metformin, victim drug steady-state plasma concentrations after administration of the highest common doses of 80 mg simvastatin (once daily, day 5) or 1000 mg metformin (three times daily, day 5) with and without co-administration of 267 mg/m² zoptarelin doxorubicin were simulated.

Testing of different time intervals between the start of zoptarelin doxorubicin infusion and administration of the victim drugs showed highest DDI impact on simvastatin acid, when the zoptarelin doxorubicin infusion is started 2 h after the administration of simvastatin (zoptarelin doxorubicin C_{\max} at the time of simvastatin acid C_{\max}); and highest DDI impact on metformin, when the zoptarelin doxorubicin

infusion is started 1 h before the administration of metformin (zoptarelin doxorubicin C_{\max} at the time of metformin C_{\max}).

The identified administration regimens for maximum DDI impact and the resulting plasma concentrations of zoptarelin doxorubicin, simvastatin acid and metformin are illustrated in Fig. 5a, b. Victim drug plasma concentrations of simvastatin acid and metformin, with and without co-administration of zoptarelin doxorubicin are presented in Fig. 5c, d. DDI impact on victim drug AUC and C_{\max} values, simulated with the different tested dosing regimens is shown in Zoptarelin Doxorubicin Supplementary Table 3. The identified worst-case co-administration scenarios result in a 0.114% increase of the plasma AUC_{96–120} of simvastatin acid and a 0.096% increase of the AUC_{96–104} of metformin, due to liver and kidney uptake inhibition.

Discussion

Doxorubicin model

The presented doxorubicin model is the first whole-body PBPK model developed with clinical data from humans and a mechanistic implementation of the binding of doxorubicin to DNA. This binding is essential to describe the pharmacokinetics of doxorubicin, as it is the driving force behind the unusual distribution behavior of this drug [33]. The developed model accurately describes doxorubicin plasma concentrations following direct administration of doxorubicin and also very successfully predicts the concentrations of doxorubicin released following administration of a variety of different doses of zoptarelin doxorubicin.

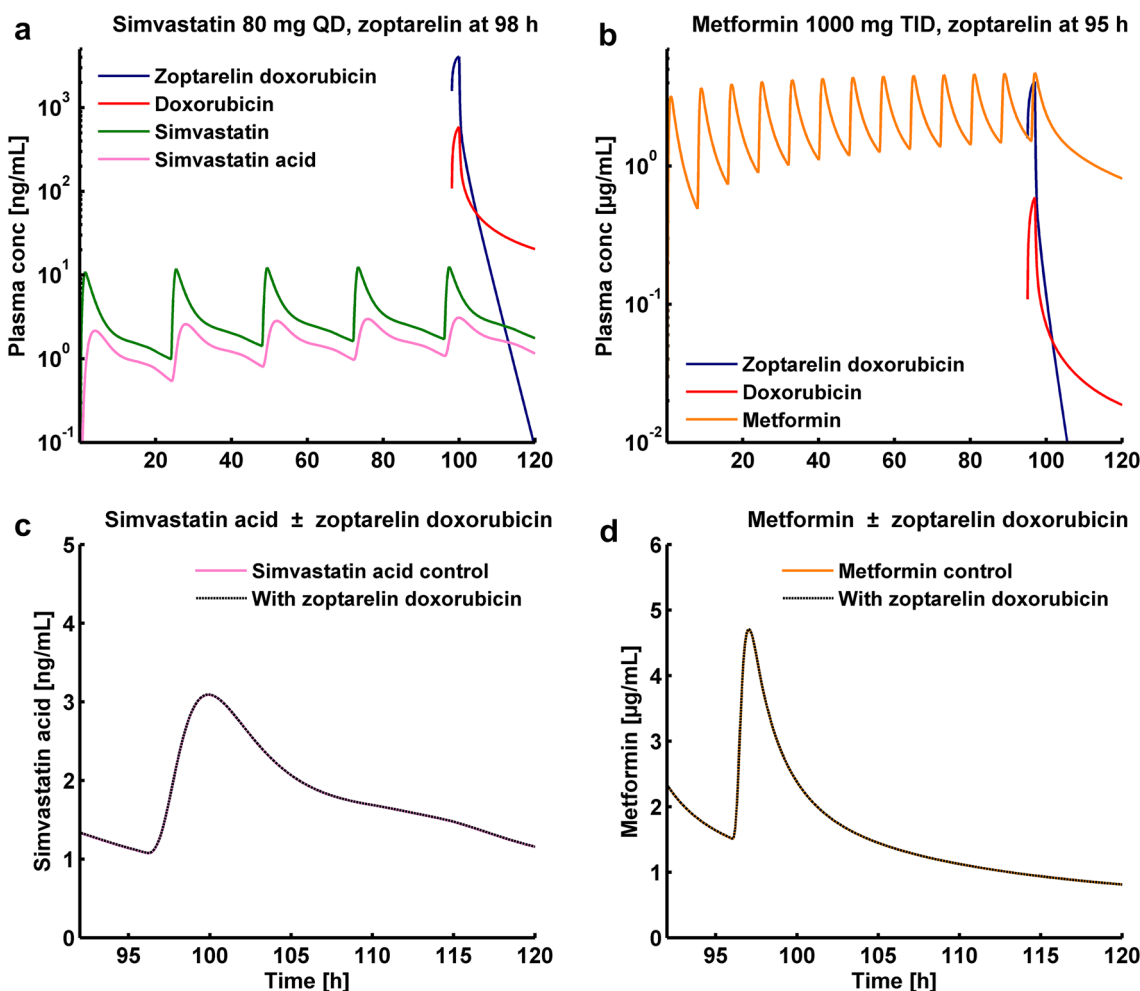


Fig. 5 Zoptarelin doxorubicin DDI potential: Specific DDI worst-case scenario predictions with simvastatin acid and metformin as OATP1B3 and OCT2 victim drugs. **a** Predicted zoptarelin doxorubicin (blue), doxorubicin (red), simvastatin (green) and simvastatin acid (pink) plasma concentrations (semilog scale) of a typical individual during administration of 80 mg simvastatin every 24 h, plus 267 mg/m² zoptarelin doxorubicin once, on the morning of day 5. The last administration of simvastatin is at 96 h; zoptarelin doxorubicin infusion (2 h) is started 2 h later at 98 h, resulting in simultaneous peak plasma concentrations of zoptarelin doxorubicin and simvastatin acid at 100 h. **b** Predicted zoptarelin doxorubicin (blue), doxorubicin (red) and metformin (dark yellow) plasma concentrations (semilog scale) of a typical individual during administration of 1000 mg metformin every 8 h, plus 267 mg/m² zoptarelin doxorubicin once, on the morning of day 5. The last administration of metformin is at 96 h; zoptarelin doxorubicin infusion (2 h) is started 1 h earlier, at 95 h, resulting in simultaneous peak plasma concentrations of zoptarelin doxorubicin and metformin at 97 h. **c** Overlay of predicted simvastatin acid plasma concentrations using the administration protocol shown in **a**, without (pink) and during co-administration of zoptarelin doxorubicin (dashed black line). **d** Overlay of predicted metformin plasma concentrations using the administration protocol shown in **b**, without (dark yellow) and during co-administration of zoptarelin doxorubicin (dashed black line)

tions (semilog scale) of a typical individual during administration of 1000 mg metformin every 8 h, plus 267 mg/m² zoptarelin doxorubicin once, on the morning of day 5. The last administration of metformin is at 96 h; zoptarelin doxorubicin infusion (2 h) is started 1 h earlier, at 95 h, resulting in simultaneous peak plasma concentrations of zoptarelin doxorubicin and metformin at 97 h. **c** Overlay of predicted simvastatin acid plasma concentrations using the administration protocol shown in **a**, without (pink) and during co-administration of zoptarelin doxorubicin (dashed black line). **d** Overlay of predicted metformin plasma concentrations using the administration protocol shown in **b**, without (dark yellow) and during co-administration of zoptarelin doxorubicin (dashed black line)

The sensitivity of the doxorubicin model to the value of fraction unbound is to be expected, as this parameter determines the doxorubicin concentration available for all pharmacokinetic processes. The value used in the model has been carefully determined in vitro at Aeterna Zentaris and has not been optimized. The doxorubicin fraction unbound measured in-house (26.3%) is in very good accordance with the literature (25%, [34]). The moderate sensitivity of the model to the cellular permeability value underlines the influence of this parameter. Adjustment of this value greatly improved

the model performance and, therefore, it has been included into the set of optimized parameters.

Several other PBPK models of doxorubicin have been developed so far, mostly established from animal data with the benefit of measured doxorubicin concentrations in different tissues [35–38]. Among those is a very nice model of doxorubicin in mice, that has been extrapolated to humans including evaluation of the predicted serum concentrations with actual clinical data, as well as mechanistic modeling of DNA binding to describe the tissue distribution of doxorubicin [35]. The only other model directly developed from

human data lacks a mechanistic implementation of the tissue binding, but features a physiologically based description of the effects of aging on the distribution clearance of doxorubicin [36].

In the presented doxorubicin model, DNA binding sites have so far only been implemented into 8 of the 22 model compartments, resulting in an overestimation of the doxorubicin accumulation in these tissues and an underestimation of the doxorubicin concentration in the tissues without binding partner (not counting the blood cell compartment, as the DNA concentration within this volume has been separately adjusted to match literature data). Although the DNA binding site reference concentration of the virtual patients has been optimized (K_d and k_{off} have been fixed to literature values), the obtained value is biologically plausible. A rough estimate of the number of DNA base pairs per human is 6.0×10^{22} (6.0×10^9 base pairs per cell, 1.0×10^{13} cells per human). This equals 0.1 mol of base pairs per human. As the doxorubicin binding partner was implemented only into the 8 most important tissues of the model patient, these DNA binding sites are distributed into 4 L of tissue with equal expression of this binding partner, resulting in a reference concentration of 0.025 mol/L. The optimized value of 0.046 mol/L is in the same order of magnitude. Furthermore, there are reports of binding of doxorubicin not only to DNA, but (with a lower affinity) also to cardiolipin and DNA-associated enzymes, which have not been implemented into the model [9, 39]. To predict the doxorubicin concentrations and pharmacodynamics within a distinct organ, the distribution of the DNA binding sites will have to be implemented in an anatomically correct way, as has been proposed by Gustafson et al. [35].

Despite minor limitations, this model is a suitable basis for further refinement and subsequent extrapolation to vulnerable populations receiving doxorubicin treatment such as children, elderly and patients with organ impairment.

Zoptarelin doxorubicin model

The presented zoptarelin doxorubicin model is the first PBPK model of zoptarelin doxorubicin and accurately describes and predicts plasma concentrations of zoptarelin doxorubicin and its active metabolite doxorubicin following infusion of different doses of zoptarelin doxorubicin. This is remarkable, as the model has been developed with data collected in three clinical trials investigating patients with different types of cancer.

As for the doxorubicin model, the sensitivity of the zoptarelin doxorubicin model to the value of fraction unbound was to be expected and the value used in the model has also been carefully measured in-house. The relatively high sensitivity of the model to the zoptarelin doxorubicin hydrolysis rate value emphasizes the impact of this parameter on the

elimination of zoptarelin doxorubicin and on the predicted AUC.

The primary aim of this PBPK analysis was to assess the DDI potential of zoptarelin doxorubicin with OATP1B3 and OCT2 victim drugs. Future applications of the presented model could include the implementation of a tumor compartment to enable the prediction of zoptarelin doxorubicin and doxorubicin concentrations in the target tissue and to answer questions regarding efficacy and pharmacodynamics of zoptarelin doxorubicin. For a first estimate, the model can be employed to simulate the internalization and intracellular concentrations of zoptarelin doxorubicin as well as the resulting concentrations of doxorubicin in the gonads. The lack of a tumor compartment (compensated by a low expression of LHRHR in the lung) does not impact the results and interpretation of the presented PBPK analysis of the interaction with OATP1B3 and OCT2, as these DDIs are determined by the concentrations in liver and kidney.

Zoptarelin doxorubicin DDI potential

Zoptarelin doxorubicin shows no inhibition or induction of cytochrome P450 enzymes in vitro, as well as no inhibition of investigated transporters other than OATP1B3 ($IC_{50} = 16.5 \mu\text{mol/L}$) and OCT2 ($IC_{50} = 3.26 \mu\text{mol/L}$). P-glycoprotein (P-gp), breast cancer resistance protein (BCRP), organic anion transporter 1 (OAT1), OAT3 and OATP1B1 are not inhibited in vitro (IC_{50} values $> 200 \mu\text{mol/L}$). The predicted maximum relative changes of transport rate during treatment with the highest clinical dose of zoptarelin doxorubicin are 0.5% for OATP1B3 and 2.5% for OCT2 at the end of the infusion. In line with this general interaction potential assessment, no impact of zoptarelin doxorubicin on plasma concentrations of the OATP1B3 and OCT2 victim drugs simvastatin acid and metformin was found in worst-case scenario simulations. These results are in accordance with the expectations due to low interstitial concentrations of zoptarelin doxorubicin in relation to the zoptarelin doxorubicin K_i values for inhibition of OATP1B3 and OCT2. As zoptarelin doxorubicin ($MW = 1893.06 \text{ g/mol}$) is a 10-amino acid polypeptide linked to doxorubicin and positively charged at two amino groups at physiological pH, its passive permeability is low, leading to low interstitial concentrations.

This example demonstrates that PBPK modeling is a valuable technique to analyze the risk of investigational drugs suspected to cause drug–drug interactions *in vivo*. In vitro results and pharmacokinetic data from early clinical studies are used to establish mechanistic and physiologically based models that allow the *in vivo* prediction of drug–drug interactions. This approach is supported by drug approval agencies [12, 13] and can help to minimize patient risk, costs

and time needed for drug development. Furthermore, PBPK modeling has the capability to generate information whenever the conduct of clinical trials is not ethical, as is the case in all frail populations such as children, elderly and patients.

Conclusion

This is the first report of a whole-body PBPK model of zoptarelin doxorubicin and its active metabolite doxorubicin. The model was applied for the evaluation of the zoptarelin doxorubicin drug–drug interaction potential (1) by a general assessment of the OATP1B3 and OCT2 inhibition potential of zoptarelin doxorubicin *in vivo* and (2) by specific DDI simulations of the impact of zoptarelin doxorubicin on simvastatin acid and metformin exposure in worst-case scenarios. No DDI potential of zoptarelin doxorubicin was detected in these analyses.

Acknowledgements The authors gratefully acknowledge the patients that participated in the clinical studies and the medical staff involved in patient care and study execution.

Compliance with ethical standards

Funding This study was funded by Aeterna Zentaris.

Conflict of interest Nina Hanke, Daniel Moj, Jan-Georg Wojtyniak and Hannah Britz declare that they have no conflict of interest. Michael Teifel, Babette Aicher, Herbert Sindermann and Nicola Ammer are employees of Aeterna Zentaris. Thorsten Lehr has received research grants from Aeterna Zentaris.

Ethical approval All procedures performed in studies involving human participants were in accordance with the ethical standards of the institutional and/or national research committee and with the 1964 Helsinki declaration and its later amendments or comparable ethical standards. This article does not contain any studies with animals performed by any of the authors.

Informed consent Informed consent was obtained from all individual participants included in the study.

References

- Nagy A, Schally A, Armatis P, Szepeshazi K, Halmos G, Kovacs M, Zarandi M, Groot K, Miyazaki M, Jungwirth A, Horvath J (1996) Cytotoxic analogs of luteinizing hormone-releasing hormone containing doxorubicin or 2-pyrrolinodoxorubicin, a derivative 500–1000 times more potent. *Proc Natl Acad Sci USA* 93:7269–7273
- Westphalen S, Kotulla G, Kaiser F, Krauss W, Werning G, Elsasser HP, Nagy A, Schulz KD, Gründker C, Schally A, Emons G (2000) Receptor mediated antiproliferative effects of the cytotoxic LHRH agonist AN-152 in human ovarian and endometrial cancer cell lines. *Int J Oncol* 17:1063–1069
- Krebs LJ, Wang X, Nagy A, Schally A, Rasad PN, Liebowa C (2002) A conjugate of doxorubicin and an analog of Luteinizing hormone-releasing hormone shows increased efficacy against oral and laryngeal cancers. *Oral Oncol* 38:657–663
- Gründker C, Völker P, Griesinger F, Ramaswamy A, Nagy A, Schally A, Emons G (2002) Antitumor effects of the cytotoxic luteinizing hormone-releasing hormone analog AN-152 on human endometrial and ovarian cancers xenografted into nude mice. *Am J Obstet Gynecol* 187:528–537
- Szepeshazi K, Schally A, Keller G, Block NL, Benten D, Halmos G, Szalontay L, Vidaurre I, Rick FG (2012) Receptor-targeted therapy of human experimental urinary bladder cancers with cytotoxic LH-RH analog AN-152 (AEZS-108). *Oncotarget* 3:686–699
- Emons G, Gorchev G, Harter P, Wimberger P, Stähle A, Hanker L, Hilpert F, Beckmann MW, Dall P, Gründker C, Sindermann H, Sehouli J (2014) Efficacy and safety of AEZS-108 (LHRH agonist linked to doxorubicin) in women with advanced or recurrent endometrial cancer expressing LHRH receptors: a multicenter phase 2 trial (AGO-GYN5). *Int J Gynecol Cancer* 24:260–265
- Emons G, Gorchev G, Sehouli J, Wimberger P, Stähle A, Hanker L, Hilpert F, Sindermann H, Gründker C, Harter P (2014) Efficacy and safety of AEZS-108 (INN: zoptarelin doxorubicin acetate) an LHRH agonist linked to doxorubicin in women with platinum refractory or resistant ovarian cancer expressing LHRH receptors: a multicenter phase II trial of the ago-study group. *Gynecol Oncol* 133:427–432
- Emons G, Kaufmann M, Gorchev G, Tsekova V, Gründker C, Günthert AR, Hanker LC, Velikova M, Sindermann H, Engel J, Schally A (2010) Dose escalation and pharmacokinetic study of AEZS-108 (AN-152), an LHRH agonist linked to doxorubicin, in women with LHRH receptor-positive tumors. *Gynecol Oncol* 119:457–461
- Tacar O, Sriamornsak P, Dass CR (2013) Doxorubicin: An update on anticancer molecular action, toxicity and novel drug delivery systems. *J Pharm Pharmacol* 65:157–170
- Pfizer Inc (2011) Doxorubicin prescribing information. Pfizer Inc, New York
- Speth PAJ, Van Hoesel Q, Haanen C (1988) Clinical pharmacokinetics of doxorubicin. *Clin Pharmacokinet* 15:15–31
- Food US and Drug Administration—Center for Drug Evaluation and Research (2016) Physiologically based pharmacokinetic analyses—format and content. Draft Guidance for Industry
- European Medicines Agency (2016) Guideline on the qualification and reporting of physiologically based pharmacokinetic (PBPK) modelling and simulation
- Yao F, Duan J, Wang Y, Zhang Y, Guo Y, Guo H, Kang X (2015) Nanopore single-molecule analysis of DNA-doxorubicin interactions. *Anal Chem* 87:338–342
- Speth PA, Linszen PC, Holdrinet RS, Haanen C (1987) Plasma and cellular adriamycin concentrations in patients with myeloma treated with ninety-six-hour continuous infusion. *Clin Pharmacol Ther* 41:661–665
- Speth PA, Linszen PC, Boezeman JB, Wessels HM, Haanen C (1987) Cellular and plasma adriamycin concentrations in long-term infusion therapy of leukemia patients. *Cancer Chemother Pharmacol* 20:305–310
- Durmus S, Naik J, Buil L, Wagenaar E, Van Tellingen O, Schinkel AH (2014) In vivo disposition of doxorubicin is affected by mouse Oatp1a/1b and human OATP1A/1B transporters. *Int J Cancer* 135:1700–1710
- American Society of Health-System Pharmacists (2009) AHFS drug information. American Society of Health-System Pharmacists, Bethesda

19. Schang AL, Quérat B, Simon V, Garrel G, Bleux C, Counis R, Cohen-Tannoudji J, Laverrière JN (2012) Mechanisms underlying the tissue-specific and regulated activity of the Gnhr promoter in mammals. *Front Endocrinol (Lausanne)* 3:162
20. Aguilar-Rojas A, Huerta-Reyes M (2009) Human gonadotropin-releasing hormone receptor-activated cellular functions and signaling pathways in extra-pituitary tissues and cancer cells. *Oncol Rep* 22:981–990
21. Halmos G, Nagy A, Lamharzi N, Schally A (1999) Cytotoxic analogs of luteinizing hormone-releasing hormone bind with high affinity to human breast cancers. *Cancer Lett* 136:129–136
22. Cho N, Harada M, Imaeda T, Imada T, Matsumoto H, Hayase Y, Sasaki S, Furuya S, Suzuki N, Okubo S, Ogi K, Endo S, Onda H, Fujino M (1998) Discovery of a novel, potent, and orally active nonpeptide antagonist of the human luteinizing hormone-releasing hormone (LHRH) receptor. *J Med Chem* 41:4190–4195
23. Valentin J (2002) Basic anatomical and physiological data for use in radiological protection: reference values. *Ann ICRP* 32:1–277
24. Miller DS, Gabra H, Emons G, McMeekin DS, Oza AM, Temkin SM, Vergote I (2014) ZoptEC: Phase III study of zoptarelin doxorubicin (AEZS-108) in platinum-taxane pretreated endometrial cancer (Study AEZS-108–050). *J Clin Oncol* 32:15 (suppl)
25. König J, Cui Y, Nies AT, Keppler D (2000) Localization and genomic organization of a new hepatocellular organic anion transporting polypeptide. *J Biol Chem* 275:23161–23168
26. Koepsell H, Endou H (2004) The SLC22 drug transporter family. *Pflugers Arch Eur J Physiol* 447:666–676
27. Gui C, Miao Y, Thompson L, Wahlgren B, Mock M, Steiger B, Hagenbuch B (2008) Effect of pregnane X receptor ligands on transport mediated by human OATP1B1 and OATP1B3. *Eur J Pharmacol* 584:57–65
28. Kimura N, Masuda S, Tanihara Y, Ueo H, Okuda M, Katsura T, Inui K (2005) Metformin is a superior substrate for renal organic cation transporter OCT2 rather than hepatic OCT1. *Drug Metab Pharmacokinet* 20:379–386
29. Yung-Chi C, Prusoff WH (1973) Relationship between the inhibition constant (K_I) and the concentration of inhibitor which causes 50 per cent inhibition (I₅₀) of an enzymatic reaction. *Biochem Pharmacol* 22:3099–3108
30. Rodrigues AD (2008) Drug-drug interactions, 2nd edn. CRC Press, Taylor and Francis, Boca Raton
31. Food US and Drug Administration (2012) Drug interaction studies—Study design, data analysis, implications for dosing, and labeling recommendations. Draft Guidance for Industry
32. Kunze A, Huwyler J, Camenisch G, Poller B (2014) Prediction of organic anion-transporting polypeptide 1B1- and 1B3-mediated hepatic uptake of statins based on transporter protein expression and activity data. *Drug Metab Dispos* 42:1514–1521
33. Terasaki T, Iga T, Sugiyama Y, Hanano M (1982) Experimental evidence of characteristic tissue distribution of adriamycin. Tissue DNA concentration as a determinant. *J Pharm Pharmacol* 34:597–600
34. Pfizer Inc (2013) Doxorubicin prescribing information. Pfizer Inc, New York
35. Gustafson DL, Rastatter JC, Colombo T, Long ME (2002) Doxorubicin pharmacokinetics: macromolecule binding, metabolism, and excretion in the context of a physiologic model. *J Pharm Sci* 91:1488–1501
36. Li J, Gwilt PR (2003) The effect of age on the early disposition of doxorubicin. *Cancer Chemother Pharmacol* 51:395–402
37. Hu L, Au JLS, Wientjes MG (2007) Computational modeling to predict effect of treatment schedule on drug delivery to prostate in humans. *Clin Cancer Res* 13:1278–1287
38. Dubbelboer IR, Lilienberg E, Sjögren E, Lennernäs H (2017) A model-based approach to assessing the importance of intracellular binding sites in doxorubicin disposition. *Mol Pharm* 14:686–698
39. Goormaghtigh E, Chatelain P, Caspers J, Ruysschaert JM (1980) Evidence of a complex between adriamycin derivatives and cardiolipin: possible role in cardiotoxicity. *Biochem Pharmacol* 29:3003–3010

4.2 Project II:

Clarithromycin, midazolam, and digoxin: Application of PBPK modeling to gain new insights into drug-drug interactions and co-medication regimens.

Research Article

Clarithromycin, Midazolam, and Digoxin: Application of PBPK Modeling to Gain New Insights into Drug–Drug Interactions and Co-medication Regimens

Daniel Moj,¹ Nina Hanke,¹ Hannah Britz,¹ Sebastian Frechen,² Tobias Kanacher,² Thomas Wendl,² Walter Emil Haefeli,³ and Thorsten Lehr^{1,4}

Received 24 June 2016; accepted 25 October 2016

Abstract. Clarithromycin is a substrate and mechanism-based inhibitor of cytochrome P450 (CYP) 3A4 as well as a substrate and competitive inhibitor of P-glycoprotein (P-gp) and organic anion-transporting polypeptides (OATP) 1B1 and 1B3. Administered concomitantly, clarithromycin causes drug–drug interactions (DDI) with the victim drugs midazolam (CYP3A4 substrate) and digoxin (P-gp substrate). The objective of the presented study was to build a physiologically based pharmacokinetic (PBPK) DDI model for clarithromycin, midazolam, and digoxin and to exemplify dosing adjustments under clarithromycin co-treatment. The PBPK model development included an extensive literature search for representative PK studies and for compound characteristics of clarithromycin, midazolam, and digoxin. Published concentration-time profiles were used for model development (training dataset), and published and unpublished individual profiles were used for model evaluation (evaluation dataset). The developed single-compound PBPK models were linked for DDI predictions. The full clarithromycin DDI model successfully predicted the metabolic (midazolam) and transporter (digoxin) DDI, the acceptance criterion ($0.5 \leq \text{AUC}_{\text{ratio,predicted}} / \text{AUC}_{\text{ratio,observed}} \leq 2$) was met by all predictions. During co-treatment with 250 or 500 mg clarithromycin (bid), the midazolam and digoxin doses should be reduced by 74 to 88% and by 21 to 22%, respectively, to ensure constant midazolam and digoxin exposures (AUC). With these models, we provide highly mechanistic tools to help researchers understand and characterize the DDI potential of new molecular entities and inform the design of DDI studies with potential CYP3A4 and P-gp substrates.

KEY WORDS: clarithromycin; digoxin; dose; drug interaction; midazolam; PBPK.

INTRODUCTION

Pharmacokinetic (PK) drug–drug interactions (DDIs) can cause negative clinical effects, either by decreasing therapeutic efficacy or by enhancing toxic side effects of drugs. DDIs play an important role in reported adverse events (1) and are a major cause of market withdrawal of drugs due to safety reasons (2). To cope with the increasing DDI risks associated with polypharmacy, the European

Medicines Agency (EMA) (3) and the US Food and Drug Administration (FDA) (4) published guidance documents to help researchers understand and characterize the DDI potential of new molecular entities. A prominent feature of these guidances is the recommendation of well-established perpetrator and victim drugs for clinical DDI studies. Perpetrators of metabolic DDIs inhibit or induce, *e.g.*, cytochrome P450 (CYP) enzymes. CYP enzymes are an important source of clinically relevant DDIs, among which CYP3A4 is the most common enzyme for the metabolic clearance of drugs (5,6). Consequently, the inhibition or induction of CYP3A4 is a frequent cause of DDI.

Until 2013, ketoconazole has been the CYP3A inhibitor of choice in clinical DDI studies (7). Due to the risk of serious hepatic toxicity, the EMA and the FDA advised against the further use of ketoconazole in clinical DDI studies (8). Clarithromycin has been proposed as a useful clinical alternative (9).

Clarithromycin is a widely prescribed antibiotic (10) that is mainly metabolized via CYP3A4 (11). It forms a non-covalent metabolic-intermediate complex with CYP3A4 (12) leading to a

Electronic supplementary material The online version of this article (doi:10.1208/s12248-016-0009-9) contains supplementary material, which is available to authorized users.

¹ Department of Pharmacy, Clinical Pharmacy, Saarland University, Campus C2 2, 66123, Saarbruecken, Germany.

² Computational Systems Biology, Bayer Technology Services GmbH, Leverkusen, Germany.

³ Department of Clinical Pharmacology and Pharmacoepidemiology, University of Heidelberg, Heidelberg, Germany.

⁴ To whom correspondence should be addressed. (e-mail: Thorsten.Lehr@mx.uni-saarland.de)

mechanism-based inhibition (MBI). This MBI is characterized by a non-linear, dose-dependent and irreversible degradation of CYP3A4. Thus, the MBI by clarithromycin leads to a mechanism-based auto-inhibition of metabolism and results in a non-linear increase of clarithromycin exposure after ascending doses of clarithromycin (13). Clarithromycin is also a substrate (14) and competitive inhibitor of P-glycoprotein (P-gp) (15) as well as a substrate (16,17) and competitive inhibitor of human organic anion-transporting polypeptides (OATP) 1B1 and 1B3 (18).

One of the recommended and most suitable victim drugs to investigate CYP3A4-mediated DDIs is midazolam. Midazolam is a short-acting, widely used sedative approved as premedication before medical interventions that is almost exclusively metabolized by CYP3A4 (19).

Digoxin is a prominent victim drug to investigate P-gp-mediated DDIs, as its disposition is mainly governed by P-gp. Any metabolism via phase I or II enzymes seems to be negligible. The primary route of digoxin elimination (~75%) is renal excretion via glomerular filtration and active tubular secretion (mainly via P-gp) of unchanged drug (20,21). Digoxin binds to and inhibits several subunits of the (Na^+,K^+)-ATPase, in particular the subunit alpha 2, which leads to the desired positive inotropic effects of digoxin in the heart (22).

OBJECTIVE

The aims of this work were as follows:

1. To develop fully mechanistic physiologically based pharmacokinetic (PBPK) models for the single compounds clarithromycin, midazolam, and digoxin
2. To couple the clarithromycin and midazolam PBPK models to predict the metabolic DDI (via CYP3A4) of these two drugs
3. To couple the clarithromycin and digoxin PBPK models to predict the transporter-based DDI (via P-gp) of these two drugs

Exemplarily, it is shown how dosing recommendations for midazolam and digoxin during co-administration with various doses of clarithromycin can be derived.

METHODS

PBPK Model Development

The PBPK model development consisted of (i) an extensive literature search for representative PK studies and (ii) for compound characteristics (physicochemical and ADME) of clarithromycin, midazolam, and digoxin. For the model development, the available, published, and unpublished individual PK data were divided into a “training” dataset for model development and an “evaluation” dataset for model qualification. The training dataset was used to optimize model parameter values to find the best overlap between observed and simulated concentration-time profiles. First, intravenous concentration-time profiles were used to determine clearance and distribution parameters. Second, oral concentration-time profiles were used to determine absorption and dissolution parameters, keeping the formerly optimized parameters fixed. Model qualification with the

evaluation dataset was carried out using visual predictive checks. The final single-compound models were then coupled to predict the pharmacokinetic effects of clarithromycin on midazolam and digoxin. The PBPK models for clarithromycin, midazolam, and digoxin were developed independently of each other. This also includes the parameterization of the CYP3A4 MBI, which has been achieved with multiple-dose studies of clarithromycin only. The parameters for the inhibition of P-gp have been taken from *in vitro* experiments without optimization. DDI PK studies were used to qualify the DDI prediction performance of the coupled clarithromycin–midazolam and clarithromycin–digoxin models. Forty-four concentration-time profiles were used in the model development process (Table I).

PBPK modeling software PK-Sim® 5.3.2 (Bayer Technology Services, Leverkusen, Germany) and MoBi 3.3.2 (Bayer Technology Services, Leverkusen, Germany) were used. Statistical analysis of the results and graphics were compiled with Matlab 2015a. Data was digitized using GetData Graph Digitizer 2.25.

PBPK Model Structure

The PBPK models of clarithromycin, midazolam, and digoxin are based on a generic 22-organ PBPK model, including the arterial and venous blood pools and the portal vein. Each organ is further divided into sub-compartments, characterizing the blood plasma, the red blood cells (RBC), the interstitial space, and the intracellular space. The mass transfer between compartments is based on a generic distribution model (passive processes). Herein, substance-specific parameters (e.g. lipophilicity) are used to determine permeabilities across membranes and partition coefficients between compartments. Active processes (binding, metabolism, and transport) are additionally implemented, depending on the PK behavior of the substance.

For clarithromycin, implemented active processes are metabolism via CYP3A4 and transport via OATP 1B3. An unspecific renal clearance of clarithromycin was assumed. As P-gp substrate, the intestinal absorption of clarithromycin is reduced by intestinal P-gp. The impact of this efflux transport of clarithromycin from intestinal mucosa to intestinal lumen was implemented by reducing the net transcellular intestinal permeability of clarithromycin (55). The midazolam model assumes metabolism by CYP3A4 with negligible renal clearance. The digoxin model incorporates active efflux transport via P-gp with a renal clearance of digoxin consisting of glomerular filtration and tubular secretion by P-gp.

The PBPK modeling software calculates the organ-specific protein expression relative to the expression in the organ with the highest concentration of the respective protein (reference concentration). The reference concentration corresponds to an expression level of 100%. Hence, organ-specific transporter protein concentrations of P-gp and OATP 1B3 used in simulations were calculated based on Eq. 1,

$$C_{T,\text{organ}} = T_{\text{REF}} \times \text{EXPR}_{\text{organ}} \quad (1)$$

where $C_{T,\text{organ}}$ denotes the molar transporter concentration in the specific organ, T_{REF} is the transporter reference

PBPK DDI Modeling of Clarithromycin, Midazolam, and Digoxin

Table I. Clinical Study Data of Clarithromycin, Midazolam, and Digoxin in Healthy Volunteers

Substrate	Route of administration	Dose [mg]	Number	Age range (mean) [years]	Weight range (mean) [kg]	Height range (mean) [cm]	BMI range (mean) [kg/m ²]	Ref.
Clarithromycin	iv (inf, 0.5 h, SD)	0.1	30	18–55	–	–	18–30	(23)
	iv (inf, 0.5 h, SD)	250	22	18–40 (29)	57.7–87.7 (71.5)	164–188 (175)	–	(24)
	po (tab, SD)	100–1200	36	19–36 (25.3)	55.9–96.6 (71.4)	158–191 (175)	–	(13)
	po (tab, MD)	250	17	18–40 (29)	57.7–87.7 (70.8)	164–188 (174.9)	–	(25)
	po (tab, MD)	250	12	21–39 (28)	68–98 (80)	–	22–28 (24)	(26) ^b
	po (tab, MD)	250, 500	12	24–38 (26.5)	65–88 (79.5)	168–197 (182)	–	(27)
	po (tab, MD)	500	17	20–39 (31)	63.9–86.8 (72.2)	160–183 (174.1)	–	(25)
	po (sol, MD)	500	12	19–41 (28)	45.1–86.1 (66.5)	150–186 (168.4)	–	(28)
	iv (inf, 0.5 h, SD)	0.05/kg	16	(34)	(78)	–	–	(29)
	iv (bolus, SD)	0.13/kg	5	28–49	70–80	–	–	(30)
Midazolam	iv (bolus, SD)	1.0	12	18–50	–	–	18–30	(31)
	iv (bolus, SD)	1.0	19	(22.9)	(68.1)	(174)	–	(32)
	iv (bolus, SD)	5.0	6	21–22	66.3–77.0	–	–	(33)
	iv (bolus, SD)	5.0	12	20–45 (29) ^a	–	–	20–26 (23) ^a	(34)
	iv (bolus, SD)	11.42	6	22–27	55–77	–	–	(35)
	po (sol, SD)	2.0	12	18–50	–	–	18–30	(31)
	po (sol, SD)	3.0	11	(31.2)	–	–	(23)	(36)
	po (tab, SD)	4.0	16	(34)	(78)	–	–	(29)
	po (sol, SD)	5.0	24	–	–	–	–	(37)
	po (tab, SD)	7.5, 15, 30	12	24–52	54.9–92.5	–	–	(38)
	po (tab, SD)	10.0	6	21–22	66.3–77.0	–	–	(33)
	po (tab, SD)	15.0	12	24–53	54–93	–	–	(39)
	po (tab, SD)	10.0, 20.0	6	22–27	55–77	–	–	(35)
	iv (inf, 0.08 h, SD)	0.01/kg	12	21–39 (28)	68–98 (80)	–	22–28 (24)	(26)
Digoxin	iv (bolus, SD)	1.0	12	–	–	–	–	(40)
	iv (bolus, SD)	0.5	6	–	66–96	–	–	(41)
	iv (bolus, SD)	0.015/kg	6	22–29 (24)	–	–	–	(42)
	iv (inf, 0.08 h, SD)	0.5	12	(28)	(74)	–	(23)	(43)
	iv (inf, 0.5 h, SD)	1.0	8	(29)	(84)	–	–	(44)
	iv (inf, 1 h, SD)	0.5	9	(27.9)	(66.6)	(169.7)	–	(45)
	iv (inf, 1 h, SD)	0.75	8	–	–	–	–	(20)
	iv (inf, 1 h, SD)	0.5, 1.0, 1.5	9	23–37 (31.3)	69–90 (77.7)	–	–	(46)
	iv (inf, 1, 3 h, SD)	0.5	6	–	66–96	–	–	(41)
	po (tab, SD)	0.5	12	22–35 (26)	–	–	19–28 (22)	(47)
	po (tab, SD)	0.25	18	(30)	(77.5)	–	–	(48)
	po (na, SD)	0.25	16	20–43 (39) ^a	(72.5) ^a	(174) ^a	(24) ^a	(49)
	po (tab, SD)	0.75	12	21–39 (28)	68–98 (80)	–	22–28 (24)	(26)
	po (tab, SD)	1.0	8	(29)	(84)	–	–	(44)
	po (tab, SD)	1.0	10	19–27 (24) ^a	61–92 (73) ^a	–	–	(50)
	po (sol, SD)	0.5	6	–	66–96	–	–	(41)
	po (tab, MD)	0.5, 0.25 ^c	8	(32.4)	(74.8)	(178.5)	–	(51)
	po (na, MD)	0.125	12	18–55 (37.8)	70–95 (87.8)	(179)	23–30 (27)	(52)
	po (tab, MD)	0.25	20	23–49	(74.8)	(171)	(25)	(53)
	po (na, MD)	0.25	22	18–45	(50)	–	–	(54)

^ainf infusion, ^biv intravenous, ^cMD multiple doses, ^dna information not available, ^epo per oral, ^fSD single dose, ^gsol solution, ^htab tablet,

^aMedian given

^bIndividual concentration-time profiles are unpublished in-house data

^c0.5 mg bid for 3 days followed by 0.25 mg bid for 2 weeks

concentration, and $\text{EXPR}_{\text{organ}}$ denotes the transporter expression relative to the organ with the highest concentration (56–58).

In our models, CYP3A4 is expressed in the liver and the intestinal mucosa. The CYP3A4 reference concentration used in the simulations was set to 3.47 $\mu\text{mol/L}$ (59) in the liver. OATP 1B3 is expressed in, e.g., the bone, liver, lung, muscle, and intestine, with the highest OATP 1B3 expression (276

nmol/L (60)) in the intestinal mucosa according to published expression databases (56,57). P-gp was expressed in, e.g., the brain, kidney, liver, and intestine, with the highest expression in the kidney (61) (101 nmol/L (62)). ATPase (subunit alpha 2), as digoxin binding partner, is implemented, e.g., in the brain, heart, and muscle with the highest expression in the brain (57,58), with a fitted reference concentration of 99.5 $\mu\text{mol/L}$.

MBI of CYP3A4 Metabolism

The metabolic clearance (CL_{met}) of clarithromycin and midazolam via CYP3A4 was incorporated using Eq. 2,

$$CL_{met} = V_{max} \times C_t / (K_{M,CYP3A4} + C_t) \text{ with } V_{max} = k_{cat,CYP3A4} \times E_t \quad (2)$$

where C_t denotes the unbound concentration of clarithromycin or midazolam in the respective intracellular organ compartment and $K_{M,CYP3A4}$ denotes the Michaelis-Menten constant of CYP3A4 for the respective substrate. The parameter $k_{cat,CYP3A4}$ is the turnover number and E_t is the amount of CYP3A4 at time point t available for metabolizing processes.

The MBI of CYP3A4 by clarithromycin was implemented and the organ-specific *de novo* synthesis rates were described by Eq. 3,

$$R_0 = E_0 \times k_{deg} \quad (3)$$

where R_0 is the *de novo* protein synthesis rate of CYP3A4, E_0 is the enzyme amount at baseline at time point 0, and k_{deg} denotes the 1st-order degradation rate constant of CYP3A4.

The rate of change of CYP3A4 amount due to the inactivation via clarithromycin in the intracellular compartments was described by Eq. 4,

$$dE_t / dt = R_0 - k_{deg} \times E_t - (k_{inact} \times CLR_t / (K_I + CLR_t)) \times E_t \quad (4)$$

where the maximum rate of enzyme inactivation (k_{inact}) and the concentration required for half-maximal enzyme inactivation (K_I) of clarithromycin are used to describe the enzyme inactivation due to the intracellular, unbound clarithromycin concentration at time point t (CLR_t). Value selection for k_{inact} and K_I (Table II) was based on the descriptive performance of the auto-inhibition in multiple-dose studies of clarithromycin.

Competitive Inhibition of P-gp Transport

The P-gp efflux transport of digoxin (J_{efflux}) was described by Eq. 5,

$$J_{efflux} = J_{max} \times DIG_t / (K_{M,Pgp} + DIG_t) \text{ with } J_{max} = k_{cat,Pgp} \times P_t \quad (5)$$

where DIG_t denotes the unbound concentration of digoxin in the respective intracellular organ compartment and $K_{M,Pgp}$ denotes the Michaelis-Menten constant of P-gp for digoxin. The parameter $k_{cat,Pgp}$ is the turnover number and P_t is the amount of P-gp at time point t available for transporting processes.

The competitive inhibition of P-gp-mediated digoxin transport by clarithromycin was implemented using Eq. 6,

$$K_{M,Pgp,app} = K_{M,Pgp} \times (1 + I / K_i) \quad (6)$$

where $K_{M,Pgp}$ denotes the digoxin Michaelis-Menten constant in the absence of clarithromycin, I is the unbound clarithromycin concentration, and K_i denotes the dissociation constant of the clarithromycin-transporter complex. Using the assumptions of Cheng and Prusoff (88), a P-gp K_i value for clarithromycin of 3.78 $\mu\text{mol/L}$ was used in the simulations, based on a published IC₅₀ of 4.1 $\mu\text{mol/L}$ (15).

Drug–Drug Interaction

The AUC_{ratio} ($AUC_{inhibition}/AUC_{normal}$) between the victim drug AUC with clarithromycin co-treatment ($AUC_{inhibition}$) and without clarithromycin co-treatment (AUC_{normal}) was determined. The AUC_{ratio} derived from the DDI model prediction was compared to AUC_{ratio} literature values observed in clinical DDI studies. A ratio of $0.5 \leq AUC_{ratio,predicted}/AUC_{ratio,observed} \leq 2$ was used as the acceptance criterion for a successful DDI prediction.

Virtual population characteristics

Interstudy variabilities of the investigated DDIs were assessed using 10 virtual populations with the same number of study individuals as described in the respective study. In virtual populations, CYP3A4 was log-normally distributed with a geometric mean reference concentration of 3.47 $\mu\text{mol/L}$ and a geometric standard deviation (GSD) of 1.6, based on a coefficient of variation of 53% (89). The standard CYP3A4 half-life in liver and intestinal mucosa was set to 36 and 23 h, respectively (90). In virtual populations, the CYP3A4 half-life was uniformly distributed within 10–140 h in the liver and 12–33 h in the intestine (91). P-gp was normally distributed with a mean reference concentration of 101 nmol/L and a standard deviation (SD) of 40% of the mean (92).

Dosing Recommendations of Midazolam and Digoxin for Clinical Practice

Dosing recommendations for midazolam and digoxin under bid (twice a day) clarithromycin co-treatment were determined as percentage of the midazolam and digoxin dose without co-medication. In the scenario of clarithromycin co-administration, doses of midazolam and digoxin were reduced until the $AUC_{inhibition}$ equaled the AUC_{normal} . For the DDI studies, mean individuals were created (mean of the study age, weight, height, and BMI) to calculate the adapted doses during clarithromycin administration of 25, 50, 100, 200, 300, 400, 500, 600, 700, 800, 900, and 1000 mg bid. For the clinically most relevant clarithromycin doses of 250 and 500 mg, virtual population simulations were performed using the adapted doses of midazolam and digoxin.

PBPK DDI Modeling of Clarithromycin, Midazolam, and Digoxin

Table II. Physicochemical and Pharmacokinetic Parameter Values Used in Simulations

Parameter	Units	Clarithromycin in simulations	Clarithromycin literature	Digoxin in simulations	Digoxin literature	Midazolam in simulations	Midazolam literature	Description
MW	g/mol	747.95	747.95	780.93	780.93	325.77	325.77	Molecular weight
f_u		0.48 ^a	0.28-0.58 (63)	0.70	0.70 (64)	0.025 ^a	0.024-0.08 (65,66)	Fraction unbound
$\log P$		2.3 ^a	2.3-3.24 (23,67)	1.67	1.67 (68)	2.98 ^a	2.7-4.33 (69,70)	Lipophilicity
B:P		1.23	1.23 (PK-SIM) ^b	0.94	0.94 (PK-SIM) ^b	0.61 ^a	0.53-0.7 (35,71)	Blood-to-plasma concentration ratio
pKa		8.99 ^a	8.76-8.99 (72,73)	13.5	13.5 (74)	6.15	6.15 (75)	Acid dissociation constant
Solubility [pH]	g/L	12.17 [2.4]	12.17 [2.4] (76)	17.0	17.0 (77)	0.024 [7] (78)	0.024 [7] (78)	Solubility
$P_{pis,bc}$	μm/s	0.40 ^c	0.55 (PK-SIM) ^b	0.99	0.99 (PK-SIM) ^b	8.24	8.24 (PK-SIM) ^b	Plasma-blood permeability
$P_{bc,pls}$	μm/s	0.03 ^c	0.55 (PK-SIM) ^b	0.99	0.99 (PK-SIM) ^b	8.24	8.24 (PK-SIM) ^b	Blood-plasma permeability
P_{intest}	nm/s	1.12 ^d	3.3 ± 0.9 (55)	4.42 ^c	16 (79)	26.2 ^c	369 (80)	Intestinal permeability
CYP3A4 K_M	μmol/L	50.0 ^e	48.7 ± 17.7 (11)	—	—	2.7	2.7 (81)	Michaelis-Menten constant
CYP3A4 k_{cat}	1/min	11.40 ^c	1.9 ± 0.7 (11)	—	—	13.1 ^c	1.96 ± 0.08 (81)	CYP3A4 turnover number
OATP K_M	μmol/L	50.0 ^e	58.0 ± 47.9 (16) ^f	—	—	—	—	Michaelis-Menten constant
OATP k_{cat}	1/min	0.15 ^c	8.1 (16) ^g	—	—	—	—	OATP turnover number
P-gp K_M	μmol/L	—	—	58.2	58.2 (82)	—	—	Michaelis-Menten constant
P-gp k_{cat}	1/min	—	—	173.8 ^c	288.8 (82) ^h	—	—	P-gp turnover number
ATPIA2 k_{off}	1/min	—	—	21.8 ^c	NA	—	—	Dissociation rate constant
ATPIA2 K_d	nmol/L	—	—	25.6	25.6 (83)	—	—	Dissociation constant
CL _R	L/h	7.9 ^a	6.7-12.8 (63)	—	j	j	j	Renal clearance
CYP3A4 K_I	μmol/L	41.4 ^a	2.25-41.4 (84,85)	—	—	—	—	Inhibition constant
CYP3A4 k_{inact}	h ⁻¹	3.3 ^a	2.4-13.8 (86,84)	—	—	—	—	Inactivation rate constant
D _{r,50}	min	5.0	—	15.0	c	2	c	Dissolution time (50% dissolved)
Shape factor		2.9	—	0.20	c	0.69	c	Dissolution shape parameter

NA not available

^aOptimized within range of minimum and maximum literature values

^bCalculated internally within PK-Sim

^cOptimized without literature-based value range

^dOptimized within range of mean ±3*SD

^eOptimized within range of mean ±1*SD

^fTaken from rat hepatic uptake assessment

^gAssuming 117 million cells per g of rat liver (87)

^hAssuming 275 fmol/cm² of P-gp of mucosal lining (62)

ⁱFor digoxin CL_R consists of GFR and additional renal secretion via P-gp

^jFor midazolam CL_R is negligible

Parameter Sensitivity Analysis

Parameter sensitivity analyses have been performed to assess the impact of critical model parameters on the predicted AUC_{ratios} for the co-treatment regimens showing the highest observed AUC_{ratios} . Co-treatment regimens were (i) 500 mg oral clarithromycin at steady state (bid) with a single oral dose of 4 mg midazolam and (ii) 250 mg oral clarithromycin at steady state (bid) with a single oral dose of 0.75 mg digoxin. Assessed parameters were: clarithromycin blood cell permeabilities (one permeability for each direction), CYP3A4 K_i , CYP3A4 k_{inact} , midazolam CYP3A4 k_{cat} , CYP3A4 half-lives in the liver and intestine, digoxin P-gp k_{cat} , digoxin P-gp K_i , and digoxin ATPase k_{off} . All parameters were varied individually over a wide range of values (via multiplication by factors between 0.1 and 10.0) and the change in AUC_{ratio} was documented. If a 10% change of a single parameter leads to a >1% change in AUC_{ratio} , the model is considered sensitive to this parameter.

RESULTS

PBPK models of clarithromycin, midazolam, and digoxin have been successfully developed using the given parameters in Table II. Best simulation results for all compounds were obtained using tissue-to-plasma partition coefficients calculated by the method of Rodgers and Rowland (93,94).

For clarithromycin, it was not possible to adequately describe the concentration-time profile after intravenous administration using standard input parameters (e.g., logP)

and calculation methods (e.g., partition coefficients). Simulated concentration-time profiles over-predicted C_{max} and under-predicted the observed data for time $> T_{max}$. According to literature, clarithromycin accumulates in mononuclear (MN) and polymorphonuclear (PMN) leukocytes, probably via active transport (95). This process was implemented, and it improved the model significantly. Due to limited knowledge on this transport (unknown transporter, unknown V_{max} , and K_M value), an adjustment of the clarithromycin permeability between plasma and RBC compartments was applied. The clarithromycin permeability optimization ($P_{plasma \rightarrow RBC}$, $P_{RBC \rightarrow plasma}$) led to an asymmetric permeability ratio $P_{plasma \rightarrow RBC}/P_{RBC \rightarrow plasma}$ of 13, indicating that clarithromycin can more easily enter than exit the RBC compartments. Using the optimized permeability values, the clarithromycin model successfully described the training dataset's concentration-time profiles after different doses of intravenous (supplementary Fig. 1) and oral clarithromycin application (Fig. 1). The prediction of the evaluation dataset's individual concentration-time profiles was successful for multiple dosing with 250 and 500 mg clarithromycin (Fig. 2) and reasonably well for single rising doses of 100–1200 mg (supplementary Fig. 2). The MBI of CYP3A4 by clarithromycin was successfully implemented. The reported loss of CYP3A4 activity in the liver and intestine (96) during treatment with 500 mg clarithromycin could be accurately simulated (supplementary Fig. 3). Our model predicts a duodenal intracellular mucosa clarithromycin concentration, after oral treatment, which is about 20 times higher than the concentration reached in the intracellular liver compartment

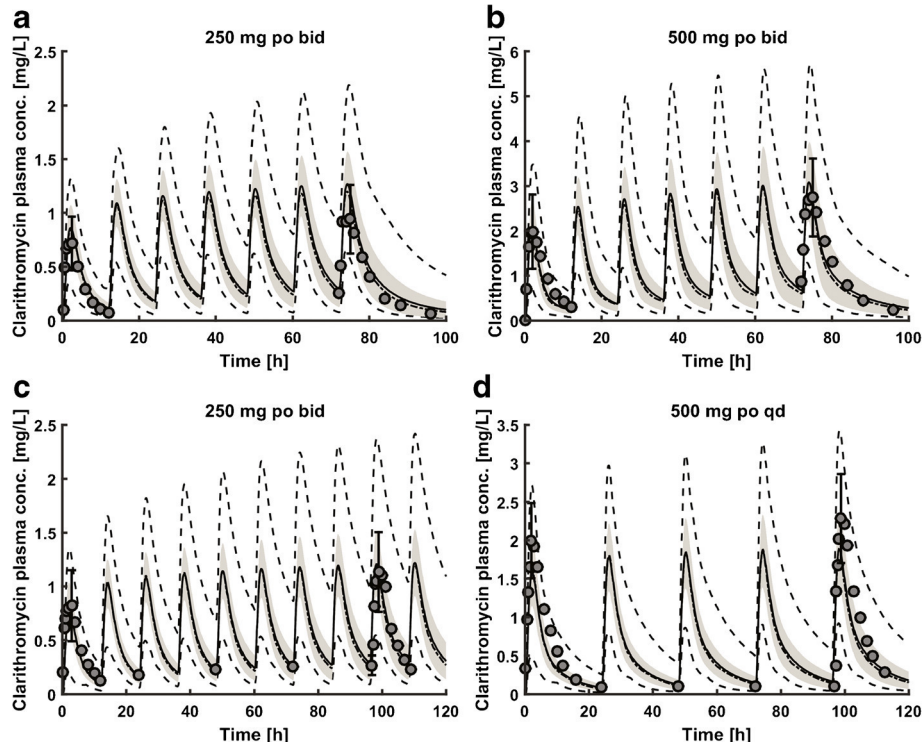


Fig. 1. Predicted concentration-time profiles of clarithromycin (a, b: ref. (25), c, d: ref. (27)) in comparison with the observed mean data (\pm standard deviation (SD)). Solid line, predicted mean; dashed-dotted line, predicted median; gray shaded area, predicted SD; dashed line, predicted minimum/maximum; gray circles observed mean data (\pm SD)

PBPK DDI Modeling of Clarithromycin, Midazolam, and Digoxin

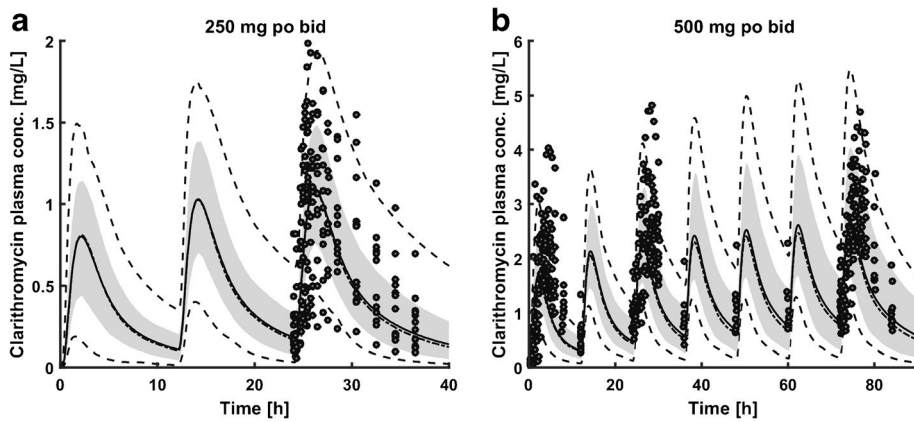


Fig. 2. Predicted concentration-time profiles of clarithromycin after multiple doses of clarithromycin (**a**: ref. (26), **b**: ref. (28)) in comparison with the observed individual data. Solid line, predicted mean; dashed-dotted line, predicted median; gray shaded area, predicted 5th–95th percentile; dashed line, predicted minimum/maximum; gray circles, observed individual data

($C_{\max,\text{intestine}}$, 621 mg/L; $C_{\max,\text{liver}}$, 31 mg/L). The maximum loss of intestinal CYP3A4 activity was about 80% whereas the hepatic loss was about 55% during simulated treatment with 500 mg clarithromycin bid.

The developed midazolam model appropriately described the training dataset (supplementary Figs. 4 and 5) and predicted the evaluation dataset's concentration-time profiles (Fig. 3, supplementary Figs. 4 and 5), of both, intravenously and orally administered midazolam.

The digoxin model also adequately described the training dataset (supplementary Figs. 6–8) and predicted the evaluation dataset's concentration-time profiles (Fig. 4, supplementary Figs. 6–8) for intravenous and oral administration.

The clarithromycin–midazolam model accurately predicted the clinically observed DDI after oral clarithromycin pretreatment and intravenously or orally administered midazolam (Fig. 5). Hence, the MBI parameter values (k_{inact} , K_1) of the clarithromycin model could be successfully used to predict the clarithromycin–midazolam DDI without further adjustments to these parameters. The clarithromycin–digoxin model adequately predicted the clinically observed DDI after

oral clarithromycin pretreatment and intravenously or orally administered digoxin (supplementary Fig. 9, Fig. 6). The predicted mean AUC_{ratios} of the clarithromycin–midazolam DDI, intravenous and oral, were comparable to the observed mean AUC_{ratios} . Dividing predicted by observed AUC_{ratios} gives ratios of 0.8 (minimum) to 1.0 (maximum) (Table III). The predicted mean AUC_{ratios} of the intravenous clarithromycin–digoxin DDI were also comparable to the observed mean AUC_{ratios} . Dividing predicted by observed AUC_{ratios} of the intravenous clarithromycin–digoxin DDI gives values of 0.9 (minimum) to 1.0 (maximum). The predicted mean AUC_{ratios} of the oral clarithromycin–digoxin DDI were over-predicted by a factor of 2.0. The predicted SDs of all AUC_{ratios} (midazolam and digoxin DDI) were close to the observed SDs except for the SD of the clarithromycin–digoxin DDI after intravenous application, which was under-predicted ($SD_{\text{pred}} = 0.01$ vs. $SD_{\text{obs}} = 2.22$).

To assess the impact of the parameters used to model the DDI processes, a sensitivity analysis was conducted which showed that 10% changes in CYP3A4 k_{inact} , CYP3A4 K_1 , liver CYP3A4 half-life, digoxin P-gp k_{cat} , and midazolam CYP3A4 k_{cat} (5 out of 10 tested parameters) lead to 13, 11,

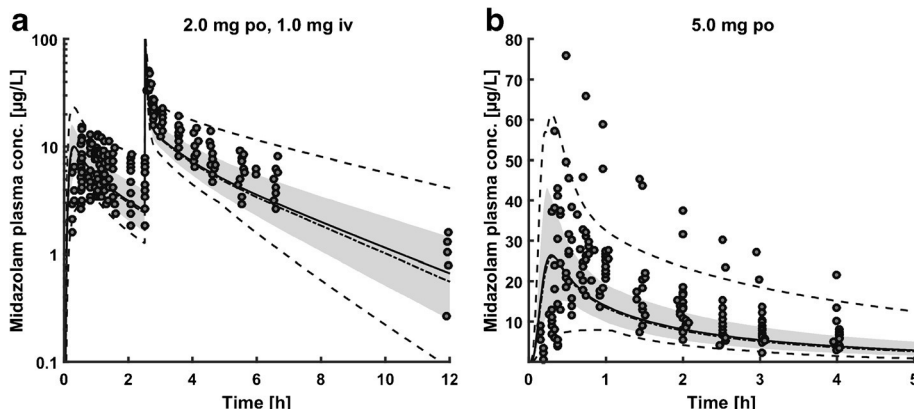


Fig. 3. Predicted concentration-time profiles of midazolam after intravenous and oral doses of midazolam (**a**: ref. (31), **b**: ref. (37)) in comparison with the observed individual data. Solid line, predicted mean; dashed-dotted line, predicted median; gray shaded area, predicted 5th–95th percentile; dashed line, predicted minimum/maximum; gray circles, observed individual data

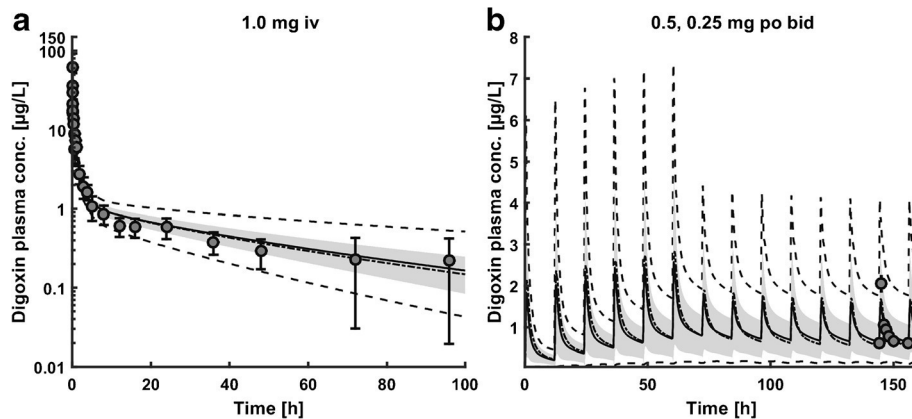


Fig. 4. Predicted concentration-time profiles of digoxin after intravenous and oral doses of digoxin (a: ref. (40), b: ref. (51)) in comparison with the observed mean data (\pm standard deviation (SD)). Solid line, predicted mean; dashed-dotted line, predicted median; gray shaded area, predicted SD; dashed line, predicted minimum/maximum; gray circles, observed mean data (\pm SD)

11, 9, and 5% changes in AUC_{ratios} , respectively (supplementary Fig. 10). The other half of the assessed parameters had no crucial impact on the predicted AUC_{ratios} .

Dosing recommendations for midazolam and digoxin under clarithromycin co-medication were calculated using mean study individuals. An overview of the recommended oral midazolam and digoxin doses with the corresponding oral clarithromycin doses from 25 to 1000 mg bid at steady state is presented in Fig. 7. At clarithromycin steady state with orally administered 500 mg bid, the intravenous midazolam dose had to be reduced by 62% to achieve a similar midazolam exposure as without co-treatment. At clarithromycin steady state with orally administered 250 or 500 mg bid, the oral midazolam doses had to be reduced by 74 and 88%, respectively. During clarithromycin treatment with orally administered 250 or 500 mg bid, the oral digoxin doses had to be reduced by 21 or 22%, to prevent elevated digoxin concentrations.

The identified adjusted midazolam and digoxin doses for co-medication with the clinically most relevant clarithromycin doses of 250 and 500 mg bid were applied in virtual populations (supplementary Table 1). In both DDI scenarios, the number of virtual individuals who experience a relevant increase in the AUC of the victim drug is significantly reduced when applying the adjusted doses. In other words, DDIs take place in all virtual individuals, but the AUCs of the victim drugs stay approximately the same. In the clarithromycin–midazolam DDI, the decline in the number of experienced DDIs is much higher than in the clarithromycin–digoxin DDI using the calculated dose adaptation.

DISCUSSION

For the first time, a whole-body PBPK model of clarithromycin has been developed. The model was able to predict a metabolic and a transporter DDI with the victim drugs midazolam and digoxin.

Apart from our presented whole-body PBPK model, two semi-physiological models of clarithromycin and a commentary on a clarithromycin PBPK model have been published to

date (9,85,97). For the semi-physiological models, empirically accentuated approaches were used, focusing exclusively on the prediction of the impact of clarithromycin on CYP3A4, which was reasonably well predicted. However, the MBIs used in these publications were either available in the liver only or not active at clarithromycin doses \leq 100 mg. Furthermore, these models are not developed for prediction of intravenous application of clarithromycin. In the case of the commentary, no model development was presented, the model structure remains unclear (full or minimal PBPK), and the parameterization was not published.

Our clarithromycin model overcomes these limitations and was built in a more comprehensive and mechanistic approach. The MBI is available in all tissues with CYP3A4 expression and active at all clarithromycin doses after intravenous and oral application. Furthermore, the DDI is not only limited to the level of CYP3A4 but also describes clarithromycin DDIs via P-gp. All three PBPK models (clarithromycin, midazolam, and digoxin) were developed and evaluated independently of each other. Hence, the prediction of the DDIs of clarithromycin with midazolam and digoxin were done without any adaptation of the parameters used in the implemented processes mediating the DDIs. The presented mechanistic models can easily be (i) coupled to other victim or perpetrator models or (ii) expanded by addition of further DDI processes (e.g., OATP inhibition). This comprehensive whole-body PBPK approach was used in the conviction that mechanistic models are better suited for the scaling to special populations like geriatric, pediatric, or diseased populations.

The MBI of CYP3A4 is crucial to understand the non-linear pharmacokinetics of clarithromycin (12). Our model adequately predicts the observed loss of duodenal and hepatic CYP3A4 activity due to the MBI (96). Although CYP3A activity encompasses CYP3A4 and CYP3A5, whose substrate specificities cannot be distinguished (6), we neglected CYP3A5 in our clarithromycin and midazolam models, since it was reported that CYP3A5 plays a negligible role in the PK of both CYP3A substrates (32,98,99).

The PK of clarithromycin further depends on the distribution into MN and PMN *in vivo*. Since the standard

PBPK DDI Modeling of Clarithromycin, Midazolam, and Digoxin

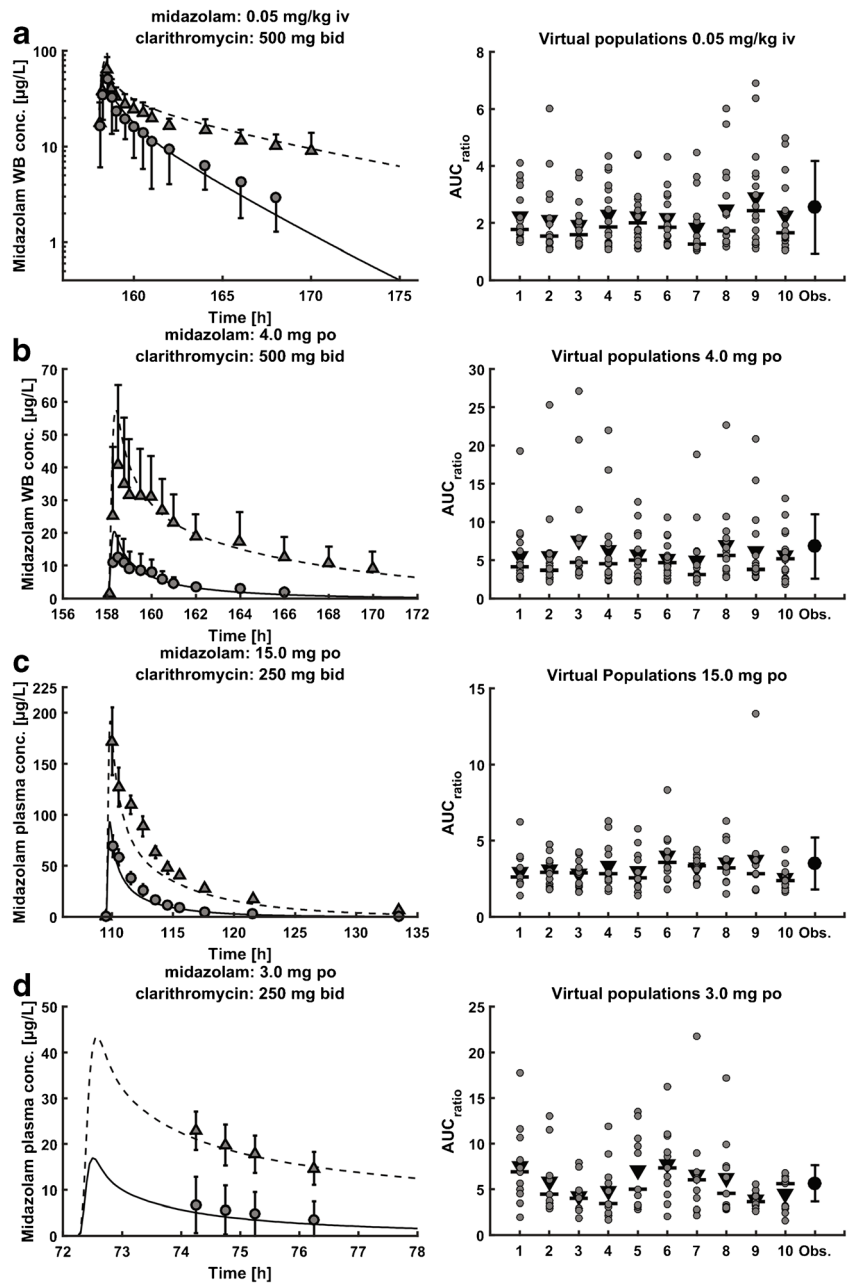


Fig. 5. *Left column:* predicted concentration-time profiles of intravenous and oral doses of midazolam (**a**, **b**: ref. (29), **c**: ref. (39), **d**: ref. (36)) with and without prior clarithromycin regimens in comparison with observed mean data (\pm standard deviation (SD)). *Solid line*, predicted midazolam mean without prior clarithromycin; *dashed line*, predicted midazolam mean with prior clarithromycin; *gray circles*, observed mean midazolam without prior clarithromycin; *gray triangles*, observed mean midazolam with prior clarithromycin. *Right column:* predicted midazolam AUC_{ratio} (AUC_{inhibition}/AUC_{normal}) in 10 virtual populations of intravenous and oral doses of midazolam in comparison with observed mean data (\pm SD). *Horizontal lines*, predicted midazolam AUC_{ratio} median; *triangles*, predicted midazolam AUC_{ratio} mean; *gray circles*, predicted individual midazolam AUC_{ratios}; *filled circles*, observed mean midazolam AUC_{ratio} (\pm SD). Clarithromycin was administered orally (bid) with 250 mg (36,39) and 500 mg (29). WB whole blood

whole-body PK-Sim model does not offer MN or PMN cell compartments, we used the RBC compartments (with adjusted permeability values) as surrogate compartments for RBC + (MN + PMN) cells to adequately describe the PK of clarithromycin. In a clinical study with 250 mg bid dosing, the

observed peak concentrations (C_{\max}) of clarithromycin in MN and PMN cells were 29 and 17 µg/mL, respectively, leading to a C_{\max} concentration ratio $C_{\max,MN+PMN}/C_{\max,plasma}$ of 10 to 30 in healthy volunteers (27). The observed C_{\max} values correspond to an amount of 17 mg of clarithromycin. The

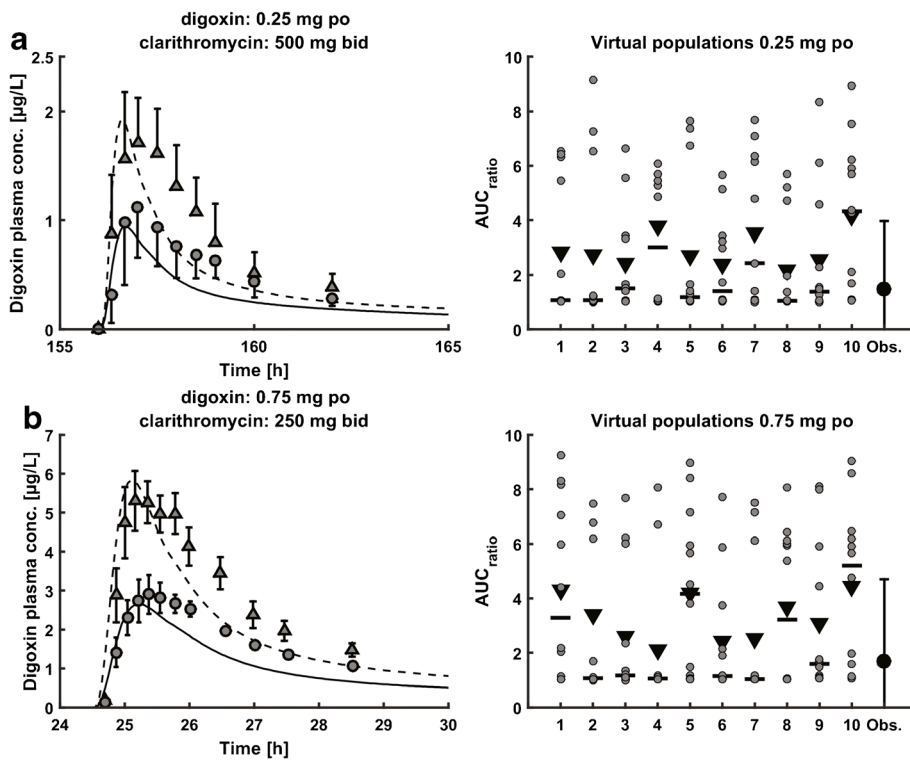


Fig. 6. Left column: predicted concentration-time profiles of digoxin after single oral doses of digoxin (a: ref. (48), b: ref. (26)) with and without prior clarithromycin regimens in comparison with observed mean data (\pm standard deviation (SD)). Solid line, predicted digoxin mean without prior clarithromycin; dashed line, predicted digoxin mean with prior clarithromycin; gray circles, observed mean digoxin without prior clarithromycin; gray triangles, observed mean digoxin with prior clarithromycin. Right column: predicted digoxin AUC_{ratio} ($AUC_{inhibition}/AUC_{normal}$) in 10 virtual populations of oral digoxin in comparison with observed mean data (\pm SD). Horizontal lines, predicted digoxin AUC_{ratio} median; triangles, predicted digoxin AUC_{ratio} mean; gray circles, predicted individual digoxin AUC_{ratios}; filled circles, observed mean digoxin AUC_{ratio} (\pm SD). Clarithromycin was administered orally (bid) with 250 mg (26) and 500 mg (48).

predicted, additional amount of clarithromycin in the RBC compartments, due to the optimized asymmetrical permeability ratio of 13, was 36 mg, which is reasonably close.

In the final digoxin model, digoxin is binding to the ATP1A2 ATPase. The ATPase concentration was fitted to a reference concentration in the brain of 99.5 µmol/L. ATPase

measurements of [³H]-ouabain binding, enzyme activity and maximum transport capacity suggest that the concentration of Na⁺-K⁺ pumps (ATPase) in mammalian skeletal muscle is about 300–800 pmol/g wet tissue (100), which translates to 0.4–1.1 µmol/L, assuming a tissue density of 1 g/mL and an expression level of 0.7 in muscle. The reason for this discrepancy

Table III. Comparison Predicted vs. Observed AUC Ratio

Application and dose [mg] of clarithromycin	Application and dose [mg] of victim drug	Number	Females [%]	Predicted mean AUC _{ratio} ^a \pm STD	Observed mean AUC _{ratio} \pm STD	AUC _{ratio,predicted} / AUC _{ratio,observed}	Ref.
Midazolam							
po (tab, MD), 500	iv (inf, 30 min), 0.05/kg	16	50	2.2 \pm 1.2	2.8 \pm 1.6	0.8	(29)
po (tab, MD), 250	po (sol, SD), 3.0	11	10	5.8 \pm 3.7	5.6 \pm 2.0	1.0	(36) ^b
po (tab, MD), 500	po (tab, SD), 4.0	16	50	5.9 \pm 4.6	7.0 \pm 4.2	0.8	(29)
po (tab, MD), 250	po (tab, SD), 15.0	12	66	3.2 \pm 1.5	3.6 \pm 1.7	0.9	(39)
Digoxin							
po (tab, MD), 400	iv (inf, 60 min), 0.5	9	0	1.01 \pm 0.01	0.98 \pm 2.22	1.0	(45)
po (tab, MD), 250	iv (inf, 4 min), 0.01/kg	12	0	1.02	1.2	0.9	(26)
po (tab, MD), 500	po (tab, SD), 0.25	18	50	2.91 \pm 2.74	1.47 \pm 2.50	2.0	(48)
po (tab, MD), 250	po (tab, SD), 0.75	12	0	3.37 \pm 2.86	1.7 \pm 3.05	2.0	(26)

inf infusion, iv intravenous, MD multiple doses, po per os, SD single dose, sol solution, STD standard deviation, tab tablet

^a AUC_{ratio} = AUC_{inhibition}/AUC_{normal}

^b Individual concentration-time profiles are unpublished in-house data

PBPK DDI Modeling of Clarithromycin, Midazolam, and Digoxin

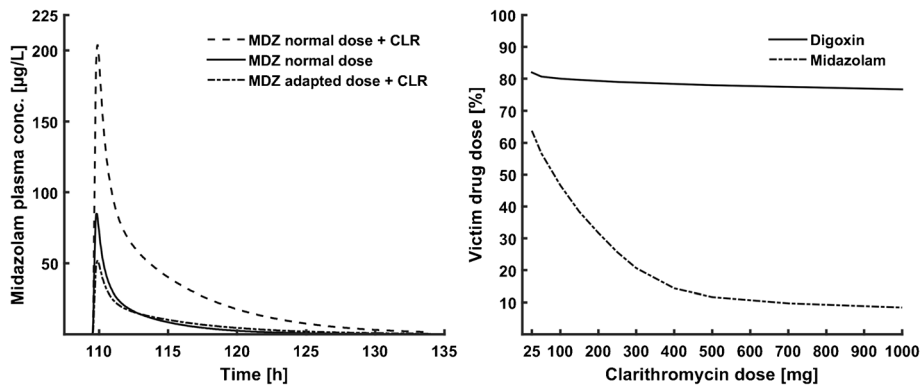


Fig. 7. *Left:* predicted concentration-time profiles of midazolam after single oral doses of midazolam (MDZ) with and without oral clarithromycin (CLR) pretreatment. *Solid line*, 100% midazolam dose without clarithromycin; *dashed line*, 100% midazolam dose with clarithromycin; *dashed-dotted line*, adapted 26% midazolam dose with clarithromycin. *Right:* victim drug dose recommendations in percent depending on the co-administered clarithromycin dose at clarithromycin steady state (bid). *Solid line*, adapted digoxin dose; *dashed-dotted line*, adapted midazolam dose

is unknown and probably reflects further mechanisms of digoxin distribution that we have not understood so far.

The performance of the clarithromycin–midazolam model is very good over the full range of administered doses and administration protocols including the predicted mean AUC_{ratio} and corresponding standard deviations. Consequently, this model can help to replace ketoconazole by guiding clinical DDI study designs with clarithromycin as a strong mechanism-based inhibitor of CYP3A4. Although a secondary objective, the clarithromycin–digoxin model shows very good performance. Nevertheless, the predicted mean AUC_{ratio} of oral digoxin (0.25, 0.75 mg) with and without clarithromycin pretreatment is over-predicted by a factor of 2. Interestingly, the predicted median AUC_{ratio} is close to the observed mean. Virtual population simulations revealed a wide range of individual AUC_{ratios} between 1 and 10 (Fig. 6). There is no over-prediction using a single mean study individual, instead of a population, to predict the AUC_{ratio} for, e.g., 0.25 mg digoxin (predicted, 1.33; observed, 1.47). The reason for the over-prediction lies in the combination of intestinal permeability of digoxin together with the mucosal P-gp activities along the intestinal tract within the virtual populations. This combination leads to a high sensitivity to P-gp transport for some individuals which in turn leads to the skewed distribution of concentration-time profiles (predicted median $AUC_{ratio} <$ predicted mean AUC_{ratio}). Further, knowledge on tissue-specific P-gp expression and its variability would greatly improve the DDI population predictions. This may also include genetic information because P-gp polymorphisms have been related to differences in digoxin distribution (101) and also to important clinical endpoints in digoxin users (102). It could also be speculated that unbound tissue concentrations of clarithromycin and/or digoxin are not adequately predicted.

Our dose adaptation analysis identified that the recommended digoxin dose is constant at ~80% across the investigated dose range, whereas the dose of midazolam is declining from 60 to 10% for clarithromycin doses of 25 to 500 mg bid, respectively. For higher clarithromycin doses (>500 mg), no further reduction of the midazolam dose seems to be required. For oral digoxin, the

competitive DDI with clarithromycin occurs predominantly in the mucosa where clarithromycin reaches local concentrations high enough to significantly inhibit the P-gp transport of digoxin even at clarithromycin doses of 25 mg. In contrast, 500 mg clarithromycin at steady state are necessary to reach the maximum MBI for CYP3A4. For clinical practice, this could imply that a single dose adaptation is sufficient for digoxin but a number of midazolam dose adaptations might be needed, depending on the given clarithromycin dose. There are several approved oral formulations and strengths available for midazolam and digoxin in the USA. According to the FDA “Orange Book,” midazolam is approved and available as an oral syrup (2 mg base/mL) and digoxin is available as oral solution (0.05 mg/mL) and tablet (0.125 and 0.25 mg). The accurate administration of the adapted doses of midazolam and digoxin is feasible with the oral solution formulations. Training in appropriate dosing of the oral solutions might be needed for the patients.

Since DDIs are a major reason for adverse events during commonplace pharmacotherapy, the FDA labels would benefit from dosing guidance to prevent avoidable DDIs with clarithromycin, midazolam, and digoxin. To assess the impact of dose adaptations on DDIs in a population, simulations could help to close this gap in the respective labels. The virtual population simulations with the adapted victim drug doses in supplementary Table 1 show that a dose adaptation is especially helpful and necessary during the MBI (clarithromycin–midazolam). Although the adapted doses prevent digoxin overdosing during the competitive inhibition (clarithromycin–digoxin) in a significant number of individuals, the reduction of individuals experiencing strong and moderate AUC changes is improbable. However, as a drug with a narrow therapeutic index, digoxin is a typical candidate drug for therapeutic drug monitoring which implies that the individualization of the digoxin dose during clarithromycin co-treatment in this study especially revolves around the determination of the digoxin starting dose. A clinical study should be considered to evaluate and add more confidence to these model predictions established in a virtual population.

Comprehensive and mechanistic whole-body PBPK models are complex and require the input of many parameters. For some of these parameters, no values are available from the literature or the reported values differ strongly. The parameter sensitivity analysis shows that the predicted DDI AUC_{ratios} are sensitive to 5 out of 10 assessed parameters. Among these 5 parameters, especially CYP3A4 liver half-life but also CYP3A4 K_I and CYP3A4 k_{inact} cannot be reliably derived from the literature. The liver half-life of CYP3A4 is reported with values from 10 to 140 h. We found that a half-life of 36 h was optimal to describe the effects of the MBI by clarithromycin. The same value has been reported as most appropriate in a dedicated modeling study by Rowland Yeo *et al.* using several CYP3A4 mechanism-dependent inhibitors and victim drugs (103). For CYP3A4 K_I and k_{inact}, the values used in the simulations were the only ones to result in an accurate description of the clinical clarithromycin data. Additional impactful parameters were the midazolam CYP3A4 k_{cat} and the digoxin P-gp k_{cat}. Both values have been optimized very carefully using a multitude of clinical studies spanning large dosing ranges of intravenous and oral application. In addition, the digoxin model has been developed including data on the fraction of digoxin excreted in urine, to increase our confidence in the optimized P-gp k_{cat} value. However, this sensitivity analysis demonstrates that the MBI of clarithromycin with CYP3A4 is strongly influenced by 3 different parameters (CYP3A4 liver half-life, CYP3A4 K_I, and CYP3A4 k_{inact}). We will continue to evaluate our DDI model by expanding it to the interactions with other victim drugs and the scientific community will probably carry on to investigate these parameters until a good validation is reached. On the *in vivo* side, these results suggest that interindividual differences in CYP3A4 and P-gp activity, CYP3A4 turnover in the liver and clarithromycin concentrations available to cause the MBI of CYP3A4 will lead to large interindividual differences in the observed AUC_{ratios} during this DDI. If this is true, DDI modeling should strive to account for these variabilities for accurate dose recommendations and study design.

In summary, our work shows that the subcompartmentalization of blood into plasma and red blood cell compartments is not sufficient to account for important distribution processes found *in vivo* for clarithromycin. This might also hold true for other eligible compounds. As models will become more mechanistic in the future and the spatial and temporal resolution will be continuously improved, a more detailed compartmentalization of the blood will be part of a general trend for more accurate descriptions of organs important for absorption, disposition, action, and toxicity (gut, liver, kidney, brain, etc.).

Further direction for future work is the measurement and the interplay of many important parameters needed as inputs for model building which are not (publicly) available yet, starting with physicochemical parameters, activity levels of drug metabolizing enzymes and transporters throughout the body and other parameters to inform ADME and DDI processes. Also, the characterization of the interindividual variability of these parameters would greatly help to understand individual differences in observed plasma concentrations and could be considered during model building.

CONCLUSION

In this paper, we present the first published whole-body PBPK model of clarithromycin. Our clarithromycin model was linked to PBPK models of the paradigm victim drugs midazolam and digoxin and was capable to predict the resulting DDIs. With the presented model, we provide a valuable, publicly available tool for drug development and clinical practice. The presented models can help researchers understand and characterize the DDI potential of new molecular entities and inform the design of DDI studies with potential CYP3A4 and P-gp substrates.

REFERENCES

- Pirmohamed M, James S, Meakin S, *et al.* Adverse drug reactions as cause of admission to hospital: prospective analysis of 18 820 patients. *BMJ*. 2004;329:15–9. doi:[10.1136/bmj.329.7456.15](https://doi.org/10.1136/bmj.329.7456.15).
- Huang S-M, Lesko LJ. Drug-drug, drug-dietary supplement, and drug-citrus fruit and other food interactions: what have we learned? *J Clin Pharmacol*. 2004;44:559–69. doi:[10.1177/091270004265367](https://doi.org/10.1177/091270004265367).
- EMA. Guideline on the investigation of drug interactions. 2012. http://www.ema.europa.eu/docs/en_GB/document_library/Scientific_guideline/2012/07/WC500129606.pdf. Accessed 28 Jan 2016.
- FDA. Guidance for industry. Drug interaction studies study design, data analysis, implications for dosing, and labeling recommendations. 2012. <http://www.fda.gov/downloads/Drugs/GuidanceComplianceRegulatoryInformation/Guidances/UCM292362.pdf>. Accessed 28 Jan 2016.
- Lin JH. CYP induction-mediated drug interactions: *in vitro* assessment and clinical implications. *Pharm Res*. 2006;23:1089–116. doi:[10.1007/s11095-006-0277-7](https://doi.org/10.1007/s11095-006-0277-7).
- Wilkinson GR. Drug metabolism and variability among patients in drug response. *N Engl J Med*. 2005;352:2211–21. doi:[10.1056/NEJMra032424](https://doi.org/10.1056/NEJMra032424).
- Zhao P, Ragueneau-Majlessi I, Zhang L, *et al.* Quantitative evaluation of pharmacokinetic inhibition of CYP3A substrates by ketoconazole: a simulation study. *J Clin Pharmacol*. 2009;49:351–9. doi:[10.1177/0091270008331196](https://doi.org/10.1177/0091270008331196).
- FDA. FDA advises against using oral ketoconazole in drug interaction studies due to serious potential side effects. 2013. <http://www.fda.gov/Drugs/DrugSafety/ucm371017.htm>. Accessed 28 Jan 2016.
- Ke AB, Zamek-Gliszczynski MJ, Higgins JW, Hall SD. Itraconazole and clarithromycin as ketoconazole alternatives for clinical CYP3A inhibition studies. *Clin Pharmacol Ther*. 2014;95:473–6. doi:[10.1038/clpt.2014.41](https://doi.org/10.1038/clpt.2014.41).
- Goossens H, Ferech M, Coenen S, Stephens P. Comparison of outpatient systemic antibacterial use in 2004 in the United States and 27 European countries. *Clin Infect Dis*. 2007;44:1091–5. doi:[10.1086/512810](https://doi.org/10.1086/512810).
- Rodrigues AD, Roberts EM, Mulford DJ, Yao Y, Ouellet D. Oxidative metabolism of clarithromycin in the presence of human liver microsomes. Major role for the cytochrome P4503A (CYP3A) subfamily. *Drug Metab Dispos*. 1997;25:623–30.
- Mayhew BS, Jones DR, Hall SD. An *in vitro* model for predicting *in vivo* inhibition of cytochrome P450 3A4 by metabolic intermediate complex formation. *Drug Metab Dispos*. 2000;28:1031–7.
- Chu SY, Sennello LT, Bunnell ST, Varga LL, Wilson DS, Sonders RC. Pharmacokinetics of clarithromycin, a new macrolide, after single ascending oral doses. *Antimicrob Agents Chemother*. 1992;36:2447–53. doi:[10.1128/AAC.36.11.2447](https://doi.org/10.1128/AAC.36.11.2447).

PBPK DDI Modeling of Clarithromycin, Midazolam, and Digoxin

14. Saito H, Fukasawa Y, Otsubo Y, Yamada K, Sezaki H, Yamashita S. Carrier-mediated transport of macrolide antimicrobial agents across Caco-2 cell monolayers. *Pharm Res.* 2000;17:761–5. doi:[10.1023/A:1007550820196](https://doi.org/10.1023/A:1007550820196).
15. Eberl S, Renner B, Neubert A, et al. Role of p-glycoprotein inhibition for drug interactions: evidence from in vitro and pharmacoepidemiological studies. *Clin Pharmacokinet.* 2007;46:1039–49. doi:[10.2165/00003088-200746120-00004](https://doi.org/10.2165/00003088-200746120-00004).
16. Yabe Y, Galetin A, Houston JB. Kinetic characterization of rat hepatic uptake of 16 actively transported drugs. *Drug Metab Dispos.* 2011;39:1808–14. doi:[10.1124/dmd.111.040477](https://doi.org/10.1124/dmd.111.040477).
17. Garver E, Hugger ED, Shearn SP, et al. Involvement of intestinal uptake transporters in the absorption of azithromycin and clarithromycin in the rat. *Drug Metab Dispos.* 2008;36:2492–8. doi:[10.1124/dmd.108.022285](https://doi.org/10.1124/dmd.108.022285).
18. Seithel A, Eberl S, Singer K, et al. The influence of macrolide antibiotics on the uptake of organic anions and drugs mediated by OATP1B1 and OATP1B3. *Drug Metab Dispos.* 2007;35:779–86. doi:[10.1124/dmd.106.014407](https://doi.org/10.1124/dmd.106.014407).
19. Patki KC, Von Moltke LL, Greenblatt DJ. In vitro metabolism of midazolam, triazolam, nifedipine, and testosterone by human liver microsomes and recombinant cytochromes p450: role of cyp3a4 and cyp3a5. *Drug Metab Dispos.* 2003;31:938–44. doi:[10.1124/dmd.31.7.938](https://doi.org/10.1124/dmd.31.7.938).
20. Koup JR, Greenblatt DJ, Jusko WJ, Smith TW, Koch-Weser J. Pharmacokinetics of digoxin in normal subjects after intravenous bolus and infusion doses. *J Pharmacokinet Biopharm.* 1975;3:181–92. doi:[10.1007/BF00162306](https://doi.org/10.1007/BF00162306).
21. Ito S, Woodland C, Harper PA, Koren G. P-glycoprotein-mediated renal tubular secretion of digoxin: the toxicological significance of the urine-blood barrier model. *Life Sci.* 1993;53:PL25–31. doi:[10.1016/0024-3205\(93\)90667-R](https://doi.org/10.1016/0024-3205(93)90667-R).
22. Dostanic-Larson I. Physiological role of the 1- and 2-isoforms of the Na+-K+-ATPase and biological significance of their cardiac glycoside binding site. *AJP Regul Integr Comp Physiol.* 2005;290:R524–8. doi:[10.1152/ajpregu.00838.2005](https://doi.org/10.1152/ajpregu.00838.2005).
23. Lappin G, Shishikura Y, Jochemsen R, et al. Comparative pharmacokinetics between a microdose and therapeutic dose for clarithromycin, sumatriptan, propafenone, paracetamol (acetaminophen), and phenobarbital in human volunteers. *Eur J Pharm Sci.* 2011;43:141–50. doi:[10.1016/j.ejps.2011.04.009](https://doi.org/10.1016/j.ejps.2011.04.009).
24. Chu SY, Deaton R, Cavanaugh J. Absolute bioavailability of clarithromycin after oral administration in humans. *Antimicrob Agents Chemother.* 1992;36:1147–50. doi:[10.1128/AAC.36.5.1147](https://doi.org/10.1128/AAC.36.5.1147).
25. Chu S, Wilson DS, Deaton RL, Mackenthun AV, Eason CN, Cavanaugh JH. Single- and multiple-dose pharmacokinetics of clarithromycin, a new macrolide antimicrobial. *J Clin Pharmacol.* 1993;33:719–26. doi:[10.1002/j.1552-4604.1993.tb05613.x](https://doi.org/10.1002/j.1552-4604.1993.tb05613.x).
26. Rengelshausen J, Göggelmann C, Burhenne J, et al. Contribution of increased oral bioavailability and reduced nonglomerular renal clearance of digoxin to the digoxin-clarithromycin interaction. *Br J Clin Pharmacol.* 2003;56:32–8. doi:[10.1046/j.1365-2125.2003.01824.x](https://doi.org/10.1046/j.1365-2125.2003.01824.x).
27. Kees F, Wollenhofer M, Grobecker H. Serum and cellular pharmacokinetics of clarithromycin 500 mg q.d. and 250 mg b.i.d. in volunteers. *Infection.* 1995;23:168–72. doi:[10.1007/BF01793859](https://doi.org/10.1007/BF01793859).
28. Abduljalil K, Kinzig M, Bulitta J, et al. Modeling the autoinhibition of clarithromycin metabolism during repeated oral administration. *Antimicrob Agents Chemother.* 2009;53:2892–901. doi:[10.1128/AAC.01193-08](https://doi.org/10.1128/AAC.01193-08).
29. Gorski JC, Jones DR, Haehner-Daniels BD, Hamman MA, O'Mara EM, Hall SD. The contribution of intestinal and hepatic CYP3A to the interaction between midazolam and clarithromycin. *Clin Pharmacol Ther.* 1998;64:133–43. doi:[10.1016/S0009-9236\(98\)90146-1](https://doi.org/10.1016/S0009-9236(98)90146-1).
30. Brown CR, Sarnquist FH, Canup CA, Pedley TA. Clinical, electroencephalographic, and pharmacokinetic studies of a water-soluble benzodiazepine, midazolam maleate. *Anesthesiology.* 1979;50:467–70.
31. van Rongen A, Kervezee L, Brill M, et al. Population pharmacokinetic model characterizing 24-hour variation in the pharmacokinetics of oral and intravenous midazolam in healthy volunteers. *CPT pharmacometrics. Syst Pharmacol.* 2015;4:454–64. doi:[10.1002/psp4.12007](https://doi.org/10.1002/psp4.12007).
32. Yu K. Effect of the CYP3A5 genotype on the pharmacokinetics of intravenous midazolam during inhibited and induced metabolic states. *Clin Pharmacol Ther.* 2004;76:104–12. doi:[10.1016/j.cpt.2004.03.009](https://doi.org/10.1016/j.cpt.2004.03.009).
33. Smith MT, Eadie MJ, Brophy TO. The pharmacokinetics of midazolam in man. *Eur J Clin Pharmacol.* 1981;19:271–8. doi:[10.1007/BF00562804](https://doi.org/10.1007/BF00562804).
34. Hardmeier M, Zimmermann R, Rüegg S, et al. Intranasal midazolam: pharmacokinetics and pharmacodynamics assessed by quantitative EEG in healthy volunteers. *Clin Pharmacol Ther.* 2012;91:856–62. doi:[10.1038/clpt.2011.316](https://doi.org/10.1038/clpt.2011.316).
35. Heizmann P, Eckert M, Ziegler WH. Pharmacokinetics and bioavailability of midazolam in man. *Br J Clin Pharmacol.* 1983;16 Suppl 1:43S–9. doi:[10.1111/j.1365-2125.1983.tb02270.x](https://doi.org/10.1111/j.1365-2125.1983.tb02270.x).
36. Markert C, Hellwig R, Burhenne J, et al. Interaction of ambrisentan with clarithromycin and its modulation by polymorphic SLCO1B1. *Eur J Clin Pharmacol.* 2013;69:1785–93. doi:[10.1007/s00228-013-1529-1](https://doi.org/10.1007/s00228-013-1529-1).
37. Zhou D, Lu Z, Sunzel M, Xu H, Al-Huniti N. Population pharmacokinetic modelling to assess clinical drug-drug interaction between AZD7325 and midazolam. *J Clin Pharm Ther.* 2014;39:404–10. doi:[10.1111/jcpt.12152](https://doi.org/10.1111/jcpt.12152).
38. Bornemann LD, Min BH, Crews T, et al. Dose dependent pharmacokinetics of midazolam. *Eur J Clin Pharmacol.* 1985;29:91–5. doi:[10.1007/BF00547375](https://doi.org/10.1007/BF00547375).
39. Yeates RA, Laufen H, Zimmermann T. Interaction between midazolam and clarithromycin: comparison with azithromycin. *Int J Clin Pharmacol Ther.* 1996;34:400–5.
40. Kramer WG, Kolibash AJ, Lewis RP, Bathala MS, Visconti J, Reaming RH. Pharmacokinetics of digoxin: relationship between response intensity and predicted compartmental drug levels in man. *J Pharmacokinet Biopharm.* 1979;7:47–61. doi:[10.1007/BF01059440](https://doi.org/10.1007/BF01059440).
41. Wagner JG, Popat KD, Das SK, Sakmar E, Movahhed H. Evidence of nonlinearity in digoxin pharmacokinetics. *J Pharmacokinet Biopharm.* 1981;9:147–66. doi:[10.1007/BF01068079](https://doi.org/10.1007/BF01068079).
42. Steiness E, Waldorff S, Hansen PB. Renal digoxin clearance: dependence on plasma digoxin and diuresis. *Eur J Clin Pharmacol.* 1982;23:151–4. doi:[10.1007/BF00545970](https://doi.org/10.1007/BF00545970).
43. Ding R, Tayrouz Y, Riedel K, et al. Substantial pharmacokinetic interaction between digoxin and ritonavir in healthy volunteers. *Clin Pharmacol Ther.* 2004;76:73–84. doi:[10.1016/j.clpt.2004.02.008](https://doi.org/10.1016/j.clpt.2004.02.008).
44. Greiner B, Eichelbaum M, Fritz P, et al. The role of intestinal P-glycoprotein in the interaction of digoxin and rifampin. *J Clin Invest.* 1999;104:147–53. doi:[10.1172/JCI6663](https://doi.org/10.1172/JCI6663).
45. Tsutsumi K, Kotegawa T, Kuranari M, et al. The effect of erythromycin and clarithromycin on the pharmacokinetics of intravenous digoxin in healthy volunteers. *J Clin Pharmacol.* 2002;42:1159–64. doi:[10.1177/009127002237992](https://doi.org/10.1177/009127002237992).
46. Ochs HR, Greenblatt DJ, Bodem G, Harmatz JS. Dose-independent pharmacokinetics of digoxin in humans. *Am Heart J.* 1978;96:507–11. doi:[10.1016/0002-8703\(78\)90162-X](https://doi.org/10.1016/0002-8703(78)90162-X).
47. Becquemont L, Verstuyft C, Kerb R, et al. Effect of grapefruit juice on digoxin pharmacokinetics in humans. *Clin Pharmacol Ther.* 2001;70:311–6. doi:[10.1067/mcp.2001.118867](https://doi.org/10.1067/mcp.2001.118867).
48. Gurley BJ, Swain A, Williams DK, Barone G, Battu SK. Gauging the clinical significance of P-glycoprotein-mediated herb-drug interactions: comparative effects of St. John's wort, Echinacea, clarithromycin, and rifampin on digoxin pharmacokinetics. *Mol Nutr Food Res.* 2008;52:772–9. doi:[10.1002/mnf.200700081](https://doi.org/10.1002/mnf.200700081).
49. Eckermann G, Lahu G, Nassr N, Bethke TD. Absence of pharmacokinetic interaction between roflumilast and digoxin in healthy adults. *J Clin Pharmacol.* 2012;52:251–7. doi:[10.1177/0091270010389467](https://doi.org/10.1177/0091270010389467).
50. Oosterhuis B, Jonkman JH, Andersson T, Zuiderwijk PB, Jedema JN. Minor effect of multiple dose omeprazole on the pharmacokinetics of digoxin after a single oral dose. *Br J Clin Pharmacol.* 1991;32:569–72. doi:[10.1111/j.1365-2125.1991.tb03953.x](https://doi.org/10.1111/j.1365-2125.1991.tb03953.x).

51. Kirch W, Logemann C, Heidemann H, Santos SR, Ohnhaus EE. Effect of two different doses of nitrendipine on steady-state plasma digoxin level and systolic time intervals. *Eur J Clin Pharmacol*. 1986;31:391–5. doi:[10.1007/BF00613512](https://doi.org/10.1007/BF00613512).
52. Qiu R, Plowchalk DR, Byon W, Terra SG, Corrigan B, Mordenti J, et al. Lack of a pharmacokinetic interaction between dimebon (latrepirdine) and digoxin in healthy subjects. ASCPT 2010 Annual Meeting, Atlanta, Georgia, USA, 17th-20th March. *Clin Pharmacol Ther*. 2010;87(S1):S91:PIII-72. doi:[10.1038/clpt.2009.277](https://doi.org/10.1038/clpt.2009.277).
53. Friedrich C, Ring A, Brand T, Sennewald R, Graefe-Mody EU, Woerle HJ. Evaluation of the pharmacokinetic interaction after multiple oral doses of linagliptin and digoxin in healthy volunteers. *Eur J Drug Metab Pharmacokinet*. 2011;36:17–24. doi:[10.1007/s13318-011-0028-y](https://doi.org/10.1007/s13318-011-0028-y).
54. Vaidyanathan S, Camenisch G, Schuetz H, et al. Pharmacokinetics of the oral direct renin inhibitor aliskiren in combination with digoxin, atorvastatin, and ketoconazole in healthy subjects: the role of P-glycoprotein in the disposition of aliskiren. *J Clin Pharmacol*. 2008;48:1323–38. doi:[10.1177/0091270008323258](https://doi.org/10.1177/0091270008323258).
55. Nožnić D, Milić A, Mikac L, Ralić J. Assessment of macrolide transport using PAMPA, Caco-2 and MDCKII-hMDR1 assays. *Croat Chem Acta*. 2010;83:323–31.
56. Wheeler DL, Church DM, Federhen S, et al. Database resources of the national center for biotechnology. *Nucleic Acids Res*. 2003;31:28–33. doi:[10.1093/nar/gks1189](https://doi.org/10.1093/nar/gks1189).
57. Meyer M, Schneckener S, Ludewig B, Kuepfer L, Lippert J. Using expression data for quantification of active processes in physiologically based pharmacokinetic modeling. *Drug Metab Dispos*. 2012;40:892–901. doi:[10.1124/dmd.111.043174](https://doi.org/10.1124/dmd.111.043174).
58. Ge X, Yamamoto S, Tsutsumi S, et al. Interpreting expression profiles of cancers by genome-wide survey of breadth of expression in normal tissues. *Genomics*. 2005;86:127–41. doi:[10.1016/j.ygeno.2005.04.008](https://doi.org/10.1016/j.ygeno.2005.04.008).
59. Rodrigues AD. Integrated cytochrome P450 reaction phenotyping: attempting to bridge the gap between cDNA-expressed cytochromes P450 and native human liver microsomes. *Biochem Pharmacol*. 1999;57:465–80. doi:[10.1016/S0006-2952\(98\)00268-8](https://doi.org/10.1016/S0006-2952(98)00268-8).
60. Badée J, Achour B, Rostami-Hodjegan A, Galetin A. Meta-analysis of expression of hepatic organic anion-transporting polypeptide (OATP) transporters in cellular systems relative to human liver tissue. *Drug Metab Dispos*. 2015;43:424–32. doi:[10.1124/dmd.114.062034](https://doi.org/10.1124/dmd.114.062034).
61. Nishimura M, Naito S. Tissue-specific mRNA expression profiles of human ATP-binding cassette and solute carrier transporter superfamilies. *Drug Metab Pharmacokinet*. 2005;20:452–77. doi:[10.2133/dmpk.20.452](https://doi.org/10.2133/dmpk.20.452).
62. Tucker TGHA, Milne AM, Fournel-Gigleux S, Fenner KS, Coughtrie MWH. Absolute immunoquantification of the expression of ABC transporters P-glycoprotein, breast cancer resistance protein and multidrug resistance-associated protein 2 in human liver and duodenum. *Biochem Pharmacol*. 2012;83:279–85. doi:[10.1016/j.bcp.2011.10.017](https://doi.org/10.1016/j.bcp.2011.10.017).
63. Rodvold KA. Clinical pharmacokinetics of clarithromycin. *Clin Pharmacokinet*. 1999;37:385–98. doi:[10.2165/00003088-199937050-00003](https://doi.org/10.2165/00003088-199937050-00003).
64. Obach RS, Lombardo F, Waters NJ. Trend analysis of a database of intravenous pharmacokinetic. *Pharmacology*. 2008;36:1385–405. doi:[10.1124/dmd.108.020479](https://doi.org/10.1124/dmd.108.020479).
65. Quinney SK, Haehner BD, Rhoades MB, Lin Z, Gorski JC, Hall SD. Interaction between midazolam and clarithromycin in the elderly. *Br J Clin Pharmacol*. 2008;65:98–109. doi:[10.1111/j.1365-2125.2007.02970.x](https://doi.org/10.1111/j.1365-2125.2007.02970.x).
66. Allonen H, Ziegler G, Klotz U. Midazolam kinetics. *Clin Pharmacol Ther*. 1981;30:653–61. doi:[10.1038/clpt.1981.217](https://doi.org/10.1038/clpt.1981.217).
67. Doucet-Populaire F, Capobianco JO, Zakula D, Jarlier V, Goldman RC. Molecular basis of clarithromycin activity against *Mycobacterium avium* and *Mycobacterium smegmatis*. *J Antimicrob Chemother*. 1998;41:179–87. doi:[10.1093/jac/41.2.179](https://doi.org/10.1093/jac/41.2.179).
68. Atkinson HC, Begg EJ. Relationship between human milk lipid-ultrafiltrate and octanol-water partition coefficients. *J Pharm Sci*. 1988;77:796–8. doi:[10.1002/jps.2600770916](https://doi.org/10.1002/jps.2600770916).
69. Mulla H, McCormack P, Lawson G, Firmin RK, Upton DR. Pharmacokinetics of midazolam in neonates undergoing extracorporeal membrane oxygenation. *Anesthesiology*. 2003;99(2):275–82.
70. Arellano C, Philibert C, Vachoux C, Woodley J, Houin G. The metabolism of midazolam and comparison with other CYP enzyme substrates during intestinal absorption: in vitro studies with rat everted gut sacs. *J Pharm Pharm Sci Publ Can Soc Pharm Sci Soc Can Sci Pharm*. 2007;10:26–36.
71. Yamano K, Yamamoto K, Katashima M, et al. Prediction of midazolam-CYP3A inhibitors interaction in the human liver from in vivo/in vitro absorption, distribution, and metabolism data. *Drug Metab Dispos*. 2001;29:443–52.
72. Zhang X-R, Chen X-Y, Hu L-D, Tang X, Li S-M, Zhong D-F. Evaluation of in-vitro dissolution and in-vivo absorption for two different film-coated pellets of clarithromycin. *Arch Pharm Res*. 2005;28:977–82. doi:[10.1007/BF02973886](https://doi.org/10.1007/BF02973886).
73. McFarland JW, Berger CM, Froshauer S, et al. Quantitative structure-activity relationships among macrolide antibacterial agents: in vitro and in vivo potency against *Pasteurella multocida*. *J Med Chem*. 1997;40:1340–6. doi:[10.1021/jm9604361](https://doi.org/10.1021/jm9604361).
74. Liu Y, Hunt CA. Studies of intestinal drug transport using an in silico epithelial-mimetic device. *BioSystems*. 2005;82:154–67. doi:[10.1016/j.biosystems.2005.06.008](https://doi.org/10.1016/j.biosystems.2005.06.008).
75. Walser A, Benjamin LE, Flynn T, Mason C, Schwartz R, Fryer RI. Quinazolines and 1,4-benzodiazepines. 84. Synthesis and reactions of imidazo[1,5-a][1,4]benzodiazepines. *J Org Chem*. 1978;43:936–44. doi:[10.1021/jo00399a029](https://doi.org/10.1021/jo00399a029).
76. Salem II, Düzgünes N. Efficacies of cyclodextrin-complexed and liposome-encapsulated clarithromycin against *Mycobacterium avium* complex infection in human macrophages. *Int J Pharm*. 2003;250:403–14. doi:[10.1016/S0378-5173\(02\)00552-5](https://doi.org/10.1016/S0378-5173(02)00552-5).
77. Alsenz J, Meister E, Haenel E. Development of a partially automated solubility screening (PASS) assay for early drug development. *J Pharm Sci*. 2007;96:1748–62. doi:[10.1002/jps.20814](https://doi.org/10.1002/jps.20814).
78. Loftsson T, Hreinsdóttir D. Determination of aqueous solubility by heating and equilibration: a technical note. *AAPS PharmSciTech*. 2006;7, E4. doi:[10.1208/pt070104](https://doi.org/10.1208/pt070104).
79. Rautio J, Humphreys JE, Webster LO, et al. In vitro P-glycoprotein inhibition assays for assessment of clinical drug interaction potential of new drug candidates: a recommendation for probe substrates. *Drug Metab Dispos*. 2006;34:786–92. doi:[10.1124/dmd.105.008615.paper](https://doi.org/10.1124/dmd.105.008615.paper).
80. Gertz M, Harrison A, Houston JB, Galetin A. Prediction of human intestinal first-pass metabolism of 25 CYP3A substrates from in vitro clearance and permeability data. *Drug Metab Dispos*. 2010;38:1147–58. doi:[10.1124/dmd.110.032649](https://doi.org/10.1124/dmd.110.032649).
81. Galetin A, Brown C, Halifax D, Ito K, Houston JB. Utility of recombinant enzyme kinetics in prediction of human clearance: impact of variability, CYP3A5, and CYP2C19 on CYP3A4 probe substrates. *Drug Metab Dispos*. 2004;32:1411–20. doi:[10.1124/dmd.104.000844](https://doi.org/10.1124/dmd.104.000844).
82. Stephens RH, O'Neill CA, Warhurst A, Carlson GL, Rowland M, Warhurst G. Kinetic profiling of P-glycoprotein-mediated drug efflux in rat and human intestinal epithelia. *J Pharmacol Exp Ther*. 2001;296:584–91.
83. Katz A, Lifshitz Y, Bab-Dinitz E, et al. Selectivity of digitalis glycosides for isoforms of human Na,K-ATPase. *J Biol Chem*. 2010;285:19582–92. doi:[10.1074/jbc.M110.119248](https://doi.org/10.1074/jbc.M110.119248).
84. Polasek TM, Miners JO. Quantitative prediction of macrolide drug-drug interaction potential from in vitro studies using testosterone as the human cytochrome P4503A substrate. *Eur J Clin Pharmacol*. 2006;62:203–8. doi:[10.1007/s00228-005-0091-x](https://doi.org/10.1007/s00228-005-0091-x).
85. Ito K, Ogihara K, Kanamitsu S, Itoh T. Prediction of the in vivo interaction between midazolam and macrolides based on in vitro studies using human liver microsomes. *Drug Metab Dispos*. 2003;31:945–54. doi:[10.1124/dmd.31.7.945](https://doi.org/10.1124/dmd.31.7.945).
86. Jones DR, Ekins S, Li L, Hall SD. Computational approaches that predict metabolic intermediate complex formation with CYP3A4 (+b5). *Drug Metab Dispos*. 2007;35(9):1466–75.
87. Sohlenius-Sternbeck A-K. Determination of the hepatocellularity number for human, dog, rabbit, rat and mouse livers from protein

PBPK DDI Modeling of Clarithromycin, Midazolam, and Digoxin

- concentration measurements. *Toxicol Vit.* 2006;20:1582–6. doi:[10.1016/j.tiv.2006.06.003](https://doi.org/10.1016/j.tiv.2006.06.003).
- 88. Cheng Y, Prusoff WH. Relationship between the inhibition constant (K_I) and the concentration of inhibitor which causes 50 per cent inhibition (I_{50}) of an enzymatic reaction. *Biochem Pharmacol.* 1973;22:3099–108.
 - 89. Shimada T, Yamazaki H, Mimura M, Inui Y, Guengerich FP. Interindividual variations in human liver cytochrome P-450 enzymes involved in the oxidation of drugs, carcinogens and toxic chemicals: studies with liver microsomes of 30 Japanese and 30 Caucasians. *J Pharmacol Exp Ther.* 1994;270:414–23.
 - 90. Venkatakrishnan K, Obach RS, Rostami-Hodjegan A. Mechanism-based inactivation of human cytochrome P450 enzymes: strategies for diagnosis and drug-drug interaction risk assessment. *Xenobiotica.* 2007;37:1225–56. doi:[10.1080/00498250701670945](https://doi.org/10.1080/00498250701670945).
 - 91. Yang J, Liao M, Shou M, et al. Cytochrome p450 turnover: regulation of synthesis and degradation, methods for determining rates, and implications for the prediction of drug interactions. *Curr Drug Metab.* 2008;9:384–94. doi:[10.2174/138920008784746382](https://doi.org/10.2174/138920008784746382).
 - 92. Prasad B, Evers R, Gupta A, et al. Interindividual variability in hepatic organic anion-transporting polypeptides and P-glycoprotein (ABCB1) protein expression: quantification by liquid chromatography tandem mass spectroscopy and influence of genotype, age, and sex. *Drug Metab Dispos.* 2013;42:78–88. doi:[10.1124/dmd.113.053819](https://doi.org/10.1124/dmd.113.053819).
 - 93. Rodgers T, Leahy D, Rowland M. Physiologically based pharmacokinetic modeling 1: predicting the tissue distribution of moderate-to-strong bases. *J Pharm Sci.* 2005;94:1259–76. doi:[10.1002/jps.20322](https://doi.org/10.1002/jps.20322).
 - 94. Rodgers T, Rowland M. Physiologically based pharmacokinetic modelling 2: predicting the tissue distribution of acids, very weak bases, neutrals and zwitterions. *J Pharm Sci.* 2006;95:1238–57. doi:[10.1002/jps.20502](https://doi.org/10.1002/jps.20502).
 - 95. Ishiguro M, Koga H, Kohno S, Hayashi T, Yamaguchi K, Hirota M. Penetration of macrolides into human polymorphonuclear leucocytes. *J Antimicrob Chemother.* 1989;24:719–29. doi:[10.1093/jac/24.5.719](https://doi.org/10.1093/jac/24.5.719).
 - 96. Quinney SK, Malireddy SR, Vuppalanchi R, et al. Rate of onset of inhibition of gut-wall and hepatic CYP3A by clarithromycin. *Eur J Clin Pharmacol.* 2013;69:439–48. doi:[10.1007/s00228-012-1339-x](https://doi.org/10.1007/s00228-012-1339-x).
 - 97. Quinney SK, Zhang X, Lucksiri A, Gorski JC, Li L, Hall SD. Physiologically based pharmacokinetic model of mechanism-based inhibition of CYP3A by clarithromycin. *Drug Metab Dispos.* 2010;38(2):241–8.
 - 98. Kharasch ED, Walker A, Isoherranen N, et al. Influence of CYP3A5 genotype on the pharmacokinetics and pharmacodynamics of the cytochrome P4503A probes alfentanil and midazolam. *Clin Pharmacol Ther.* 2007;82:410–26. doi:[10.1038/sj.cpt.6100237](https://doi.org/10.1038/sj.cpt.6100237).
 - 99. Williams JA, Ring BJ, Cantrell VE, et al. Comparative metabolic capabilities of CYP3A4, CYP3A5, and CYP3A7. *Drug Metab Dispos.* 2002;30:883–91. doi:[10.1124/dmd.30.8.883](https://doi.org/10.1124/dmd.30.8.883).
 - 100. Hansen O, Clausen T. Quantitative determination of Na⁺-K⁺-ATPase and other sarcolemmal components in muscle cells. *Am J Physiol.* 1988;254:C1–7.
 - 101. Comets E, Verstuyft C, Lavielle M, Jaillon P, Becquemont L, Mentré F. Modelling the influence of MDR1 polymorphism on digoxin pharmacokinetic parameters. *Eur J Clin Pharmacol.* 2007;63:437–49. doi:[10.1007/s00228-007-0269-5](https://doi.org/10.1007/s00228-007-0269-5).
 - 102. Niemeijer MN, van den Berg ME, Deckers JW, et al. ABCB1 gene variants, digoxin and risk of sudden cardiac death in a general population. *Heart.* 2015;101:1973–9. doi:[10.1136/heartjnl-2014-307419](https://doi.org/10.1136/heartjnl-2014-307419).
 - 103. Rowland Yeo K, Walsky RL, Jamei M, Rostami-Hodjegan A, Tucker GT. Prediction of time-dependent CYP3A4 drug-drug interactions by physiologically based pharmacokinetic modelling: impact of inactivation parameters and enzyme turnover. *Eur J Pharm Sci.* 2011;43:160–73. doi:[10.1016/j.ejps.2011.04.008](https://doi.org/10.1016/j.ejps.2011.04.008).

4.3 Project III:

A physiologically-based pharmacokinetic and pharmacodynamic (PBPK/PD) model of the histone deacetylase (HDAC) inhibitor vorinostat for pediatric and adult patients and its application for dose specification.



ORIGINAL ARTICLE

A physiologically based pharmacokinetic and pharmacodynamic (PBPK/PD) model of the histone deacetylase (HDAC) inhibitor vorinostat for pediatric and adult patients and its application for dose specification

Daniel Moj¹ · Hannah Britz¹ · Jürgen Burhenne⁴ · Clinton F. Stewart² ·
Gerlinde Egerer³ · Walter E. Haefeli⁴ · Thorsten Lehr¹

Received: 30 May 2017 / Accepted: 23 September 2017

© Springer-Verlag GmbH Germany 2017

Abstract

Purpose This study aimed at recommending pediatric dosages of the histone deacetylase (HDAC) inhibitor vorinostat and potentially more effective adult dosing regimens than the approved standard dosing regimen of 400 mg/day, using a comprehensive physiologically based pharmacokinetic/pharmacodynamic (PBPK/PD) modeling approach.

Methods A PBPK/PD model for vorinostat was developed for predictions in adults and children. It includes the maturation of relevant metabolizing enzymes. The PBPK model was expanded by (1) effect compartments to describe vorinostat concentration–time profiles in peripheral blood mononuclear cells (PBMCs), (2) an indirect response model to predict the HDAC inhibition, and (3) a thrombocyte model to predict the dose-limiting thrombocytopenia. Parameterization of drug and system-specific processes was based on published and unpublished in silico, *in vivo*, and *in vitro* data. The PBPK modeling software used was PK-Sim and MoBi.

Results The PBPK/PD model suggests dosages of 80 and 230 mg/m² for children of 0–1 and 1–17 years of age, respectively. In comparison with the approved standard treatment, in silico trials reveal 11 dosing regimens (9 oral, and 2 intravenous infusion rates) increasing the HDAC inhibition by an average of 31%, prolonging the HDAC inhibition by 181%, while only decreasing the circulating thrombocytes to a tolerable 53%. The most promising dosing regimen prolongs the HDAC inhibition by 509%.

Conclusions Thoroughly developed PBPK models enable dosage recommendations in pediatric patients and integrated PBPK/PD models, considering PD biomarkers (e.g., HDAC activity and platelet count), are well suited to guide future efficacy trials by identifying dosing regimens potentially superior to standard dosing regimens.

Keywords Vorinostat · Pediatrics · Physiologically based pharmacokinetics · Histone deacetylase · Thrombocytopenia · Pharmacodynamics

Introduction

Histone deacetylases (HDACs) regulate gene transcription and cell signaling pathways. Changes in the structure, activity, or expression of HDACs can result in abnormal gene transcription and cell signaling leading to cancer [1]. HDAC inhibitors (HDACi), such as vorinostat, show anti-neoplastic effects *in vitro* and *in vivo*, and offer therefore a new approach in chemotherapy [2]. Vorinostat is a fast, light-binding inhibitor with short residence time at the target that inhibits the enzymatic activity of Class I (HDACs 1–3) and Class II (HDAC 6) HDACs at nanomolar concentrations ($IC_{50}=30\text{--}86\text{ nM}$) [3, 4]. It was approved by the U.S. Food and Drug Administration (FDA) for the treatment of

Electronic supplementary material The online version of this article (doi:10.1007/s00280-017-3447-x) contains supplementary material, which is available to authorized users.

✉ Thorsten Lehr
Thorsten.Lehr@mx.uni-saarland.de

¹ Department of Pharmacy, Clinical Pharmacy, Saarland University, Campus C2 2, 66123 Saarbruecken, Germany

² Department of Pharmaceutical Sciences, St. Jude Children's Research Hospital, Memphis, TN, USA

³ Department of Hematology, Oncology, and Rheumatology, Heidelberg University Hospital, Heidelberg, Germany

⁴ Department of Clinical Pharmacology and Pharmacoepidemiology, University of Heidelberg, Heidelberg, Germany

cutaneous manifestations in patients with cutaneous T-cell lymphoma (CTCL) who have progressive, persistent, or recurrent disease on, or following two systemic therapies [4, 5].

Vorinostat shows a dose-proportional exposure increase after oral or intravenous doses of 100–800 mg or 75–900 mg/m², respectively, with an absorption rate-limited drug disposition in the gastrointestinal tract after oral dosing, leading to flip-flop pharmacokinetics (PK) [6]. Elimination primarily comprises metabolism, involving glucuronidation and hydrolysis followed by β-oxidation without the contribution of CYP enzymes [7]. Renal excretion is negligible accounting for ~1% of total body clearance [8]. While the UDP-glucuronosyltransferases (UGTs) 1A9, 2B7, and 2B17 are the major enzymes of vorinostat glucuronidation, the enzyme responsible for hydrolysis and β-oxidation remains unidentified [7]. These enzymes exhibit nonlinear age-dependent maturation completed within 10 years after birth [9–14]. Genetic polymorphisms of UGT 2B17 might play a role in the clearance of vorinostat and in clinical outcomes [15–17]. In general, vorinostat exhibits a short half-life of 1 (intravenous) to 2 h (oral) and multiple-dose PK similar to single-dose administration [7].

Clinical studies of vorinostat in patients with stage Ib and higher CTCL and in patients with refractory CTCL demonstrated overall objective responses of 30 and 31%, respectively [18, 19]. The most common adverse reactions, with an incidence ≥10%, associated with vorinostat treatment are anorexia, diarrhea, dysgeusia, fatigue, nausea, and thrombocytopenia, with thrombocytopenia being the most common hematologic event [5, 20]. In pediatric studies, vorinostat was well tolerated at 230 mg/m²/day (alone or in combination with bortezomib) or 300 mg/m²/day (in combination with temozolomide) and showed a drug disposition similar to that observed in adults [21–23].

While in vitro experiments suggest that vorinostat concentrations of 2.5 μmol/l lead to the maximum accumulation of acetylated histones, it has also been shown that the HDAC inhibition has to be maintained over a significant period of time to show antitumor activity [24, 25]. Furthermore, vorinostat enhances the effect of other chemotherapeutics such as cisplatin and gemcitabine at concentrations > 2 μmol/l, which is, nevertheless, inconsistently achieved in patients at the approved 400 mg/day (qd) dose [6, 26, 27]. Little is known about the impact of different dosing regimens on its efficacy [6]. Hence, Dickson and co-workers attempted to achieve maximum vorinostat concentrations (C_{\max}) of > 2.5 μmol/l by an intermittent oral pulse dosing protocol of vorinostat in combination with the cyclin-dependent kinase inhibitor flavopiridol [28]. In this attempt, the C_{\max} of vorinostat could be increased, but unfortunately the incidence of myelosuppression was also increased. However, these promising results demand further assessment of alternative

vorinostat dosing strategies that might show more effectiveness and still tolerable toxicity compared to the vorinostat standard treatment.

Here, physiologically based pharmacokinetic and pharmacodynamic (PBPK/PD) modeling and simulation enable the assessment of dosing regimens in *in silico* trials, while also being able to test clinical trial designs.

Objectives

1. Build and evaluate an adult whole-body PBPK model of vorinostat able to describe and predict the PK of varying doses of intravenously and orally administered vorinostat.
2. Develop and evaluate a pediatric PBPK model for vorinostat and estimate vorinostat doses for children between 0 and 17 years.
3. Build and evaluate a PBPK/PD model incorporating (1) a HDAC inhibition model and (2) a thrombocytopenia model.
4. Identify potentially effective vorinostat dosing regimens while considering HDAC activity and the number of circulating thrombocytes.
5. Perform parameter sensitivity analysis for the developed whole-body PBPK model of vorinostat.

Materials and methods

Model development and evaluation

A schematic overview of the PBPK model development and evaluation steps is shown in supplemental Fig. S1. The detailed steps of the model building are outlined in the following sections. In brief, PBPK modeling was performed in a stepwise procedure. First, an intravenous model of vorinostat was developed for adults. Second, an oral PBPK model for adults was established. Third, age-dependent physiological and anatomical changes were implemented enabling pediatric predictions and dose estimations. Fourth, PD models were incorporated into the PBPK model to describe HDAC inhibition and thrombocytopenia. Fifth, the PBPK/PD model was used to identify new dosing regimens. Finally, a parameter sensitivity analysis was performed.

Experimental datasets from 13 published and unpublished clinical studies were used to support the PBPK model development and evaluation (Table 1). The experimental datasets were split into an internal development ($n=4$ trials) dataset and an external evaluation dataset ($n=9$), such that wide dose ranges were covered in both datasets. The PBPK model was fitted to the development dataset and the prediction quality of the model was assessed by predicting the

Table 1 Clinical study data of vorinostat

Route of administration	Dose (mg)	Dosing schedule	n	Male patients (%)	Age median (range) (years)	Internal (in) or external (ex) dataset	Ref.
iv (inf. 2 h)	75, 150, 300, 600, 900 /m ²	sd	39	65	19–81	in	[30]
iv (inf. 2 h)	200, 400	sd	20	—	—	ex	[4]
po	400, 600, 800, 1000	qd	24	68	59 (31–85)	ex	[28]
po	100, 200, 400, 500	qd	18	83	58 (25–72)	in	[8]
po	200, 300, 400, 600	qd	73	69	(20–79)	ex	[6]
po	400	sd	10	50	62 (31–73)	in	[60]
po	400	qd	27	44	(46–80)	ex	[31]
po	800	sd	24	52	(29–78)	ex	[32]
po	400	qd	28	75	64 (30–77)	ex	[33]
po	400	qd	23	48	(39–84)	ex	[34]
po	400	qd	6	100	53.5 (34–75)	ex	[35]
po	180, 230, 300 /m ²	sd	13	60	14 (5–22)	ex	[21] ^a
po	400	qd	63	49	64 (29–82)	in	[36]

iv intravenous, inf infusion, po per oral, sd single dose, qd once daily

^aUnpublished

evaluation dataset. Parameter optimizations were carried out using either a Monte-Carlo or Nelder–Mead method [29]. An overview of fitted parameters and the applied optimization method is given in supplemental Table S1. The Monte-Carlo approach was used if no initial information on parameter values was available.

Model evaluation was carried out using (1) comparison of observed and simulated PK parameters and the fraction of vorinostat dose excreted unchanged into urine, (2) mean prediction errors (MPE) of pharmacokinetic profiles [37] and (3) visual predictive checks (VPC), which are tools for evaluating the performance of PK and PD models, where percentiles of experimental and simulated data are compared [38]. PK parameter comparisons were deemed successful when they satisfied the twofold acceptance criterion.

Simulations were carried out using virtual PBPK individuals and populations. Virtual PBPK populations were created as described by Willmann and co-workers using ranges for age, height, and weight reported in the internal and external datasets [39]. In this approach, the organ weights and the cardiac output (CO) of a target individual are allometrically scaled with height and the organ blood flows are scaled to the total CO [39]. To assess the inter-study variability of PK parameters, 10 virtual populations were created for each study. Applied dosing schedules and doses were used as published. The parameters of anatomy and physiology were varied as pre-defined in PK-Sim [40–43], parameters of the pharmacodynamic models were varied with a coefficient of variation (CV) of 20%.

An overview of important assumptions made during model development and evaluation is given in supplemental Table S2.

PBPK simulations were carried out using PK-Sim and MoBi (Version 6.3.2, Bayer Technology Services, Leverkusen, Germany). Statistical analyses of the results and graphics were compiled using MATLAB (Version R2013b, The MathWorks Inc., Natick, MA, USA).

Adult PBPK model—intravenous

Intravenous concentration–time profiles were used to establish a PBPK model for vorinostat. The partition coefficients for vorinostat were calculated using the PK-Sim standard model [44, 45]. To describe the distribution phase correctly, the cellular permeability of vorinostat was estimated. The reference concentrations for UGT 1A9, 2B7, and 2B17 were kept at the PK-Sim default values of 1 μmol/l, respectively. The UGT V_{max} values were gathered from the literature. The PK-Sim gene expression database was used to distribute the enzymes to the specific organs [46, 47]. To fit the vorinostat half-life and concentration–time profiles, the unidentified hydrolytic and oxidative enzyme were implemented as a generic enzyme with a reference concentration of 1 μmol/l assuming similar availability across organs. The clearance value for hydrolysis and oxidation was fitted. All metabolic reactions were modeled as first-order processes. The unbound vorinostat was assumed to be filtered and excreted with the glomerular filtration rate (GFR).

Adult PBPK model—oral

The developed intravenous PBPK model of vorinostat was expanded by an oral formulation. The particle dissolution module of PK-Sim was used to describe vorinostat drug

release in the intestine. This module calculates the dissolution kinetics of spherical particles with a predefined particle size distribution based on the Noyes–Whitney approach [48]. To describe the absorption of vorinostat correctly, the intestinal permeability coefficient was estimated. To capture the whole-blood-to-plasma ratio of 2.87, the red blood cell permeability was estimated [50].

Model evaluation of the intravenous and oral adult PBPK model was carried out comparing observed and predicted PK parameters and concentration–time profiles of the external evaluation dataset.

Pediatric PBPK model and dosage recommendations

The developed oral PBPK model of vorinostat was expanded by importing available age-dependent anatomical and physiological changes in human development from the PK-Sim databases [40]. The age-dependent maturation of UGT 1A9 and 2B7 was already available in PK-Sim, whereas the UGT 2B17 maturation was implemented using a Hill function (Eq. 1) based on recently published mRNA data [14],

$$\text{UGT 2B17 ontogeny factor (OF)} = \text{OF}_{\min} + \frac{\text{OF}_{\max} \times \text{Age}^{\gamma}}{\text{OF}_{50}^{\gamma} + \text{Age}^{\gamma}} \quad (1)$$

where OF_{\min} denotes the intercept with the y-axis, and OF_{\max} and OF_{50} represent the maximum adult ontogeny factor ($=1$) and the post-menstrual age needed to reach 50% of the maximum ontogeny factor, respectively. Age denotes the post-menstrual age in years and γ denotes the Hill factor. The unidentified enzyme responsible for the hydrolysis and oxidation of vorinostat was assumed to be fully developed from birth on.

Model evaluation of the pediatric PBPK model was carried out comparing observed and predicted PK parameters and concentration–time profiles of the external evaluation dataset that consisted of 13 individual vorinostat plasma concentration–time profiles with individual ages ranging from 4.7 to 22 years.

The developed pediatric PBPK model of vorinostat was used to identify age-stratified mg/m²/day doses for children and adolescents from birth to 17 years of age. Pediatric doses were selected when the 25th, 50th, and 75th percentiles of predicted AUC_{0–inf} or C_{\max} values for the pediatric age groups were comparable to the values of the adult population dosed with the approved oral dose of 400 mg/day. Two virtual populations were generated, first, for adults (age ≥ 18 , $n=500$) and second, for children (age 0–17, $n=10,000$). The body surface areas were calculated using the DuBois equation [49].

Adult PBPK model—HDAC activity

The oral PBPK model of vorinostat was expanded by an indirect response model to describe the HDAC activity in peripheral blood mononuclear cells (PBMCs) during vorinostat treatment [6]. PBMCs are not offered as physiological compartments in the default PK-Sim PBPK model [50]. Therefore, two PBMC effect compartments were implemented in the default model (Fig. 1). First, the rate constants $k_{\text{effect},1}$, $k_{\text{effect},2}$, $k_{\text{effect,deep},1}$, and $k_{\text{effect,deep},2}$ of the PBMC effect compartmental model were estimated. Second, the HDAC activity in the central PBMC compartment was modeled using an indirect response model, where the HDAC activity R was described by Eq. 2 [51],

$$\frac{dR}{dt} = k_{\text{in}} - k_{\text{out}} \times \left(1 + \frac{S_{\max} \times C_{V, \text{PBMC}}}{SC_{50} + C_{V, \text{PBMC}}} \right) \times R \quad (2)$$

where k_{in} is the apparent zero-order rate constant for the production of the activity, k_{out} represents the first-order rate constant for activity loss, and R is assumed to be stationary with an initial value of $R_0 \left(= \frac{k_{\text{in}}}{k_{\text{out}}} \right)$. The SC_{50} value represents the PBMC vorinostat concentration ($C_{V, \text{PBMC}}$) producing 50% of the maximum k_{out} stimulation achieved at the effect site, whereas S_{\max} is the maximum k_{out} stimulation achieved at the effect site. Predictions of HDAC activity following multiple oral vorinostat doses were carried out using intracellular vorinostat concentrations of the bone instead of PBMC vorinostat concentrations.

Model evaluation of the HDAC activity was carried out by comparing the observed and simulated HDAC activity–time profiles of the internal development dataset using a virtual population.

Adult PBPK model—platelet count

Thrombocytopenia was defined as a platelet count $< 150 \times 10^9$ cells/l [52]. The adult PBPK model of vorinostat was expanded by a thrombocytopenia model as a pharmacodynamic toxicity biomarker. The platelet model was first published and comprehensively described by Friberg and co-workers and refined by du Rieu and co-workers [53, 54]. The refined thrombocytopenia model was used in the presented PBPK modeling approach (Fig. 1).

In brief, the thrombocytopenia model consists of five compartments (cmts) describing proliferating cells (1 cmt), developing thrombocytes (3 transit cmts) and circulating thrombocytes (1 cmt). Both, the mean transit time (MTT) of the developing thrombocytes and the proliferation rate constant are influenced by the number of circulating thrombocytes by a feedback mechanism. Vorinostat reduces the proliferation or induces cell loss of thrombocytes.

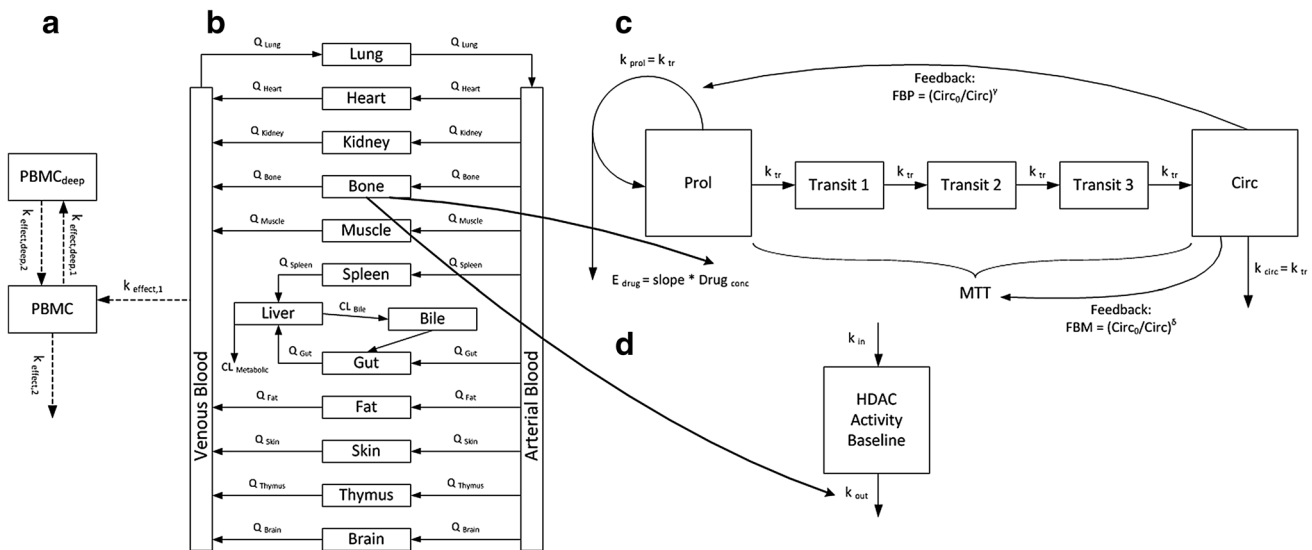


Fig. 1 Schematic structural PBPK/PD model representation. **a** PBMC effect compartment model. **b** Schematic default PBPK model. **c** Thrombocytopenia model. **d** HDAC activity indirect response model. *PBMC* peripheral blood mononuclear effect compartment, *PBMC_{deep}* peripheral blood mononuclear deep effect compartment, $k_{effect,1/2}$ and $k_{effect,deep,1/2}$ concentration transfer rate constants, Q specific organ blood flow, CL clearance, *Prol* proliferating cells, *Transit*

sit 1/2/3 cells in transit state, *Circ* circulating cells, $Circ_0$ circulating cells baseline, k_{prol} proliferation rate constant, k_{tr} transit rate constant, k_{circ} elimination rate constant, *MTT* mean transit time, *slope* slope parameter, $Drug_{conc}$ vorinostat concentration, E_{drug} vorinostat effect on the proliferating cells, *FBP* circulating cells feedback on proliferating cells, *FBM* circulating cells feedback on MTT, k_{in} HDAC activity synthesis rate, and k_{out} HDAC activity degradation rate

Parameter values of the thrombocytopenia model were gathered from the literature (suppl. Table S3), except for the slope parameter of vorinostat, which was estimated using clinical study data of thrombocytosis patients [36].

The thrombocytopenia model was evaluated by comparing the observed and predicted fraction of patients with normal platelet counts that develop thrombocytopenia during a 24-week treatment with 400 mg vorinostat per day.

Identification of new vorinostat dosing regimens

The adult PBPK/PD model of vorinostat, including the HDAC activity and the thrombocytopenia model was used in *in silico* trials to identify vorinostat doses and dosing schedules that are potentially more effective than the standard dosing regimen of 400 mg qd, where ‘more effective’ is defined as causing a larger decrease in HDAC activity. Tested dosing regimens were chosen from a range of potential dosing frequencies per day (qd, bid, tid) and week (e.g. every 2nd week, 3 consecutive days per week). Intravenous and oral routes of administration were considered.

In silico trials—part 1

25 dosing regimens with varying administration routes, administered doses, and dosing schemes of vorinostat were tested. New regimens were declared potentially more effective when they showed higher maximum (HDAC_{activity,bone}

[%]) and longer HDAC inhibition than the standard treatment during a 10-week treatment period without decreasing the thrombocyte count [10^9 cells/l] more than the standard dosing regimen. A simulation time of 10 weeks was necessary to ensure that the circulating thrombocytes were at steady-state ($MTT \sim 95$ h).

In silico trials—part 2

Maximum doses were estimated for 15 dosing schedules from *in silico trials – part 1*. In trial 2, the minimum thrombocyte count was set at 50×10^9 cells/l and the maximum possible single vorinostat dose was set to 3000 mg.

All trial results were compared to the standard treatment based on the change of HDAC activity (%), the change in the accumulated time of HDAC activity < 50% (%), and the change in the thrombocyte count (%).

Parameter sensitivity analysis

A parameter sensitivity analysis of the adult PBPK model was performed to assess the impact of estimated model parameters on the predicted values of $AUC_{0-\infty}$, C_{max} , half-life, and T_{max} . Assessed parameters were: hydrolysis and β -oxidation clearance, intestinal permeability, cellular permeability, red blood cell permeabilities, and the unstirred layer of the particle dissolution. All parameters were varied individually over a wide range of values (via multiplication

by factors between 0.1 and 10.0) and the changes in $AUC_{0-\infty}$, C_{\max} , half-life, and T_{\max} was documented [55]. If a 10% change of a single parameter led to a >1% change in $AUC_{0-\infty}$, C_{\max} , half-life, and T_{\max} , the model was considered sensitive to this parameter [56].

Results

A comprehensive PBPK model for the prediction of vorinostat concentrations after different intravenous and oral doses of vorinostat has been successfully developed. The model can be applied in adult and pediatric patients and has been used to recommend doses for children from 0 to 17 years. Furthermore, the PBPK model has been expanded by (1) PBMC effect compartments and (2) pharmacodynamic models of HDAC activity and thrombocytopenia. Finally, the vorinostat PBPK/PD model has been successfully used to identify new vorinostat dosing regimens that are potentially more effective than the approved standard treatment.

The developed vorinostat PBPK model shows good descriptive and predictive performance. In summary, 90 and 96% of the predicted $AUC_{0-\infty}$ and C_{\max} values satisfy the twofold acceptance criterion, respectively (Fig. 2, suppl. Fig. S2). The MPE of the simulated and predicted adult and pediatric pharmacokinetic profiles is 44%. Trial-specific MPEs are summarized in supplemental Table S4. The final model parameters on the drug release, absorption, distribution, metabolism, and excretion of vorinostat are shown in Table 2.

Adult PBPK model—intravenous

The intravenous model is able to describe and predict vorinostat concentration–time profiles in close agreement with the observed values over a wide range (75–900 mg/

m^2) of intravenous single dosages (Fig. 3, suppl. Fig. S3). The mean observed dose-independent half-life of vorinostat across available doses and studies is 0.65 h [4, 30] where the PBPK model predicts 0.75 h, a slight over-prediction of 15%. The C_{\max} and the $AUC_{0-\infty}$ have been predicted with mean deviations of 4 and 25% from the observed values, respectively [4, 30]. The simulated fraction of unchanged vorinostat dose excreted in urine (f_e) has been consistently below 1% over all doses, which is also in good agreement with observed values [4].

Adult PBPK model—oral

The oral PBPK model also shows a good descriptive and predictive performance (Fig. 3, suppl. Fig. S3). The $AUC_{0-\infty}$, C_{\max} , and T_{\max} have been predicted with mean deviations of 5, 1 and 22% from the observed values across available doses, respectively [6, 8, 28, 31–35, 50]. The absorption rate-limited PK is well predicted. The observed oral half-life is 1.75 h [6, 8, 28, 31–35, 50], where the PBPK model predicts a half-life of 1.66 h. The predicted bioavailability ($F_{\text{pred}} = \frac{AUC_{\text{oral,pred}}}{AUC_{\text{IV,pred}}} \times \frac{\text{Dose}_{\text{oral,pred}}}{\text{Dose}_{\text{IV,pred}}}$) is comparable to the observed bioavailability (F_{obs}) with $F_{\text{pred}} = 30\%$ and $F_{\text{obs}} = 40\%$ [6]. The contribution of the implemented metabolic clearance processes via UGT 1A9, 2B7, 2B17, and hydrolysis/oxidation to the overall metabolized fraction (f_m) has been estimated at 3, 56, 11, and 30%, respectively.

Pediatric PBPK model and dosage recommendations

The age-dependent maturation of UGT 2B17 has been successfully described and implemented using a Hill function with final parameter values of $OF_{\max} = 0.46$, $OF_{50} = 6.0$ years, and $\gamma = 1.63$, and $OF_{\min} = 0.58$ (suppl. Fig. S4). The maturation time of the primary metabolizing enzymes of vorinostat can be ranked as follows: UGT 2B17

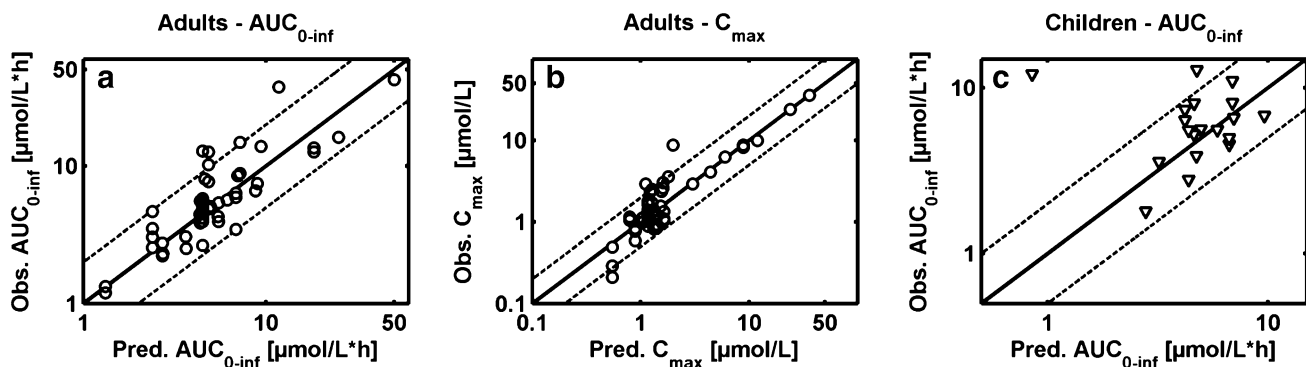


Fig. 2 Predicted versus observed PK parameters. **a** $AUC_{0-\infty}$ in adults ($n=52$). **b** C_{\max} in adults ($n=52$). **c** $AUC_{0-\infty}$ in children ($n=19$). Circles indicate adults and triangles children. Dashed line: twofold acceptance limits

Table 2 Vorinostat physicochemical and ADME parameters

Parameter	Unit	Literature value	Ref.	Value used for simulations	Parameter description
MW	g/mol	264.32	–	264.32	Molecular weight
logP	–	0.89	[57]	0.89	Lipophilicity
fu	[%]	28.8±2.9	[4]	28.8	Fraction unbound
pKa	–	9.2	[4]	9.2	Acid dissociation constant
Solubility	mg/ml	0.1–0.4	[4, 58]	0.2	Solubility
UGT 1A9 CL _{in-vitro}	μl/min/mg	38.55	[15, 16] ^a	38.55	UGT 1A9 in vitro metabolic clearance
UGT 2B7 CL _{in-vitro}	μl/min/mg	580	[16]	580	UGT 1A9 in vitro metabolic clearance
UGT 2B17 CL _{in-vitro}	μl/min/mg	53	[15, 16] ^a	53	UGT 1A9 in vitro metabolic clearance
UGT 1A9 content	pmol/mg	30.11	[59] ^b	30.11	Microsomal UGT 1A9 liver content
UGT 2B7 content	pmol/mg	78.49	[59] ^b	78.49	Microsomal UGT 2B7 liver content
UGT 2B17 content	pmol/mg	22.17	[59] ^c	22.17	Microsomal UGT 2B17 liver content
CL _{hydr,β-ox}	l/h	NA	NA	1.8 ^d	Clearance via hydrolysis and β-oxidation
P _{intest}	dm/min	1.56E-07	[4]	2.20E-07 ^d	Intestinal permeability
P _{cell}	dm/min	6.55E-5	PK-Sim	9.60E-06 ^d	Cellular permeability
P _{RBC->PLS}	dm/min	6.48E-5	PK-Sim	4.20E-06 ^d	Blood-plasma permeability
P _{PLS->RBC}	dm/min	6.45E-5	PK-Sim	1.00E-04 ^d	Plasma-blood permeability
B:P	–	2.87	[50]	2.87	Blood-to-plasma concentration ratio
Layer _{PD,unstirred,water}	μm	20	PK-Sim	108 ^d	Particle dissolution unstirred water layer

NA not available

^aMean of 2 reported values

^bMean of 7 reported values

^cMean of 3 reported values

^dFitted

(longest)>1A9>2B7. Given that there is (1) no clear relationship between pediatric doses and exposures and (2) no inter-individual variability estimated, the individually predicted vorinostat concentration–time profiles are in adequate agreement with the observed data in the age range between 4.7 and 22.0 years (suppl. Fig. S5).

Because the, so far, proposed pediatric dosage of 230 mg/m²/day leads to very high exposure in children between 0 and 1 years (suppl. Fig. S6a), the pediatric PBPK model has been used to identify dosages for all age groups from 0 to 17 years leading to C_{max} values similar to the ones in adults. The recommended dosages are 80 mg/m² for children from 0 to 1 year and 230 mg/m² for children and adolescents between 1 and 17 years (suppl. Fig. S6b).

Adult PBPK model—HDAC activity

The default PK-Sim PBPK model has been successfully expanded by two effect compartments describing PBMC concentrations and by an indirect response model of HDAC activity. The PBMC concentration–time profiles are best described using a two-compartment model (Fig. 4a). A comparison between vorinostat PBMC concentration–time profiles simulated using a 1- or 2-compartmental model

is depicted in supplemental Fig. S7. The observed half-life of oral vorinostat in PBMCs is 5.30 h, 3.0-fold longer than observed in plasma, and the predicted half-life in PBMCs (2-cmt) is 5.66 h, 3.4-fold longer than predicted in plasma [60]. The indirect response model is able to accurately describe the HDAC inhibition caused by a single dose of 400 mg vorinostat (Fig. 4b). The minimum observed and predicted HDAC activities are 21.6 and 26.6%, respectively [60]. The final model parameters of both the PBMC effect compartment model and the HDAC indirect response model are given in supplemental Table S5. The structural model alterations of the default PK-Sim PBPK model are depicted in Fig. 1.

Adult PBPK model—platelet count

The PBPK model has been successfully expanded by the thrombocytopenia model. The integrated PBPK/PD model is able to capture the thrombocyte count over a 36-week standard vorinostat treatment period in a thrombocytosis population (Fig. 4c). In a population with normal thrombocyte counts, the model has successfully predicted the thrombocytopenia prevalence of 27.9% which is in close agreement with the published observed value of 25.6% [61]. The

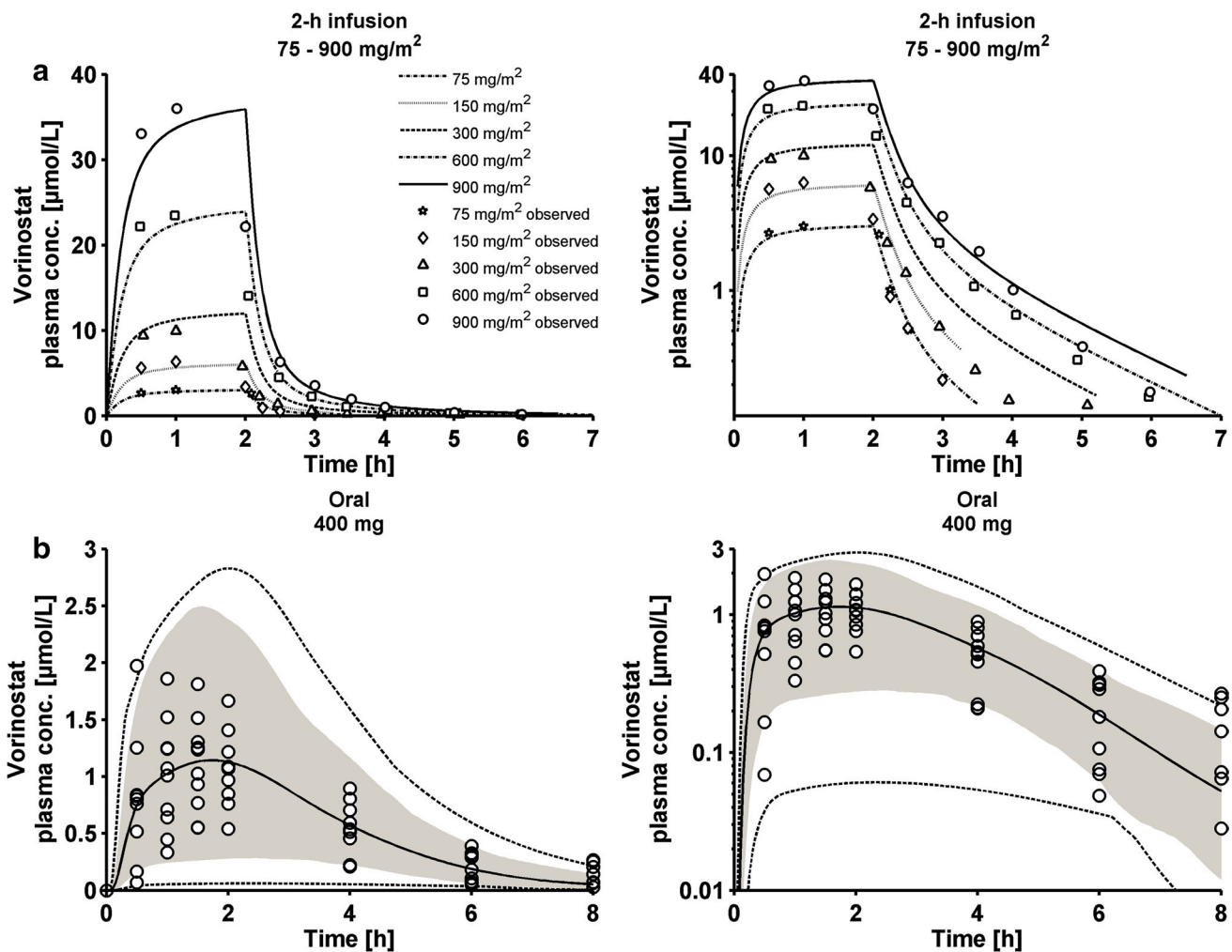


Fig. 3 Concentration–time profiles after intravenous (a) and oral administration of vorinostat single doses (b) [30, 50]. Simulated data are represented as median (black lines), 90% prediction interval (gray shaded area), and minimum and maximum values (dotted lines)

model parameter values used in the simulations are compiled in supplemental Table S3. The manually estimated slope parameter for vorinostat is $0.22 \mu\text{M}^{-1}$.

Identification of new vorinostat dosing regimens

The adult PBPK/PD model of vorinostat including the HDAC activity and the thrombocytopenia model has been successfully used in in silico trials to identify new vorinostat doses and dosing schedules which are potentially more effective than the standard dosing regimen of 400 mg qd.

Although part 1 suggests that none of the tested 25 dosing regimens offers a higher maximum and/or prolonged HDAC inhibition when the target thrombocyte count is that of the approved standard treatment ($\sim 193 \times 10^9 \text{ cells/l}$), the alternative treatment D (800 mg, every 2nd day) might be a replacement of the standard treatment showing a 14% higher

maximum HDAC inhibition but a 10% shorter HDAC inhibition time (suppl. Table S6).

However, part 2 reveals that 11 (9 oral, and 2 infusions) out of the 15 tested dosing schedules offer higher maximum and prolonged HDAC inhibitions (suppl. Table S7). Compared to the standard treatment, the potentially beneficial dosing regimens exhibit a mean maximum HDAC inhibition that is 27% higher (min: 16%, max: 62%) and the mean accumulated time of the HDAC inhibition being $>50\%$ is 180% longer (min: 6%, max: 509%). Based on the accumulated time of HDAC inhibition, trial C with three daily doses of the maximum 3000 mg dose has shown the best results with a HDAC inhibition time increase of 509% and a platelet decrease of -72% which is close to the lower thrombocyte limit at -74% .

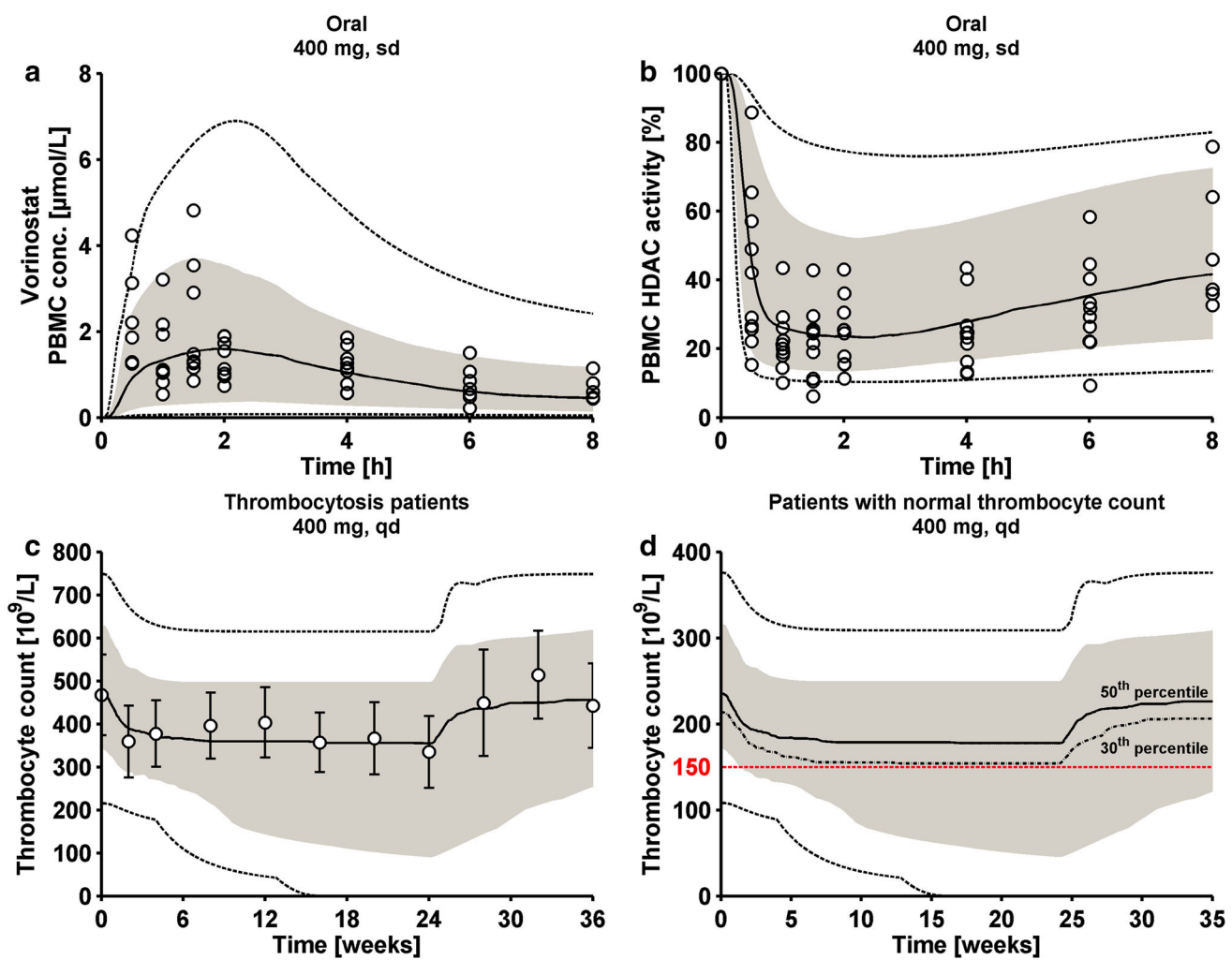


Fig. 4 PBPK/PD model results. **a** PBMC concentration–time profiles [50]. **b** HDAC activity over time [50]. **c** Thrombocyte count in thrombocytosis patients during a 24-week vorinostat treatment with 400 mg qd [36]. **d** Thrombocyte count in patients with normal thrombocyte counts. Simulated data are represented as median (black line), 90%

prediction interval (gray shaded area) and minimum and maximum values (dotted lines). The red dotted line represents the thrombocyte counts justifying the diagnosis of thrombocytopenia ($=150 \times 10^9 \text{ cells/l}$). Single doses: sd, repeated once daily doses: qd

Parameter sensitivity analysis

The parameter sensitivity analysis (suppl. Fig. S8) reveals that, among the tested parameters, the intestinal permeability, the clearance via hydrolysis and oxidation, and the unstirred layer of the particle dissolution have the biggest impact on the tested vorinostat PK parameters $AUC_{0-\infty}$, C_{\max} , half-life, and T_{\max} .

Discussion

A PBPK model for the prediction of vorinostat concentrations after different intravenous and oral vorinostat doses has been successfully developed. The model was able to

accurately predict vorinostat concentrations in adult and pediatric patients and to recommend dosages for different pediatric age groups. After successful implementation of PBMC effect compartments, PD models of HDAC activity (measured in PBMCs) and thrombocytopenia were integrated in the PBPK model. The final integrated PBPK/PD model of vorinostat was successfully applied in *in silico* trials, thereby identifying potentially more effective vorinostat dosing regimens in comparison with standard treatment.

The cellular permeability drives the permeation rate of vorinostat across the interstitial—intracellular membrane in the PK-Sim PBPK model. The permeability was initially calculated within PK-Sim according to an empirically derived formula, using logMA and molecular weight as

input variables, based on the procedure presented by Kawai and co-workers [62]. However, using the calculated cellular permeability value, the plasma concentration–time profiles of vorinostat were under-predicted. With the estimated permeability value, the model successfully predicted the intravenous profiles of the evaluation dataset.

In vitro tests found that UGT 2B17 is the major metabolizing enzyme of vorinostat. However, by compiling all available metabolic data of UGT 1A9, 2B7, and 2B17 in the model, the PBPK analysis suggested that UGT 2B17 is only of minor importance for the vorinostat clearance in vivo. This has important implications for the evaluation of other studies aiming to assess the impact of UGT 2B17 polymorphisms on survival of patients treated with vorinostat. Furthermore, it was reported that the UGT 2B17*2 polymorphism, which leads to reduced vorinostat glucuronidation, was associated with a longer progression-free survival in Asian breast cancer patients [17]. Although, this polymorphism is present in 92% of Asian populations, based on the presented modeling results, it seems unlikely that the reported results are mainly due to the low glucuronidation capacity of UGT 2B17*2 as only a small fraction of the administered vorinostat dose is metabolized by UGT 2B17 ($f_m = 11\%$) [63, 64]. The PBPK analysis suggests that UGT 2B7 ($f_m = 56\%$) polymorphisms, for instance, could play a vital role in the elimination, which is in accordance with the literature [16]. It is important to point out, that the clinical trial populations used in model development and evaluation were not tested for their UGT genotypes. Hence, additional information on their genotypes might alter the interpretation of these modeling results.

The PBPK analysis suggests that hydrolysis and oxidation are responsible for 30% of vorinostat metabolism and therefore more important than UGT 2B17 that accounts for 11%. Additionally, the sensitivity analysis underlined that the vorinostat PBPK model is sensitive to changes to the hydrolytic and oxidative clearance. In the model, it was assumed that both hydrolysis and oxidation would be carried out by a single enzyme available in all tissues. Unfortunately, we do not know the contribution of either hydrolysis or oxidation to the metabolized fraction, which means that the tissue-specific expression of hydrolytic or oxidative enzymes cannot be accounted for in the model. It is known that carboxylesterases, responsible for the hydrolysis of other drugs, are not equally expressed in all tissues [65]. In the model, it was further assumed that hydrolysis and oxidation would be fully developed from birth in all tissues, whereas studies have shown that the developmental regulation of esterases occurs in a gene, organ, and age-dependent manner [65–68]. As no details on the oxidative enzymes are available, it was decided to assume a scenario in which children would have adult enzyme levels for hydrolysis and oxidation available, and thus the highest possible clearance via this metabolic

pathway. This might lead to an over-prediction of hydrolytic and oxidative clearance. Thereby, the recommended dose of 80 mg/m² for children from 0 to 1 year of age might be overpredicted and should therefore be viewed as a maximum recommended dose.

The maturation of the UGTs should have the biggest impact on the pediatric vorinostat PK between the age 0 and 3 years as the maturation progresses considerably. The youngest observed pediatric patient was 4.7 years old, thus it was not possible to evaluate the model prediction quality in the critical age below 3 years. Although there is uncertainty in the recommended doses for an age < 4.7 years, the PBPK methodology has demonstrated for several other drugs that the pediatric PK can be successfully predicted below the age of 5 [69, 70].

Both, the PBMC concentration–time profiles and the HDAC inhibition could be very well described. Yet, the effect compartment model and the indirect model were based on a single 400 mg dose only. Hence, there is some uncertainty to the *in silico* trials that were carried out using a wide range of doses. While most parameters of the thrombocytopenia model were gathered from the literature, the slope parameter of vorinostat had to be estimated. Because no other data were available, this parameter was estimated using a thrombocytosis population. It was assumed that all gathered parameters (*e.g.* MTT) but the baseline cell counts (proliferating (Prol) and circulating (Circ) cells) were similar in patients with and without thrombocytosis, which might not be true. Nevertheless, the integrated PBPK/PD model was able to accurately predict the prevalence of thrombocytopenia in patients with normal thrombocyte counts.

Recommended doses for children were determined by targeting an exposure (AUC_{0–inf}) in children similar to the one observed in adults assuming the same efficacy and safety in these populations. Although data on the impact of vorinostat on the HDAC activity over time or the platelet count over time was not available in children, the assumption appears reasonable. First, the pediatric dose of 230 mg/m² and the comparable approved standard dose of 400 mg/day for adults both led to significant accumulation of acetylated H3 histones in PBMCs in children and adults, respectively [21]. Second, dose-limiting toxicities at comparable doses in children and adults are similar [21].

In part 2 of the *in silico* trials, the lower thrombocyte limit was set to 50 × 10⁹ cells/l (part 1: 193 × 10⁹ cells/l) since platelet counts ≥ 50 × 10⁹ cells/l typically do not lead to clinical interventions; for instance, prophylactic platelet transfusions are recommended for thrombocyte counts of ≤ 10 × 10⁹ cells/l [71]. The upper vorinostat dose limit of 3000 mg was defined by two factors. First, the highest vorinostat dose administered *in vivo* was 1000 mg (suppl. Fig. S3). As the PBPK model could not be evaluated above doses of 1000 mg, there is some uncertainty in

simulations above doses of 1000 mg. Second, vorinostat is typically available in 100 mg capsules, which makes dosing of high doses (> 400 mg) difficult in clinical practice. However, there are already promising new formulations under research that should simplify higher vorinostat dose administrations [72, 73].

Finally, the parameter sensitivity analysis has shown that the vorinostat half-life mainly depends on the intestinal permeability and the unstirred water layer parameter of the particle dissolution, which underlines that the absorption rate-limited flip-flop PK of vorinostat has been correctly implemented. Although the absorption was adequately predicted with the particle dissolution module, there might be other reasons responsible for the limited absorption such as drug-disease interactions or transporters. Vorinostat was found to be a substrate of P-gp and BCRP as well as an inducer of P-gp at the blood–brain barrier [58, 74, 75].

Despite some limitations, the presented work clearly demonstrates the applicability and usefulness of PBPK and PBPK/PD models in pediatric dose identification and in *in silico* trials. The PBPK modeling approach helps to integrate and leverage all available *in vitro*, *in vivo*, and *in silico* information while potentially reducing the number of clinical trials and study participants. Still, future clinical trials are needed to evaluate efficacy and safety of the newly proposed dosing regimens.

Conclusion

For the first time, a comprehensive PBPK/PD model of vorinostat has been developed which can predict (1) vorinostat concentration–time profiles in adults and (2) the impact of vorinostat on its major PD biomarkers, the HDAC inhibition and the dose-limiting decrease in thrombocytes. The PBPK/PD model was used to recommend (1) pediatric doses from 0 to 17 years and (2) potentially more effective vorinostat dosing regimens for adults. However, further research on (1) the yet unidentified enzymes involved in vorinostat metabolism, (2) the vorinostat PK in pediatric patients < 5 years of age, and (3) the PK/PD relationship in pediatric patients is necessary to increase the confidence in the model predictions. These results exemplify a mechanistic modeling approach that might help researchers to design clinical studies and to potentially improve dosing regimens of newly developed and already established drugs.

Acknowledgements The analyses of vorinostat were supported by Merck & Co., Inc., USA that provided deuterium-labeled and unlabeled reference standards of vorinostat and its metabolites M1 and M2. Some of the studies were financially supported by MSD Sharp & Dohme GmbH, Germany.

Compliance with ethical standards

Ethical standards All procedures performed in studies involving human participants were in accordance with the legal requirements and ethical standards of the responsible institutional and/or national research committee and with the 1964 Helsinki declaration and its later amendments or comparable ethical standards.

Informed consent Informed consent was obtained from all individual participants before inclusion.

Conflict of interest Daniel Moj, Hannah Britz, Thorsten Lehr and Clinton F. Stewart have reported no potential conflicts of interest. Walter E. Haefeli and Jürgen Burhenne have received financial and non-financial (analytical standards) support from Merck & Co., Inc., USA for the development and application of the vorinostat assay. Jürgen Burhenne has received travel support and lecture fees from MSD Sharp & Dohme GmbH, Germany.

References

- Marks P, Rifkind RA, Richon VM, Breslow R, Miller T, Kelly WK (2001) Histone deacetylases and cancer: causes and therapies. *Nat Rev Cancer* 1(3):194–202. doi:[10.1038/35106079](https://doi.org/10.1038/35106079)
- Falkenberg KJ, Johnstone RW (2014) Histone deacetylases and their inhibitors in cancer, neurological diseases and immune disorders. *Nat Rev Drug Discov* 13(9):673–691. doi:[10.1038/nrd4360](https://doi.org/10.1038/nrd4360)
- Laufer BE, Mintzer R, Fong R, Mukund S, Tam C, Zilberleyb I, Flicke B, Ritscher A, Fedorowicz G, Vallero R, Ortwin DF, Gunzner J, Modrusan Z, Neumann L, Koth CM, Lupardus PJ, Kaminker JS, Heise CE, Steiner P (2013) Histone deacetylase (HDAC) inhibitor kinetic rate constants correlate with cellular histone acetylation but not transcription and cell viability. *J Biol Chem* 288(37):26926–26943. doi:[10.1074/jbc.M113.490706](https://doi.org/10.1074/jbc.M113.490706)
- U.S. Food and Drug Administration (2006) Center for Drug Evaluation and Research. Vorinostat NDA 021991 Clinical Pharmacology and Biopharmaceutics Review. http://www.accessdata.fda.gov/drugsatfda_docs/nda/2006/021991s000_Zolinza_Clin-PharmR.pdf. Accessed 11 Nov 2016
- Merck Sharp & Dohme Corp.. A subsidiary of Merck & Co., Inc. Full prescribing information: Zolinza. http://www.accessdata.fda.gov/drugsatfda_docs/label/2011/021991s002lbl.pdf. Accessed 22 Feb 2017]
- Kelly WK (2005) Phase I study of an oral histone deacetylase inhibitor, suberoylanilide hydroxamic acid, in patients with advanced cancer. *J Clin Oncol* 23(17):3923–3931. doi:[10.1200/jco.2005.14.167](https://doi.org/10.1200/jco.2005.14.167)
- Iwamoto M, Friedman EJ, Sandhu P, Agrawal NG, Rubin EH, Wagner JA (2013) Clinical pharmacology profile of vorinostat, a histone deacetylase inhibitor. *Cancer Chemother Pharmacol* 72(3):493–508. doi:[10.1007/s00280-013-2220-z](https://doi.org/10.1007/s00280-013-2220-z)
- Fujiwara Y, Yamamoto N, Yamada Y, Yamada K, Otsuki T, Kanazu S, Iwasa T, Hardwick JS, Tamura T (2009) Phase I and pharmacokinetic study of vorinostat (suberoylanilide hydroxamic acid) in Japanese patients with solid tumors. *Cancer Sci* 100(9):1728–1734. doi:[10.1111/j.1349-7006.2009.01237.x](https://doi.org/10.1111/j.1349-7006.2009.01237.x)
- Strassburg CP, Strassburg A, Kneip S, Barut A, Tukey RH, Rodeck B, Manns MP (2002) Developmental aspects of human hepatic drug glucuronidation in young children and adults. *Gut* 50(2):259–265

10. Zaya MJ, Hines RN, Stevens JC (2006) Epirubicin glucuronidation and UGT2B7 developmental expression. *Drug Metab Dispos* 34(12):2097–2101. doi:[10.1124/dmd.106.011387](https://doi.org/10.1124/dmd.106.011387)
11. Pacifici GM, Sawe J, Kager L, Rane A (1982) Morphine glucuronidation in human fetal and adult liver. *Eur J Clin Pharmacol* 22(6):553–558
12. McRorie TI, Lynn AM, Nespeca MK, Opheim KE, Slattery JT (1992) The maturation of morphine clearance and metabolism. *Am J Dis Child* (1960) 146(8):972–976
13. Edginton AN, Schmitt W, Willmann S (2006) Development and evaluation of a generic physiologically based pharmacokinetic model for children. *Clin Pharmacokinet* 45(10):1013–1034. doi:[10.2165/000003088-200645100-00005](https://doi.org/10.2165/000003088-200645100-00005)
14. Neumann E, Mehboob H, Ramirez J, Mirkov S, Zhang M, Liu W (2016) Age-dependent hepatic UDP-glucuronosyltransferase gene expression and activity in children. *Front Pharmacol* 7:437. doi:[10.3389/fphar.2016.00437](https://doi.org/10.3389/fphar.2016.00437)
15. Balliet RM, Chen G, Gallagher CJ, Dellinger RW, Sun D, Lazarus P (2009) Characterization of UGTs active against SAHA and association between SAHA glucuronidation activity phenotype with UGT genotype. *Cancer Res* 69(7):2981–2989. doi:[10.1158/0008-5472.CAN-08-4143](https://doi.org/10.1158/0008-5472.CAN-08-4143)
16. Kang SP, Ramirez J, House L, Zhang W, Mirkov S, Liu W, Haverfield E, Ratain MJ (2010) A pharmacogenetic study of vorinostat glucuronidation. *Pharmacogenet Genomics* 20(10):638–641. doi:[10.1097/FPC.0b013e32833e1b37](https://doi.org/10.1097/FPC.0b013e32833e1b37)
17. Wong NS, Seah E, Wang LZ, Yeo WL, Yap HL, Chuah B, Lim YW, Ang PC, Tai BC, Lim R, Goh BC, Lee SC (2011) Impact of UDP-gluconorlytransferase 2B17 genotype on vorinostat metabolism and clinical outcomes in Asian women with breast cancer. *Pharmacogenet Genom* 21(11):760–768. doi:[10.1097/FPC.0b013e32834a8639](https://doi.org/10.1097/FPC.0b013e32834a8639)
18. Olsen EA, Kim YH, Kuzel TM, Pacheco TR, Foss FM, Parker S, Frankel SR, Chen C, Ricker JL, Arduino JM, Duvic M (2007) Phase IIb multicenter trial of vorinostat in patients with persistent, progressive, or treatment refractory cutaneous T-cell lymphoma. *J Clin Oncol* 25(21):3109–3115. doi:[10.1200/jco.2006.10.2434](https://doi.org/10.1200/jco.2006.10.2434)
19. Duvic M, Talpur R, Ni X, Zhang C, Hazarika P, Kelly C, Chiao JH, Reilly JF, Ricker JL, Richon VM, Frankel SR (2007) Phase 2 trial of oral vorinostat (suberoylanilide hydroxamic acid, SAHA) for refractory cutaneous T-cell lymphoma (CTCL). *Blood* 109(1):31–39. doi:[10.1182/blood-2006-06-025999](https://doi.org/10.1182/blood-2006-06-025999)
20. Subramanian S, Bates SE, Wright JJ, Espinoza-Delgado I, Piekarz RL (2010) Clinical toxicities of histone deacetylase inhibitors. *Pharmaceuticals* 3(9):2751–2767. doi:[10.3390/ph3092751](https://doi.org/10.3390/ph3092751)
21. Fouladi M, Park JR, Stewart CF, Gilbertson RJ, Schaiquevich P, Sun J, Reid JM, Ames MM, Speights R, Ingle AM, Zwiebel J, Blaney SM, Adamson PC (2010) Pediatric phase I trial and pharmacokinetic study of vorinostat: a Children's Oncology Group phase I consortium report. *J Clin Oncol* 28(22):3623–3629. doi:[10.1200/JCO.2009.25.9119](https://doi.org/10.1200/JCO.2009.25.9119)
22. Muscal JA, Thompson PA, Horton TM, Ingle AM, Ahern CH, McGovern RM, Reid JM, Ames MM, Espinoza-Delgado I, Weigel BJ, Blaney SM (2013) A phase I trial of vorinostat and bortezomib in children with refractory or recurrent solid tumors: a Children's Oncology Group phase I consortium study (ADVL0916). *Pediatr Blood Cancer* 60(3):390–395. doi:[10.1002/pbc.24271](https://doi.org/10.1002/pbc.24271)
23. Hummel TR, Wagner L, Ahern C, Fouladi M, Reid JM, McGovern RM, Ames MM, Gilbertson RJ, Horton T, Ingle AM, Weigel B, Blaney SM (2013) A pediatric phase 1 trial of vorinostat and temozolamide in relapsed or refractory primary brain or spinal cord tumors: a Children's Oncology Group phase 1 consortium study. *Pediatr Blood Cancer* 60(9):1452–1457. doi:[10.1002/pbc.24541](https://doi.org/10.1002/pbc.24541)
24. Munshi A, Tanaka T, Hobbs ML, Tucker SL, Richon VM, Meyn RE (2006) Vorinostat, a histone deacetylase inhibitor, enhances the response of human tumor cells to ionizing radiation through prolongation of gamma-H2AX foci. *Mol Cancer Ther* 5(8):1967–1974. doi:[10.1158/1535-7163.mct-06-0022](https://doi.org/10.1158/1535-7163.mct-06-0022)
25. Wilson PM, Labonte MJ, Martin SC, Kuwahara ST, El-Khoueiry A, Lenz HJ, Ladner RD (2013) Sustained inhibition of deacetylases is required for the antitumor activity of the histone deacetylase inhibitors panobinostat and vorinostat in models of colorectal cancer. *Invest New Drugs* 31(4):845–857. doi:[10.1007/s10637-012-9914-7](https://doi.org/10.1007/s10637-012-9914-7)
26. Arnold NB, Arkus N, Gunn J, Korc M (2007) The histone deacetylase inhibitor suberoylanilide hydroxamic acid induces growth inhibition and enhances gemcitabine-induced cell death in pancreatic cancer. *Clin Cancer Res* 13(1):18–26. doi:[10.1158/1078-0432.ccr-06-0914](https://doi.org/10.1158/1078-0432.ccr-06-0914)
27. Shen J, Huang C, Jiang L, Gao F, Wang Z, Zhang Y, Bai J, Zhou H, Chen Q (2007) Enhancement of cisplatin induced apoptosis by suberoylanilide hydroxamic acid in human oral squamous cell carcinoma cell lines. *Biochem Pharmacol* 73(12):1901–1909. doi:[10.1016/j.bcp.2007.03.009](https://doi.org/10.1016/j.bcp.2007.03.009)
28. Dickson MA, Rathkopf DE, Carvajal RD, Grant S, Roberts JD, Reid JM, Ames MM, McGovern RM, Lefkowitz RA, Gonon M, Cane LM, Dials HJ, Schwartz GK (2011) A phase I pharmacokinetic study of pulse-dose vorinostat with flavopiridol in solid tumors. *Invest New Drugs* 29(5):1004–1012. doi:[10.1007/s10637-010-9447-x](https://doi.org/10.1007/s10637-010-9447-x)
29. Nelder JA, Mead R (1965) A simplex method for function minimization. *Comput J* 7(4):308–313. doi:[10.1093/comjnl/7.4.308](https://doi.org/10.1093/comjnl/7.4.308)
30. Kelly WK, Richon VM, O'Connor O, Curley T, MacGregor-Curtelli B, Tong W, Klang M, Schwartz L, Richardson S, Rosa E, Drobniak M, Cordon-Cordozo C, Chiao JH, Rifkind R, Marks PA, Scher H (2003) Phase I clinical trial of histone deacetylase inhibitor suberoylanilide hydroxamic acid administered intravenously. 9 (10):3578–3588
31. Mahalingam D, Mita M, Sarantopoulos J, Wood L, Amaravadi RK, Davis LE, Mita AC, Curiel TJ, Espitia CM, Nawrocki ST, Giles FJ, Carew JS (2014) Combined autophagy and HDAC inhibition. *Autophagy* 10(8):1403–1414. doi:[10.4161/auto.29231](https://doi.org/10.4161/auto.29231)
32. Munster PN, Rubin EH, Van Belle S, Friedman E, Patterson JK, Van Dyck K, Li X, Comisar W, Chodakewitz JA, Wagner JA, Iwamoto M (2009) A single supratherapeutic dose of vorinostat does not prolong the QTc interval in patients with advanced cancer. *Clin Cancer Res* 15(22):7077–7084. doi:[10.1158/1078-0432.CCR-09-1214](https://doi.org/10.1158/1078-0432.CCR-09-1214)
33. Ramalingam SS, Parise RA, Ramanathan RK, Lagattuta TF, Musguire LA, Stoller RG, Potter DM, Argiris AE, Zwiebel JA, Egorin MJ, Belani CP (2007) Phase I and pharmacokinetic study of vorinostat, a histone deacetylase inhibitor, in combination with carboplatin and paclitaxel for advanced solid malignancies. *Clin Cancer Res* 13(12):3605–3610. doi:[10.1158/1078-0432.CCR-07-0162](https://doi.org/10.1158/1078-0432.CCR-07-0162)
34. Rubin EH, Agrawal NG, Friedman EJ, Scott P, Mazina KE, Sun L, Du L, Ricker JL, Frankel SR, Gottesdiener KM, Wagner JA, Iwamoto M (2006) A study to determine the effects of food and multiple dosing on the pharmacokinetics of vorinostat given orally to patients with advanced cancer. *Clin Cancer Res* 12(23):7039–7045. doi:[10.1158/1078-0432.CCR-06-1802](https://doi.org/10.1158/1078-0432.CCR-06-1802)
35. Wada H, Tsuboi R, Kato Y, Sugaya M, Tobinai K, Hamada T, Shimamoto T, Noguchi K, Iwatsuki K (2012) Phase I and pharmacokinetic study of the oral histone deacetylase inhibitor vorinostat in Japanese patients with relapsed or refractory cutaneous T-cell lymphoma. *J Dermatol* 39(10):823–828. doi:[10.1111/j.1346-8138.2012.01554.x](https://doi.org/10.1111/j.1346-8138.2012.01554.x)
36. Andersen CL, McMullin MF, Ejerblad E, Zweegman S, Harrison C, Fernandes S, Bareford D, Knapper S, Samuelsson J, Lofvenberg E, Linder O, Andreasson B, Ahlstrand E, Jensen MK, Bjerrum OW, Vestergaard H, Larsen H, Klausen TW,

- Mourits-Andersen T, Hasselbalch HC (2013) A phase II study of vorinostat (MK-0683) in patients with polycythaemia vera and essential thrombocythaemia. *Br J Haematol* 162(4):498–508. doi:[10.1111/bjh.12416](https://doi.org/10.1111/bjh.12416)
37. Wu G, Baraldo M, Furlanet M (1995) Calculating percentage prediction error: a user's note. *Pharmacol Res* 32(4):241–248
 38. Post TM, Freijer JI, Ploeger BA, Danhof M (2008) Extensions to the visual predictive check to facilitate model performance evaluation. *J Pharmacokinet Pharmacodyn* 35(2):185–202. doi:[10.1007/s10928-007-9081-1](https://doi.org/10.1007/s10928-007-9081-1)
 39. Willmann S, Hohn K, Edginton A, Sevestre M, Solodenko J, Weiss W, Lippert J, Schmitt W (2007) Development of a physiology-based whole-body population model for assessing the influence of individual variability on the pharmacokinetics of drugs. *J Pharmacokinet Pharmacodyn* 34(3):401–431. doi:[10.1007/s10928-007-9053-5](https://doi.org/10.1007/s10928-007-9053-5)
 40. Claassen K, Thelen K, Coboeken K, Gaub T, Lippert J, Allegaert K, Willmann S (2015) Development of a physiologically-based pharmacokinetic model for preterm neonates: evaluation with *in vivo* data. *Curr Pharm Des* 21(39):5688–5698
 41. Willmann S, Becker C, Burghaus R, Coboeken K, Edginton A, Lippert J, Siegmund H-U, Thelen K, Mück W (2014) Development of a paediatric population-based model of the pharmacokinetics of rivaroxaban. *Clin Pharmacokinet* 53(1):89–102. doi:[10.1007/s40262-013-0090-5](https://doi.org/10.1007/s40262-013-0090-5)
 42. Thelen K, Coboeken K, Willmann S, Burghaus R, Dressman JB, Lippert J (2011) Evolution of a detailed physiological model to simulate the gastrointestinal transit and absorption process in humans, part 1: oral solutions. *J Pharm Sci* 100(12):5324–5345. doi:[10.1002/jps.22726](https://doi.org/10.1002/jps.22726)
 43. Thelen K, Coboeken K, Willmann S, Dressman JB, Lippert J (2012) Evolution of a detailed physiological model to simulate the gastrointestinal transit and absorption process in humans, part II: extension to describe performance of solid dosage forms. *J Pharm Sci* 101(3):1267–1280. doi:[10.1002/jps.22825](https://doi.org/10.1002/jps.22825)
 44. Willmann S, Lippert J, Schmitt W (2005) From physicochemistry to absorption and distribution: predictive mechanistic modeling and computational tools. *Expert Opin Drug Metab Toxicol* 1(1):159–168. doi:[10.1517/17425255.1.1.159](https://doi.org/10.1517/17425255.1.1.159)
 45. Willmann S, Lippert J, Sevestre M, Solodenko J, Fois F, Schmitt W (2003) PK-Sim®: a physiologically based pharmacokinetic 'whole-body' model. *Biosilico* 1(4):121–124. doi:[10.1016/S1478-5382\(03\)02342-4](https://doi.org/10.1016/S1478-5382(03)02342-4)
 46. Meyer M, Schneckener S, Ludewig B, Kuepfer L, Lippert J (2012) Using expression data for quantification of active processes in physiologically based pharmacokinetic modeling. *Drug Metab Dispos* 40(5):892–901. doi:[10.1124/dmd.111.043174](https://doi.org/10.1124/dmd.111.043174)
 47. Wheeler DL, Church DM, Federhen S, Lash AE, Madden TL, Pontius JU, Schuler GD, Schriml LM, Sequeira E, Tatusova TA, Wagner L (2003) Database resources of the National Center for Biotechnology. *Nucleic Acids Res* 31(1):28–33
 48. Johnson KC (2003) Dissolution and absorption modeling: model expansion to simulate the effects of precipitation, water absorption, longitudinally changing intestinal permeability, and controlled release on drug absorption. *Drug Dev Ind Pharm* 29(8):833–842. doi:[10.1081/ddc-120024179](https://doi.org/10.1081/ddc-120024179)
 49. Du BD, Du BE (1916) Clinical calorimetry: Tenth paper a formula to estimate the approximate surface area if height and weight be known. *Archives of Internal Medicine XVII* (6_2):863–871. doi:[10.1001/archinte.1916.00080130010002](https://doi.org/10.1001/archinte.1916.00080130010002)
 50. Liu L, Detering JC, Milde T, Haefeli WE, Witt O, Burhenne J (2014) Quantification of vorinostat and its main metabolites in plasma and intracellular vorinostat in PBMCs by liquid chromatography coupled to tandem mass spectrometry and its relation to histone deacetylase activity in human blood. *J Chromatogr B* Analyt Technol Biomed Life Sci 964:212–221. doi:[10.1016/j.jchromb.2014.02.014](https://doi.org/10.1016/j.jchromb.2014.02.014)
 51. Sharma A, Jusko WJ (1998) Characteristics of indirect pharmacodynamic models and applications to clinical drug responses. *Br J Clin Pharmacol* 45(3):229–239. doi:[10.1046/j.1365-2125.1998.00676.x](https://doi.org/10.1046/j.1365-2125.1998.00676.x)
 52. Izak M, Bussel JB (2014) Management of thrombocytopenia. *F1000Prime Reports* 6:45. doi:[10.12703/P6-45](https://doi.org/10.12703/P6-45)
 53. Friberg LE, Henningsson A, Maas H, Nguyen L, Karlsson MO (2002) Model of chemotherapy-induced myelosuppression with parameter consistency across drugs. *J Clin Oncol* 20(24):4713–4721. doi:[10.1200/jco.2002.02.140](https://doi.org/10.1200/jco.2002.02.140)
 54. Chalret du Rieu Q, Fouliard S, White-Koning M, Kloos I, Chatelut E, Chenel M (2014) Pharmacokinetic/Pharmacodynamic modeling of abexinostat-induced thrombocytopenia across different patient populations: application for the determination of the maximum tolerated doses in both lymphoma and solid tumour patients. *Invest New Drugs* 32(5):985–994. doi:[10.1007/s10637-014-0118-1](https://doi.org/10.1007/s10637-014-0118-1)
 55. Peters SA, Hultin L (2008) Early identification of drug-induced impairment of gastric emptying through physiologically based pharmacokinetic (PBPK) simulation of plasma concentration-time profiles in rat. *J Pharmacokinet Pharmacodyn* 35(1):1–30. doi:[10.1007/s10928-007-9073-1](https://doi.org/10.1007/s10928-007-9073-1)
 56. Moj D, Hanke N, Britz H, Frechen S, Kanacher T, Wendl T, Haefeli WE, Lehr T (2017) Clarithromycin, midazolam, and digoxin: application of PBPK modeling to gain new insights into drug–drug interactions and co-medication regimens. *AAPS J* 19(1):298–312. doi:[10.1208/s12248-016-0009-9](https://doi.org/10.1208/s12248-016-0009-9)
 57. Nakashima S, Yamamoto K, Arai Y, Ikeda Y (2013) Impact of physicochemical profiling for rational approach on drug discovery. *Chem Pharm Bull* 61(12):1228–1238. doi:[10.1248/cpb.c13-00436](https://doi.org/10.1248/cpb.c13-00436)
 58. Konsoula R, Jung M (2008) In vitro plasma stability, permeability and solubility of mercaptoacetamide histone deacetylase inhibitors. *Int J Pharm* 361(1–2):19–25. doi:[10.1016/j.ijpharm.2008.05.001](https://doi.org/10.1016/j.ijpharm.2008.05.001)
 59. Margaillan G, Rouleau M, Klein K, Fallon JK, Caron P, Villerme L, Smith PC, Zanger UM, Guillermette C (2015) Multiplexed targeted quantitative proteomics predicts hepatic glucuronidation potential. *Drug Metab Dispos* 43(9):1331–1335. doi:[10.1124/dmd.115.065391](https://doi.org/10.1124/dmd.115.065391)
 60. Burhenne J, Liu L, Heilig CE, Meid AD, Leisen M, Schmitt T, Kasper B, Haefeli WE, Mikus G, Egerer G (2017) Intracellular vorinostat accumulation and its relationship to histone deacetylase activity in soft tissue sarcoma patients. *Cancer Chemother Pharm* 80(2):433–439
 61. Mann BS, Johnson JR, Cohen MH, Justice R, Pazdur R (2007) FDA approval summary: vorinostat for treatment of advanced primary cutaneous T-cell lymphoma. *Oncologist* 12(10):1247–1252. doi:[10.1634/theoncologist.12-10-1247](https://doi.org/10.1634/theoncologist.12-10-1247)
 62. Kawai R, Lemaire M, Steimer JL, Brue lisauer A, Niederberger W, Rowland M (1994) Physiologically based pharmacokinetic study on a cyclosporin derivative, SDZ IMM 125. *J Pharmacokinet Biopharm* 22(5):327–365
 63. Park J, Chen L, Ratnashinge L, Sellers TA, Tanner JP, Lee JH, Dossett N, Lang N, Kadlubar FF, Ambrosone CB, Zachariah B, Heysek RV, Patterson S, Pow-Sang J (2006) Deletion polymorphism of UDP-glucuronosyltransferase 2B17 and risk of prostate cancer in African American and Caucasian men. *Cancer epidemiology, biomarkers & prevention: a publication of the American Association for Cancer Research. Cosponsored Am Soc Prev Oncol* 15(8):1473–1478. doi:[10.1158/1055-9965.epi-06-0141](https://doi.org/10.1158/1055-9965.epi-06-0141)
 64. Xue Y, Sun D, Daly A, Yang F, Zhou X, Zhao M, Huang N, Zerjal T, Lee C, Carter NP, Hurles ME, Tyler-Smith C (2008) Adaptive evolution of UGT2B17 copy-number variation. *Am J Hum Genet* 83(3):337–346. doi:[10.1016/j.ajhg.2008.08.004](https://doi.org/10.1016/j.ajhg.2008.08.004)

65. Imai T (2006) Human carboxylesterase isozymes: catalytic properties and rational drug design. *Drug Metab Pharmacokinet* 21(3):173–185
66. Boberg M, Vrana M, Mehrotra A, Pearce RE, Gaedigk A, Bhatt DK, Leeder JS, Prasad B (2017) Age-dependent absolute abundance of hepatic carboxylesterases (CES1 and CES2) by LC-MS/MS proteomics: application to PBPK modeling of oseltamivir in vivo pharmacokinetics in infants. *Drug Metab Dispos* 45(2):216–223. doi:[10.1124/dmd.116.072652](https://doi.org/10.1124/dmd.116.072652)
67. Chen YT, Trzoss L, Yang D, Yan B (2015) Ontogeny expression of human carboxylesterase-2 and cytochrome P450 3A4 in liver and duodenum: postnatal surge and organ-dependent regulation. *Toxicology* 330:55–61. doi:[10.1016/j.tox.2015.02.007](https://doi.org/10.1016/j.tox.2015.02.007)
68. Zhu HJ, Appel DI, Jiang Y, Markowitz JS (2009) Age- and sex-related expression and activity of carboxylesterase 1 and 2 in mouse and human liver. *Drug Metab Dispos* 37(9):1819–1825. doi:[10.1124/dmd.109.028209](https://doi.org/10.1124/dmd.109.028209)
69. Zhou W, Johnson TN, Xu H, Cheung SYA, Bui KH, Li J, Al-Huniti N, Zhou D (2016) Predictive performance of physiologically based pharmacokinetic and population pharmacokinetic modeling of renally cleared drugs in children. *CPT: Pharm Syst Pharmacol* 5(9):475–483. doi:[10.1002/psp4.12101](https://doi.org/10.1002/psp4.12101)
70. Jiang XL, Zhao P, Barrett JS, Lesko LJ, Schmidt S (2013) Application of physiologically based pharmacokinetic modeling to predict acetaminophen metabolism and pharmacokinetics in children. *CPT Pharm Syst Pharmacol* 2:e80. doi:[10.1038/psp.2013.55](https://doi.org/10.1038/psp.2013.55)
71. Estcourt LJ, Stanworth SJ, Doree C, Hopewell S, Trivella M, Murphy MF (2015) Comparison of different platelet count thresholds to guide administration of prophylactic platelet transfusion for preventing bleeding in people with haematological disorders after myelosuppressive chemotherapy or stem cell transplantation. *Cochrane Database Syst Rev* (11):Cd010983. doi:[10.1002/14651858.CD010983.pub2](https://doi.org/10.1002/14651858.CD010983.pub2)
72. Cai YY, Yap CW, Wang Z, Ho PC, Chan SY, Ng KY, Ge ZG, Lin HS (2010) Solubilization of vorinostat by cyclodextrins. *J Clin Pharm Ther* 35(5):521–526. doi:[10.1111/j.1365-2710.2009.01095.x](https://doi.org/10.1111/j.1365-2710.2009.01095.x)
73. Jayant RD, Atluri VS, Agudelo M, Sagar V, Kaushik A, Nair M (2015) Sustained-release nanoART formulation for the treatment of neuroAIDS. *Int J Nanomed* 10:1077–1093. doi:[10.2147/ijn.s76517](https://doi.org/10.2147/ijn.s76517)
74. Sajja RK, Liles TR, Prasad S, Cucullo L (2016) Vorinostat induces blood-brain barrier P-Glycoprotein drug efflux activity: implications for limited brain disposition of co-administered chemotherapeutics. *FASEB J* 30(1 Supplement):935.933
75. Hanson JE, La H, Plise E, Chen Y-H, Ding X, Hanania T, Sabath EV, Alexandrov V, Brunner D, Leahy E, Steiner P, Liu L, Scearce-Levie K, Zhou Q (2013) SAHA enhances synaptic function and plasticity in vitro but has limited brain availability in vivo and does not impact cognition. *PLoS One* 8(7):e69964. doi:[10.1371/journal.pone.0069964](https://doi.org/10.1371/journal.pone.0069964)

4. RESULTS

4.4 Project IV:

The feasibility of physiologically-based pharmacokinetic modeling in forensic medicine illustrated by the example of morphine.

The feasibility of physiologically based pharmacokinetic modeling in forensic medicine illustrated by the example of morphine

Nadine Schaefer¹  · Daniel Moj² · Thorsten Lehr² · Peter H. Schmidt¹ · Frank Ramsthaler¹

Received: 21 August 2017 / Accepted: 28 November 2017
© Springer-Verlag GmbH Germany, part of Springer Nature 2017

Abstract

In forensic medicine, expert opinion is often required concerning dose and time of intake of a substance, especially in the context of fatal intoxications. In the present case, a 98-year-old man died 4 days after admission to a hospital due to a femur neck fracture following a domestic fall in his retirement home. As he had obtained high morphine doses in the context of palliative therapy and a confusion of his supplemental magnesium tablets with a diuretic by the care retirement home was suspected by the relatives, a comprehensive postmortem examination was performed. Forensic toxicological GC- and LC-MS analyses revealed, besides propofol, ketamine, and a metamizole metabolite in blood and urine, toxic blood morphine concentrations of approximately 3 mg/l in femoral and 5 mg/l in heart blood as well as 2, 7, and 10 mg/kg morphine in brain, liver, and lung, respectively. A physiologically based pharmacokinetic (PBPK) model was developed and applied to examine whether the morphine concentrations were (i) in agreement with the morphine doses documented in the clinical records or (ii) due to an excessive morphine administration. PBPK model simulations argue against an overdosing of morphine. The immediate cause of death was respiratory and cardiovascular failure due to pneumonia following a fall, femur neck fracture, and immobilization accompanied by a high and probably toxic concentration of morphine, attributable to the administration under palliative care conditions. The presented case indicates that PBPK modeling can be a useful tool in forensic medicine, especially in question of a possible drug overdosing.

Keywords Palliative care · Morphine · Physiologically based pharmacokinetic modeling · Forensic medicine

Introduction

In forensic medicine, profound knowledge on the pharmacokinetic (PK) properties of various drugs and drugs of abuse is necessary when interpreting analytical data in the context of potential intoxications. If expert opinion is required regarding dose and time of intake of a specific pharmaceutical, the toxicologist can draw on PK data examined in clinical studies, at least to give a vague assessment [1, 2]. As far as illicit drugs are concerned, only few controlled clinical and forensic toxicological studies dealing with the determination of PK models in order to answer the abovementioned issues have been performed [3–5]. These

studies have been conducted with healthy individuals. However, when attempting to estimate antemortem drug concentrations and the consumed dose from postmortem analyses, processes occurring during agony and postmortem have additionally to be taken into consideration [6].

In model-informed drug discovery and development, physiologically based (PB) PK modeling has become a useful tool to predict drug concentrations and consequently optimize drug therapy in particular patient populations [7–13]. Absorption, distribution, metabolism, and excretion parameters are calculated by implementing anatomical structures such as organ volumes and physiological processes in distinct body systems/organs such as blood flow rates and pH values at different locations [14]. These drug-independent data are supplemented with drug-dependent data such as lipophilicity, molecular weight, and protein binding.

The PK properties of morphine, commonly administered in palliative therapy [15], are well studied by means of various PK models in healthy volunteers after different routes of administration [16, 17]. Morphine is metabolized by cytochrome P450 (CYP) 3A4 [18] and several UDP-glucuronosyltransferases

✉ Nadine Schaefer
nadine.schaefer@uks.eu

¹ Institute of Legal Medicine, Saarland University, Building 80.2, 66421 Homburg (Saar), Germany

² Clinical Pharmacy, Saarland University, 66123 Saarbrücken, Germany

(UGTs). The highly potent morphine metabolite morphine-6-glucuronide is exclusively formed by UGT2B7 [19].

Several models investigating a possible influence of age [7], impaired renal [20, 21] or hepatic function [22, 23], or even terminal illness [24] on the PK of morphine have been developed. Requested expert opinion on a probable overdosing of morphine in a palliative care patient initiated the development of a PBPK model comprising morphine and its major metabolite morphine-6-glucuronide.

Case report

A 98-year-old man (height 170 cm, weight 73 kg) who had lived in a care retirement home was admitted to the hospital due to a femur neck fracture following a domestic fall. Because of incipient pneumonia after clinical immobilization and severe pre-existing cardiac insufficiency, operative treatment of the fracture was not indicated and a palliative therapy with morphine (intravenous (i.v.) infusion, dose 200 mg/50 mL) and oxycodone (peroral, dose 5 mg) was applied. The documented clinical doses of morphine and oxycodone are listed in Table 1. Three days after admission, anuresis was observed (for laboratory findings including values of creatinine and glomerular filtration rate, see Table 2) and the patient died on day 4. His daughter accused the care retirement home of having replaced his magnesium tablets by a diuretic, because she had recognized an increasing impairment of her father's mental health for 3 months. Furthermore, he had wet himself with increasing frequency and had always been thirsty. According to the allegation of the daughter, the suspected replacement of the tablets had been responsible for the fall and the following death. In addition, it could not unequivocally be deduced from the clinical patient record, whether the documented morphine doses (see Table 1) were administered in milligrams or milliliters. To examine a probable overdosing of morphine, a comprehensive postmortem examination was performed and a PBPK model was developed and applied.

Autopsy

Autopsy was performed 6 days after death. The following essential autopic findings were assessed:

- sufficient dietary and care condition
- frontal cephalhematoma
- fracture of the right femur neck without relevant loss of blood
- findings indicative of recurrent strokes
- severe aspiration pneumonia
- coronary atherosclerosis and pathological cardiac enlargement

Table 1 Clinically documented doses of morphine and oxycodone; no dosing unit of morphine given

Therapy day	Time (h)	Morphine i.v. ^a	Oxycodone p.o.
1	16:00		5 mg
	20:00		5 mg
	24:00		5 mg
2	04:00		5 mg
	08:00		5 mg
	13:00		5 mg
3	18:00	1	
	19:00	2	5 mg
	21:00	4	
4	06:00	6	
	09:00	6	
	13:00	6	
	17:30	4	
	20:00	6	
	21:00	6	
	21:30	8	
	03:00	8	
	09:00	8	
	12:30	8	
	14:00	8	
	18:00	10	
	18:45	10	
	20:00	13	
	22:46	death	

i.v. intravenous; p.o. per os

^a MSI (200 mg/50 mL infusion; bolus assumed)

- chronic blood congestion of inner organs indicative of chronic heart failure

The autopsy report concluded that the cause of death was respiratory and cardiovascular failure due to pneumonia following a fall, fracture of femur neck, and immobilization.

Methods

Toxicological analyses

At first, an enzyme immunoassay screening (EIA, Bio-Rad Laboratories GmbH, Muenchen, Germany) was performed in heart blood (collected from the inlet of the V. cava inferior to the right atrium) including opiates, methadone, buprenorphine, benzodiazepines, amphetamines, methamphetamines, cannabinoids, and cocaine. Afterwards, aliquots of heart blood and urine (0.5 mL each) were extracted liquid-liquidly (diethyl ether/ethyl acetate; 1:1 v/v) with 50 µL of trimipramine-D3 (0.5 µg/mL, LGC, Wesel, Germany) as internal standard (IS)

Table 2 Laboratory parameters

Therapy day	Time (h)	Creatinine (mg/dL)	GFR (mL/min)	GOT (U/I)	γ -GT (U/I)	GPT (U/I)
0	20:18			30	26	17
1	15:48	1.1	60			
2	04:00	1.2	54			

GFR glomerular filtration rate, GOT glutamate oxaloacetate transaminase, γ -GT gamma-glutamyl transferase, GPT glutamate pyruvate transaminase

and analyzed (with and without acetylation) by gas chromatography-mass spectrometry (GC-MS; GC: 6890 N, Agilent Technologies (AT), Waldbronn, Germany; MS: AT 5975 B) in full scan mode. Furthermore, an aliquot was analyzed by liquid chromatography (LC)-MS/MS (LC: Shimadzu prominence, Duisburg, Germany; MS: AB Sciex 3200 QTRAP, Darmstadt, Germany) for pharmaceutical drugs such as benzodiazepines, antidepressants, and neuroleptics. For the detection of oxycodone, a solid-phase extraction (SPE) was applied using 1.0 mL of heart blood (IS: 50 μ L oxycodone-D6, 1 μ g/mL, LGC, Wesel, Germany) and AT HCX cartridges (130 mg/3 mL) with a subsequent analysis by LC-MS/MS (Shimadzu prominence LC, AB Sciex 3200 QTRAP MS).

For quantification of free morphine in blood and tissue specimens, a fully validated GC-MS method after SPE was performed. SPE was carried out using AT HCX cartridges (130 mg/3 mL). They were conditioned with 2 \times 3 mL of methanol and 3 mL of potassium dihydrogen phosphate (pH 6). Aliquots of blood (1.0 mL of heart blood, 0.5 mL of femoral blood) as well as homogenized liver, lung, and brain tissue (cerebrum) specimens (1:5 with H₂O; 0.5 mL each) were mixed with 1.0 mL of potassium dihydrogen phosphate (pH 6) and 50 μ L of morphine-D3 (2 μ g/mL; LGC, Wesel, Germany), respectively. After vortexing, the specimens were centrifuged at 3200g for 8 min and loaded to the cartridges. Subsequently, two washing steps with 1.5 mL of potassium dihydrogen phosphate (pH 6) and 3 mL of hydrochloric acid (0.01 M) were applied. After adding 1.5 mL of methanol, the columns were dried under maximum vacuum for 2 min. Analyte elution was then performed with 1.75 mL of dichloromethane/methanol/ammonia (30/15/1.5, v/v/v). The eluates were evaporated under a stream of nitrogen at 45 °C. The dry residues were dissolved in 100 μ L of pentafluoropropionic acid and 75 μ L of pentafluoropropanol and incubated for

45 min at 60 °C. Then, the derivatized extracts were evaporated under a stream of nitrogen at 45 °C and reconstituted in 30 μ L of ethyl acetate. The extracts were analyzed by GC-MS (GC: AT 6890; MS: AT 5973 N) using an Optima 1 MS column (Macherey-Nagel, Duren, Germany) and the following temperature gradient: 70 °C kept for 1.5 min, increase up to 220 °C (30 °C/min), then increase up to 285 °C (8 °C/min), and further increase up to 315 °C (30 °C/min), kept for 12.37 min. The limit of detection of the validated method was calculated as 0.9 ng/mL, the limit of quantification as 2.2 ng/mL, and the calibration ranged from 5 to 200 ng/mL.

The supposedly replaced tablets delivered by the daughter were macerated in ethanol and analyzed by GC-MS (GC: AT 5890; MS: AT 5972) in scan mode (with and without acetylation).

PBPK modeling

PBPK modeling and subsequent simulations were performed in a stepwise procedure. First, i.v. models of morphine and morphine-6-glucuronide were developed. Second, the previously developed models of morphine and morphine-6-glucuronide were coupled in a parent-metabolite PBPK model. Finally, the coupled PBPK was applied to (i) suggest which dosing unit ("mg" or "mL") appeared more likely, (ii) assess whether the analytically determined morphine concentrations could be explained by the clinically documented morphine administration, and (iii) explore potential physiological and mechanistic reasons that could explain the documented morphine concentrations.

Experimental datasets from two published clinical studies were used to support the PBPK model development and evaluation (Table 3). The experimental datasets were split into an internal development dataset ($n = 1$ trial) and an external

Table 3 Clinical study data of morphine

Route of administration	M dose (mg)	M6G dose (mg)	Dosing schedule	Matrix	Measured compound	n	Male patients (%)	Age mean (range) (years)	Internal (in) or external (ex) dataset	Ref.
i.v. bolus	5.64	1.0	sd	Plasma	M, M6G, M + M6G	8	50	26 (23–30)	in	[16]
i.v. inf. 20 min	7.59	—	sd	Plasma	M + M6G	14	79	(20–39)	ex	[41]

i.v. intravenous, inf infusion, sd single dose, M morphine measured only, M6G morphine-6-glucuronide measured only, M + M6G morphine and morphine-6-glucuronide measured after morphine dosing

Table 4 Physicochemical and ADME (absorption, distribution, metabolism, excretion) parameters of morphine and morphine-6-glucuronide

Parameter	Unit	Literature value	Ref.	Value used for simulations	Parameter description
Morphine					
MW	g/mol	285.34	—	285.34	Molecular weight
logP	—	0.9	[37]	0.9	Lipophilicity
fu (%)	(%)	65	[38]	65	Fraction unbound
pKa	—	8.21	a	8.21	Acid dissociation constant
Solubility	mg/L	149.0	a	149.0	Solubility
CL _{UGT 2B7}	L/min	4.6	[25, 39]	1.47	Intrinsic UGT 2B17 clearance
CL _{CYP 3A4}	L/min	22.7	[18, 25]	0.64	Intrinsic CYP 3A4 clearance
GFR fraction	—	—	—	1	b
P _{cell}	dm/min		[PK-Sim]	7.82E-5	Cellular permeability
Morphine-6-glucuronide					
MW	g/mol	461.50	—	461.50	Molecular weight
logP	—	0.79	[40]	0.79	Lipophilicity
fu (%)	(%)	83	[40]	83	Fraction unbound
pKa	—	8.22	[40]	8.22	Acid dissociation constant
Solubility	mg/mL	9.19	a	9.19	Solubility
GFR fraction	—	—	—	1	b
TS _{kidney}	L/min	1.14	[40]	0.35	Tubular secretion
P _{cell}	dm/min		[PK-Sim]	1.84E-6	Cellular permeability

^a Information obtained from DrugBank (<http://www.drugbank.ca>)

^b Fraction of glomerular filtration rate (GFR) used for passive renal elimination

evaluation dataset ($n = 1$), such that morphine and its major metabolite morphine-6-glucuronide were covered. The PBPK model was fitted to the development dataset, and the prediction quality of the model was assessed by predicting the evaluation dataset. Parameter optimizations were carried out using a Monte-Carlo method.

Model evaluation was carried out using (i) comparison of observed and simulated PK parameters and the fraction of morphine dose excreted unchanged into urine and (ii) visual predictive checks, which is a tool for evaluating the performance of PK and pharmacodynamic models, where percentiles of experimental and simulated data are compared [26].

Simulations were carried out using virtual PBPK individuals and populations. Virtual PBPK populations were created as described by Willmann and co-workers using ranges for age, height, and weight reported in the internal and external datasets [27]. In this approach, the organ weights and the cardiac output (CO) of a target individual are allometrically scaled with height and the organ blood flows are scaled to the total CO [27]. Applied dosing schedules and doses were used as published. The parameters of anatomy and physiology were varied as pre-defined in PK-Sim [28–31].

PBPK simulations were carried out using PK-Sim and MoBi (Version 5.6.5, Bayer Technology Services, Leverkusen, Germany). Statistical analyses of the results and graphics were compiled using MATLAB (Version R2013b, The MathWorks Inc., Natick, MA, USA).

i.v. concentration-time profiles were used to establish PBPK models of morphine and morphine-6-glucuronide. The

partition coefficients of both compounds were calculated using the PK-Sim standard model, and the cellular permeabilities were fitted [32, 33]. The reference concentrations of CYP3A4 and UGT2B7 were kept at the PK-Sim default values of 1 $\mu\text{mol}/\text{L}$, respectively, and the metabolic reactions were modeled as first-order processes. The PK-Sim gene expression database was used to distribute the enzymes to the specific organs [34, 35]. The unbound morphine was assumed to be filtered and excreted with the glomerular filtration rate (GFR). The unbound morphine-6-glucuronide was assumed to be eliminated solely by the kidney. This elimination consisted of filtration via the GFR and an additional tubular secretion that was modeled and fitted as a first-order process [36].

In the PBPK model, morphine was always administered as the free base; hence, the morphine sulfate or hydrochloride trihydrate doses stated in the clinical study publications were converted to the free base.

Results

Toxicological analyses

The EIA analysis tested positive for opiates. GC-MS and LC-MS/MS screenings revealed the presence of propofol, ketamine, and a metabolite of metamizole in blood and urine. No oxycodone could be detected in heart blood. The concentrations of free morphine amounted to approximately 3 and 5 mg/L in femoral and heart blood, respectively, to 2, 7, and 10 mg/kg morphine in brain, liver, and lung tissue. In the

supposedly replaced tablets, delivered by the daughter, no central nervous acting or diuretic drugs could be detected.

PBPK modeling

The final model parameters on the absorption, distribution, metabolism, and excretion of morphine and its metabolite morphine-6-glucuronide are shown in Table 4. The morphine and the morphine-6-glucuronide PBPK models were able to describe and predict the internal (Fig. 1a–c) and external (Fig. 1d) model development datasets. The simulated fraction of the administered i.v. dose of morphine excreted unchanged into urine was 6% which is in close agreement with the literature value of 5% [40]. The simulated and observed half-lives of morphine (predicted 2 h, observed 1.9 h [16, 41]) and morphine-6-glucuronide (predicted 1.5 h, observed 1.2 h [16]) were also in close agreement. The area under the curve (0—infinity) of morphine-6-glucuronide formed from administered i.v. morphine could be well predicted (predicted 277 nmol/L h⁻¹, observed 248 nmol/L h⁻¹ [16]).

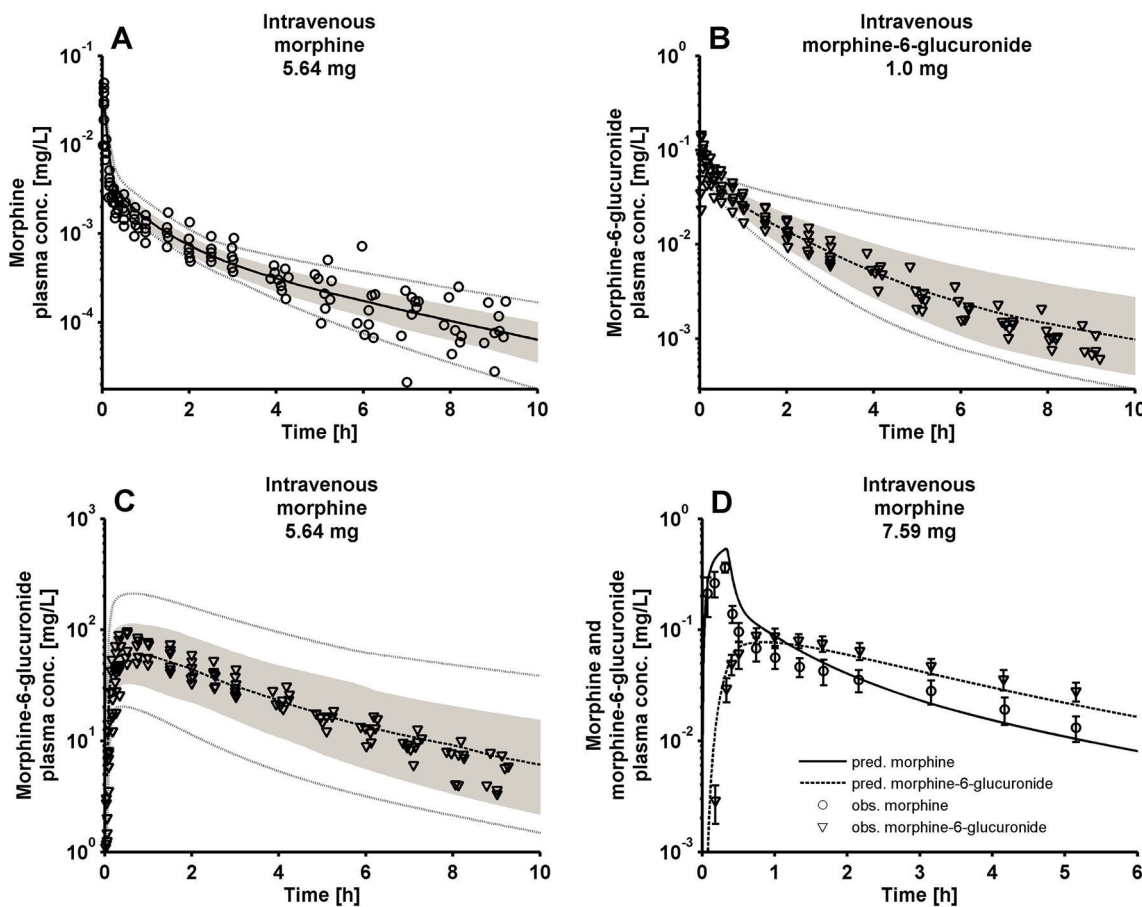
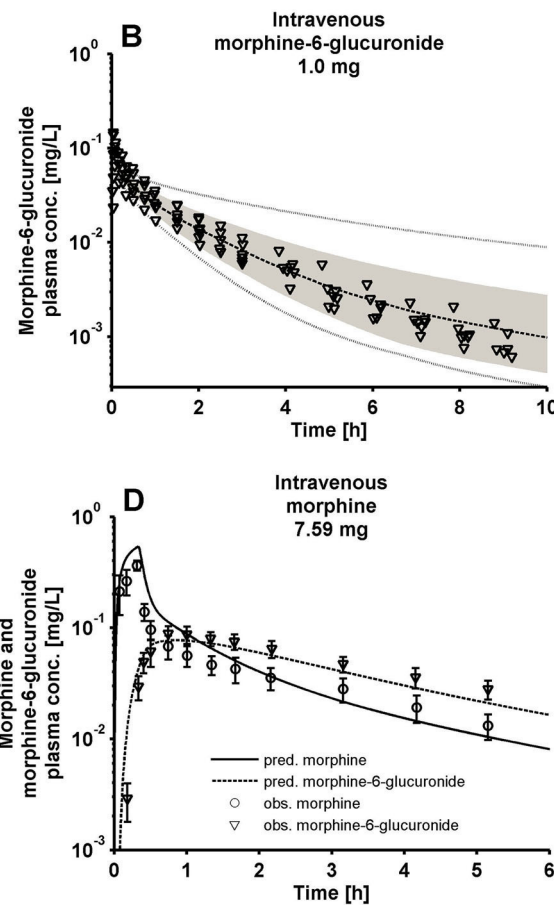


Fig. 1 **a** Morphine concentration-time profile [16]. **b** Morphine-6-glucuronide concentration-time profile [16]. **c** Morphine-6-glucuronide formation after intravenous morphine dose [16]. **d** Morphine concentration-time profile and morphine-6-glucuronide formation [41].

Assuming the dosing unit “mL” led to threefold higher morphine concentrations than the “mg” dosing, however, the coupled PBPK model underestimated the observed morphine concentrations irrespective of the applied dosing unit (Fig. 2).

Renal clearance was disabled after 26 h of the simulation because the patient was anuric from that time point on. Hence, the predicted morphine concentrations increased but did not match the observed concentrations (Fig. 3a, c). Disabling additionally the metabolism of morphine improved the model performance (Fig. 3b, d). Providing these conditions, the predicted femoral model concentration (2.9 mg/L) matched the observed femoral morphine concentration (3.0 mg/L). Nevertheless, the model underestimated the concentrations of morphine in heart blood as well as in brain, liver, and lung tissue (Fig. 3c, d). The predicted free morphine concentrations for heart blood, brain, liver, and lung were 2.9 mg/L, 0.82 mg/kg, 2.1 mg/kg, and 2.5 mg/kg, respectively, whereas the observed concentrations were 5.1 mg/L, 2.6 mg/kg, 10 mg/kg, and 7.8 mg/kg, respectively.



Simulated data are represented as median (black lines), 90% prediction interval (gray-shaded area), and minimum and maximum values (dotted lines). Observed data are presented as circles and triangles

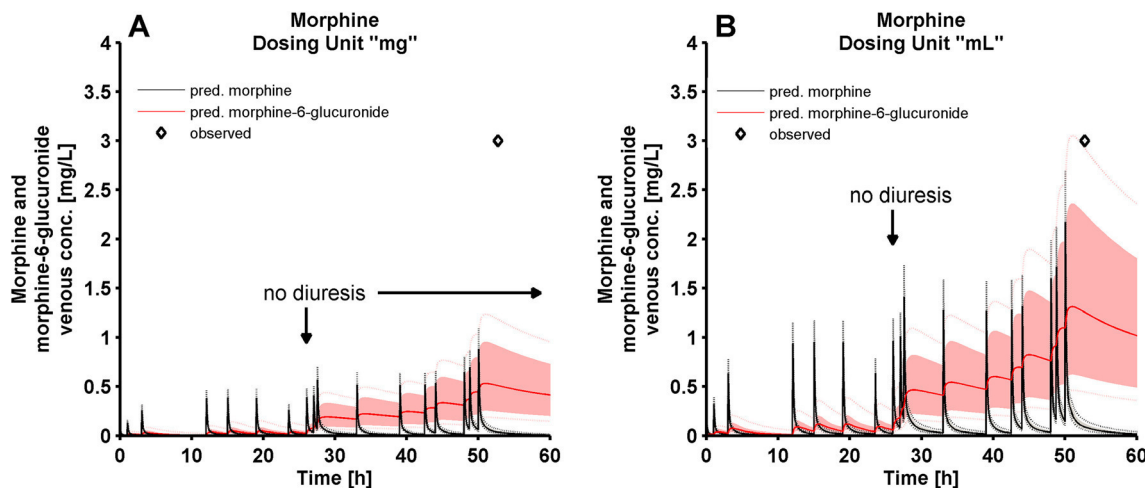


Fig. 2 The impact of switching dosing units (“mg” or “mL”) on morphine concentrations following repeated morphine administrations. Morphine (black) and morphine-6-glucuronide (red) concentration-time profiles after multiple intravenous morphine doses with regard to the

documented doses **a** in “mg” and **b** in “mL.” Simulated data are represented as median (black line: morphine, red line: morphine-6-glucuronide), 90% prediction interval (shaded areas), and minimum and maximum values (dotted lines)

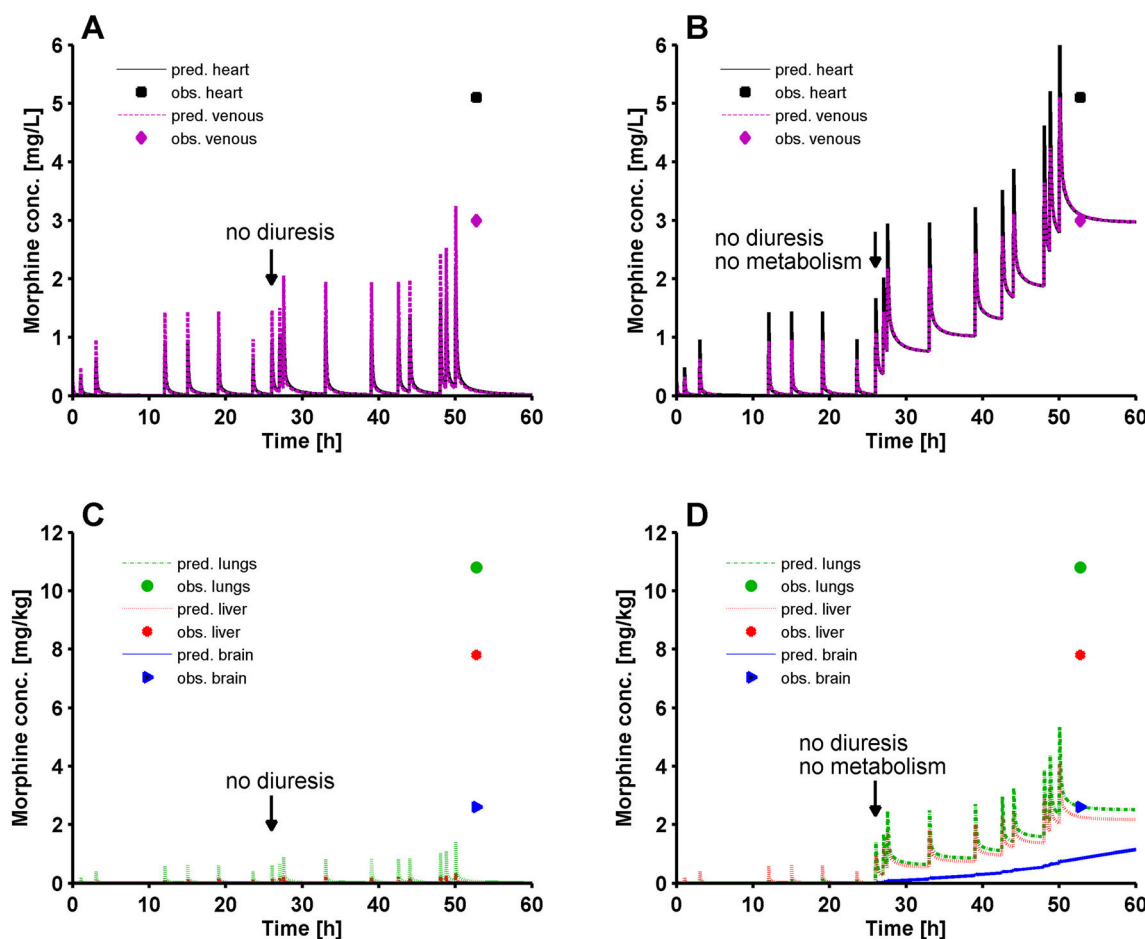


Fig. 3 The impact of disabled renal clearance and/or metabolism on morphine concentrations following repeated morphine administrations. **a, b** Simulation of morphine concentrations in heart (black) and veins (purple). **c, d** Simulation of morphine concentrations in brain (blue), liver

(red), and lung (green) tissue. Simulations were carried out applying repeated morphine administrations with regard to the documented doses (assuming “mL” dosing)

Discussion

The therapeutic morphine blood concentrations are within 0.01–0.1 mg/L [42]. The quantified free morphine concentrations in both femoral and heart blood were present in toxic concentrations of 3.0 and 5.1 mg/L, respectively [42], and have been detected in morphine- or heroin-related deaths [43]. However, in the treatment of cancer pain, morphine administration (dosing amount, dosing interval) is often individually adjusted for each patient [44]. In this context, intravenously administered morphine resulted in blood concentrations of 1.59–11.4 mg/L [45]. It is important to notice that the PK of high-dose morphine is similar to smaller doses [46].

Regarding the two possible dosing units “mg” and “mL,” the mg dosing did not fit the analytical results, as the simulation applying the developed PBPK model yielded threefold lower concentrations than the mL dosing. Hence, the PBPK model simulations are in favor of the mL dosing. Nevertheless, even assuming an administration of morphine in mL, the predicted morphine concentrations did not match the observed concentrations either. To explore physiological explanations for the underprediction of the model, firstly, a renal failure was assumed during agony as indicated by anuresis 1 day before death. Thus, a simulation by disabling renal elimination was performed, but the observed morphine concentrations were still underestimated. One reason could be that only a negligible amount of morphine is glomerularly filtrated and excreted into urine [47]. However, a possible agonal renal failure could have resulted in increasing uremic toxin blood concentrations, which could have led to an impaired morphine glucuronidation [48, 49]. Morphine is converted to its main metabolites morphine-3-glucuronide and morphine-6-glucuronide by uridine 5'-diphospho-glucuronosyltransferase-mediated glucuronidation in the liver [50]. In hepatically impaired patients, the action of these metabolizing enzymes might be decreased as well as hepatic blood flow leading to an accumulation of the parent compound [22, 23]. Hence, secondly, simulating a hepatorenal syndrome by disabling renal and hepatic clearance finally resulted in good correspondence of the predicted and the observed morphine concentration in femoral blood. However, the calculated concentration in heart blood as well as the tissue concentrations were underestimated using the PBPK model. To explain this discrepancy, postmortem changes have to be taken into consideration as an important issue. After death, processes such as cell lysis are initiated that can alter blood and tissue concentrations of a drug depending on its physicochemical properties [6]. Morphine is known to underlie this so-called postmortem redistribution (PMR [51]). Increases of 0.4–240% (median 44%) of the initial morphine concentration were observed in postmortem blood samples depending on various postmortem intervals. In heart blood concentration changes of –5–680% (median 37%), in liver changes of –100–160% (median –3.1%), and in lung tissue ranges from –100 to 300% (median –8.6%)

were detected [51]. Besides that, heart blood/femoral blood ratios averaged 1.2 and 2.2 in a series of different cases [43]. Considering a postmortem interval of 6 days, PMR of morphine might be a plausible explanation for the higher concentrations observed in heart blood and tissues.

The PBPK prediction performance for heart blood and tissues could not be tested in living human subjects, hence the morphine concentrations might not be captured correctly in the living which subsequently adds uncertainty to the postmortem predictions. Due to the fact that data concerning PBPK modeling on the basis of postmortem tissue specimens are sparse and to obtain first knowledge, it has been tested whether the model also predicted the measured morphine concentrations in tissue samples. Therefore, future research should include widened assessment and consideration of (patho)physiological parameters and postmortem changes in order to improve the modeling performance.

In addition, morphine-6-glucuronide as well as morphine-3-glucuronide have been tested to be unstable when stored above –20 °C [52]. Thus, the higher free morphine concentrations might also be a result of degradation of the glucuronides.

Morphine was modeled in dependence on age-related changes in liver size and hepatic blood flow only. Liver size declines with 6.1% per decade after the age of 40 followed by a more rapid loss of 11.4% per decade after the age of 60 [53]. The hepatic blood flow in males decreases from 423.0 mL/min at the age of 30 to 141.6 mL/min at the age of 100 [7]. As a result, the terminal half-life of morphine after intravenous administration was reported to be 2.7 ± 3.6 h [54], which is 40% higher than the reported half-life in adult (1.9 h). However, these age-dependent changes in liver size and hepatic blood flow were not implemented, because the PBPK model results are independent of these changes when the hepatic clearance was disabled (Fig. 3b, d). In addition, implementing the physiological and anatomical changes in the elderly does not impact the predictive performance of the morphine model in a meaningful manner even if the hepatic clearance is active [7].

Although PMR, the chemical instability of the morphine glucuronides, and age-related changes in liver size and hepatic blood flow were not specifically implemented, the PBPK model offers a mechanistic explanation for the toxic morphine concentrations, namely, the physiologically plausible severe renal and hepatic impairment in this patient. Thus, the PBPK modeling results argue against the notion of a morphine overdose being the only eligible cause of the toxic morphine concentrations.

In the context of this specific case, there are further uncertainties remaining. In general, due to the abovementioned postmortem changes, one may argue whether it is adequate to compare model predictions of the concentrations at the time point of death with concentrations in specimens obtained

6 days after. Furthermore, there was no reliable information on the renal function until death leading to the question, if it is justified to suppose that there is no renal elimination when there is no diuresis. In addition, no information on liver function was available. It remains therefore questionable, whether it is appropriate to presume that there is no morphine metabolism when there is no diuresis. Finally, it has to be kept in mind that morphine-6-glucuronide is pharmacologically active. Thus, in renally impaired patients, a prolonged elimination of this metabolite can lead to additional severe adverse effects [55].

Apart from these issues, with respect to the cause of death, the question arose whether an accidental or intentional dosing error might have been responsible for a potential lethal morphine concentration. To answer this question, recommendations about palliative therapy regimes have to be taken into account. Before establishing an i.v. therapy with morphine on therapy day 2, oxycodone was orally administered in a dose of 15 mg/day on therapy day 1 and 20 mg/day on therapy day 2 (Table 1). The equianalgesic dose of intravenously administered morphine corresponds to 10 mg/day [56]. As documented in the clinical records (Table 1), the daily dose of morphine amounted to 28 mg (assuming an administration in "mL") on therapy day 1 and was continuously increased to 260 mg on therapy day 4 due to progressive pain. According to literature, doses of morphine in the range administered in the present case—assuming an administration in mL—may be medically indicated in the treatment of severe pain [55, 57] and are also tolerated in individual cases. Nevertheless, it has to be kept in mind that elderly patients may be more sensitive to morphine and that its PK can be altered in this particular population due to (patho)physiological changes associated with aging [50]. At last, signs of a morphine intoxication, such as respiratory depression, coma, bradycardia, and urinary retention might have been disguised by the fact that the patient was intubated/under anesthesia and in a prefinal state.

Considering the autopic and forensic toxicological findings in combination with the results of the PBPK modeling, the cause of death was a cardiovascular failure due to pre-existing cardiovascular pathology and pneumonia following a fall, fracture of femur neck, and immobilization, accompanied by a high and potentially toxic morphine concentration, attributable to the administration under the condition of palliative care.

Conclusion

In this case study, the PBPK model simulations argue against a suspected morphine overdose administered to a 98-year-old patient by demonstrating that disease-related, physiological changes in organ functions are a plausible explanation for the analytically determined toxic morphine concentrations in

various specimens. PBPK modeling and simulation might qualify as a quantitative in silico tool suited to develop hypotheses for forensic questions in the context of a potential overdosing (e.g., of morphine). Perspectively, future research should include widened assessment and consideration of (patho)physiological parameters and postmortem changes as well as dynamic implementations of disease- and age-related physiological changes in order to improve analogous modeling of further pharmaceuticals and drugs of abuse.

References

1. Lötsch J (2005) Pharmacokinetic–pharmacodynamic modeling of opioids. *J Pain Symptom Manag* 29(5, Supplement):90–103. <https://doi.org/10.1016/j.jpainsympman.2005.01.012>
2. Altamura AC, Moliterno D, Paletta S, Maffini M, Mauri MC, Bareggi S (2013) Understanding the pharmacokinetics of anxiolytic drugs. *Expert Opin Drug Metab Toxicol* 9(4):423–440. <https://doi.org/10.1517/17425255.2013.759209>
3. Schaefer N, Wojtyniak J-G, Kettner M, Schlotte J, Laschke MW, Ewald AH, Lehr T, Menger MD, Maurer HH, Schmidt PH (2016) Pharmacokinetics of (synthetic) cannabinoids in pigs and their relevance for clinical and forensic toxicology. *Toxicol Lett* 253:7–16. <https://doi.org/10.1016/j.toxlet.2016.04.021>
4. Marsot A, Audebert C, Attolini L, Lacarelle B, Micallef J, Blin O (2017) Population pharmacokinetics model of THC used by pulmonary route in occasional cannabis smokers. *J Pharmacol Toxicol Methods* 85:49–54. <https://doi.org/10.1016/j.vascn.2017.02.003>
5. Dubois N, Hallet C, Seidel L, Demaret I, Luppens D, Ansseau M, Rozet E, Albert A, Hubert P, Charlier C (2015) Estimation of the time interval between the administration of heroin and the sampling of blood in chronic inhalers. *J Anal Toxicol* 39(4):300–305. <https://doi.org/10.1093/jat/bkv001>
6. Cook DS, Braithwaite RA, Hale KA (2000) Estimating antemortem drug concentrations from postmortem blood samples: the influence of postmortem redistribution. *J Clin Pathol* 53(4):282–285. <https://doi.org/10.1136/jcp.53.4.282>
7. Schlender J-F, Meyer M, Thelen K, Krauss M, Willmann S, Eissing T, Jaehde U (2016) Development of a whole-body physiologically based pharmacokinetic approach to assess the pharmacokinetics of drugs in elderly individuals. *Clin Pharmacokinet* 55(12):1573–1589. <https://doi.org/10.1007/s40262-016-0422-3>
8. Alqahtani S, Kaddoumi A (2015) Development of physiologically based pharmacokinetic/pharmacodynamic model for indometacin disposition in pregnancy. *PLoS One* 10(10):e0139762. <https://doi.org/10.1371/journal.pone.0139762>
9. Mahmood I, Ahmad T, Mansoor N, Sharib SM (2017) Prediction of clearance in neonates and infants (≤ 3 months of age) for drugs that are glucuronidated: a comparative study between allometric scaling and physiologically based pharmacokinetic modeling. *J Clin Pharmacol* 57(4):476–483. <https://doi.org/10.1002/jcpp.837>
10. Sager JE, Yu J, Ragueneau-Majlessi I, Isoherranen N (2015) Physiologically based pharmacokinetic (PBPK) modeling and simulation approaches: a systematic review of published models, applications, and model verification. *Drug Metab Dispos* 43(11):1823–1837. <https://doi.org/10.1124/dmd.115.065920>
11. Workgroup EM, Marshall SF, Burghaus R, Cosson V, Cheung SYA, Chenel M, DellaPasqua O, Frey N, Hamré B, Harnisch L, Ivanow F, Kerbusch T, Lippert J, Milligan PA, Rohou S, Staab A, Steimer JL, Tornøe C, Visser SAG (2016) Good practices in model-

- informed drug discovery and development: practice, application, and documentation. *CPT: Pharmacometrics Syst Pharmacol* 5(3): 93–122. <https://doi.org/10.1002/psp4.12049>
12. Jones HM, Rowland-Yeo K (2013) Basic concepts in physiologically based pharmacokinetic modeling in drug discovery and development. *CPT: Pharmacometrics Syst Pharmacol* 2(8):1–12. <https://doi.org/10.1038/psp.2013.41>
 13. Tsamandouras N, Rostami-Hodjegan A, Aarons L (2015) Combining the ‘bottom up’ and ‘top down’ approaches in pharmacokinetic modelling: fitting PBPK models to observed clinical data. *Br J Clin Pharmacol* 79(1):48–55. <https://doi.org/10.1111/bcp.12234>
 14. Nestorov I (2007) Whole-body physiologically based pharmacokinetic models. *Expert Opin Drug Metab Toxicol* 3(2):235–249. <https://doi.org/10.1517/17425255.3.2.235>
 15. National Guideline C (2012) Opioids in palliative care: safe and effective prescribing of strong opioids for pain in palliative care of adults
 16. Lötsch J, Skarke C, Schmidt H, Liebold J, Geisslinger G (2002) Pharmacokinetic modeling to predict morphine and morphine-6-glucuronide plasma concentrations in healthy young volunteers. *Clin Pharmacol Ther* 72(2):151–162. <https://doi.org/10.1067/mcp.2002.126172>
 17. Ing Lorenzini K, Daali Y, Dayer P, Desmeules J (2012) Pharmacokinetic–pharmacodynamic modelling of opioids in healthy human volunteers. A MiniReview. *Basic Clin Pharmacol Toxicol* 110(3):219–226. <https://doi.org/10.1111/j.1742-7843.2011.00814.x>
 18. Projean D, Morin PE, Tu TM, Ducharme J (2003) Identification of CYP3A4 and CYP2C8 as the major cytochrome P450s responsible for morphine N-demethylation in human liver microsomes. *Xenobiotica* 33(8):841–854. <https://doi.org/10.1080/0049825031000121608>
 19. Stone AN, Mackenzie PI, Galetin A, Houston JB, Miners JO (2003) Isoform selectivity and kinetics of morphine 3- and 6-glucuronidation by human UDP-glucuronosyltransferases: evidence for atypical glucuronidation kinetics by UGT2B7. *Drug Metab Dispos* 31(9):1086–1089. <https://doi.org/10.1124/dmd.31.9.1086>
 20. Mazoit JX, Butscher K, Samii K (2007) Morphine in postoperative patients: pharmacokinetics and pharmacodynamics of metabolites. *Anesth Analg* 105(1):70–78. <https://doi.org/10.1213/01.ane.0000265557.73688.32>
 21. Oosten AW, Abrantes JA, Jönsson S, Matic M, van Schaik RHN, de Brujin P, van der Rijt CCD, Mathijssen RHJ (2016) A prospective population pharmacokinetic study on morphine metabolism in cancer patients. *Clin Pharmacokinet* :1–14. doi:<https://doi.org/10.1007/s40262-016-0471-7>
 22. Tegeder I, Lötsch J, Geisslinger G (1999) Pharmacokinetics of opioids in liver disease. *Clin Pharmacokinet* 37(1):17–40. <https://doi.org/10.2165/00003088-199937010-00002>
 23. Hasselstrom J, Eriksson S, Persson A, Rane A, Svensson J, Sawe J (1990) The metabolism and bioavailability of morphine in patients with severe liver cirrhosis. *Br J Clin Pharmacol* 29(3):289–297. <https://doi.org/10.1111/j.1365-2125.1990.tb03638.x>
 24. Franken LG, de Winter BCM, van Esch HJ, van Zuylen L, Baar FPM, Tibboel D, Mathôt RAA, van Gelder T, Koch BCP (2016) Pharmacokinetic considerations and recommendations in palliative care, with focus on morphine, midazolam and haloperidol. *Expert Opin Drug Metab Toxicol* 12(6):669–680. <https://doi.org/10.1080/17425255.2016.1179281>
 25. Achour B, Russell MR, Barber J, Rostami-Hodjegan A (2014) Simultaneous quantification of the abundance of several cytochrome P450 and uridine 5'-diphospho-glucuronosyltransferase enzymes in human liver microsomes using multiplexed targeted proteomics. *Drug Metab Dispos* 42(4):500–510. <https://doi.org/10.1124/dmd.113.055632>
 26. Post TM, Freijer JI, Ploeger BA, Danhof M (2008) Extensions to the visual predictive check to facilitate model performance evaluation. *J Pharmacokinet Pharmacodyn* 35(2):185–202. <https://doi.org/10.1007/s10928-007-9081-1>
 27. Willmann S, Hohn K, Edginton A, Sevestre M, Solodenko J, Weiss W, Lippert J, Schmitt W (2007) Development of a physiology-based whole-body population model for assessing the influence of individual variability on the pharmacokinetics of drugs. *J Pharmacokinet Pharmacodyn* 34(3):401–431. <https://doi.org/10.1007/s10928-007-9053-5>
 28. Claassen K, Thelen K, Coboeken K, Gaub T, Lippert J, Allegaert K, Willmann S (2015) Development of a physiologically-based pharmacokinetic model for preterm neonates: evaluation with in vivo data. *Curr Pharm Des* 21(39):5688–5698. <https://doi.org/10.2174/138161281666150901110533>
 29. Willmann S, Becker C, Burghaus R, Coboeken K, Edginton A, Lippert J, Siegmund H-U, Thelen K, Mück W (2014) Development of a paediatric population-based model of the pharmacokinetics of rivaroxaban. *Clin Pharmacokinet* 53(1):89–102. <https://doi.org/10.1007/s40262-013-0090-5>
 30. Thelen K, Coboeken K, Willmann S, Burghaus R, Dressman JB, Lippert J (2011) Evolution of a detailed physiological model to simulate the gastrointestinal transit and absorption process in humans, part 1: oral solutions. *J Pharm Sci* 100(12):5324–5345. <https://doi.org/10.1002/jps.22726>
 31. Thelen K, Coboeken K, Willmann S, Dressman JB, Lippert J (2012) Evolution of a detailed physiological model to simulate the gastrointestinal transit and absorption process in humans, part II: extension to describe performance of solid dosage forms. *J Pharm Sci* 101(3):1267–1280. <https://doi.org/10.1002/jps.22825>
 32. Willmann S, Lippert J, Schmitt W (2005) From physicochemistry to absorption and distribution: predictive mechanistic modelling and computational tools. *Expert Opin Drug Metab Toxicol* 1(1): 159–168. <https://doi.org/10.1517/17425255.1.1.159>
 33. Willmann S, Lippert J, Sevestre M, Solodenko J, Fois F, Schmitt W (2003) PK-Sim®: a physiologically based pharmacokinetic ‘whole-body’ model. *Biosilico* 1(4):121–124. [https://doi.org/10.1016/S1478-5382\(03\)02342-4](https://doi.org/10.1016/S1478-5382(03)02342-4)
 34. Meyer M, Schneckener S, Ludewig B, Kuepfer L, Lippert J (2012) Using expression data for quantification of active processes in physiologically based pharmacokinetic modeling. *Drug Metab Dispos* 40(5):892–901. <https://doi.org/10.1124/dmd.111.043174>
 35. Wheeler DL, Church DM, Federhen S, Lash AE, Madden TL, Pontius JU, Schuler GD, Schriml LM, Sequeira E, Tatusova TA, Wagner L (2003) Database resources of the National Center for Biotechnology. *Nucleic Acids Res* 31(1):28–33. <https://doi.org/10.1093/nar/gkg033>
 36. Hasselstrom J, Sawe J (1993) Morphine pharmacokinetics and metabolism in humans. Enterohepatic cycling and relative contribution of metabolites to active opioid concentrations. *Clin Pharmacokinet* 24(4):344–354. <https://doi.org/10.2165/00003088-199324040-00007>
 37. Avdeef A, Barrett DA, Shaw PN, Knaggs RD, Davis SS (1996) Octanol–, chloroform–, and propylene glycol dipelargonate–water partitioning of morphine-6-glucuronide and other related opiates. *J Med Chem* 39(22):4377–4381. <https://doi.org/10.1021/jm960073m>
 38. Olsen GD, Bennett WM, Porter GA (1975) Morphine and phenytoin binding to plasma proteins in renal and hepatic failure. *Clin Pharmacol Ther* 17(6):677–684. <https://doi.org/10.1002/cpt1975176677>
 39. Chau N, Elliot DJ, Lewis BC, Burns K, Johnston MR, Mackenzie PI, Miners JO (2014) Morphine glucuronidation and glucosidation represent complementary metabolic pathways that are both catalyzed by UDP-glucuronosyltransferase 2B7: kinetic, inhibition,

- and molecular modeling studies. *J Pharmacol Exp Ther* 349(1): 126–137. <https://doi.org/10.1124/jpet.113.212258>
40. Eissing T, Lippert J, Willmann S (2012) Pharmacogenomics of codeine, morphine, and morphine-6-glucuronide: model-based analysis of the influence of CYP2D6 activity, UGT2B7 activity, renal impairment, and CYP3A4 inhibition. *Mol Diagn Ther* 16(1):43–53. <https://doi.org/10.2165/11597930-00000000-00000>
 41. Westerling D, Persson C, Hoglund P (1995) Plasma concentrations of morphine, morphine-3-glucuronide, and morphine-6-glucuronide after intravenous and oral administration to healthy volunteers: relationship to nonanalgesic actions. *Ther Drug Monit* 17(3):287–301. <https://doi.org/10.1097/00007691-199506000-00013>
 42. Schulz M, Iwersen-Bergmann S, Andresen H, Schmoldt A (2012) Therapeutic and toxic blood concentrations of nearly 1,000 drugs and other xenobiotics. *Crit Care* 16(4):R136–R136. <https://doi.org/10.1186/cc11441>
 43. Baselt, R.C., Cravey RH (2014). In: Disposition of toxic drugs and chemicals in man, 10th edition. Biomedical Publications, Seal Beach, California (USA), pp 1399–1403
 44. Blinderan CD, Billings JA (2015) Comfort care for patients dying in the hospital. *N Engl J Med* 373(26):2549–2561. <https://doi.org/10.1056/NEJMra1411746>
 45. Lee YJ, Suh S-Y, Song J, Lee SS, Seo A-R, Ahn H-Y, Lee MA, Kim C-M, Klepstad P (2015) Serum and urine concentrations of morphine and morphine metabolites in patients with advanced cancer receiving continuous intravenous morphine: an observational study. *BMC Palliat Care* 14(1):53. <https://doi.org/10.1186/s12904-015-0052-9>
 46. Stanski DR, Greenblatt DJ, Lappas DG, Weser JK, Lowenstein E (1976) Kinetics of high-dose intravenous morphine in cardiac surgery patients. *Clin Pharm Ther* 19(6):752–756. <https://doi.org/10.1002/cpt.1976196752>
 47. Chauvin M, Sandouk P, Scherrmann J, Farinotti R, Strumza P, Duvaldestin P (1987) Morphine pharmacokinetics in renal failure. *Anesthesiology* 66(3):327–331. <https://doi.org/10.1097/00000542-198703000-00011>
 48. Barnes KJ, Rowland A, Polasek TM, Miners JO (2014) Inhibition of human drug-metabolising cytochrome P450 and UDP-glucuronosyltransferase enzyme activities in vitro by uremic toxins. *Eur J Clin Pharmacol* 70(9):1097–1106. <https://doi.org/10.1007/s00228-014-1709-7>
 49. Nolin TD, Naud J, Leblond FA, Pichette V (2008) Emerging evidence of the impact of kidney disease on drug metabolism and transport. *Clin Pharmacol Ther* 83(6):898–903. <https://doi.org/10.1038/clpt.2008.59>
 50. Glare P, Walsh T (1991) Clinical pharmacokinetics of morphine. *Ther Drug Monit* 13(1):1–23. <https://doi.org/10.1097/00007691-199101000-00001>
 51. Staeheli SN, Gascho D, Ebert LC, Kraemer T, Steuer AE (2017) Time-dependent postmortem redistribution of morphine and its metabolites in blood and alternative matrices—application of CT-guided biopsy sampling. *Int J Legal Med* 131(2):379–389. <https://doi.org/10.1007/s00414-016-1485-2>
 52. Skopp G, Pötsch L, Klingmann A, Mattern R (2001) Stability of morphine, morphine-3-glucuronide, and morphine-6-glucuronide in fresh blood and plasma and postmortem blood samples. *J Anal Toxicol* 25(1):2–7. <https://doi.org/10.1093/jat/25.1.2>
 53. Meyer WW, Peter B, Solth K (1963) Die Organgewichte in den höheren Altersstufen (70–92 Jahre) in ihrer Beziehung zum Alter und Körpergewicht. *Virchows Arch Pathol Anat Physiol Klin Med* 337(1):17–32. <https://doi.org/10.1007/bf00965815>
 54. Villesen HH, Banning A-M, Petersen RH, Weinelt S, Poulsen JB, Hansen SH, Christrup LL (2007) Pharmacokinetics of morphine and oxycodone following intravenous administration in elderly patients. *Ther Clin Risk Manag* 3(5):961–967
 55. Tiseo PJ, Thaler HT, Lapin J, Inturrisi CE, Portenoy RK, Foley KM (1995) Morphine-6-glucuronide concentrations and opioid-related side effects: a survey in cancer patients. *Pain* 61(1):47–54. [https://doi.org/10.1016/0304-3959\(94\)00148-8](https://doi.org/10.1016/0304-3959(94)00148-8)
 56. Indelicato RA, Portenoy RK (2002) Opioid rotation in the management of refractory cancer pain. *J Clin Oncol* 20(1):348–352. <https://doi.org/10.1200/jco.2002.20.1.348>
 57. Klepstad P, Hilton P, Moen J, Kaasa S, Borchgrevink PC, Zahlsen K, Dale O (2004) Day-to-day variations during clinical drug monitoring of morphine, morphine-3-glucuronide and morphine-6-glucuronide serum concentrations in cancer patients. A prospective observational study. *BMC Clin Pharmacol* 4(1):7–7. <https://doi.org/10.1186/1472-6904-4-7>

5 Conclusions

As of today, drug development and pharmacotherapy face a variety of challenges. Drug development is a longsome, complex, costly and risky process. To meet the rightly increasing ethical standards and regulatory expectations, tools to rationalize decision making during critical development steps are needed. Pharmacotherapy also tends to increase in complexity as it becomes clearer that the “one dose fits all” approach can lead to ineffective and unsafe drug therapies. To cope with the high variability in the PK, PD and PK/PD relationships of drugs due to differences in anatomy and physiology among children, adults and elderly patients and due to additional factors, such as genetics, co-medication, and diseases, ways of leveraging all the existing drug- and patient information are needed.

An emerging innovative mathematical tool to support drug development and pharmacotherapy is PBPK modeling and simulation. By integrating all available drug- and patient information, these complex models can be used to test hypotheses, waive clinical studies and to improve decision making.

In project I, a PBPK parent-metabolite model was developed to support the drug development for the new chemotherapeutic agent zoptarelin doxorubicin and its major metabolite doxorubicin. The model helped to rule out the potential of zoptarelin doxorubicin to act as an inhibitor of OATP1B3 and OCT2 by specific DDI simulations with simvastatin and metformin in worst-case scenarios and hence increased the confidence in moving the drug forward in the development process. In addition, not only did this project help to generate knowledge about an IND, but it also provided a new methodology to assess the general potential for transporter DDIs when a PBPK model is available for the perpetrator drug (e.g. zoptarelin doxorubicin) but not for the victim drugs. This approach helps to facilitate earlier DDI potential analyses in drug development.

5. CONCLUSIONS

In project II, the first coupled whole-body PBPK DDI model for clarithromycin, midazolam and digoxin was presented to support drug development and pharmacotherapy. For the first time, the tissue-specific mechanism-based inhibition of CYP3A4 in the intestine and the liver via clarithromycin was correctly described and successfully evaluated. This was accomplished by implementing a mechanism-based inhibition model of CAP3A4 into the MoBi software for the first time. This software enhancement was integrated into the software package and is now available for users of this software. Furthermore, this project showed the first successful tissue-specific competitive inhibition of digoxin transport by P-gp in the intestine and the kidney. The final PBPK DDI model of all three compounds was subsequently used to determine safe victim drug doses of midazolam and digoxin during clarithromycin treatment and thus provides rationally designed DDI management options to physicians and pharmacists.

Project III dealt with the development and application a PBPK/PD model for the chemotherapeutic agent vorinostat, a HDAC inhibitor, to support pharmacotherapy. The model was developed for adult and pediatric patients. As all relevant metabolic enzymes were incorporated in the final model, state-of-the-art PBPK fitting algorithms were used to determine the enzymatic contributions of the major enzymes to the total clearance of vorinostat. For pediatric patients maturation functions for all relevant enzymes were incorporated and subsequent dosing simulations identified important dosage reductions for very young children to avoid overdosing. This is a significant step towards safer future pediatric trials. Furthermore, the adult PBPK model was expanded by pharmacodynamic biomarker models of vorinostat, namely, the number of circulating thrombocytes and the HDAC inhibition in peripheral mononuclear cells. This again was accomplished by implementing these pharmacodynamic models into the MoBi software for the first time. This complex PBPK/PD model was finally used to determine potentially safer and more effective drug regimens for adults. Important new drug regimens were identified which

could be used in the future design of clinical trials in adults. As PBPK/PD models are often a neglected option in PBPK research, this case example may encourage other researchers to intensify their work in this area.

Finally, in project IV, a PBPK parent-metabolite model was developed for the pharmacotherapy with morphine and its metabolite morphine-6-glucuronide. In a forensic case study, this PBPK model helped to argue against a suspected morphine overdose administered to a 98-year-old patient by demonstrating that age- and disease-related changes in liver- and renal functions were a plausible explanation for the analytically determined toxic morphine concentrations. Project IV is the first attempt to use a PBPK model in the area of forensic science. Although the model developer could provide enough certainty in the model predictions to rule out the suspected morphine overdose, this modeling attempt also revealed major future research directions. Especially the so-called postmortem redistribution (PMR) and the decline in organ functions over time should be intensely investigated.

The presented projects span from drug development to pharmacotherapy and they nicely underline the translational character of the PBPK modeling and simulation approach. Furthermore, the results presented in this doctoral thesis did not only successfully overcome major obstacles in the field of PBPK research, but they provided sophisticated, data-driven and rational support for drug development and pharmacotherapy. The presented work contributed significantly to the overall undertaking to cut the time drug development takes as well as its costs and to offer more patient-specific and, at the same time, safer and more effective pharmacotherapies. The PBPK software PK-Sim and MoBi has been further developed providing the PBPK research community with a state-of-the-art foundation for further model development as all presented models are either directly available for download via the “Open Systems Pharmacology” community

5. CONCLUSIONS

(<https://github.com/Open-Systems-Pharmacology>) or easily re-built by the provided information in the project manuscripts.

6 Summary

The Physiologically-based Pharmacokinetic (PBPK) approach was successfully used within four projects to meet challenges in drug development and pharmacotherapy. Firstly, PBPK modeling and simulation revealed that the chemotherapeutic drug in development zoptarelvin doxorubicin has no drug-drug-interaction (DDI) potential. It decreases the organic anion-transporting polypeptide 1B3 (OAT1B3) and organic cation transporter 2 (OCT2) transport rates of metformin and simvastatin by only 0.5 and 2.5%, respectively. Secondly, to improve the DDI management during pharmacotherapy, the PBPK approach revealed that midazolam and digoxin doses should be reduced by 74 to 88% and by 21 to 22% during co-medication with 250 or 500 mg of clarithromycin (bid). Thirdly, pediatric and adult pharmacotherapy of vorinostat could be improved by specifying pediatric drug dosages of 80 and 230 mg/m² at the ages of 0-1 and 1-17 years and by specifying an effective and safe adult vorinostat dose of 3000 mg (tid). Finally, the PBPK approach helped to refuse a suspected morphine overdose by assessing the impact of an impaired hepatic and renal function on morphine. This doctoral thesis has successfully overcome major obstacles in PBPK research, enhanced existing PBPK software, helped to ease the drug development process and improved pharmacotherapy.

7 Zusammenfassung

Der Ansatz der Physiologie-basierten Pharmakokinetik (PBPK) wurde innerhalb von vier Projekten erfolgreich verwendet, um Herausforderungen in der Arzneimittelentwicklung und der Pharmakotherapie zu meistern. Erstens enthüllte die PBPK Modellierung und Simulation, dass das sich in Entwicklung befindliche Chemotherapeutikum Zoptarelin Doxorubicin keine Potenzial für Arzneimittelinteraktionen (DDI) aufweist. Es vermindert die organic anion-transporting polypeptide 1B3 (OAT1B3) und organic cation transporter 2 (OCT2) Transportraten von Metformin und Simvastatin um 0,5 und 2,5%. Zweitens wurde der Umgang mit DDI während der Pharmakotherapie verbessert. Der PBPK Ansatz konnte zeigen, dass die Dosierung von Midazolam und Digoxin während der Ko-medikation mit 250 oder 500 mg Clarithromycin (bid) um 74 bis 88% und 21 bis 22% reduziert werden sollte. Drittens konnte die pädiatrische und adulte Pharmakotherapie mit Vorinostat verbessert werden durch eine Dosisspezifikation für Kinder von 80 und 230 mg/m² im Alter von 0-1 und 1-17 Jahren und durch die Spezifikation einer sicheren und effektiven Dosis von 3000 mg (tid) für Erwachsene. Schließlich half der PBPK Ansatz, durch Simulation des Effekts einer Leber- und Nierenfunktionsstörung auf die Morphin Pharmakokinetik, eine vermutete Morphinüberdosierung zurückzuweisen. Diese Dissertation hat Hindernisse in der PBPK Forschung beseitigt, bestehende PBPK Software verbessert und den Arzneimittelentwicklungsprozess vereinfacht.

8 Bibliography

1. US Food and Drug Administration. The Drug Development Process. (2018). Available at: <https://www.fda.gov/ForPatients/Approvals/Drugs/default.htm>. (Accessed: 12th February 2018)
2. Paul, S. M. *et al.* How to improve R&D productivity: the pharmaceutical industry's grand challenge. *Nat. Rev. Drug Discov.* **9**, 203–2014 (2010).
3. DiMasi, J. A., Grabowski, H. G. & Hansen, R. W. Innovation in the pharmaceutical industry: New estimates of R&D costs. *J. Health Econ.* **47**, 20–33 (2016).
4. Gobburu, J. V. S. Pharmacometrics 2020. *J. Clin. Pharmacol.* **50**, 151S–157S (2010).
5. Dost, F. H. *Der Blutspiegel: Kinetik der Konzentrationsabläufe in der Kreislaufflüssigkeit*. (Georg Thieme, 1953).
6. Sheiner, L. B., Rosenberg, B. & Melmon, K. L. Modelling of individual pharmacokinetics for computer-aided drug dosage. *Comput. Biomed. Res.* **5**, 441–459 (1972).
7. Sheiner, L. B. & Beal, S. L. Evaluation of methods for estimating population pharmacokinetic parameters. I. Michaelis-menten model: Routine clinical pharmacokinetic data. *J. Pharmacokinet. Biopharm.* **8**, 553–571 (1980).
8. Sheiner, L. B. & Beal, S. L. Evaluation of methods for estimating population pharmacokinetic parameters II. Biexponential model and experimental pharmacokinetic data. *J. Pharmacokinet. Biopharm.* **9**, 635–651 (1981).
9. Sheiner, L. B. & Beal, S. L. Evaluation of methods for estimating population pharmacokinetic parameters. III. Monoexponential model: Routine clinical pharmacokinetic data. *J. Pharmacokinet. Biopharm.* **11**, 303–319 (1983).
10. Karlsson, M. O. & Sheiner, L. B. The importance of modeling interoccasion variability in population pharmacokinetic analyses. *J. Pharmacokinet. Biopharm.* **21**, 735–750 (1993).
11. US Food and Drug Administration. Guidance for Industry Population Pharmacokinetics: Center for Drug Evaluation and Research (CDER) & Center for Biologics Evaluation and Research (CBER) (1999). Available at: <https://www.fda.gov/downloads/drugs/guidances/UCM072137.pdf>. (Accessed: 12th February 2018)
12. US Food and Drug Administration. Guidance for Industry Exposure-Response Relationships – Study Design, Data Analysis, and Regulatory Applications: Center for Drug Evaluation and Research (CDER) & Center for Biologics Evaluation and Research (CBER) (2003). Available at: <http://www.fda.gov/downloads/Drugs/Guidances/UCM072137.pdf>. (Accessed:

8. BIBLIOGRAPHY

- 12th February 2018)
13. European Medicines Agency. Guideline on reporting the results of population pharmacokinetic analysis CHMP (2007). Available at:
http://www.ema.europa.eu/docs/en_GB/document_library/Scientific_guideline/2009/09/WC500003067.pdf. (Accessed: 12th February 2018)
 14. US Food and Drug Administration. Guidance for Industry Clinical Drug Interaction Studies - Study Design, Data Analysis, and Clinical Implications: Center for Drug Evaluation and Research (CDER) (2017). Available at:
<https://www.fda.gov/downloads/Drugs/GuidanceComplianceRegulatoryInformation/Guidances/UCM292362.pdf>. (Accessed: 12th February 2018)
 15. US Food and Drug Administration. Guidance for Industry In Vitro Metabolism- and Transporter-Mediated Drug-Drug Interaction Studies: Center for Drug Evaluation and Research (CDER) (2017). Available at:
<https://www.fda.gov/downloads/Drugs/GuidanceComplianceRegulatoryInformation/Guidances/UCM581965.pdf>. (Accessed: 12th February 2018)
 16. European Medicines Agency. Guideline on the Investigation of drug interactions CHMP (2012). Available at:
http://www.ema.europa.eu/docs/en_GB/document_library/Scientific_guideline/2012/07/WC500129606.pdf. (Accessed: 12th February 2018)
 17. European Medicines Agency. Guideline on the Qualification and Reporting of Physiologically based Pharmacokinetic (PBPK) Modelling and Simulation CHMP (2016). Available at:
http://www.ema.europa.eu/docs/en_GB/document_library/Scientific_guideline/2016/07/WC500211315.pdf. (Accessed: 12th February 2018)
 18. US Food and Drug Administration. Guidance for Industry Physiologically Based Pharmacokinetic Analyses - Format and Content: Center for Drug Evaluation and Research (CDER) (2016). Available at:
<https://www.fda.gov/downloads/Drugs/GuidanceComplianceRegulatoryInformation/Guidances/UCM531207.pdf>. (Accessed: 12th February 2018)
 19. US Food and Drug Administration. FDA Innovation or stagnation: challenges and opportunity on the critical path to new medical products (2004). Available at:
<https://www.fda.gov/downloads/ScienceResearch/SpecialTopics/CriticalPathInitiative/CriticalPathOpportunitiesReports/ucm113411.pdf>. (Accessed: 12th February 2018)
 20. Reigner, B. G. *et al.* An evaluation of the integration of pharmacokinetic and pharmacodynamic principles in clinical drug development. *Clin. Pharmacokinet.* **33**, 142–152 (1997).
 21. Milligan, P. *et al.* Model-based drug development: A rational approach to

- efficiently accelerate drug development. *Clin. Pharmacol. Ther.* **93**, 502–5014 (2013).
- 22. Visser, S. A. G., de Alwis, D. P., Kerbusch, T., Stone, J. A. & Allerheiligen, S. R. B. Implementation of quantitative and systems pharmacology in large pharma. *CPT pharmacometrics Syst. Pharmacol.* **3**, e142 (2014).
 - 23. Chien, J. Y., Friedrich, S., Heathman, M. A., de Alwis, D. P. & Sinha, V. Pharmacokinetics/pharmacodynamics and the stages of drug development: Role of modeling and simulation. *AAPS J.* **7**, E544–E559 (2005).
 - 24. Lee, J. Y. *et al.* Impact of pharmacometric analyses on new drug approval and labelling decisions. *Clin. Pharmacokinet.* **50**, 627–635 (2011).
 - 25. Benson, N. *et al.* Systems pharmacology of the nerve growth factor pathway: Use of a systems biology model for the identification of key drug targets using sensitivity analysis and the integration of physiology and pharmacology. *Interface Focus* **3**, (2013).
 - 26. M Jauslin, P., O Karlsson, M. & Frey, N. Identification of the mechanism of action of a glucokinase activator from oral glucose tolerance test data in type 2 diabetic patients based on an integrated glucose-insulin model. *J. Clin. Pharmacol.* **52**, 1861–1871 (2011).
 - 27. Visser, S. A. G. *et al.* Model-based drug discovery: implementation and impact. *Drug Discov. Today* **18**, 764–775 (2013).
 - 28. Bueters, T., Ploeger, B. A. & Visser, S. A. G. The virtue of translational PKPD modeling in drug discovery: Selecting the right clinical candidate while sparing animal lives. *Drug Discov. Today* **18**, 853–862 (2013).
 - 29. Viberg, A., Martino, G., Lessard, E. & Laird, J. M. A. Evaluation of an innovative population pharmacokinetic-based design for behavioral pharmacodynamic endpoints. *AAPS J.* **14**, 657–663 (2012).
 - 30. Kretzschmar, K. *et al.* Model-based optimal design and execution of the first-inpatient trial of the anti-IL-6, ollokizumab. *CPT pharmacometrics Syst. Pharmacol.* **3**, e119 (2014).
 - 31. G Dodds, M., H Salinger, D., Mandema, J., Gibbs, J. & A Gibbs, M. Clinical trial simulation to inform phase 2: Comparison of concentrated vs. distributed first-in-patient study designs in psoriasis. *CPT pharmacometrics Syst. Pharmacol.* **2**, e58 (2013).
 - 32. Parkinson, J. *et al.* Translational pharmacokinetic–pharmacodynamic modeling of QTc effects in dog and human. *J. Pharmacol. Toxicol. Methods* **68**, 357–366 (2013).
 - 33. Chain, A. S. Y. *et al.* Identifying the translational gap in the evaluation of drug-induced QT(c) interval prolongation. *Br. J. Clin. Pharmacol.* **76**, 708–724 (2013).
 - 34. Kjellsson, M., F Cosson, V., Mazer, N., Frey, N. & O Karlsson, M. A model-

8. BIBLIOGRAPHY

- based approach to predict longitudinal HbA1c, using early phase glucose data from type 2 diabetes mellitus patients after anti-diabetic treatment. *J. Clin. Pharmacol.* **53**, 589–600 (2013).
35. Burghaus, R. *et al.* Evaluation of the efficacy and safety of rivaroxaban using a computer model for blood coagulation. *PLoS One* **6**, e17626 (2011).
36. Riggs, M. M., Bennetts, M., van der Graaf, P. H. & Martin, S. W. Integrated pharmacometrics and systems pharmacology model-based analyses to guide GnRH receptor modulator development for management of endometriosis. *CPT pharmacometrics Syst. Pharmacol.* **1**, 1–9 (2012).
37. Higgins, B. *et al.* Preclinical optimization of MDM2 antagonist scheduling for cancer treatment by using a model-based approach. *Clin. Cancer Res.* **20**, 3742–3752 (2014).
38. Hoeben, E., Neyens, M., Mannaert, E., Schmidt, M. & Vermeulen, A. Population pharmacokinetics of JNJ-37822681, a selective fast-dissociating dopamine D₂-receptor antagonist, in healthy subjects and subjects with schizophrenia and dose selection based on simulated D₂-receptor occupancy. *Clin. Pharmacokinet.* **52**, 1005–1015 (2013).
39. Roy, A. *et al.* Modeling and simulation of abatacept exposure and interleukin-6 response in support of recommended doses for rheumatoid arthritis. *J. Clin. Pharmacol.* **47**, 1408–1420 (2007).
40. Olsen, C. K., Brennum, L. T. & Kreilgaard, M. Using pharmacokinetic–pharmacodynamic modelling as a tool for prediction of therapeutic effective plasma levels of antipsychotics. *Eur. J. Pharmacol.* **584**, 318–327 (2008).
41. Møller, J. B. *et al.* Longitudinal modeling of the relationship between mean plasma glucose and HbA1c following antidiabetic treatments. *CPT pharmacometrics Syst. Pharmacol.* **2**, 1–8 (2013).
42. Demin, I., Hamrén, B., Luttringer, O., Pillai, G. & Jung, T. Longitudinal model-based meta-analysis in rheumatoid arthritis: An application toward model-based drug development. *Clin. Pharmacol. Ther.* **92**, 352–359 (2012).
43. Mandema, J. W., Cox, E. & Alderman, J. Therapeutic benefit of eletriptan compared to sumatriptan for the acute relief of migraine pain — results of a model-based meta-analysis that accounts for encapsulation. *Cephalgia* **25**, 715–725 (2005).
44. Rostami-Hodjegan, A. Reverse Translation in PBPK and QSP: Going Backwards in Order to Go Forward With Confidence. *Clin. Pharmacol. Ther.* doi:10.1002/cpt.904
45. Rostami-Hodjegan, A. Physiologically based pharmacokinetics joined with in vitro-in vivo extrapolation of ADME: A marriage under the arch of systems pharmacology. *Clin. Pharmacol. Ther.* **92**, 50–61 (2012).

46. Rowland, M., Peck, C. & Tucker, G. Physiologically-based pharmacokinetics in drug development and regulatory science. *Annu. Rev. Pharmacol. Toxicol.* **51**, 45–73 (2011).
47. Jones, H. & Rowland-Yeo, K. Basic concepts in physiologically based pharmacokinetic modeling in drug discovery and development. *CPT pharmacometrics Syst. Pharmacol.* **2**, e63 (2013).
48. Teorell, T. Kinetics of distribution of substances administered to the body, I: The extravascular modes of administration. *Arch. Int. Pharmacodyn. Ther.* **57**, 205–225 (1937).
49. Teorell, T. Kinetics of distribution of substances administered to the body, II: The intravascular modes of administration. *Arch. Int. Pharmacodyn. Ther.* **57**, 226–240 (1937).
50. Wagner, J. G. History of pharmacokinetics. *Pharmacol. Ther.* **12**, 537–562 (1981).
51. Paalzow, L. K. Torsten Teorell, the father of pharmacokinetics. *Ups. J. Med. Sci.* **100**, 41–6 (1995).
52. Harrison, L. I. & Gibaldi, M. Physiologically based pharmacokinetic model for digoxin disposition in dogs and its preliminary application to humans. *J. Pharm. Sci.* **66**, 1679–1683 (1977).
53. Rostami-Hodjegan, A. Physiologically based pharmacokinetics joined with in vitro-in vivo extrapolation of ADME: A marriage under the arch of systems pharmacology. *Clin. Pharmacol. Ther.* **92**, 50–61 (2012).
54. Cao, Y. & Jusko, W. J. Applications of minimal physiologically-based pharmacokinetic models. *J. Pharmacokinet. Pharmacodyn.* **39**, 711–23 (2012).
55. Cao, Y., Balthasar, J. P. & Jusko, W. J. Second-generation minimal physiologically-based pharmacokinetic model for monoclonal antibodies. *J. Pharmacokinet. Pharmacodyn.* **40**, 597–607 (2013).
56. Nestorov, I. Whole-body physiologically based pharmacokinetic models. *Expert Opin. Drug Metab. Toxicol.* **3**, 235–49 (2007).
57. Edginton, A. N., Theil, F., Schmitt, W. & Willmann, S. Whole body physiologically-based pharmacokinetic models: Their use in clinical drug development. *Expert Opin. Drug Metab. Toxicol.* **4**, 1143–1152 (2008).
58. Schaller, S. *et al.* A generic integrated physiologically based whole-body model of the glucose-insulin-glucagon regulatory system. *CPT pharmacometrics Syst. Pharmacol.* **2**, e65 (2013).
59. Knight-Schrijver, V. R., Chelliah, V., Cucurull-Sanchez, L. & Le Novère, N. The promises of quantitative systems pharmacology modelling for drug development. *Comput. Struct. Biotechnol. J.* **14**, 363–370 (2016).
60. Pilari, S. & Huisings, W. Lumping of physiologically-based pharmacokinetic

8. BIBLIOGRAPHY

- models and a mechanistic derivation of classical compartmental models. *J. Pharmacokinet. Pharmacodyn.* **37**, 365–405 (2010).
61. Nestorov, I., Aarons, L. J., Arundel, P. & Rowland, M. Lumping of whole-body physiologically based pharmacokinetic models. *J. Pharmacokinet. Biopharm.* **26**, 21–46 (1998).
 62. Björkman, S., Fyge, A. & Qi, Z. Determination of the steady state tissue distribution of midazolam in the rat. *J. Pharm. Sci.* **85**, 887–889 (1996).
 63. Gaohua, L. *et al.* Development of a multicompartment permeability-limited lung PBPK model and its application in predicting pulmonary pharmacokinetics of antituberculosis drugs. *CPT pharmacometrics Syst. Pharmacol.* **4**, 605–613 (2015).
 64. Gaohua, L., Neuhoff, S., Johnson, T. N., Rostami-Hodjegan, A. & Jamei, M. Development of a permeability-limited model of the human brain and cerebrospinal fluid (CSF) to integrate known physiological and biological knowledge: Estimating time varying CSF drug concentrations and their variability using in vitro data. *Drug Metab. Pharmacokinet.* **31**, 224–233 (2016).
 65. Tylutki, Z. & Polak, S. A four-compartment PBPK heart model accounting for cardiac metabolism - model development and application. *Sci. Rep.* **7**, 39494 (2017).
 66. Hsu, V. *et al.* Towards quantitation of the effects of renal impairment and probenecid inhibition on kidney uptake and efflux transporters, using physiologically based pharmacokinetic modelling and simulations. *Clin. Pharmacokinet.* **53**, 283–293 (2014).
 67. Li, R., Barton, H. A. & Maurer, T. S. A mechanistic pharmacokinetic model for liver transporter substrates under liver cirrhosis conditions. *CPT pharmacometrics Syst. Pharmacol.* **4**, 338–349 (2015).
 68. Kety, S. The theory and applications of the exchange of inert gas at the lungs and tissues. *Pharmacol. Rev.* **3**, 1–41 (1951).
 69. Fiserova-Bergerova, V. in (eds. Gut, I., Cikrt, M. & Plaa, G. L.) 211–220 (Springer Berlin Heidelberg, 1981). doi:10.1007/978-3-642-68195-0_24
 70. Fiserova-Bergerova, V. Toxicokinetics of organic solvents. *Scand. J. Work. Environ. Health* **11**, 7–21 (1985).
 71. Bessems, J. G. *et al.* PBTK modelling platforms and parameter estimation tools to enable animal-free risk assessment: Recommendations from a joint EPAA – EURL ECVAM ADME workshop. *Regul. Toxicol. Pharmacol.* **68**, 119–139 (2014).
 72. Zhou, D., Bui, K., Sostek, M. & Al-Huniti, N. Simulation and prediction of the drug-drug interaction potential of naloxegol by physiologically based pharmacokinetic modeling. *CPT pharmacometrics Syst. Pharmacol.* **5**, 250–257

- (2016).
73. Shebley, M., Fu, W., Badri, P., Bow, D. A. J. & Fischer, V. Physiologically based pharmacokinetic modeling suggests limited drug–drug interaction between clopidogrel and dasabuvir. *Clin. Pharmacol. Ther.* **102**, 679–687 (2017).
74. Moj, D. *et al.* Clarithromycin, midazolam, and digoxin: Application of PBPK modeling to gain new insights into drug–drug interactions and co-medication regimens. *AAPS J.* **19**, 298–312 (2017).
75. Hanke, N. *et al.* A physiologically based pharmacokinetic (PBPK) parent-metabolite model of the chemotherapeutic zoxtarelin doxorubicin—integration of in vitro results, Phase I and Phase II data and model application for drug–drug interaction potential analysis. *Cancer Chemother. Pharmacol.* **81**, 291–304 (2017).
76. Xu, C. *et al.* CYP2B6 pharmacogenetics-based in vitro–in vivo extrapolation of efavirenz clearance by physiologically based pharmacokinetic modeling. *Drug Metab. Dispos.* **41**, 2004–2011 (2013).
77. Riedmaier, A. E., Burt, H., Abduljalil, K. & Neuhoff, S. More power to OATP1B1: An evaluation of sample size in pharmacogenetic studies using a rosuvastatin PBPK model for intestinal, hepatic, and renal transporter-mediated clearances. *J. Clin. Pharmacol.* **56**, S132–S142 (2016).
78. Dickschen, K. *et al.* Concomitant use of tamoxifen and endoxifen in postmenopausal early breast cancer: prediction of plasma levels by physiologically-based pharmacokinetic modeling. *Springerplus* **3**, 285 (2014).
79. Dickschen, K. J. R., Willmann, S., Hempel, G. & Block, M. Addressing adherence using genotype-specific PBPK modeling—impact of drug holidays on tamoxifen and endoxifen plasma levels. *Front. Pharmacol.* **8**, 67 (2017).
80. Maharaj, A. R. & Edginton, A. N. Physiologically based pharmacokinetic modeling and simulation in pediatric drug development. *CPT Pharmacometrics Syst. Pharmacol.* **3**, e148 (2014).
81. Rioux, N. & Waters, N. J. Physiologically based pharmacokinetic modeling in pediatric oncology drug development. *Drug Metab. Dispos.* **44**, 934–943 (2016).
82. Maharaj, R., Barrett, J. S. & Edginton, N. A workflow example of PBPK modeling to support pediatric research and development: case study with lorazepam. *AAPS J.* **15**, 455–464 (2013).
83. Rhee, S., Chung, H., Yi, S., Yu, K.-S. & Chung, J.-Y. Physiologically based pharmacokinetic modelling and prediction of metformin pharmacokinetics in renal/hepatic-impaired young adults and elderly populations. *Eur. J. Drug Metab. Pharmacokinet.* **42**, 973–980 (2017).
84. Schlender, J.-F. *et al.* Development of a whole-body physiologically based pharmacokinetic approach to assess the pharmacokinetics of drugs in elderly

8. BIBLIOGRAPHY

- individuals. *Clin. Pharmacokinet.* **55**, 1573–1589 (2016).
85. Jogiraju, V. K., Avvari, S., Gollen, R. & Taft, D. R. Application of physiologically based pharmacokinetic modeling to predict drug disposition in pregnant populations. *Biopharm. Drug Dispos.* **38**, 426–438 (2017).
86. Dallmann, A. *et al.* Physiologically based pharmacokinetic modeling of renally cleared drugs in pregnant women. *Clin. Pharmacokinet.* **56**, 1525–1541 (2017).
87. Edginton, A. N. & Willmann, S. Physiology-based simulations of a pathological condition: prediction of pharmacokinetics in patients with liver cirrhosis. *Clin. Pharmacokinet.* **47**, 743–52 (2008).
88. Ono, C., Hsyu, P.-H., Abbas, R., Loi, C.-M. & Yamazaki, S. Application of physiologically based pharmacokinetic modeling to the understanding of bosutinib pharmacokinetics: Prediction of drug–drug and drug–disease interactions. *Drug Metab. Dispos.* **45**, 390 LP-398 (2017).
89. Rowland Yeo, K., Aarabi, M., Jamei, M. & Rostami-Hodjegan, A. Modeling and predicting drug pharmacokinetics in patients with renal impairment. *Expert Rev. Clin. Pharmacol.* **4**, 261–74 (2011).
90. Grillo, J. *et al.* Utility of a physiologically-based pharmacokinetic (PBPK) modeling approach to quantitatively predict a complex drug-drug-disease interaction scenario for rivaroxaban during the drug review process: Implications for clinical practice. *Biopharm. Drug Dispos.* **33**, 99–110 (2012).
91. Zhuang, X. & Lu, C. PBPK modeling and simulation in drug research and development. *Acta Pharm. Sin. B* **6**, 430–440 (2016).
92. Shah, D. K. & Betts, A. M. Towards a platform PBPK model to characterize the plasma and tissue disposition of monoclonal antibodies in preclinical species and human. *J. Pharmacokinet. Pharmacodyn.* **39**, 67–86 (2012).
93. Yang, B. *et al.* Virtual population pharmacokinetic using physiologically based pharmacokinetic model for evaluating bioequivalence of oral lacidipine formulations in dogs. *Asian J. Pharm. Sci.* **12**, 98–104 (2017).
94. Sweeney, L. M. *et al.* Development of a physiologically based pharmacokinetic (PBPK) model for methyl iodide in rats, rabbits, and humans. *Inhal. Toxicol.* **21**, 552–582 (2009).
95. DDMoRe Model Repository. Available at: <http://repository.ddmore.eu/>. (Accessed: 12th February 2018)
96. Kearns, G. L. *et al.* Developmental pharmacology — drug disposition, action, and therapy in infants and children. *N. Engl. J. Med.* **349**, 1157–1167 (2003).
97. Gillis, J. & Loughlan, P. Not just small adults: the metaphors of paediatrics. *Arch. Dis. Child.* **92**, 946–947 (2007).
98. Ferro, A. Paediatric prescribing: why children are not small adults. *Br. J. Clin. Pharmacol.* **79**, 351–353 (2015).

99. Moore, P. Children are not small adults. *Lancet* **352**, 630 (2017).
100. Lu, H. & Rosenbaum, S. Developmental pharmacokinetics in pediatric populations. *J. Pediatr. Pharmacol. Ther. JPPT* **19**, 262–276 (2014).
101. Fernandez, E. *et al.* Factors and mechanisms for pharmacokinetic differences between pediatric population and adults. *Pharmaceutics* **3**, 53–72 (2011).
102. Wagner, J. & Abdel-Rahman, S. M. Pediatric pharmacokinetics. *Pediatr. Rev.* **34**, 258–269 (2013).
103. Funk, R. S., Brown, J. T. & Abdel-Rahman, S. M. Pediatric pharmacokinetics. *Pediatr. Clin.* **59**, 1001–1016 (2017).
104. Blei, K. *et al.* Development of a physiologically-based pharmacokinetic model for preterm neonates: Evaluation with in vivo data. *Curr. Pharm. Des.* **21**, 5688–5698 (2015).
105. Friis-Hansen, B. Water distribution in the foetus and newborn infant. *Acta Paediatrica* **72**, 7–11 (1983).
106. Agata, Y. *et al.* Changes in left ventricular output from fetal to early neonatal life. *J. Pediatr.* **119**, 441–445 (1991).
107. Mielke, G. & Benda, N. Cardiac output and central distribution of blood flow in the human fetus. *Circulation* **103**, 1662–1668 (2001).
108. Visser, M. O., Leighton, J. O., van de Bor, M. & Walther, F. J. Renal blood flow in neonates: quantification with color flow and pulsed Doppler US. *Radiology* **183**, 441–444 (1992).
109. Yanowitz, T. D. *et al.* Postnatal hemodynamic changes in very-low-birthweight infants. *J. Appl. Physiol.* **87**, 370–380 (1999).
110. Powers, W. F. & Wampler, N. Gender pair combination, and maternal age and race moderate risks confronting twins. *Pediatr. Res.* **39**, 275 (1996).
111. Martinussen, M., Brubakk, A.-M., Linker, D. T., Vik, T. & Yao, A. C. Mesenteric blood flow velocity and its relation to circulatory adaptation during the first week of life in healthy term infants. *Pediatr. Res.* **36**, 334–339 (1994).
112. Agunod, M., Yamaguchi, N., Lopez, R., Luhby, A. L. & Glass, G. B. J. Correlative study of hydrochloric acid, pepsin, and intrinsic factor secretion in newborns and infants. *Am. J. Dig. Dis.* **14**, 400–414 (1969).
113. Rødbro, P., Kräslinikoff, P. A. & Christiansen, P. M. Parietal cell secretory function in early childhood. *Scand. J. Gastroenterol.* **2**, 209–213 (1967).
114. Huang, N. N. & High, R. H. Comparison of serum levels following the administration of oral and parenteral preparations of penicillin to infants and children of various age groups. *J. Pediatr.* **42**, 657–668 (1953).
115. Suchy, F. J., Balistreri, W. F., Heubi, J. E., Searcy, J. E. & Levin, R. S. Physiologic cholestasis: Elevation of the primary serum bile acid concentrations in normal infants. *Gastroenterology* **80**, 1037–1041 (2017).

8. BIBLIOGRAPHY

116. Poley, J. R., Dower, J. C., Owen Jr., C. A. & Stickler, G. B. Bile acids in infants and children. *J. Lab. Clin. Med.* **63**, 838–846 (2017).
117. Berseth, C. L. Gestational evolution of small intestine motility in preterm and term infants. *J. Pediatr.* **115**, 646–651 (1989).
118. Brouwer, K. L. R. *et al.* Human ontogeny of drug transporters: Review and recommendations of the pediatric transporter working group. *Clin. Pharmacol. Ther.* **98**, 266–287 (2015).
119. Tanigawara, Y. Role of p-glycoprotein in drug disposition. *Ther. Drug Monit.* **22**, 134–140 (2000).
120. Niemi, M. Role of OATP transporters in the disposition of drugs. *Pharmacogenomics* **8**, 787–802 (2007).
121. McNamara, P. J. & Alcorn, J. Protein binding predictions in infants. *AAPS PharmSci* **4**, 19–26 (2002).
122. Ehrnebo, M., Agurell, S., Jalling, B. & Boréus, L. O. Age differences in drug binding by plasma proteins: Studies on human foetuses, neonates and adults. *Eur. J. Clin. Pharmacol.* **3**, 189–193 (1971).
123. Koukouritaki, S. B. *et al.* Developmental expression of human hepatic CYP2C9 and CYP2C19. *J. Pharmacol. Exp. Ther.* **308**, 965–974 (2004).
124. Läpple, F. *et al.* Differential expression and function of CYP2C isoforms in human intestine and liver. *Pharmacogenet. Genomics* **13**, 565–575 (2003).
125. Tréluyer, J.-M., Gueret, G., Cheron, G., Sonnier, M. & Cresteil, T. Developmental expression of CYP2C and CYP2C-dependent activities in the human liver: In-vivo/in-vitro correlation and inducibility. *Pharmacogenetics* **7**, 441–452 (1998).
126. Lacroix, D., Sonnier, M., Moncion, A., Cheron, G. & Cresteil, T. Expression of CYP3A in the human liver — evidence that the shift between CYP3A7 and CYP3A4 occurs immediately after birth. *Eur. J. Biochem.* **247**, 625–634 (1997).
127. Tréluyer, J. M. *et al.* Oxidative metabolism of amprenavir in the human liver. Effect of the CYP3A maturation. *Drug Metab. Dispos.* **31**, 275–281 (2003).
128. Stevens, J. C. *et al.* Developmental expression of the major human hepatic CYP3A enzymes. *J. Pharmacol. Exp. Ther.* **307**, 573–582 (2003).
129. Blanco, J. G., Harrison, P. L., Evans, W. E. & Relling, M. V. Human cytochrome P450 maximal activities in pediatric versus adult liver. *Drug Metab. Dispos.* **28**, 379–382 (2000).
130. Strassburg, C. P. *et al.* Developmental aspects of human hepatic drug glucuronidation in young children and adults. *Gut* **50**, 259–265 (2002).
131. Zaya, M. J., Hines, R. N. & Stevens, J. C. Epirubicin glucuronidation and UGT2B7 developmental expression. *Drug Metab. Dispos.* **34**, 2097–2101 (2006).
132. Pacifici, G. M., Säwe, J., Kager, L. & Rane, A. Morphine glucuronidation in

- human fetal and adult liver. *Eur. J. Clin. Pharmacol.* **22**, 553–558 (1982).
- 133. Rhodin, M. M. *et al.* Human renal function maturation: a quantitative description using weight and postmenstrual age. *Pediatr. Nephrol.* **24**, 67–76 (2009).
 - 134. Janssen, I., Heymsfield, S. B., Wang, Z. & Ross, R. Skeletal muscle mass and distribution in 468 men and women aged 18–88 yr. *J. Appl. Physiol.* **89**, 81–88 (2000).
 - 135. Gallagher, D. *et al.* Appendicular skeletal muscle mass: effects of age, gender, and ethnicity. *J. Appl. Physiol.* **83**, 229–239 (1997).
 - 136. Kyle, U. G., Genton, L., Slosman, D. O. & Pichard, C. Fat-free and fat mass percentiles in 5225 healthy subjects aged 15 to 98 years. *Nutrition* **17**, 534–541 (2017).
 - 137. Grasedyck, K., Jahnke, M., Friedrich, O., Schulz, D. & Lindner, J. Aging of liver: Morphological and biochemical changes. *Mech. Ageing Dev.* **14**, 435–442 (1980).
 - 138. Wynne, H. A. *et al.* The effect of age upon liver volume and apparent liver blood flow in healthy man. *Hepatology* **9**, 297–301 (1989).
 - 139. Choukér, A. *et al.* Estimation of liver size for liver transplantation: The impact of age and gender. *Liver Transplant.* **10**, 678–685 (2004).
 - 140. Griffiths, G. J., Robinson, K. B., Cartwright, G. O. & McLachlan, M. S. F. Loss of renal tissue in the elderly. *Br. J. Radiol.* **49**, 111–117 (1976).
 - 141. Tauchi, H., Tsuboi, K. & Okutomi, J. Age changes in the human kidney of the different races. *Gerontology* **17**, 87–97 (1971).
 - 142. Kuikka, J. T. & Lansimies, E. Effect of age on cardiac index, stroke index and left ventricular ejection fraction at rest and during exercise as studied by radiocardiography. *Acta Physiol. Scand.* **114**, 339–343 (1982).
 - 143. Hoang, K. *et al.* Determinants of glomerular hypofiltration in aging humans. *Kidney Int.* **64**, 1417–1424 (2017).
 - 144. Luzon, E. *et al.* Physiologically based pharmacokinetic modeling in regulatory decision-making at the European Medicines Agency. *Clin. Pharmacol. Ther.* **102**, 98–105 (2017).
 - 145. Zhao, P. *et al.* Applications of physiologically based pharmacokinetic (PBPK) modeling and simulation during regulatory review. *Clin. Pharmacol. Ther.* **89**, 259–67 (2011).
 - 146. Wagner, C. *et al.* Predicting the effect of cytochrome P450 inhibitors on substrate drugs: Analysis of physiologically based pharmacokinetic modeling submissions to the US Food and Drug Administration. *Clin. Pharmacokinet.* **54**, 117–127 (2015).
 - 147. Rodrigues, A. D. *Drug-Drug Interactions*. (CRC Press, 2008).

8. BIBLIOGRAPHY

148. Quinn, K. J. & Shah, N. H. A dataset quantifying polypharmacy in the United States. *Sci. Data* **4**, (2017).
149. Payne, R. A. The epidemiology of polypharmacy. *Clin. Med.* **16**, 465–469 (2016).
150. Hajjar, E. R., Cafiero, A. C. & Hanlon, J. T. Polypharmacy in elderly patients. *Am. J. Geriatr. Pharmacother.* **5**, 345–351 (2007).
151. Meyer, M., Schneckener, S., Ludewig, B., Kuepfer, L. & Lippert, J. Using expression data for quantification of active processes in physiologically based pharmacokinetic modeling. *Drug Metab. Dispos.* **40**, 892–901 (2012).
152. Nishimura, M., Yaguti, H., Yoshitsugu, H., Naito, S. & Satoh, T. Tissue distribution of mRNA expression of human cytochrome P450 isoforms assessed by high-sensitivity real-time reverse transcription PCR. *Yakugaku Zasshi* **123**, 369–375 (2003).
153. Nishimura, M. & Naito, S. Tissue-specific mRNA expression profiles of human ATP-binding cassette and solute carrier transporter superfamilies. *Drug Metab. Pharmacokinet.* **20**, 452–477 (2005).
154. Kuepfer, L. *et al.* Applied Concepts in PBPK Modeling: How to Build a PBPK/PD Model. *CPT pharmacometrics Syst. Pharmacol.* **5**, 516–531 (2016).
155. Burghaus, R. *et al.* Computational investigation of optimal dosing schedules for a switch of medication from Warfarin to direct inhibitors of vitamin K dependent factors. *Front. Pharmacol.* **5**, (2014).
156. Rodgers, T., Leahy, D. & Rowland, M. Physiologically based pharmacokinetic modeling 1: Predicting the tissue distribution of moderate-to-strong bases. *J. Pharm. Sci.* **94**, 1259–1276 (2005).
157. Rodgers, T. & Rowland, M. Physiologically based pharmacokinetic modelling 2: Predicting the tissue distribution of acids, very weak bases, neutrals and zwitterions. *J. Pharm. Sci.* **95**, 1238–1257 (2006).
158. Schmitt, W. General approach for the calculation of tissue to plasma partition coefficients. *Toxicol. In Vitro* **22**, 457–467 (2008).
159. Poulin, P. & Theil, F. P. A priori prediction of tissue:plasma partition coefficients of drugs to facilitate the use of physiologically-based pharmacokinetic models in drug discovery. *J. Pharm. Sci.* **89**, 16–35 (2000).
160. Poulin, P., Schoenlein, K. & Theil, F. P. Prediction of adipose tissue: plasma partition coefficients for structurally unrelated drugs. *J. Pharm. Sci.* **90**, 436–447 (2001).
161. Berezhkovskiy, L. M. Volume of distribution at steady state for a linear pharmacokinetic system with peripheral elimination. *J. Pharm. Sci.* **93**, 1628–1640 (2004).
162. Kolesnikov, N. *et al.* ArrayExpress update—simplifying data submissions.

- Nucleic Acids Res.* **43**, D1113–D1116 (2015).
- 163. Wheeler, D. L. *et al.* Database resources of the National Center for Biotechnology. *Nucleic Acids Res.* **31**, 28–33 (2003).
 - 164. Fedorov. GetData Graph Digitizer. (2012). Available at: <http://getdata-graph-digitizer.com/>. (Accessed: 12th February 2018)
 - 165. Sheiner, L. B. Learning versus confirming in clinical drug development. *Clin. Pharmacol. Ther.* **61**, 275–291 (1997).

9 Supporting Information

9.1 Supporting Information of Project I

A physiologically-based pharmacokinetic (PBPK) parent-metabolite model of the chemotherapeutic zoxtarelin doxorubicin - integration of in vitro results, Phase I and Phase II data and model application for drug-drug interaction potential analysis

Metformin Supplementary

Nina Hanke ¹, Michael Teifel ², Daniel Moj ¹, Jan-Georg Wojtyniak ¹, Hannah Britz ¹, Babette Aicher ²,
Herbert Sindermann ², Nicola Ammer ², Thorsten Lehr ¹

¹ Clinical Pharmacy, Saarland University, Saarbruecken, Germany

² Aeterna Zentaris GmbH, Weismuellerstr. 50, Frankfurt, Germany

Corresponding Author: Thorsten Lehr, Clinical Pharmacy, Saarland University, Campus C2 2, 66123
Saarbruecken, +49 681 302 70255, thorsten.lehr@mx.uni-saarland.de

PBPK model of metformin

1. Introduction

The biguanide metformin is the first-line therapeutic agent for the treatment of type 2 diabetes mellitus. Metformin reduces hepatic gluconeogenesis, reduces intestinal absorption of glucose and increases insulin sensitivity and glucose uptake into peripheral tissues [1].

Because of its hydrophilic structure, metformin shows an exceptionally low lipophilicity ($\log P = -1.43$) and is not bound to plasma proteins [2]. Following oral administration, 50 - 60% of a dose are absorbed and peak plasma concentrations are reached within 2 h. The plasma half-life of metformin is 2.5 - 7 h after intravenous infusion and 4 - 8 h following oral administration [3]. Metformin is not subject to hepatic metabolism and mainly renally excreted. After intravenous administration 80 - 100% of the dose are recovered unchanged in the urine; following oral administration the fraction excreted unchanged alternates between 50 and 75%. The observed renal clearance of metformin is much higher than the glomerular filtration rate (GFR), suggesting active renal secretion [2–4]. Metformin is reported to be a substrate of the organic cation transporter (OCT) 1, the kidney specific OCT2 and of OCT3 [5, 6]. These transporters are localized at the basolateral membranes of renal cells, hepatocytes, enterocytes and cells of many other organs. Metformin is also transported by the H^+ organic cation antiporters "multidrug and toxin extrusion protein" (MATE) 1 and MATE2-K [7]. These efflux transporters are primarily expressed in the liver (MATE1) and in the kidney (MATE1, MATE2-K) at the apical (luminal) membranes. In vivo, OCT and MATE transporters form a functional unit to transport organic cations from the blood through hepatocytes and renal tubule cells into the bile and urine, resulting in effective biliary and renal secretion.

2. Materials and Methods

Software

PBPK modeling was performed with PK-Sim 7.0.0. Parameter optimization was accomplished using the Monte Carlo algorithm implemented in PK-Sim. Digitization of published plasma concentration-time curves was performed with GetData Graph Digitizer (V 2.26). Graphics and further statistical analyses were generated with R (V 3.3.2) using the graphical interface RStudio (V 1.0.136).

Model development

For model development, physicochemical parameters as well as individual and mean plasma concentration-time profiles of metformin after intravenous single dose (250 - 1000 mg), oral single dose (250 - 2550 mg) and oral multiple dose (250 - 1000 mg) administration were obtained from literature. Data was separated into training and test datasets for model development and evaluation, respectively (for a detailed study summary see Suppl. Tab. 1). The training dataset contained a study describing the extent of metformin distribution into erythrocytes [8]. Furthermore, fraction excreted to urine data following intravenous (250 and 500 mg) and oral administration (500 mg) of metformin was used in the training dataset to inform the renal secretion process.

For population simulations, a virtual Caucasian population was generated containing 50 male and 50 female individuals, 20 - 50 years of age, with body weights of 40 - 120 kg. The ICRP (International Commission on Radiological Protection) database in PK-Sim was used for generation of this population [9]. For model evaluation, the medians and 90% prediction intervals of population simulation plasma concentration-time profiles were calculated and used to generate visual predictive checks (predicted versus observed plasma concentrations) for the training and test datasets.

3. Results

Metformin modeling

To limit the number of parameters to be optimized, only the most important processes were implemented into the final metformin model. These are (1) passive distribution into blood cells and the cells of all organs except renal cells, (2) active uptake from blood into renal cells by OCT2 and (3) renal secretion into urine by MATE2-K. Glomerular filtration and enterohepatic cycling were enabled, as these processes are active under physiological conditions.

Drug-dependent parameters

All drug-dependent parameters taken from literature with their references as well as all optimized parameter values are given in Suppl. Tab. 2.

System-dependent parameters

Expression of the implemented transporters and the geometric standard deviation of their log-normal distribution in virtual populations are given in Suppl. Tab. 3. No other system-dependent parameters were changed or adjusted.

Model performance

Training dataset: The training dataset performance of the final metformin model, predicting plasma concentrations following intravenous (250 mg and 500 mg) and oral (500 - 1500 mg) administration of metformin, is presented in Suppl. Fig. 1, 3 and 5 - 8.

Predicted compared to observed fraction excreted to urine following intravenous (250 mg and 500 mg) and oral (500 mg) administration is presented in Suppl. Fig. 2 and 4.

Suppl. Fig. 6 shows predicted and observed plasma and erythrocyte concentrations following oral administration of 850 mg metformin.

Test dataset: The test dataset performance of the final metformin model, predicting plasma concentrations following intravenous (1000 mg) and oral (250 - 2550 mg) administration of metformin, is presented in Suppl. Fig. 9 - 20.

4. Discussion

Model performance

Metformin pharmacokinetics show high inter-individual variability in absorption, apparent volume of distribution (654 ± 358 L) and renal clearance (335 - 615 mL/min) [1, 10]. The slow absorption of metformin rate-limits its disposition [2, 3] so that variability in absorption causes additional variation during the elimination phase of metformin plasma concentration-time profiles. Evaluation of predicted compared to observed clinical data following intravenous application suggests that the current model overpredicts the velocity of distribution into tissues and underpredicts the rate of excretion of metformin (Suppl. Fig. 1, 2, 9). The model accurately describes the plasma and urine concentrations after single oral administration of 500 mg (Suppl. Fig. 3, 4). The 500 mg multiple dose simulations show a good prediction of the trough concentrations with too rapid absorption and an overprediction of C_{max} (Suppl. Fig. 5, 12, 13). The same phenomenon can be observed for some of the other studies, especially with administration of higher doses of metformin in the fasted state (Suppl. Fig. 14, 16 – 18), but there are also simulations that underpredict C_{max} (Suppl. Fig. 8, 10, 15), due to the documented inter-individual variability. The model simulations of metformin administration together with food nicely

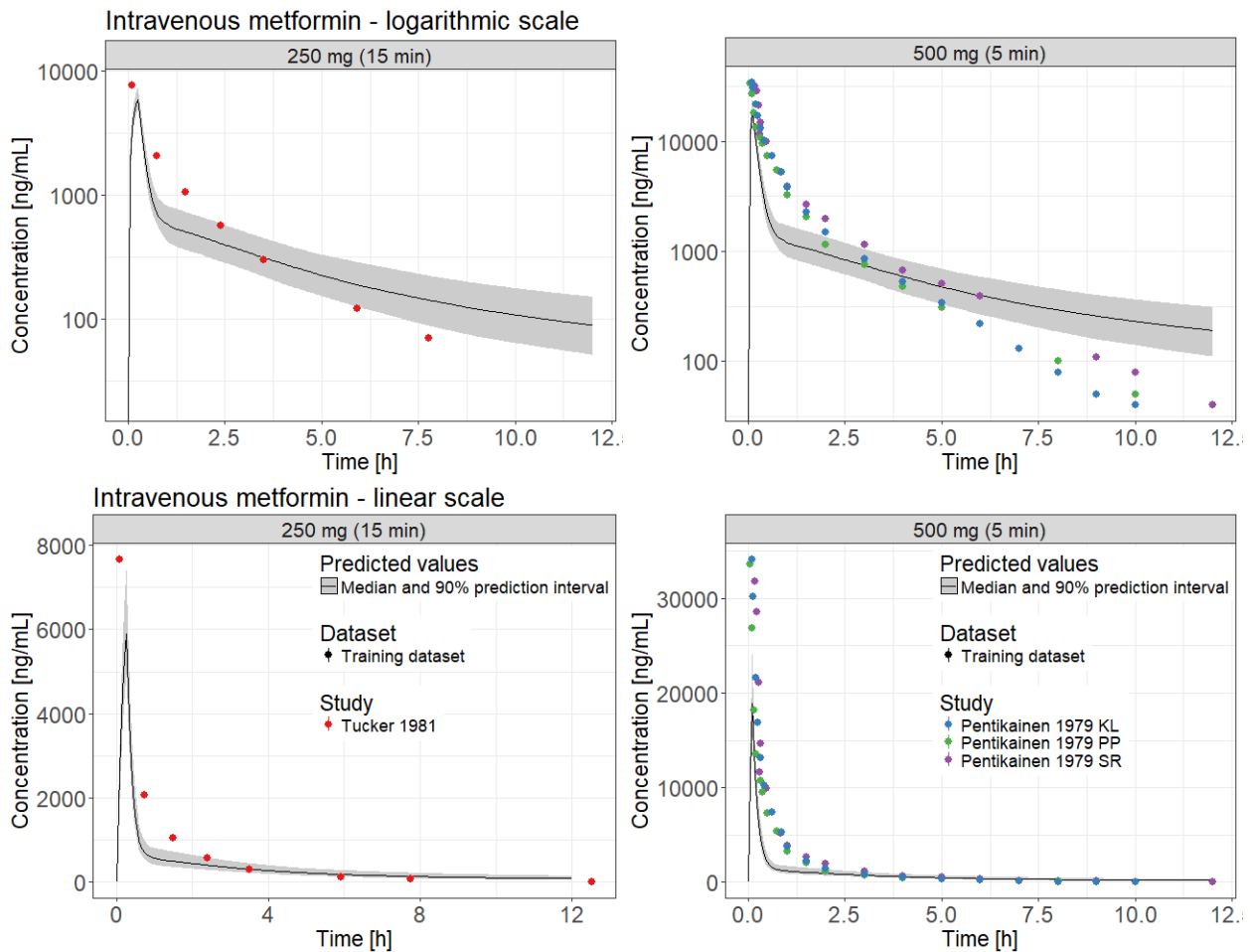
predict the plateau-like shape of the measured plasma concentration-time curves around C_{\max} (Suppl. Fig. 6, 11). Plasma and erythrocyte concentrations of the study of Robert et al. [8] are also very well described (Suppl. Fig. 6).

Model limitations

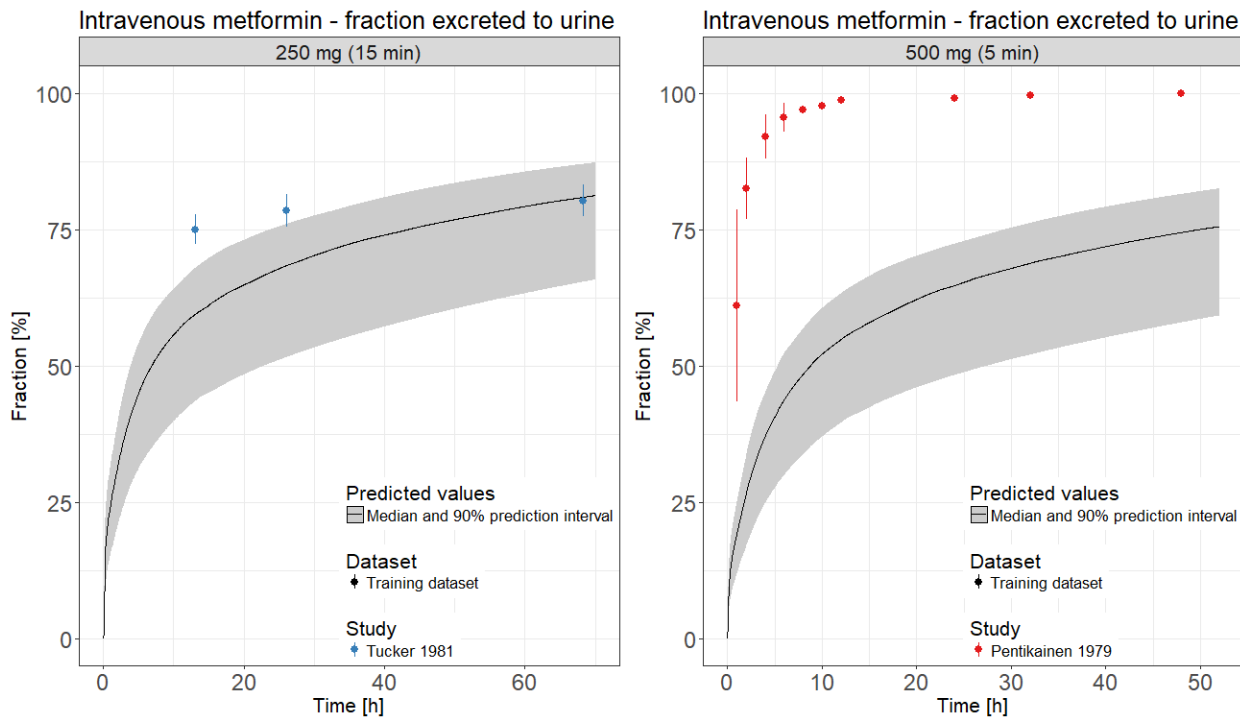
Metformin is recommended by the FDA as OCT2/MATE transport victim drug for the use in clinical DDI studies [11]. The purpose of the presented metformin PBPK model is to accurately incorporate these processes so that this model is fit to be coupled to models of OCT2 and MATE2-K perpetrator drugs and applied for DDI prediction.

Metformin is positively charged at physiological pH ($pK_a = 11.5$ (base)) and highly hydrophilic ($\log P = -1.43$). Therefore, passive diffusion of metformin through lipid bilayers is very slow. Nevertheless, distribution and accumulation into red blood cells has been described, with a much longer elimination half-life from erythrocytes (23 h), than from plasma (3 h) [8]. Furthermore, the apparent volume of distribution of metformin is high, in spite of its exceptionally low lipophilicity. The mechanism of this partitioning into red blood cells is currently not understood. Transport in combination with target-binding, binding to other intracellular components, some kind of trapping within organelles or sticking to the cellular membranes of red blood cells are possible explanations. As the mechanism of this accumulation is unclear, an asymmetric permeability from plasma into red blood cells was incorporated. The wide distribution into body tissues is most probably mediated by active transport processes and was modeled by an overall asymmetric permeability from the interstitial space into the cells of all organs except kidney, as so far, only the kidney specific isoforms of OCT and MATE transporters have been incorporated into this model.

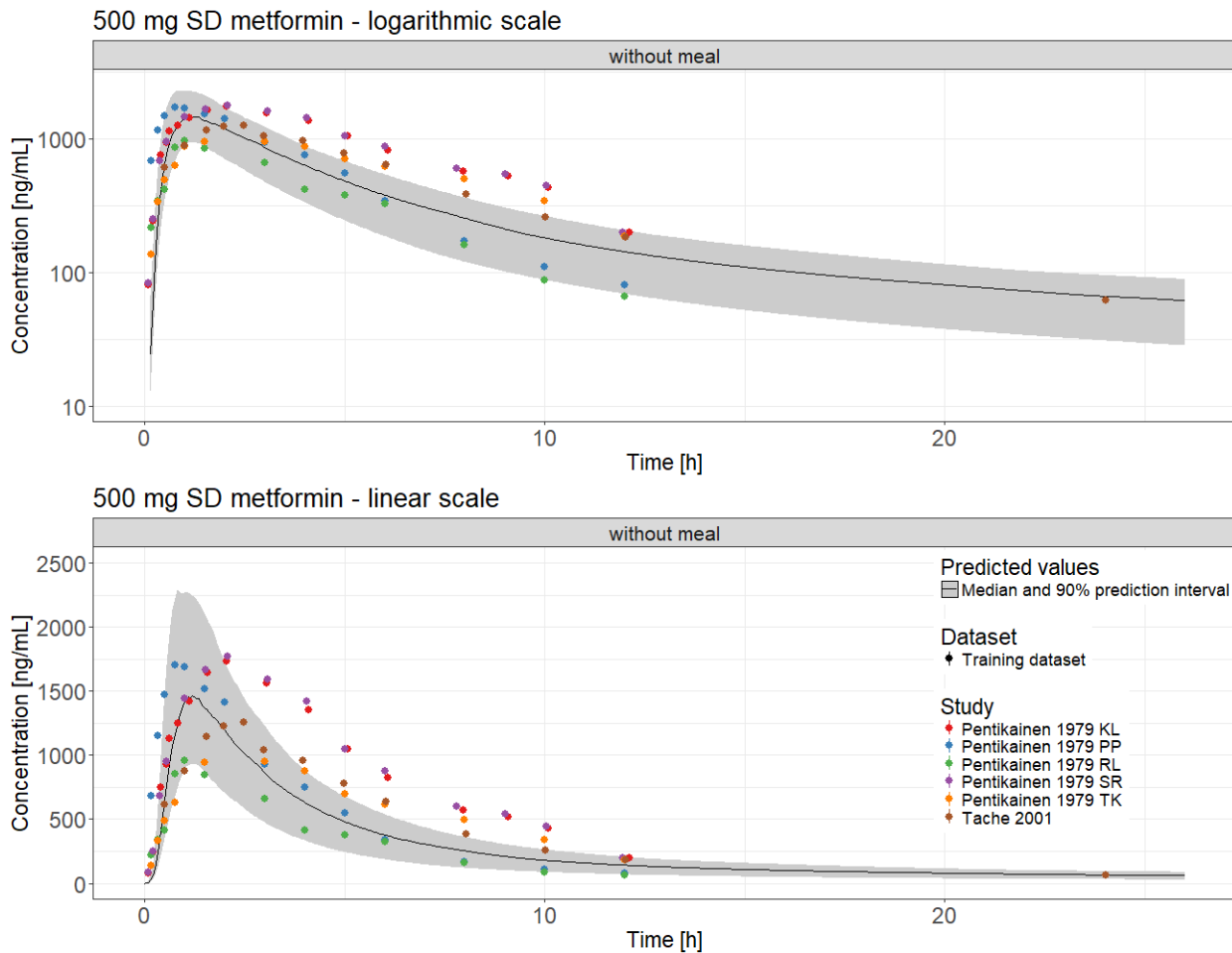
To define the contribution of the two implemented transport processes by OCT2 and MATE2-K, fraction excreted to urine data after intravenous and oral administration of metformin have been included into the training dataset. In addition to an accurate description of unchanged drug recovered in urine, evaluation of this model with measured metformin concentrations in the kidney and by prediction of OCT2 and MATE2-K mediated DDIs is needed.



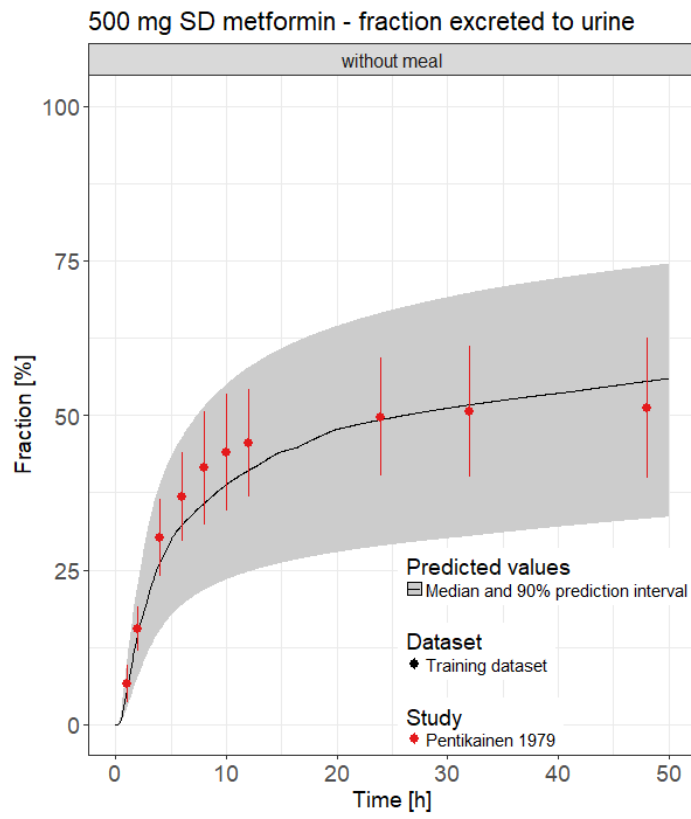
Suppl. Fig. 1 Training dataset: Population simulations compared to observed data of metformin plasma concentrations following intravenous administration of 250 mg (left panel) and 500 mg (right panel). Clinical data are shown as dots (Pentikainen KL, PP and SR are individual data) [2, 3]. Population simulation medians are shown as lines; the shaded areas depict the 5th - 95th percentile population prediction intervals



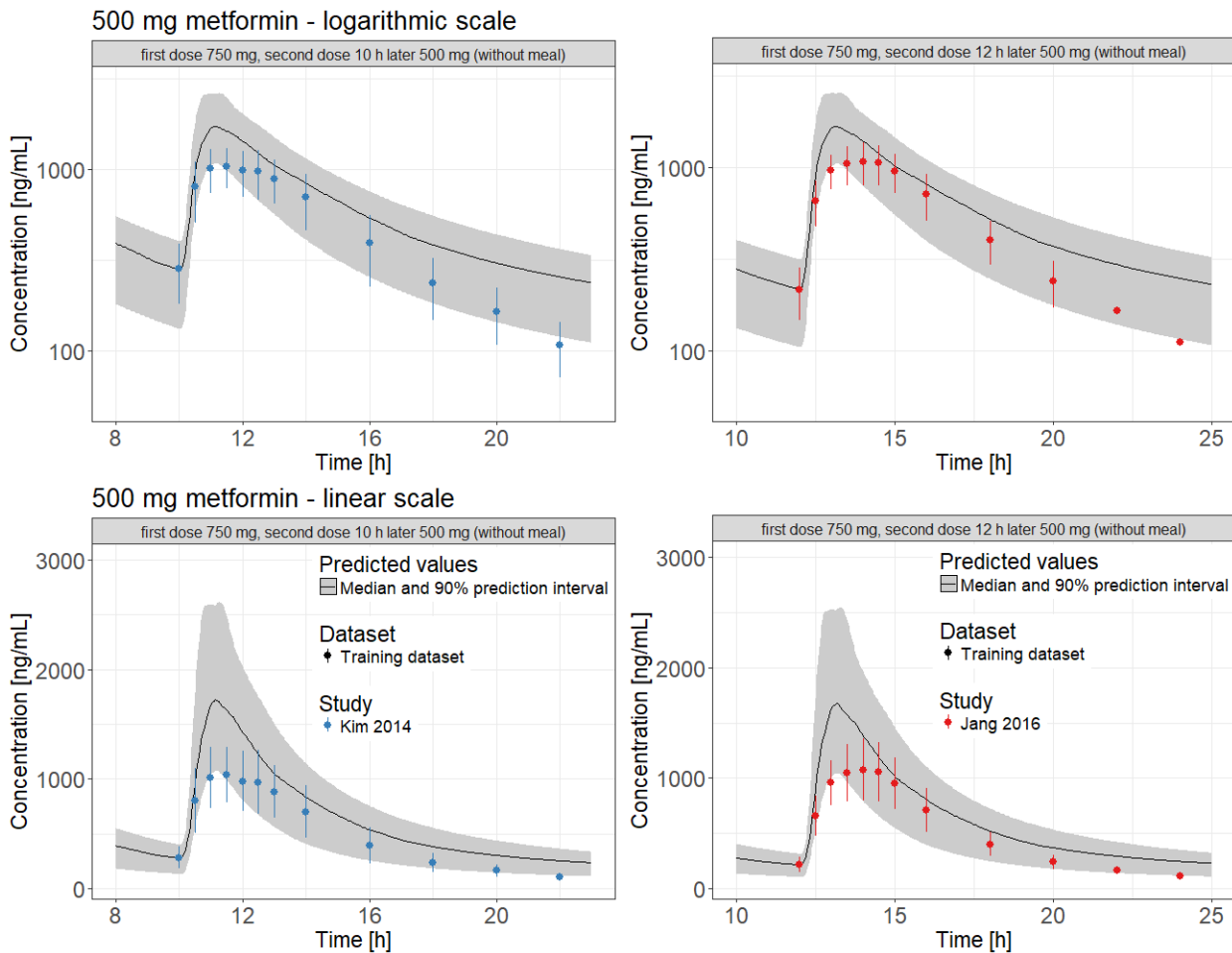
Suppl. Fig. 2 Training dataset: Population simulations compared to observed data of metformin fraction excreted to urine following intravenous administration of 250 mg (left panel) and 500 mg (right panel). Clinical data are shown as dots (+/- standard deviation) [2, 3]. Population simulation medians are shown as lines; the shaded areas depict the 5th - 95th percentile population prediction intervals



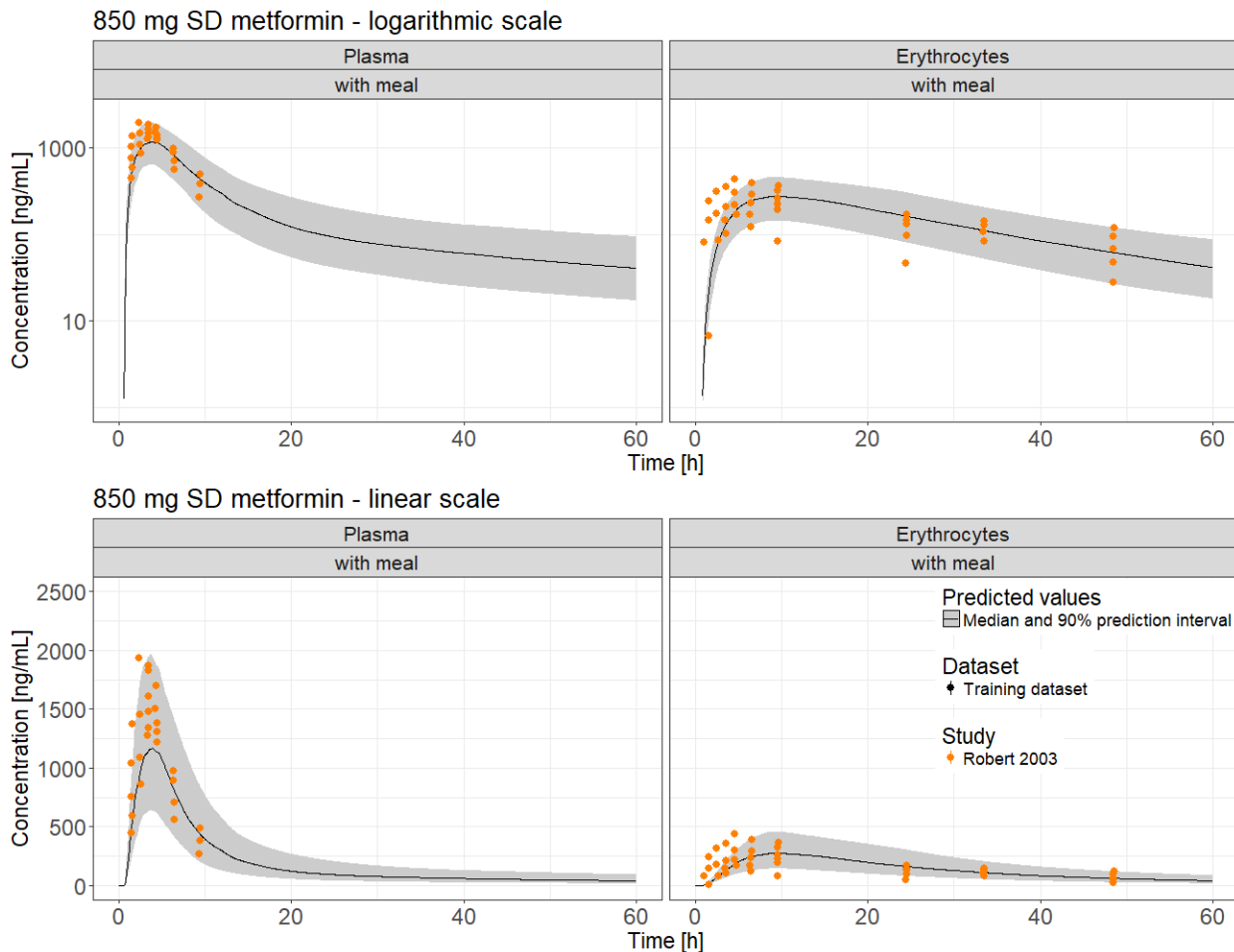
Suppl. Fig. 3 Training dataset: Population simulations compared to observed data of metformin plasma concentrations following single oral administration of 500 mg. Clinical data are shown as dots (Pentikainen KL, PP, RL, SR and TK are individual data) [2, 12]. Population simulation medians are shown as lines; the shaded areas depict the 5th - 95th percentile population prediction intervals



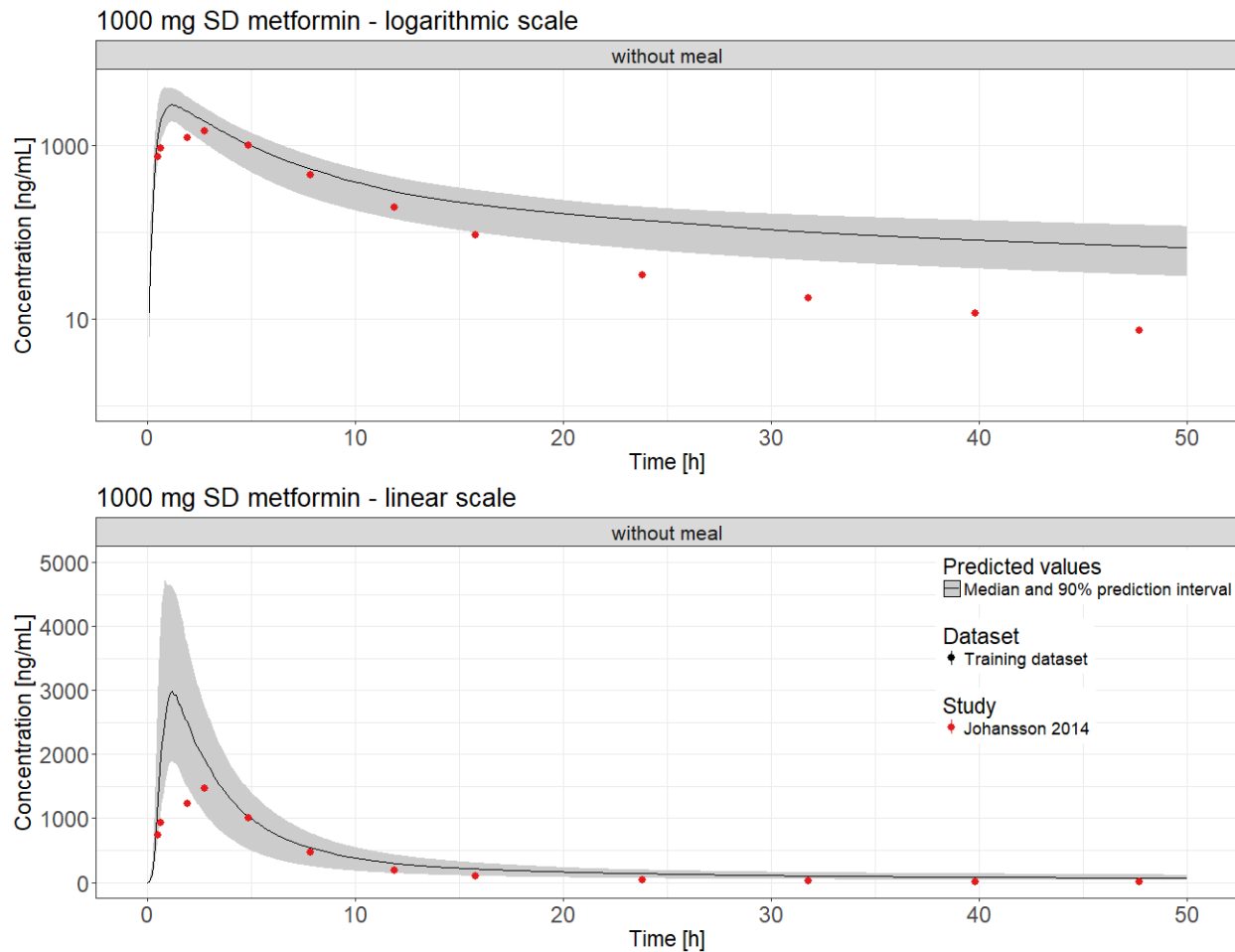
Suppl. Fig. 4 Training dataset: Population simulations compared to observed data of metformin fraction excreted to urine following single oral administration of 500 mg. Clinical data are shown as dots (+/- standard deviation) [2]. Population simulation medians are shown as lines; the shaded areas depict the 5th - 95th percentile population prediction intervals



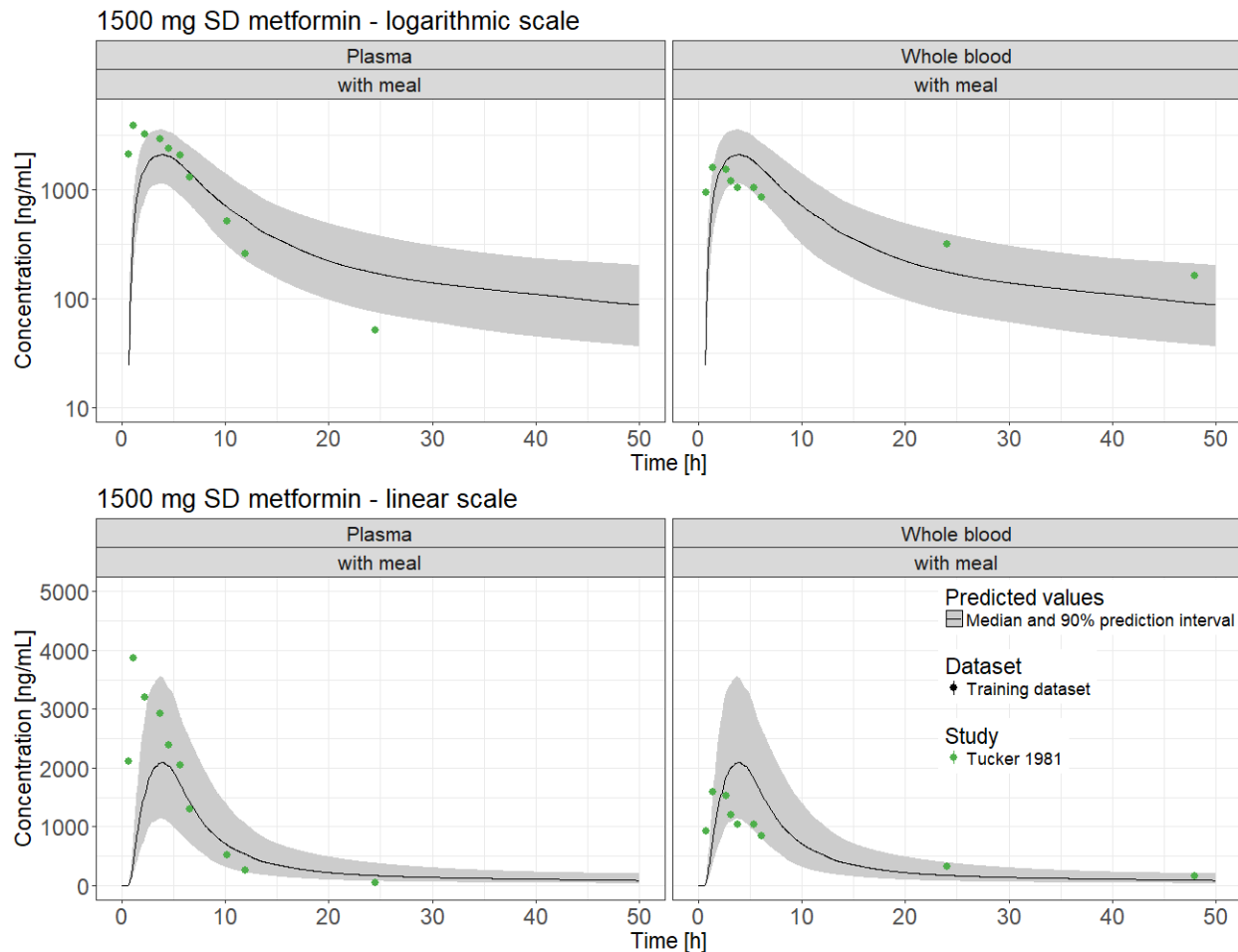
Suppl. Fig. 5 Training dataset: Population simulations compared to observed data of metformin plasma concentrations following oral administration of 500 mg, 10 h (left panel) and 12 h (right panel) after a single oral administration of 750 mg metformin. Clinical data are shown as dots (+/- standard deviation) [13, 14]. Population simulation medians are shown as lines; the shaded areas depict the 5th - 95th percentile population prediction intervals



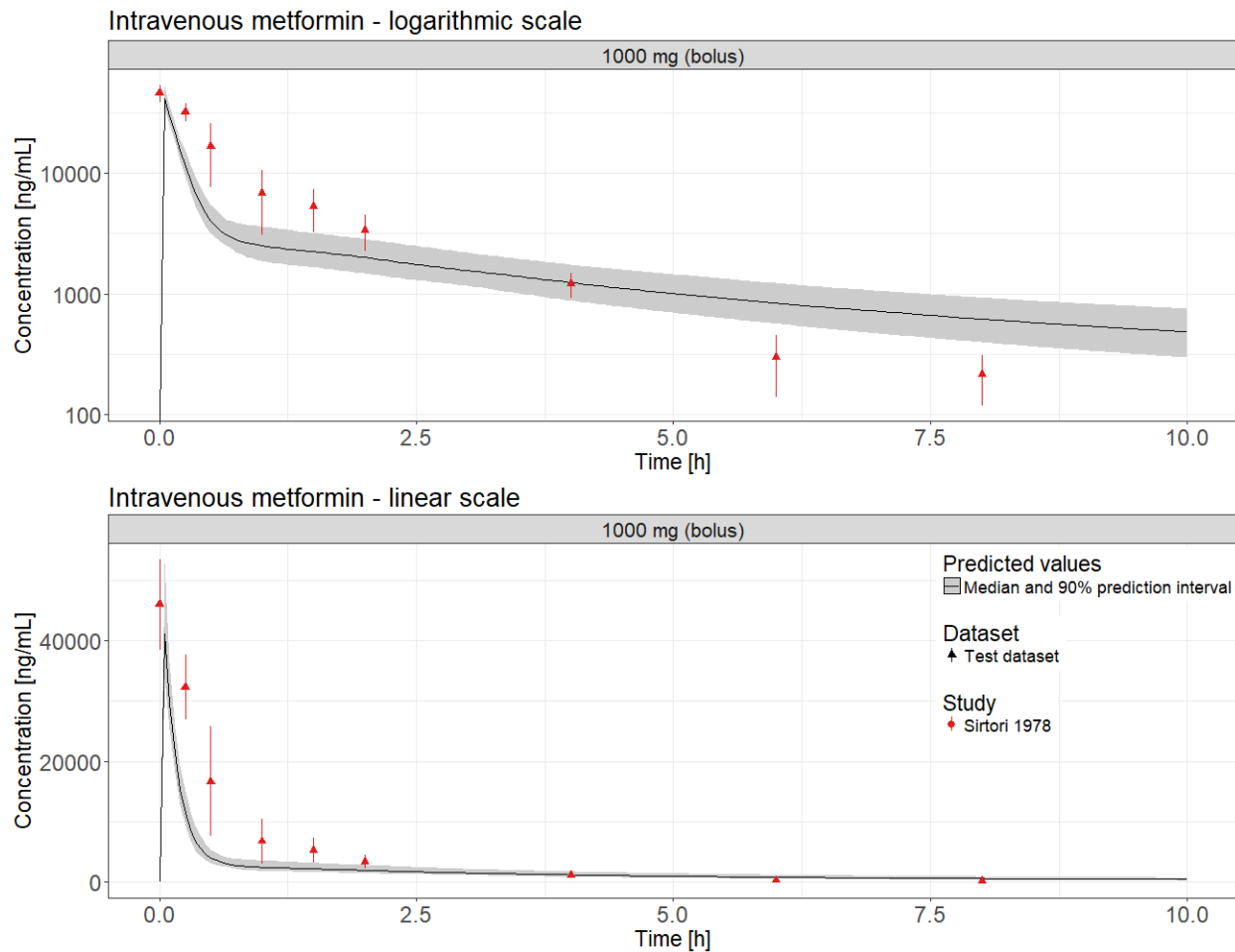
Suppl. Fig. 6 Training dataset: Population simulations compared to observed data of metformin plasma (left panel) and erythrocyte (right panel) concentrations following single oral administration of 850 mg. Clinical data are shown as dots [8]. Population simulation medians are shown as lines; the shaded areas depict the 5th - 95th percentile population prediction intervals



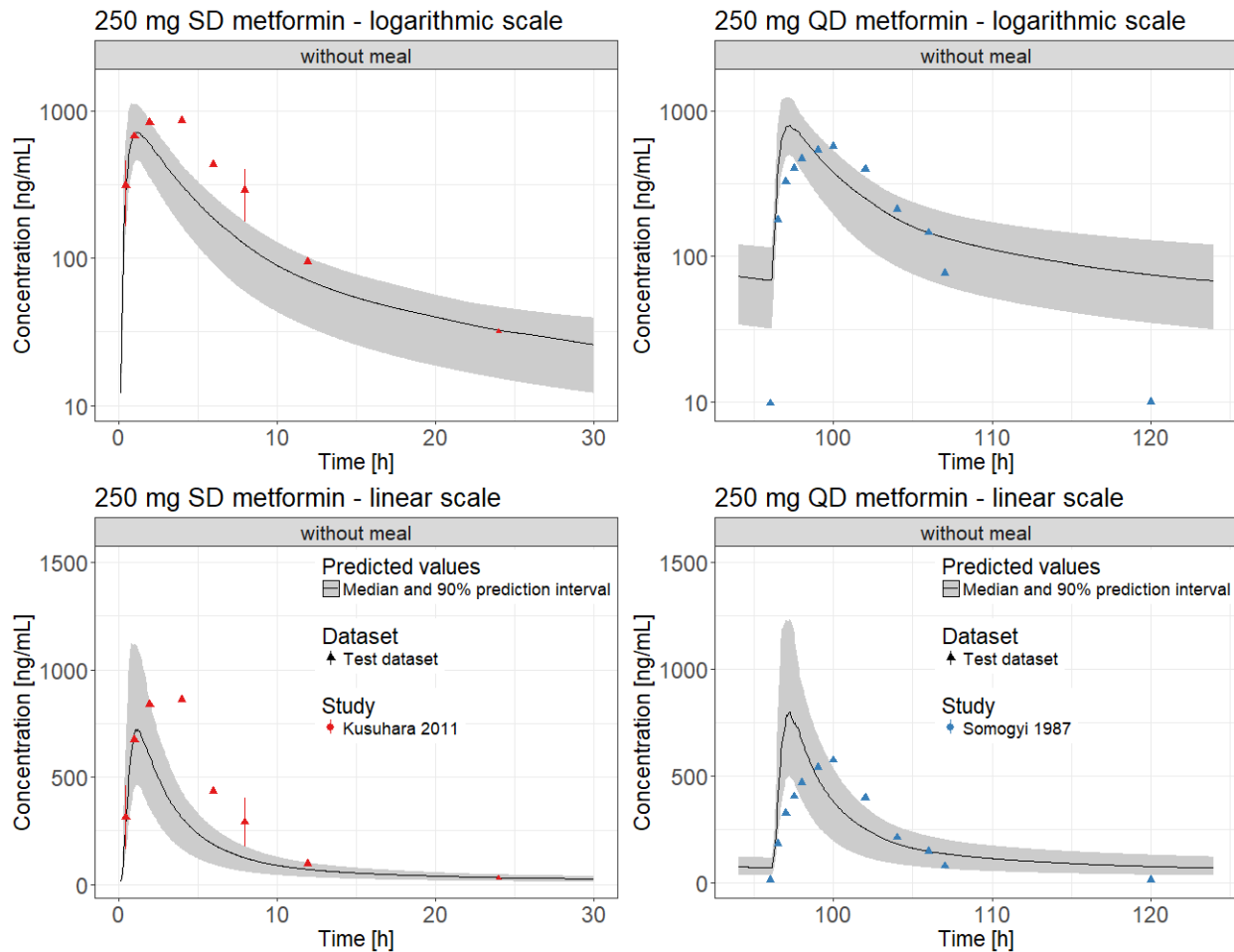
Suppl. Fig. 7 Training dataset: Population simulations compared to observed data of metformin plasma concentrations following single oral administration of 1000 mg. Clinical data are shown as dots [15]. Population simulation medians are shown as lines; the shaded areas depict the 5th - 95th percentile population prediction intervals



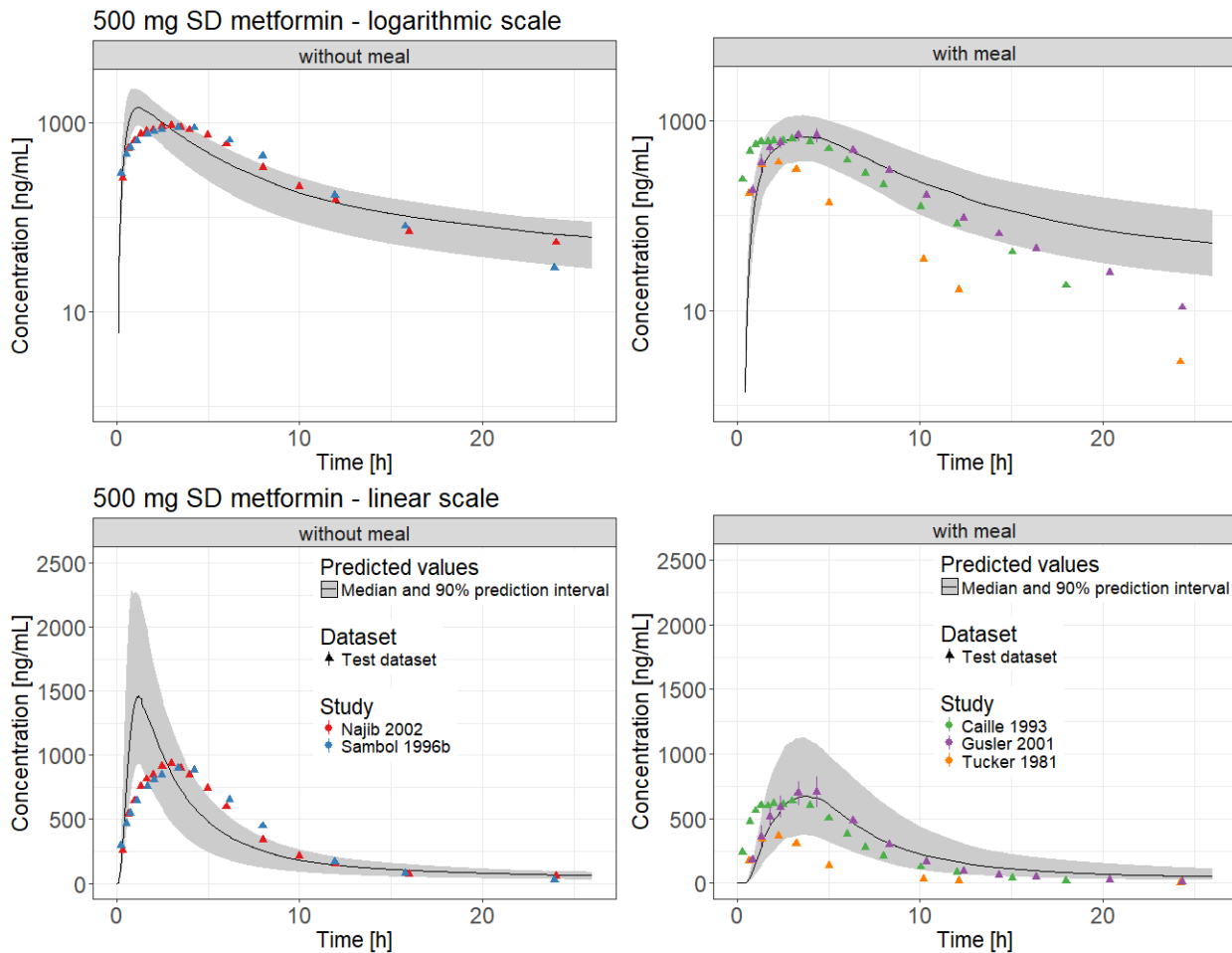
Suppl. Fig. 8 Training dataset: Population simulations compared to observed data of metformin plasma (left panel) and whole blood (right panel) concentrations following single oral administration of 1500 mg. Clinical data are shown as dots [3]. Population simulation medians are shown as lines; the shaded areas depict the 5th - 95th percentile population prediction intervals



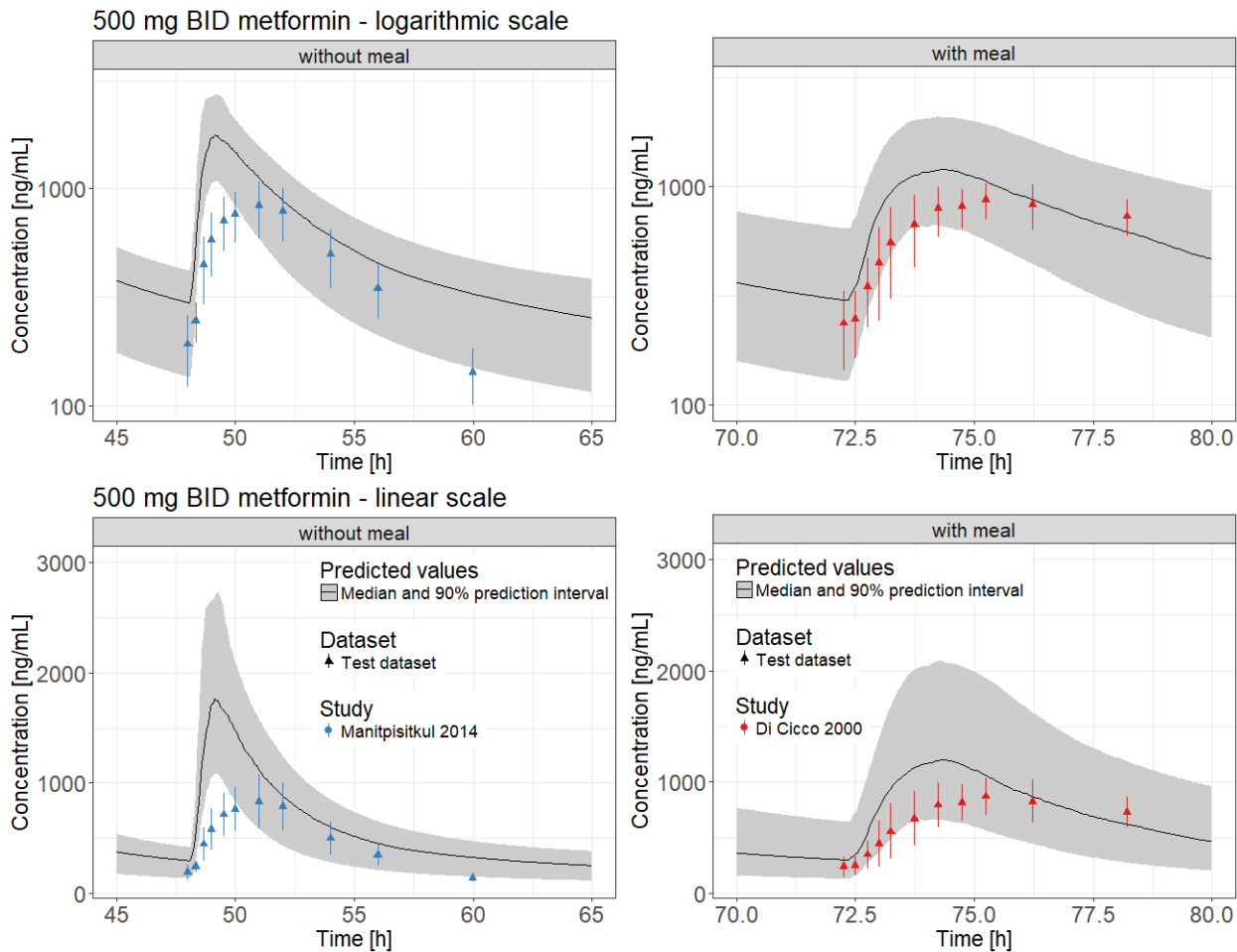
Suppl. Fig. 9 Test dataset: Population simulations compared to observed data of metformin plasma concentrations following intravenous administration of 1000 mg. Clinical data are shown as triangles (+/- standard deviation) [16]. Population simulation medians are shown as lines; the shaded areas depict the 5th - 95th percentile population prediction intervals



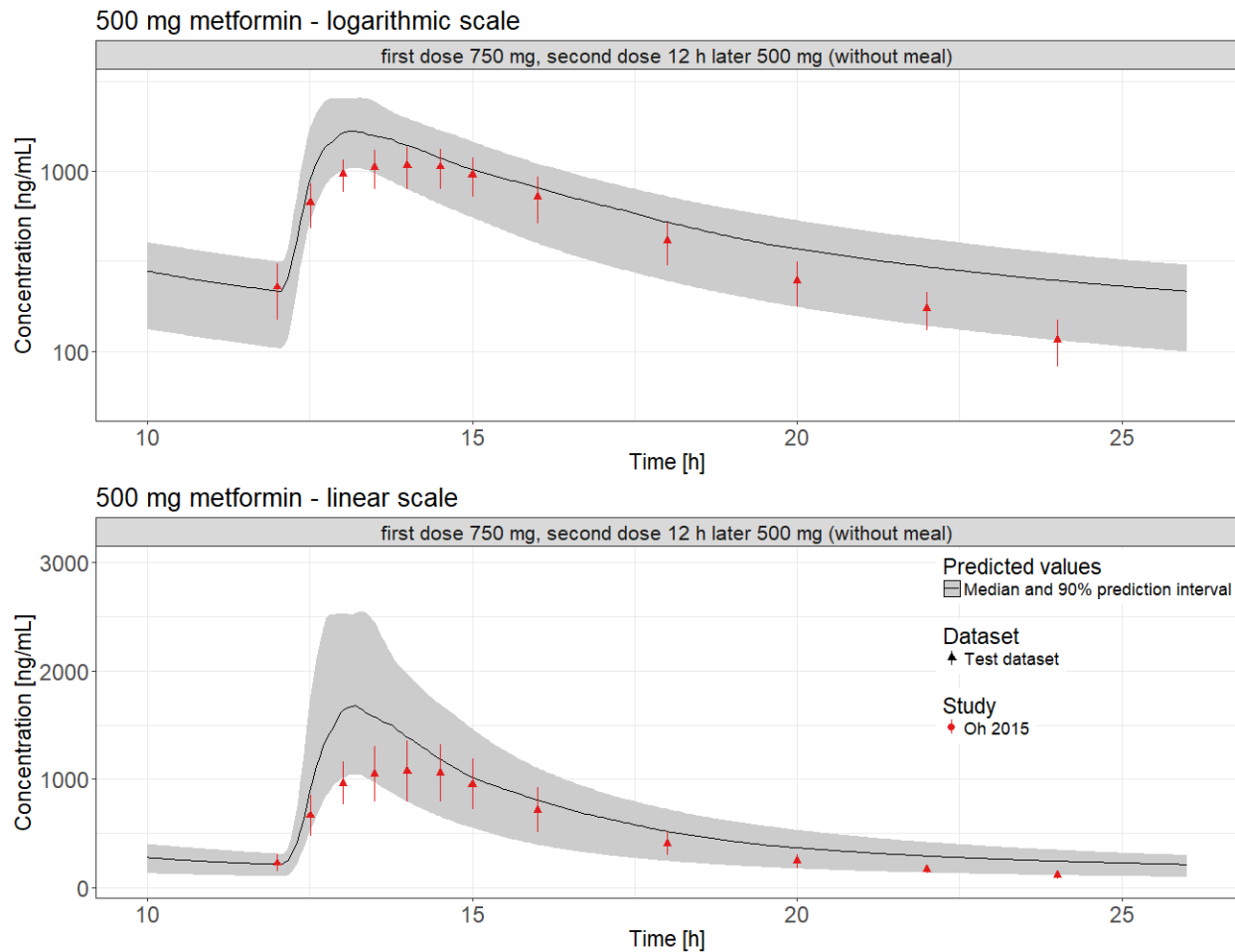
Suppl. Fig. 10 Test dataset: Population simulations compared to observed data of metformin plasma concentrations following single oral administration (left panel) and once daily oral administration (right panel) of 250 mg. Clinical data are shown as triangles (+/- standard deviation) [7, 17]. Population simulation medians are shown as lines; the shaded areas depict the 5th - 95th percentile population prediction intervals



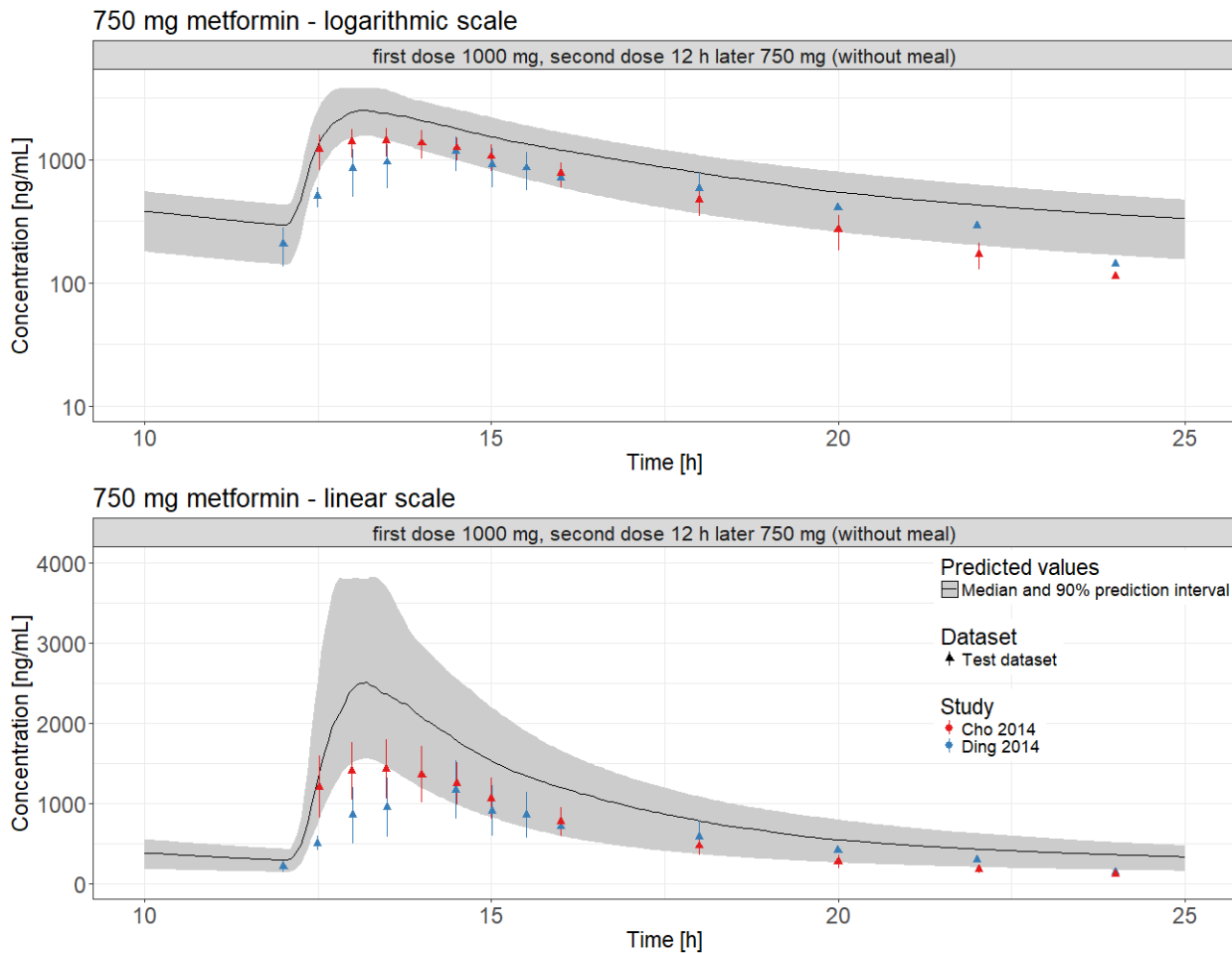
Suppl. Fig. 11 Test dataset: Population simulations compared to observed data of metformin plasma concentrations following single oral administration of 500 mg without meal (left panel) and with meal (right panel). Clinical data are shown as triangles (+/- standard deviation) [3, 18–21]. Population simulation medians are shown as lines; the shaded areas depict the 5th - 95th percentile population prediction intervals



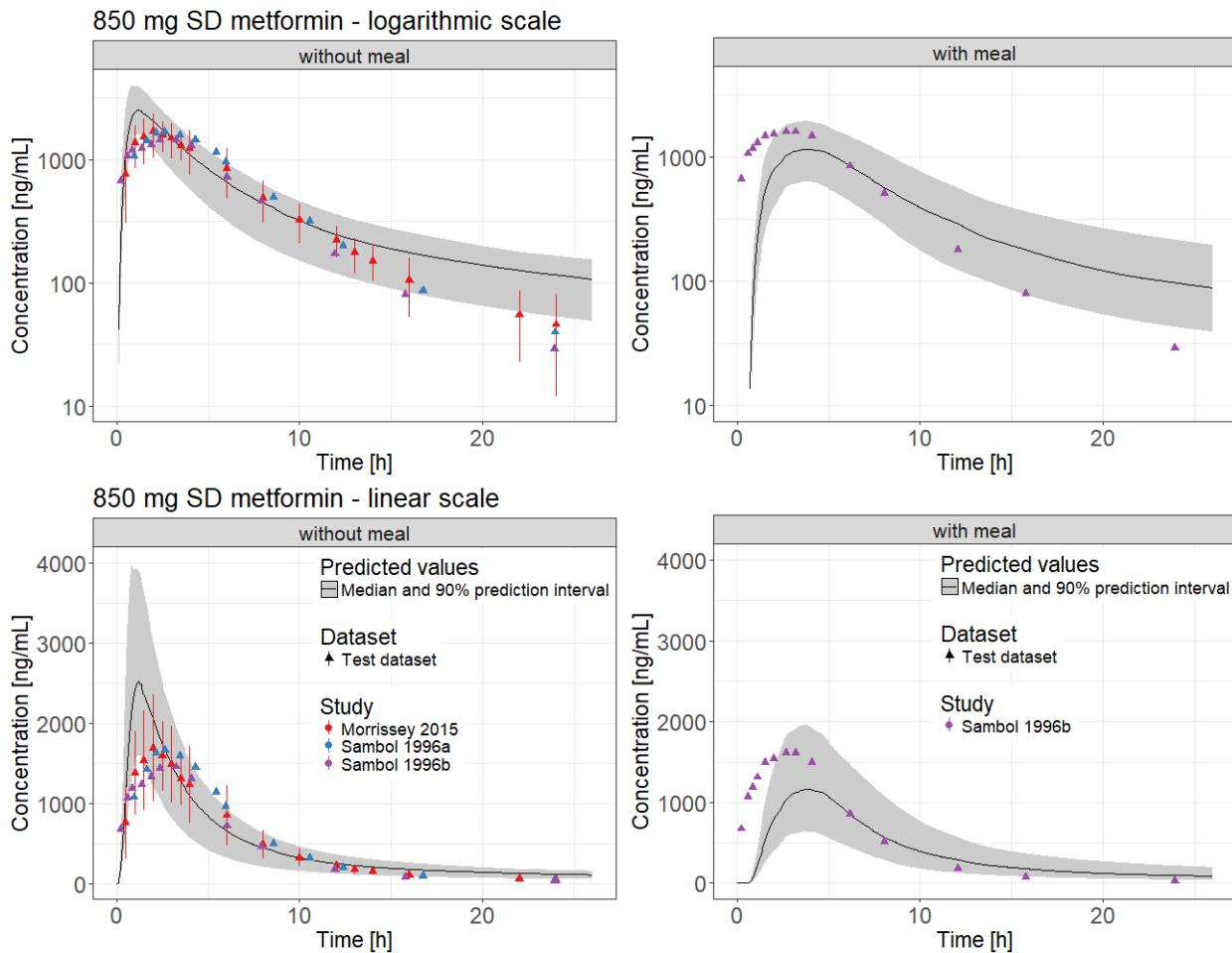
Suppl. Fig. 12 Test dataset: Population simulations compared to observed data of metformin plasma concentrations following twice daily oral administration of 500 mg without meal (left panel) and with meal (right panel). Clinical data are shown as triangles (+/- standard deviation) [22, 23]. Population simulation medians are shown as lines; the shaded areas depict the 5th - 95th percentile population prediction intervals



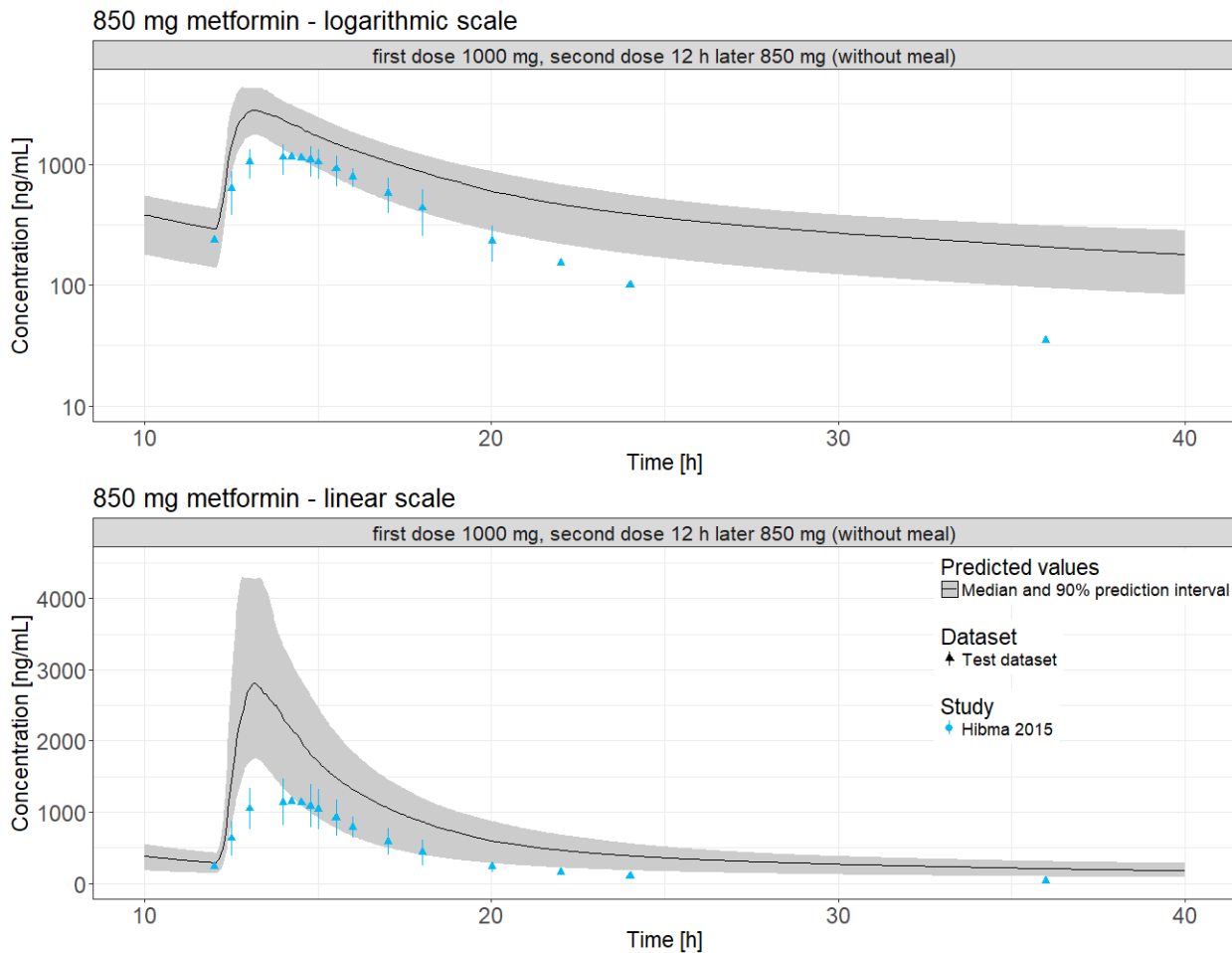
Suppl. Fig. 13 Test dataset: Population simulations compared to observed data of metformin plasma concentrations following oral administration of 500 mg, 12 h after a single oral administration of 750 mg metformin. Clinical data are shown as triangles (+/- standard deviation) [24]. Population simulation medians are shown as lines; the shaded areas depict the 5th - 95th percentile population prediction intervals



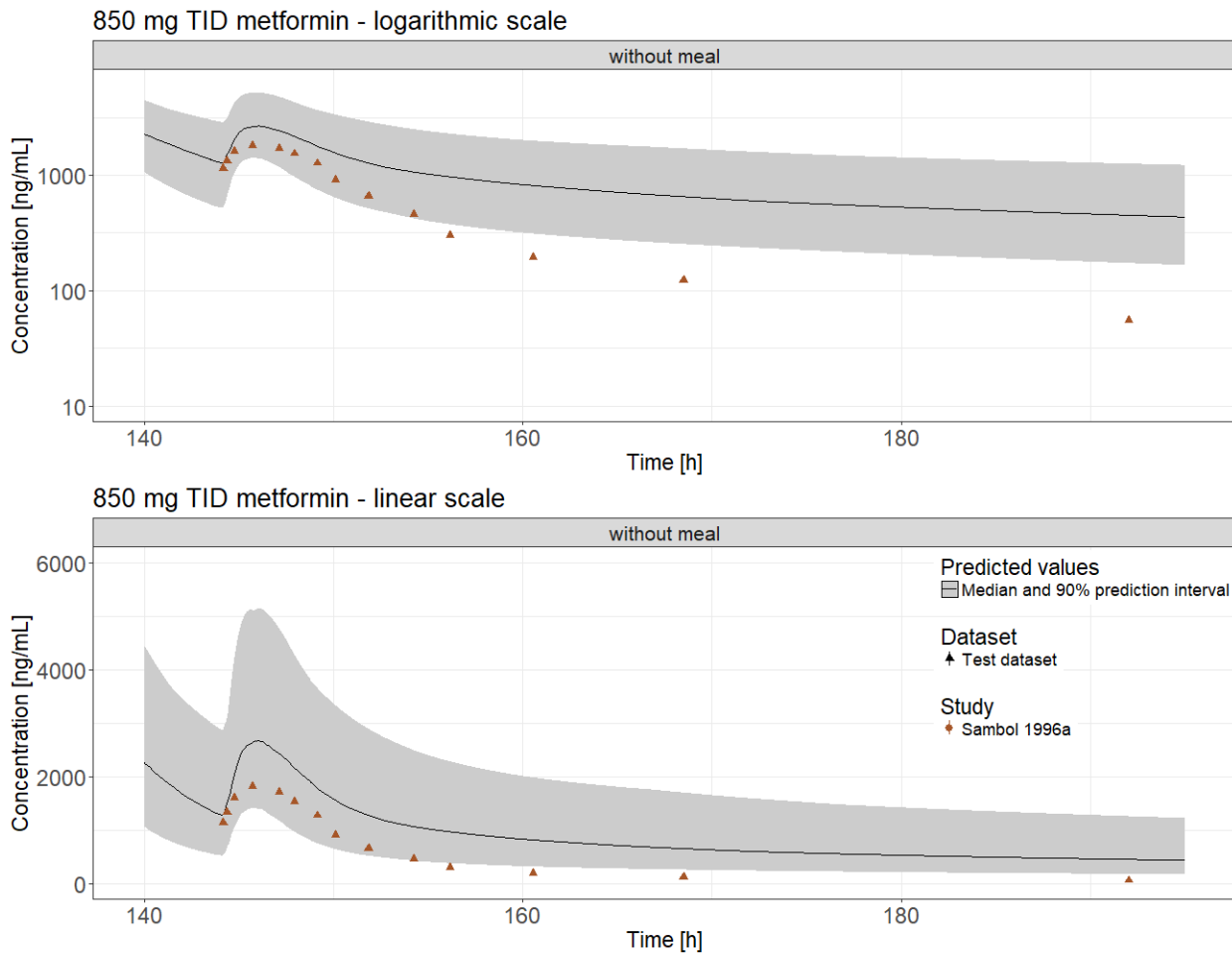
Suppl. Fig. 14 Test dataset: Population simulations compared to observed data of metformin plasma concentrations following oral administration of 750 mg, 12 h after a single oral administration of 1000 mg metformin. Clinical data are shown as triangles (+/- standard deviation) [25, 26]. Population simulation medians are shown as lines; the shaded areas depict the 5th - 95th percentile population prediction intervals



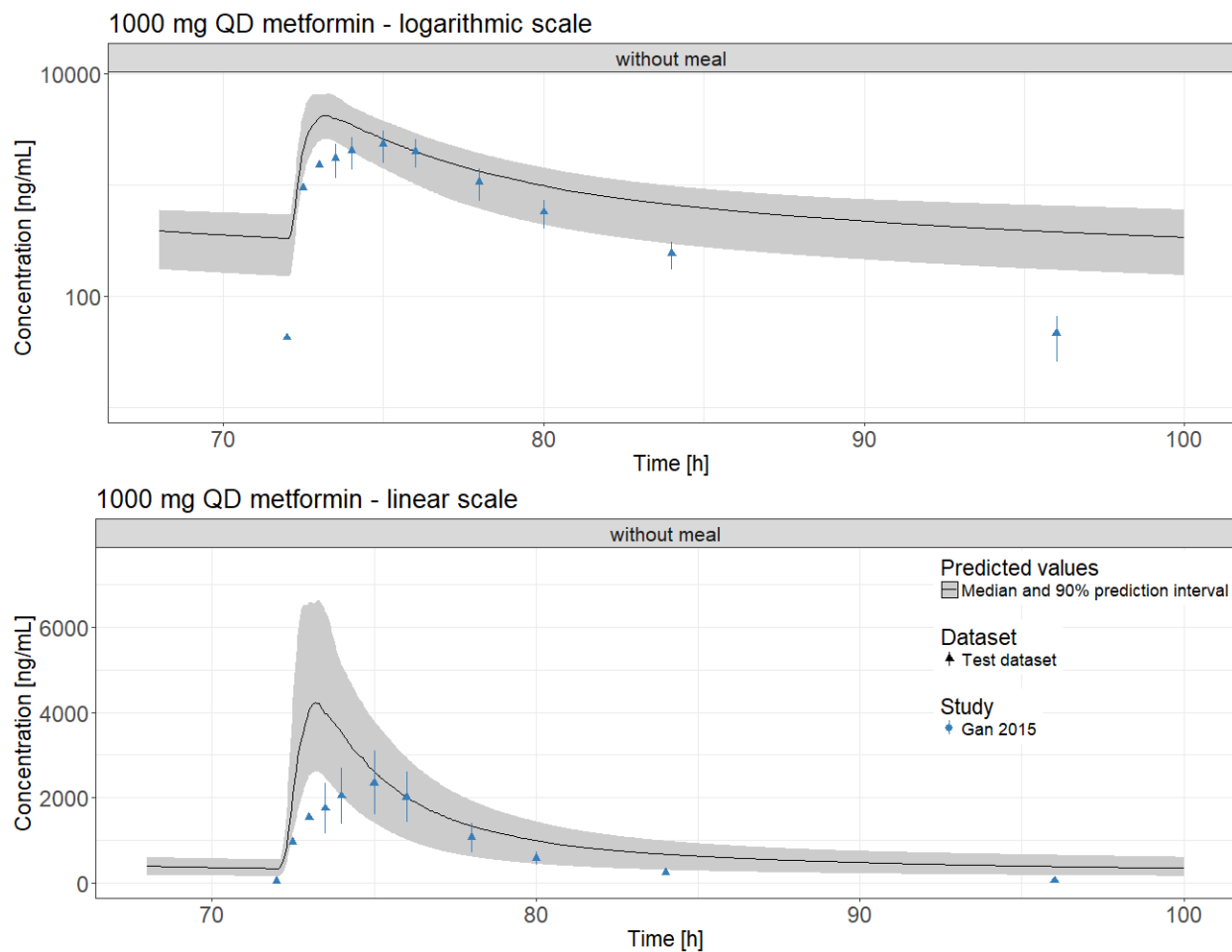
Suppl. Fig. 15 Test dataset: Population simulations compared to observed data of metformin plasma concentrations following single oral administration of 850 mg without meal (left panel) and with meal (right panel). Clinical data are shown as triangles (+/- standard deviation) [21, 27, 28]. Population simulation medians are shown as lines; the shaded areas depict the 5th - 95th percentile population prediction intervals



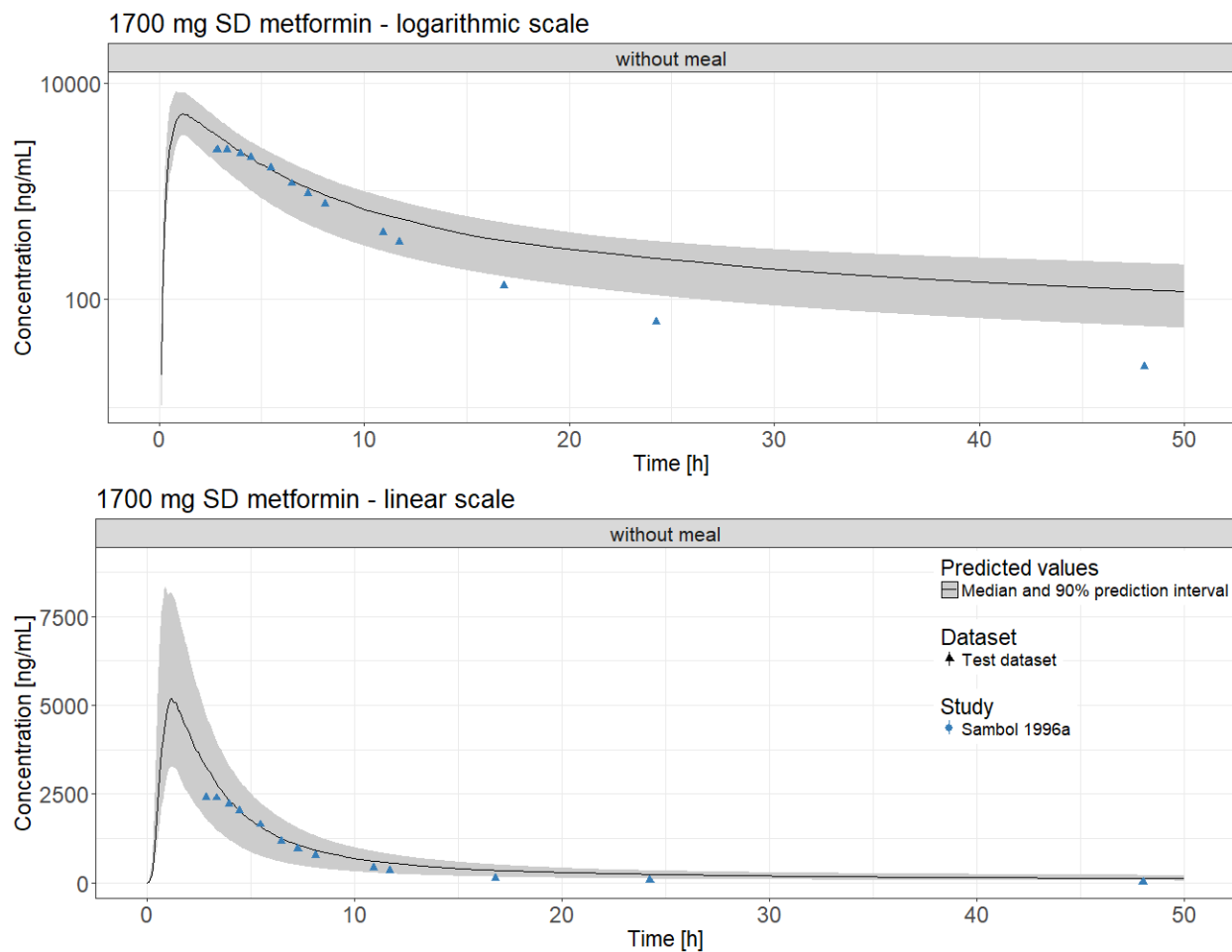
Suppl. Fig. 16 Test dataset: Population simulations compared to observed data of metformin plasma concentrations following oral administration of 850 mg, 12 h after a single oral administration of 1000 mg metformin. Clinical data are shown as triangles (+/- standard deviation) [4]. Population simulation medians are shown as lines; the shaded areas depict the 5th - 95th percentile population prediction intervals



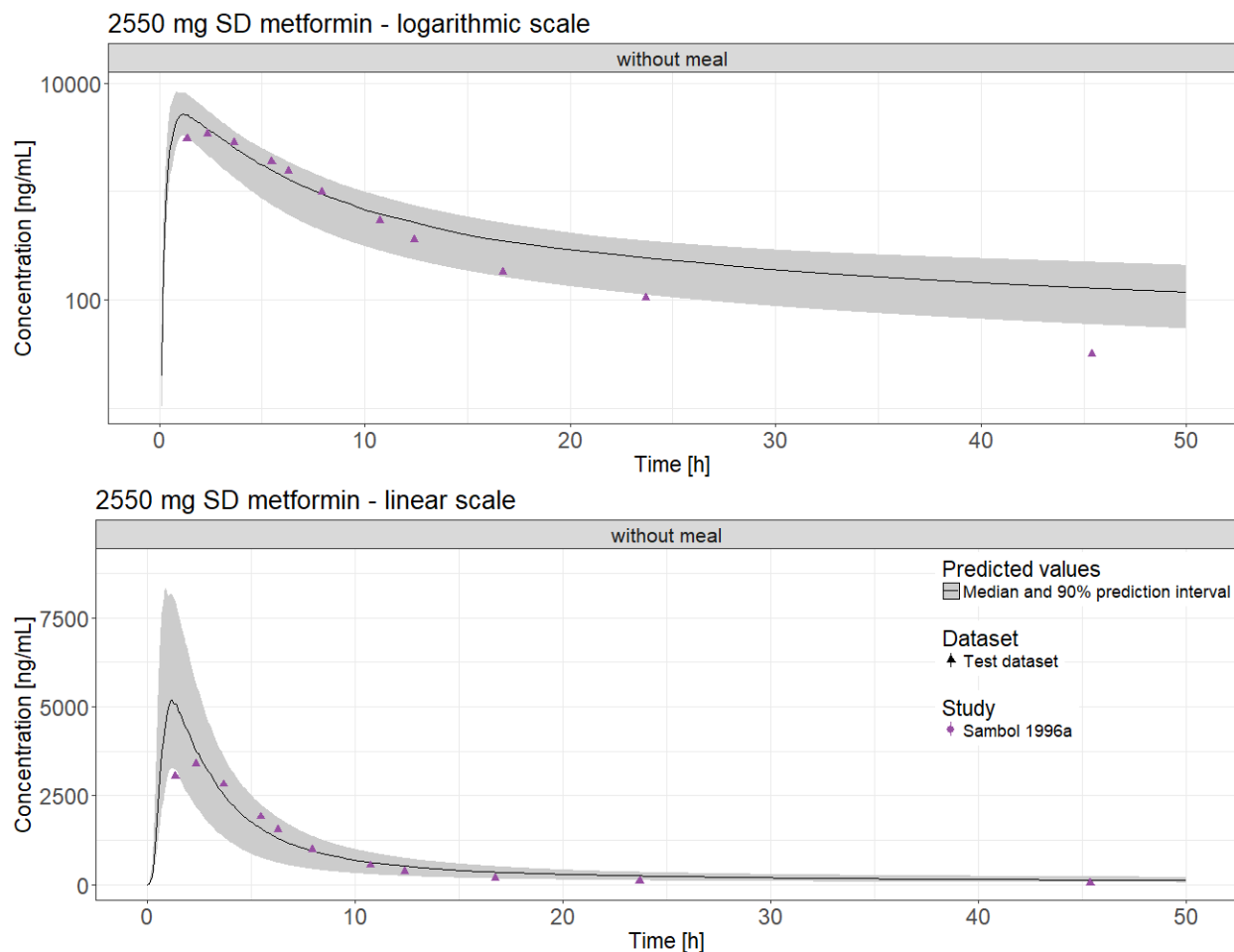
Suppl. Fig. 17 Test dataset: Population simulations compared to observed data of metformin plasma concentrations following three times daily oral administration of 850 mg. Clinical data are shown as triangles [28]. Population simulation medians are shown as lines; the shaded areas depict the 5th - 95th percentile population prediction intervals



Suppl. Fig. 18 Test dataset: Population simulations compared to observed data of metformin plasma concentrations following once daily oral administration of 1000 mg. Clinical data are shown as triangles (+/- standard deviation) [29]. Population simulation medians are shown as lines; the shaded areas depict the 5th - 95th percentile population prediction intervals



Suppl. Fig. 19 Test dataset: Population simulations compared to observed data of metformin plasma concentrations following single oral administration of 1700 mg. Clinical data are shown as triangles [28]. Population simulation medians are shown as lines; the shaded areas depict the 5th - 95th percentile population prediction intervals



Suppl. Fig. 20 Test dataset: Population simulations compared to observed data of metformin plasma concentrations following single oral administration of 2550 mg. Clinical data are shown as triangles [28]. Population simulation medians are shown as lines; the shaded areas depict the 5th - 95th percentile population prediction intervals

Suppl. Tab. 1 Studies used for metformin PBPK model development and evaluation

Dose (mg)	Administration	n	Women (%)	Age (years)	Weight (kg)	Food intake	Dataset	Study reference
250	iv (15 min), SD	4	0	30-36	64-83	no	training	[3]
500	iv (5 min), SD	3	67	36-39	58-63	no	training	[2]
1000	iv (bolus), SD	5	20	36-60	64-81	no	test	[16]
250	po (tab), SD	8	0	22-34	54-77	no	test	[7]
250	po (tab), QD	7	57	19-23	55-78	no	test	[17]
500	po (tab), SD	24	0	26	-	yes	test	[18]
500	po (tab), SD	15	53	37	82	yes	test	[19]
500	po (tab), SD	24	0	18-31	52-80	no	test	[20]
500	po (tab), SD	5	60	36-51	56-80	no	training	[2]
500	po (tab), SD	24	0	21-35	-	no	test	[21]
500	po (tab), SD	12	-	-	-	no	training	[12]
500	po (tab), SD	4	0	30-36	64-83	yes	test	[3]
500	po (tab), BID	16	0	22-55	71-119	yes	test	[22]
500	po (tab), BID	18	44	18-37	53-104	no	test	[23]
500	po (tab), MD ^a	20	0	23	67	no	training	[13]
500	po (tab), MD ^b	24	0	26	71	no	training	[14]
500	po (tab), MD ^a	20	0	-	-	no	test	[24]
750	po (tab), MD ^c	20	0	35	-	no	test	[26]
750	po (tab), MD ^c	12	0	27	71	no	test	[25]
850	po (tab), SD	12	50	23-33	49-101	no	test	[27]
850	po (tab), SD	6	33	25-46	-	yes	training	[8]
850	po (tab), SD	9	44	46	76	no	test	[28]
850	po (tab), SD	24	0	21-35	-	no	test	[21]
850	po (tab), SD	24	0	21-35	-	yes	test	[21]
850	po (tab), MD ^d	12	33	21-40	-	no	test	[4]
850	po (tab), TID	9	44	46	76	no	test	[28]
1000	po (tab), QD	27	11	20-55	-	no	test	[29]
1000	po (tab), SD	14	0	20-47	60-106	no	training	[15]
1500	po (tab), SD	4	0	30-36	64-83	yes	training	[3]
1700	po (tab), SD	9	44	46	76	no	test	[28]
2550	po (tab), SD	9	44	46	76	no	test	[28]

^a: first dose 750 mg, second dose 12 hours later 500 mg, ^b: first dose 750 mg, second dose 10 hours later 500 mg, ^c: first dose 1000 mg, second dose 12 hours later 750 mg, ^d: first dose 1000 mg, second dose 12 hours later 850 mg, BID: twice daily, iv: intravenous, MD: multiple dosing, n: number of individuals studied, po: peroral, QD: once daily, SD: single dose, tab: tablet, test: test dataset (model evaluation), TID: three times daily, training: training dataset (model development and parameter optimization), -: no data available. Values given for age and weight are arithmetic means, minima and maxima

Suppl. Tab. 2 Drug-dependent parameters of the metformin PBPK model

Parameter	Unit	Metformin model	Metformin reference	Description
MW	g/mol	129.16	-	Molecular weight
pKa	-	11.50 (base)	[30]	Acid dissociation constant
Solubility	g/L	100	not solubility limited	Solubility
logP	-	-1.43	[30]	Lipophilicity
fu	%	100	[2]	Fraction unbound
OCT2 K _M	μmol/L	22.22	optimized	Michaelis-Menten constant
OCT2 k _{cat}	1/min	92.79	optimized	Transportation rate
MATE2-K K _M	μmol/L	362.00	[7]	Michaelis-Menten constant
MATE2-K k _{cat}	1/min	184.11	optimized	Transportation rate
GFR fraction	-	1	-	Fraction of glomerular filtration
EHC continuous fraction	-	1 ^a	-	Fraction of bile bypassing gallbladder
Administration	-	tab	[31]	Route of administration
Perm. (plasma-blood cells)	cm/min	6.95E-08	optimized	Plasma to blood cell perm.
Perm. (blood cells-plasma)	cm/min	8.12E-08	optimized	Blood cell to plasma perm.
Perm. (interstitial-intracellular)	cm/min	4.53E-05 ^b	optimized	Interstitial to intracellular perm.
Perm. (intracellular-interstitial)	cm/min	2.20E-06 ^b	optimized	Intracellular to interstitial perm.
Partition coefficients	-	calculated	R + R	Organ-plasma partitioning
Specific intest. perm. (para.)	cm/min	3.65E-06	optimized	Normalized paracellular intest. perm.
Specific intest. perm. (trans.)	cm/min	0	[32]	Normalized transcellular intest. perm.

^a: changes to 0.35 after food intake, ^b: in kidney 0, EHC: enterohepatic circulation, intest.: intestinal, MATE2-K: multidrug and toxin extrusion protein

2-K, OCT2: organic cation transporter 2, para.: paracellular, perm.: permeability, PK-Sim: PK-Sim standard calculation method, R + R: Rodgers and

Rowland calculation method [33, 34], tab: tablet - digitized dissolution profile from literature used, trans.: transcellular

Suppl. Tab. 3 System-dependent parameters of the metformin PBPK model

Transporter	Reference concentration, tissue of highest expression ($\mu\text{mol/L}$)	Geometric standard deviation in virtual populations	Tissue localization (relative expression, normalized to tissue with highest expression)
OCT2	1.09 [35, 36]	1.28 ($\triangle 25\% \text{CV}$)	Kidney 1.0 [37]
MATE2-K	1.0 [38]	1.28 ($\triangle 25\% \text{CV}$)	Kidney 1.0 [39]

MATE2-K: multidrug and toxin extrusion protein 2-K, OCT2: organic cation transporter 2. If no information on reference concentration was available it was set to 1.0 $\mu\text{mol/L}$ and the transportation rate (k_{cat}) was optimized according to [38]

Supplementary References

1. Squibb B-M (2008) Glucophage® XR Label. Bristol-Myers Squibb Co 3–32
2. Pentikainen PJ, Neuvonen PJ, Penttila A (1979) Pharmacokinetics of metformin after intravenous and oral administration to man. *Eur J Clin Pharmacol* 16:195–202
3. Tucker GT, Casey C, Phillips PJ, Connor H, Ward JD, Woods HF (1981) Metformin kinetics in healthy subjects and in patients with diabetes mellitus. *Br J Clin Pharmacol* 12:235–246
4. Hibma JE, Zur AA, Castro RA, Wittwer MB, Keizer RJ, Yee SW, Goswami S, Stocker SL, Zhang X, Huang Y, Brett CM, Savic RM, Giacomini KM (2015) The effect of famotidine, a MATE1-selective inhibitor, on the pharmacokinetics and pharmacodynamics of metformin. *Clin Pharmacokinet* 55:711–721
5. Chen L, Pawlikowski B, Schlessinger A, More SS, Stryke D, Johns SJ, Portman MA, Chen E, Ferrin TE, Sali A, Giacomini KM (2010) Role of organic cation transporter 3 (SLC22A3) and its missense variants in the pharmacologic action of metformin. *Pharmacogenet Genomics* 20:687–699
6. Kimura N, Masuda S, Tanihara Y, Ueo H, Okuda M, Katsura T, Inui K-I (2005) Metformin is a superior substrate for renal organic cation transporter OCT2 rather than hepatic OCT1. *Drug Metab Pharmacokinet* 20:379–386
7. Kusuhsara H, Ito S, Kumagai Y, Jiang M, Shiroshita T, Moriyama Y, Inoue K, Yuasa H, Sugiyama Y (2011) Effects of a MATE protein inhibitor, pyrimethamine, on the renal elimination of metformin at oral microdose and at therapeutic dose in healthy subjects. *Clin Pharmacol Ther* 89:837–844
8. Robert F, Fendri S, Hary L, Lacroix C, Andréjak M, Lalau J (2003) Kinetics of plasma and erythrocyte metformin after acute administration in healthy subjects. *Diabetes Metab* 29:279–283
9. Valentin J (2002) Basic anatomical and physiological data for use in radiological protection: reference values. *Ann ICRP* 32:1–277
10. Scheen AJ (1996) Clinical pharmacokinetics of metformin. *Clin Pharmacokinet* 30:359–371
11. U.S. Food and Drug Administration (2012) Drug Interaction Studies - Study Design, Data Analysis, Implications for Dosing, and Labeling Recommendations. Draft Guidance for Industry.
12. Tache F, David V, Farca A, Medvedovici A (2001) HPLC-DAD determination of metformin in human plasma using derivatization with p-nitrobenzoyl chloride in a biphasic system. *Microchem J* 68:13–19
13. Jang K, Chung H, Yoon J, Moon S-J, Yoon SH, Yu K-S, Kim K, Chung J-Y (2016) Pharmacokinetics, safety, and tolerability of metformin in healthy elderly subjects. *J Clin Pharmacol* 56:1104–1110
14. Kim A, Chung I, Yoon SH, Yu K-S, Lim KS, Cho J-Y, Lee H, Jang I-J, Chung JY (2014) Effects of proton pump inhibitors on metformin pharmacokinetics and pharmacodynamics. *Drug Metab Dispos* 42:1174–1179
15. Johansson S, Read J, Oliver S, Steinberg M, Li Y, Lisbon E, Mathews D, Leese PT, Martin P (2014) Pharmacokinetic evaluations of the co-administrations of vandetanib and metformin, digoxin, midazolam, omeprazole or ranitidine. *Clin Pharmacokinet* 53:837–847
16. Sirtori CR, Franceschini G, Galli-Kienle M, Cighetti G, Galli G, Bondioli A, Conti F (1978) Disposition of metformin (N,N-dimethylbiguanide) in man. *Clin Pharmacol Ther* 24:683–693
17. Somogyi A, Stockley C, Keal J, Rolan P, Bochner F (1987) Reduction of metformin renal tubular secretion by cimetidine in man. *Br J Clin Pharmacol* 23:545–551
18. Caillé G, Lacasse Y, Raymon M, Landriault H, Perrotta M, Picirilli G, Thiffault J, Spénard J (1993) Bioavailability of metformin in tablet form using a new high pressure liquid chromatography assay method. *Biopharm Drug Dispos* 14:257–263
19. Gusler G, Gorsline J, Levy G, Zhang SZ, Weston IE, Naret D, Berner B (2001) Pharmacokinetics of metformin gastric-retentive tablets. *J Clin Pharmacol* 41:655–661
20. Najib N, Idkaidek N, Beshtawi M, Bader M, Admour I, Alam SM, Zaman Q, Dham R (2002)

- Bioequivalence evaluation of two brands of metformin 500 mg tablets (Dialon ® & Glucophage ®) - in healthy human volunteers. *Biopharm Drug Dispos* 23:301–306
21. Sambol NC, Brookes LG, Chiang J, Goodman AM, Lin ET, Liu CY, Benet LZ (1996) Food intake and dosage level, but not tablet vs solution dosage form, affect the absorption of metformin HCl in man. *Br J Clin Pharmacol* 42:510–2
22. Di Cicco R a, Allen A, Carr A, Fowles S, Jorkasky DK, Freed MI (2000) Rosiglitazone does not alter the pharmacokinetics of metformin. *J Clin Pharmacol* 40:1280–5
23. Manitpitsitkul P, Curtin CR, Shalayda K, Wang S-S, Ford L, Heald D (2014) Pharmacokinetic interactions between topiramate and pioglitazone and metformin. *Epilepsy Res* 108:1519–1532
24. Oh J, Chung H, Park S-I, Yi SJ, Jang K, Kim AH, Yoon J, Cho J-Y, Yoon SH, Jang I-J, Yu K-S, Chung J-Y (2016) Inhibition of the multidrug and toxin extrusion (MATE) transporter by pyrimethamine increases the plasma concentration of metformin but does not increase antihyperglycaemic activity in humans. *Diabetes, Obes Metab* 18:104–108
25. Cho SK, Kim CO, Park ES, Chung J-Y (2014) Verapamil decreases the glucose-lowering effect of metformin in healthy volunteers. *Br J Clin Pharmacol* 78:1426–1432
26. Ding Y, Jia Y, Song Y, Lu C, Li Y, Chen M, Wang M, Wen A (2014) The effect of lansoprazole, an OCT inhibitor, on metformin pharmacokinetics in healthy subjects. *Eur J Clin Pharmacol* 70:141–146
27. Morrissey KM, Stocker SL, Chen EC, Castro RA, Brett CM, Giacomini KM (2015) The effect of nizatidine, a MATE2K selective inhibitor, on the pharmacokinetics and pharmacodynamics of metformin in healthy volunteers. *Clin Pharmacokinet* 55:495–506
28. Sambol NC, Chiang J, O'Conner M, Liu CY, Lin ET, Goodman AM, Benet LZ, Karam JH (1996) Pharmacokinetics and pharmacodynamics of metformin in healthy subjects and patients with noninsulin-dependent diabetes mellitus. *J Clin Pharmacol* 36:1012–1021
29. Gan L, Jiang X, Mendonza A, Swan T, Reynolds C, Nguyen J, Pal P, Neelakantham S, Dahlke M, Langenickel T, Rajman I, Akahori M, Zhou W, Rebello S, Sunkara G (2016) Pharmacokinetic drug-drug interaction assessment of LCZ696 (an angiotensin receptor neprilysin inhibitor) with omeprazole, metformin or levonorgestrel-ethynodiol in healthy subjects. *Clin Pharmacol Drug Dev* 5:27–39
30. Graham GG, Punt J, Arora M, Day RO, Doogue MP, Duong JK, Furlong TJ, Greenfield JR, Greenup LC, Kirkpatrick CM, Ray JE, Timmins P, Williams KM (2011) Clinical pharmacokinetics of metformin. *Clin Pharmacokinet* 50:81–98
31. Block LC, Schemling LO, Couto AG, Mourão SC, Bresolin TMB (2008) Pharmaceutical equivalence of metformin tablets with various binders. *Rev Cienc Farm Basica Apl* 29:29–35
32. Proctor WR, Bourdet DL, Thakker DR (2008) Mechanisms underlying saturable intestinal absorption of metformin. *Drug Metab Dispos* 36:1650–1658
33. Rodgers T, Leahy D, Rowland M (2005) Physiologically based pharmacokinetic modeling 1: Predicting the tissue distribution of moderate-to-strong bases. *J Pharm Sci* 94:1259–1276
34. Rodgers T, Rowland M (2006) Physiologically based pharmacokinetic modelling 2: Predicting the tissue distribution of acids, very weak bases, neutrals and zwitterions. *J Pharm Sci* 95:1238–1257
35. Chen Y, Li S, Brown C, Cheatham S, Castro RA., Leabman MK., Urban TJ, Chen L, Yee SW, Choi JH, Huang Y, Brett CM., Burchard EG., Giacomini KM (2009) Effect of genetic variation in the organic cation transporter 2 on the renal elimination of metformin. *Pharmacogenet Genomics* 19:497–504
36. National Center for Biotechnology Information dbSNP entry for rs316019
37. Nishimura M, Naito S (2005) Tissue-specific mRNA expression profiles of human ATP-binding cassette and solute carrier transporter superfamilies. *Drug Metab Pharmacokinet* 20:452–477
38. Meyer M, Schneckener S, Ludewig B, Kuepfer L, Lippert J (2012) Using expression data for

quantification of active processes in physiologically-based pharmacokinetic modeling. *Drug Metab Dispos* 40:892–901

39. Masuda S, Terada T, Yonezawa A, Tanihara Y, Kishimoto K, Katsura T, Ogawa O, Inui K (2006) Identification and functional characterization of a new human kidney-specific H⁺/organic cation antiporter, kidney-specific multidrug and toxin extrusion 2. *J Am Soc Nephrol* 17:2127–2135

A physiologically-based pharmacokinetic (PBPK) parent-metabolite model of the chemotherapeutic zoxtarelin doxorubicin - integration of in vitro results, Phase I and Phase II data and model application for drug-drug interaction potential analysis

Simvastatin Supplementary

Nina Hanke ¹, Michael Teifel ², Daniel Moj ¹, Jan-Georg Wojtyniak ¹, Hannah Britz ¹, Babette Aicher ²,
Herbert Sindermann ², Nicola Ammer ², Thorsten Lehr ¹

¹ Clinical Pharmacy, Saarland University, Saarbruecken, Germany

² Aeterna Zentaris GmbH, Weismuellerstr. 50, Frankfurt, Germany

Corresponding Author: Thorsten Lehr, Clinical Pharmacy, Saarland University, Campus C2 2, 66123
Saarbruecken, +49 681 302 70255, thorsten.lehr@mx.uni-saarland.de

PBPK model of simvastatin lactone and simvastatin acid

1. Introduction

Simvastatin is a 3-hydroxy-3-methylglutaryl (HMG) coenzyme A reductase inhibitor. It is widely used in the treatment of hypercholesterolemia and belongs to the ten most prescribed drugs in industrial nations [1]. Simvastatin is administered orally as a prodrug in its lactone form (dosing range 5 - 80 mg/day [2]) and is converted to the active acid by a combination of enzyme-mediated hydrolysis and spontaneous chemical conversion [3]. The enzyme predominantly responsible for the hydrolysis of simvastatin lactone to simvastatin acid is paraoxonase 3 (PON3) [4, 5]. Simvastatin lactone is highly lipophilic, resulting in good absorption of approximately 60% of an administered dose, but shows extensive first pass metabolism reducing its oral bioavailability to 5% [3]. Simvastatin lactone is mainly metabolized by CYP3A4 [6], while simvastatin acid is metabolized by CYP3A4 (>80%) and CYP2C8 (<20%) as well as transported by organic anion-transporting polypeptide 1B (OATP1B) [7]. A further process discussed for the pharmacokinetics of simvastatin acid is recyclization to the lactone form, either spontaneously, or via enzymatic formation of an intermediate glucuronide. Suppl. Fig. 1 depicts the metabolism pathways of statins in general.

Objectives

The purpose of this work was to establish a whole body parent-metabolite PBPK model of simvastatin lactone (prodrug) and acid (pharmacologically active metabolite) as a CYP3A and OATP1B victim drug model for drug-drug interaction studies

- that accurately predicts plasma concentrations of simvastatin lactone and acid over a broad dosing range
- that has been evaluated by showing good prediction of simvastatin lactone and acid plasma concentrations in drug-drug interaction (DDI) studies with rifampicin and clarithromycin as CYP3A4 perpetrator drugs
- that has been evaluated by showing good prediction of simvastatin lactone and acid plasma concentrations in individuals with different OATP1B1 genotypes

2. Materials and Methods

Software

PBPK modeling was performed with PK-Sim 7.0.0. Parameter optimization was accomplished using the Monte Carlo algorithm implemented in PK-Sim. Digitization of published plasma concentration-time curves was performed with GetData Graph Digitizer (V 2.26). Graphics and further statistical analyses were generated with R (V 3.3.2) and the graphical user interface RStudio (V 1.0.136).

Model development

For model development, physicochemical parameters as well as plasma concentration-time profiles of simvastatin lactone and simvastatin acid after oral single dose (SD) and multiple dose (MD) administration (range 20 - 80 mg) were obtained from the literature. Data was separated into training and test datasets for model development and evaluation, respectively (for a detailed study summary see Suppl. Tab. 1). The training dataset contained a study showing the impact of different OATP1B1 genotypes on the plasma concentrations of simvastatin acid [8]. This study was included to define the contribution of this transporter to simvastatin acid pharmacokinetics. For studies that did not specify

the OATP1B1 genotype, the wild type variant was assumed. Due to the lack of clinical trials of direct administration of simvastatin acid, simvastatin lactone and simvastatin acid model development was performed in parallel.

For population simulations, a virtual Caucasian population was generated containing 50 male and 50 female individuals, 20 - 50 years of age, with body weights of 40 - 120 kg. The ICRP (International Commission on Radiological Protection) database in PK-Sim was used for generation of this population [13]. For model evaluation, the arithmetic means and 90% prediction intervals of population simulation plasma concentration-time profiles were calculated and used to generate visual predictive checks (predicted versus observed plasma concentrations) for the training and test datasets.

To test the contribution of the implemented CYP3A4 metabolism, the final simvastatin model was coupled to PBPK models of the CYP3A4 perpetrators rifampicin (CYP3A4 inducer, [9]) and clarithromycin (CYP3A4 inhibitor, [10]). Plasma concentrations of simvastatin lactone and simvastatin acid during co-administration with these perpetrator drugs were predicted and compared to observed data.

3. Results

Simvastatin modeling

To limit the number of parameters to be optimized, only the most important processes were implemented into the final simvastatin parent-metabolite model. For simvastatin lactone these are (1) PON3 mediated hydrolysis to generate simvastatin acid and (2) CYP3A4 mediated clearance. For simvastatin acid these are (3) hepatic uptake by OATP1B1 and (4) CYP3A4 mediated clearance. The OATP1B1 transport was implemented with two different K_m values and two different transport rates, to describe the impact of the investigated OATP1B1 polymorphism on simvastatin acid plasma concentrations. For both, parent and metabolite, glomerular filtration and enterohepatic cycling were enabled.

Drug-dependent parameters

All drug-dependent parameters taken from the literature with their references as well as all optimized parameter values are given in Suppl. Tab. 2.

System-dependent parameters

Expression of the implemented enzymes and transporters as well as the geometric standard deviation of their log-normal distribution in virtual populations are given in Suppl. Tab. 3. No other system-dependent parameters were changed or adjusted.

Model performance

Training dataset: The training dataset performance of the final model, predicting simvastatin lactone and simvastatin acid plasma concentrations following oral administration of 20, 40, 60 or 80 mg simvastatin lactone, is presented in Suppl. Fig. 2 - 6.

Suppl. Fig. 7 shows the predicted compared to observed plasma concentrations following oral administration of 40 mg simvastatin lactone to individuals with different OATP1B1 genotypes [8]. The transport rates of the two homozygous OATP1B1 isoforms (c.521TT wild type and c.521CC) were optimized, the transport rate of the heterozygous isoform (c.521TC) has been predicted.

Test dataset: The test dataset performance of the final model, predicting simvastatin lactone and simvastatin acid plasma concentrations following oral administration of 20, 40 or 80 mg simvastatin lactone, is presented in Suppl. Fig. 8 - 10.

Model application

As a further means of model evaluation, the final simvastatin model was applied to predict clinical DDI studies. Simvastatin plasma concentrations during two different trials studying co-administration of simvastatin lactone and the CYP3A4 perpetrator drugs rifampicin [11] and clarithromycin [12] were predicted and compared to observed data.

In the rifampicin DDI study, a single dose of 40 mg simvastatin lactone was administered 17 h after the last dose of a 600 mg QD, 5 day rifampicin regimen. Thus, no inhibitory effects of rifampicin on CYP3A4 or OATP1B1 are expected, solely pure CYP3A4 induction. In the clarithromycin DDI study, once daily doses of 40 mg simvastatin lactone were administered together with the morning doses of a 500 mg BID, 7 day clarithromycin regimen. Unfortunately, only simvastatin lactone plasma concentrations have been reported from this study, allowing no interpretation of the effect of clarithromycin on OATP1B1 and simvastatin acid. Predicted and observed plasma concentrations are shown in Suppl. Fig. 11 and 12. Predicted and observed AUC ratios (AUC during perpetrator treatment / AUC without co-administration of DDI perpetrator) of these DDIs are compared in Suppl. Tab. 4 and 5.

4. Discussion

Model performance

The final parent-metabolite PBPK model accurately describes the plasma concentration-time profiles of simvastatin lactone and simvastatin acid after oral administration of 20 - 80 mg simvastatin lactone. There is a slight terminal overprediction of the lactone, but not of the acid concentrations, following single dose administration of 40 mg simvastatin lactone. Nevertheless, the studies of multiple dose administration of 40 mg simvastatin lactone are well predicted. This phenomenon might be caused by variability in body weight or genetic polymorphisms of involved metabolizing enzymes or transporters of these relatively small study populations that have not been taken into account for the model predictions.

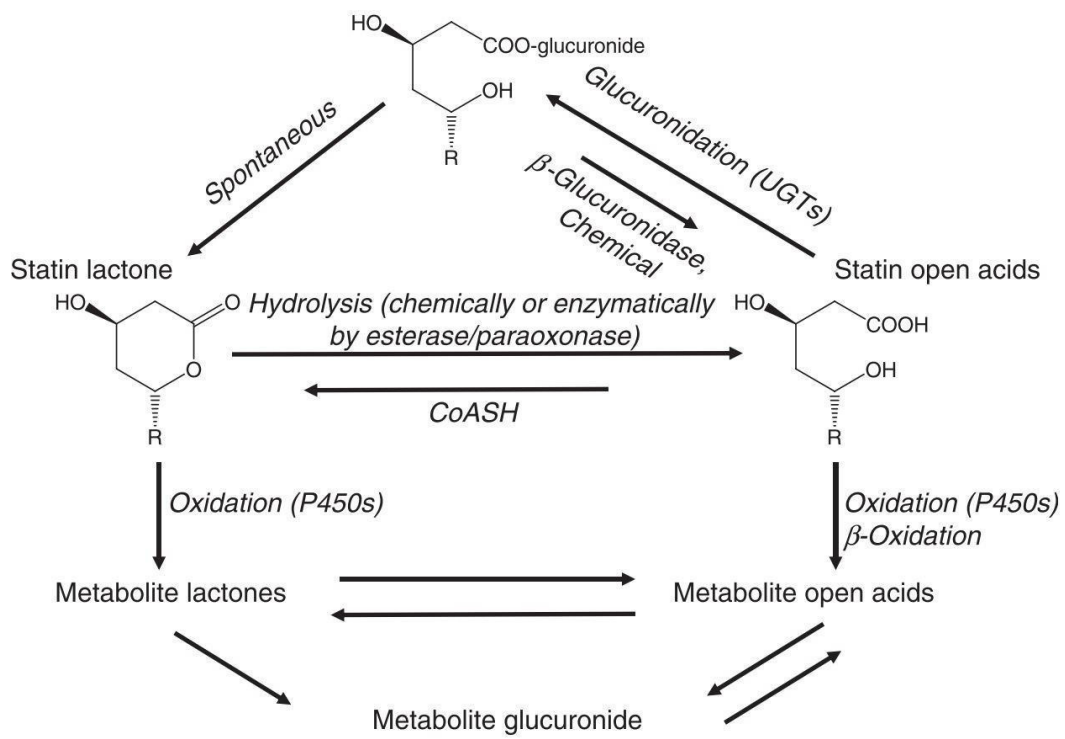
To define the contribution of OATP1B1 to the disposition of simvastatin acid, information of a clinical trial studying the impact of the OATP1B1 c.521 polymorphism on simvastatin acid pharmacokinetics has been included into the training dataset. The final simvastatin model accurately predicts the simvastatin acid plasma concentrations of individuals of the three possible OATP1B1 genotypes.

To evaluate the contribution of CYP3A4 to the metabolism of simvastatin lactone and simvastatin acid, clinical DDI studies with the CYP3A4 perpetrators rifampicin and clarithromycin have been predicted and compared to observed data. During the DDI with rifampicin, simvastatin lactone and simvastatin acid plasma concentrations are adequately predicted. In the DDI study with clarithromycin only simvastatin lactone concentrations have been reported and the effect of clarithromycin on simvastatin lactone peak plasma concentrations is underpredicted. Nevertheless, the predicted AUC ratios of simvastatin lactone and simvastatin acid are within twofold of the observed AUC ratios for both of the tested DDIs (see Suppl. Tab. 4 and 5).

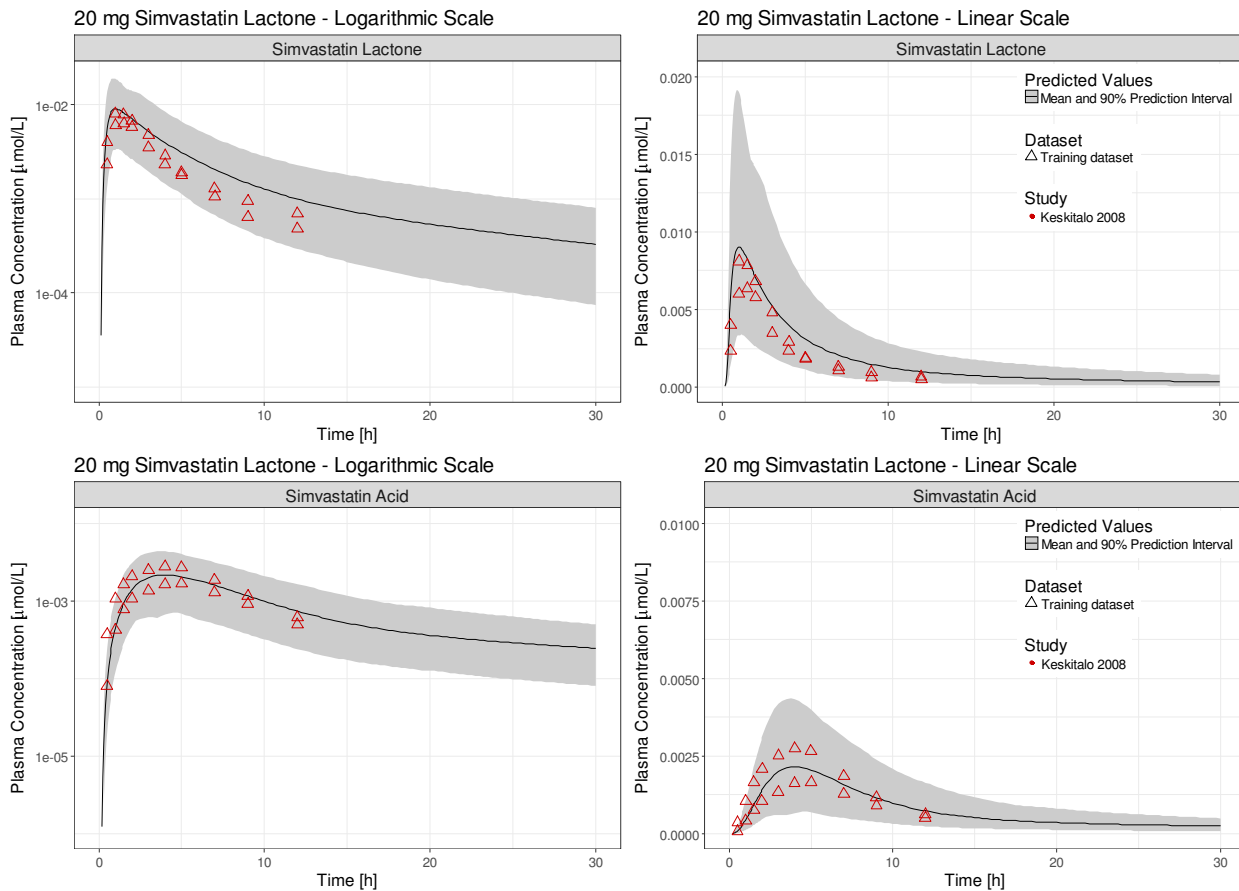
Model limitations

Simvastatin is listed by the FDA as a sensitive CYP3A substrate for the use in clinical DDI studies, and simvastatin acid is an approved OATP1B victim drug [13]. The purpose of the presented simvastatin PBPK model is to accurately incorporate these processes so that this model is fit to be coupled to models of CYP3A and OATP1B perpetrator drugs and applied for DDI prediction.

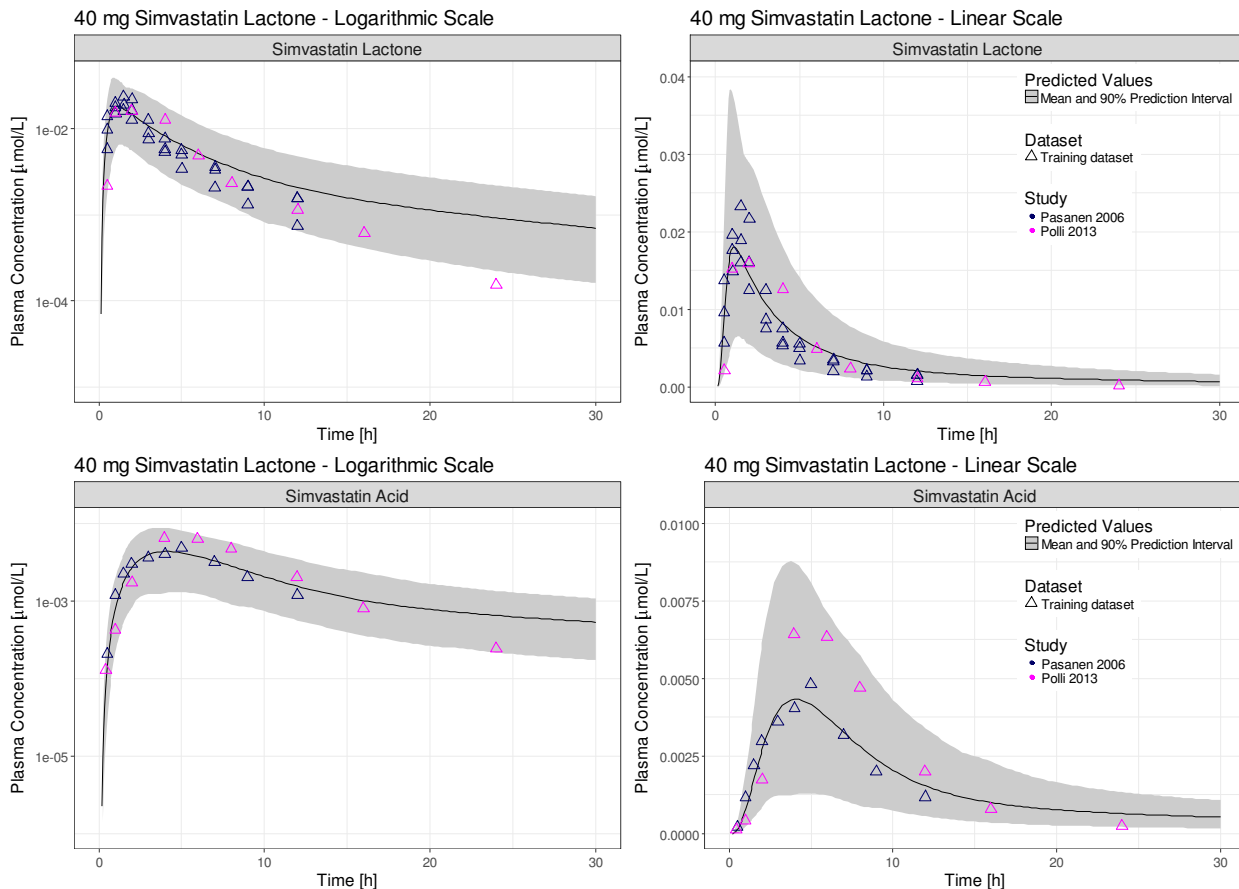
Mechanisms not implemented into the final simvastatin model include transport by breast cancer resistance protein (BCRP) or p-glycoprotein (P-gp). Genetic polymorphism in the ABCG2 gene encoding for BCRP has been described to influence the plasma concentrations of simvastatin lactone [14], while genetic polymorphisms in ABCB1 (P-gp) have been described to affect the plasma concentrations of simvastatin acid [15]. Implementation of these transport processes would further diminish the contribution of CYP3A4 and was therefore not retained in the final model. Another possible mechanism involved in simvastatin pharmacokinetics is reabsorption (enterohepatic cycling) following BCRP-mediated transport of simvastatin lactone into the bile, or following P-gp-mediated transport of simvastatin acid into bile with subsequent recyclization to the lactone. Information on the pharmacokinetics of simvastatin lactone and acid after intravenous administration, on bioavailability and on enterohepatic cycling would greatly help to improve our current understanding of the mechanisms affecting the plasma concentrations and DDI behaviour of this widely used lipid-lowering drug.



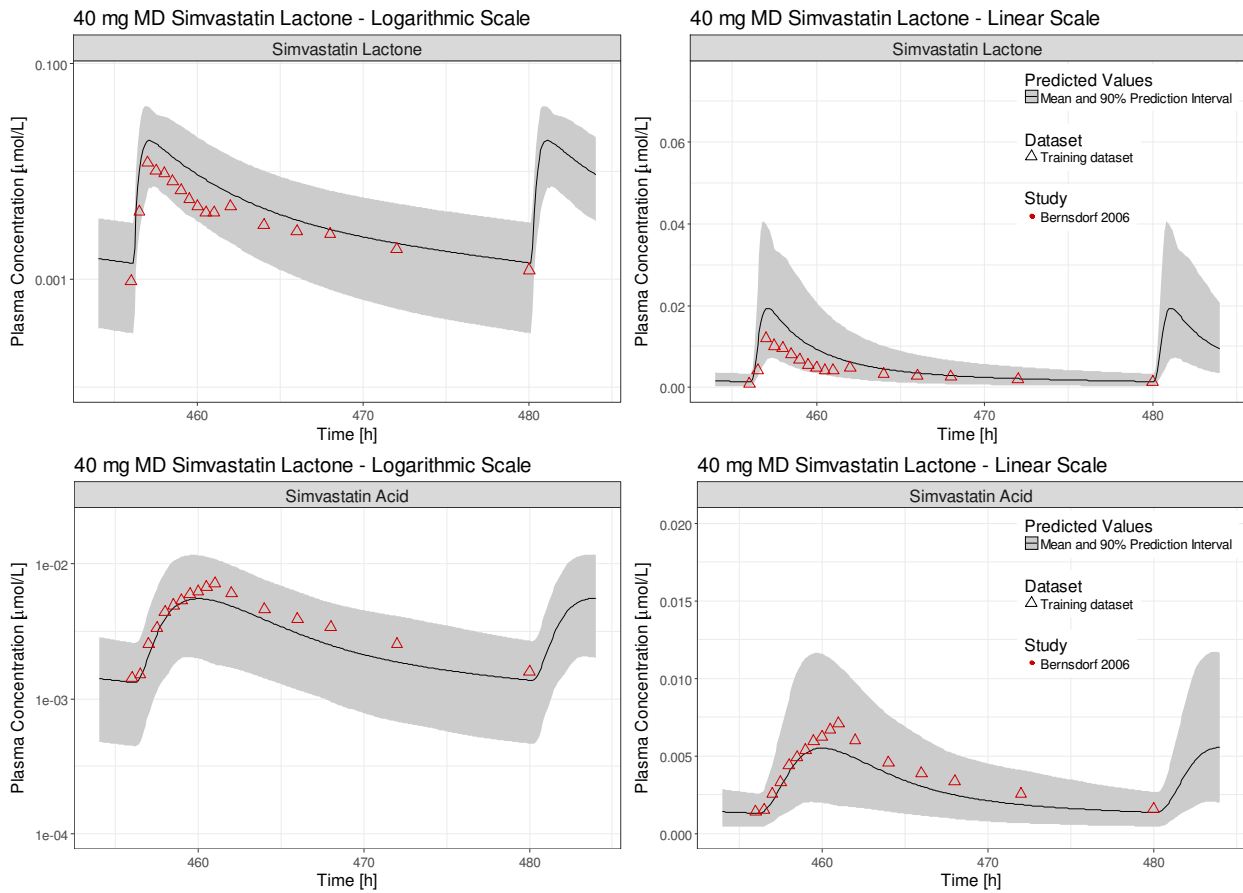
Suppl. Fig. 1 General scheme for statin metabolism. Original proposed by [16]



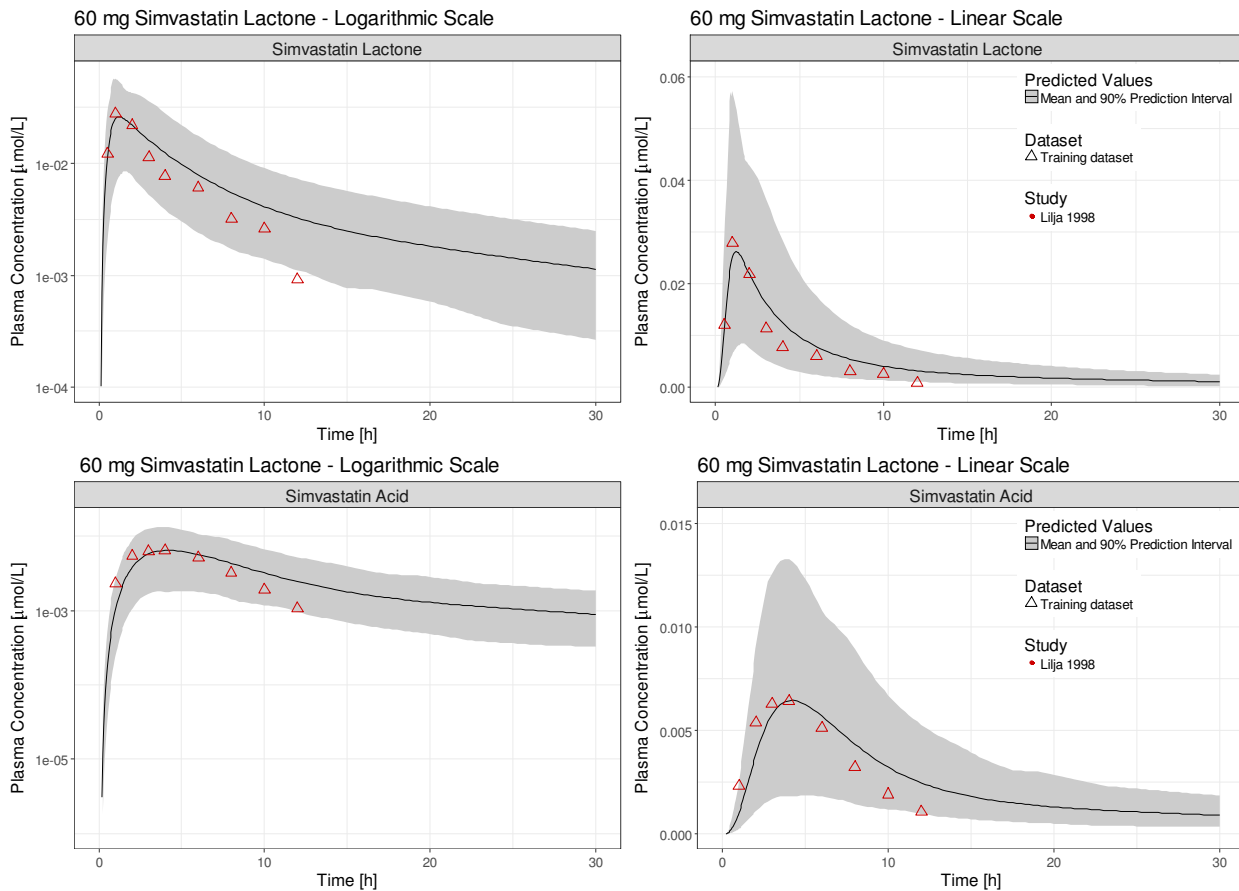
Suppl. Fig. 2 Training dataset: Population simulations compared to observed data of simvastatin lactone (upper panel) and simvastatin acid (lower panel) plasma concentrations following single oral administration of 20 mg simvastatin lactone. Clinical data [15] are shown as triangles. Population simulation means are shown as lines; the shaded areas depict the 5th - 95th percentile population prediction intervals



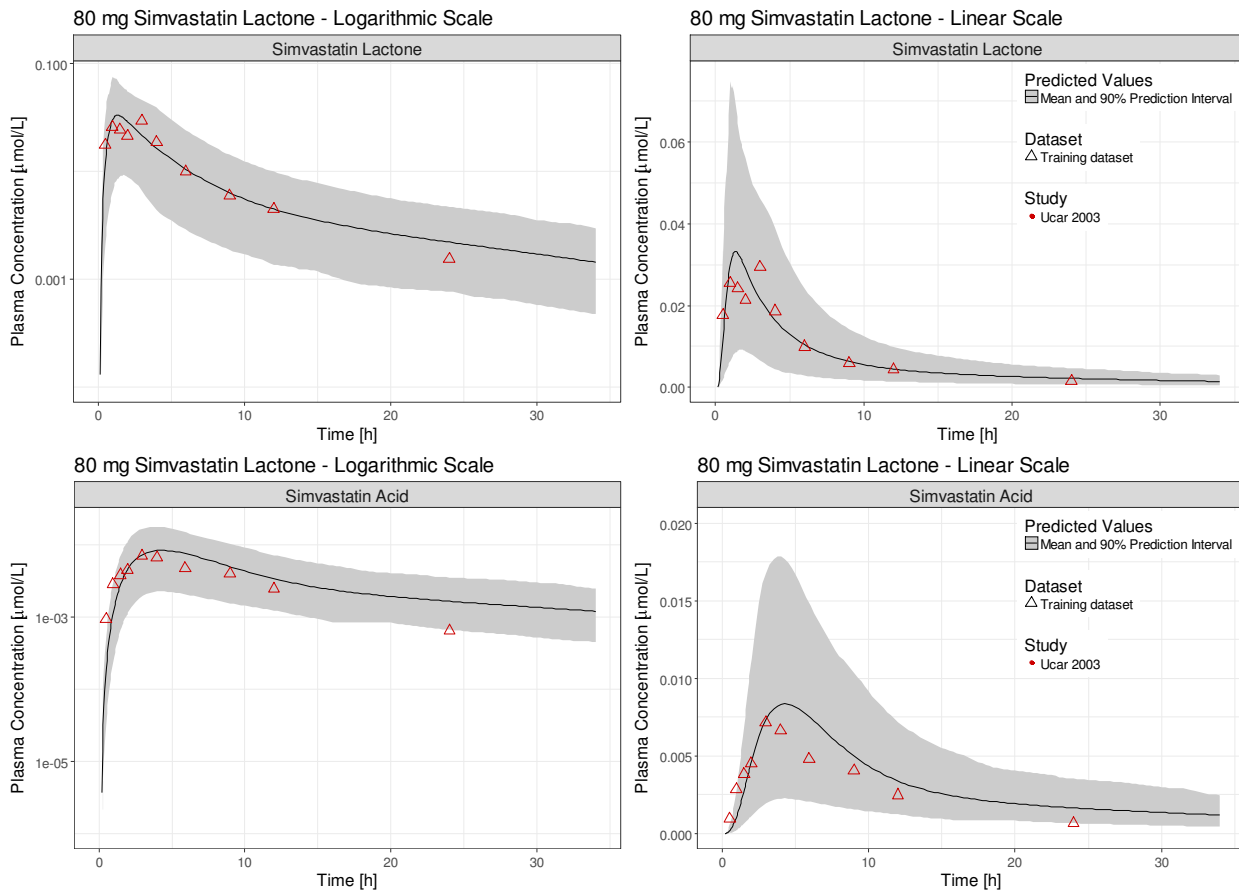
Suppl. Fig. 3 Training dataset: Population simulations compared to observed data of simvastatin lactone (upper panel) and simvastatin acid (lower panel) plasma concentrations following single oral administration of 40 mg simvastatin lactone. Clinical data [8, 17] are shown as triangles. Population simulation means are shown as lines; the shaded areas depict the 5th - 95th percentile population prediction intervals



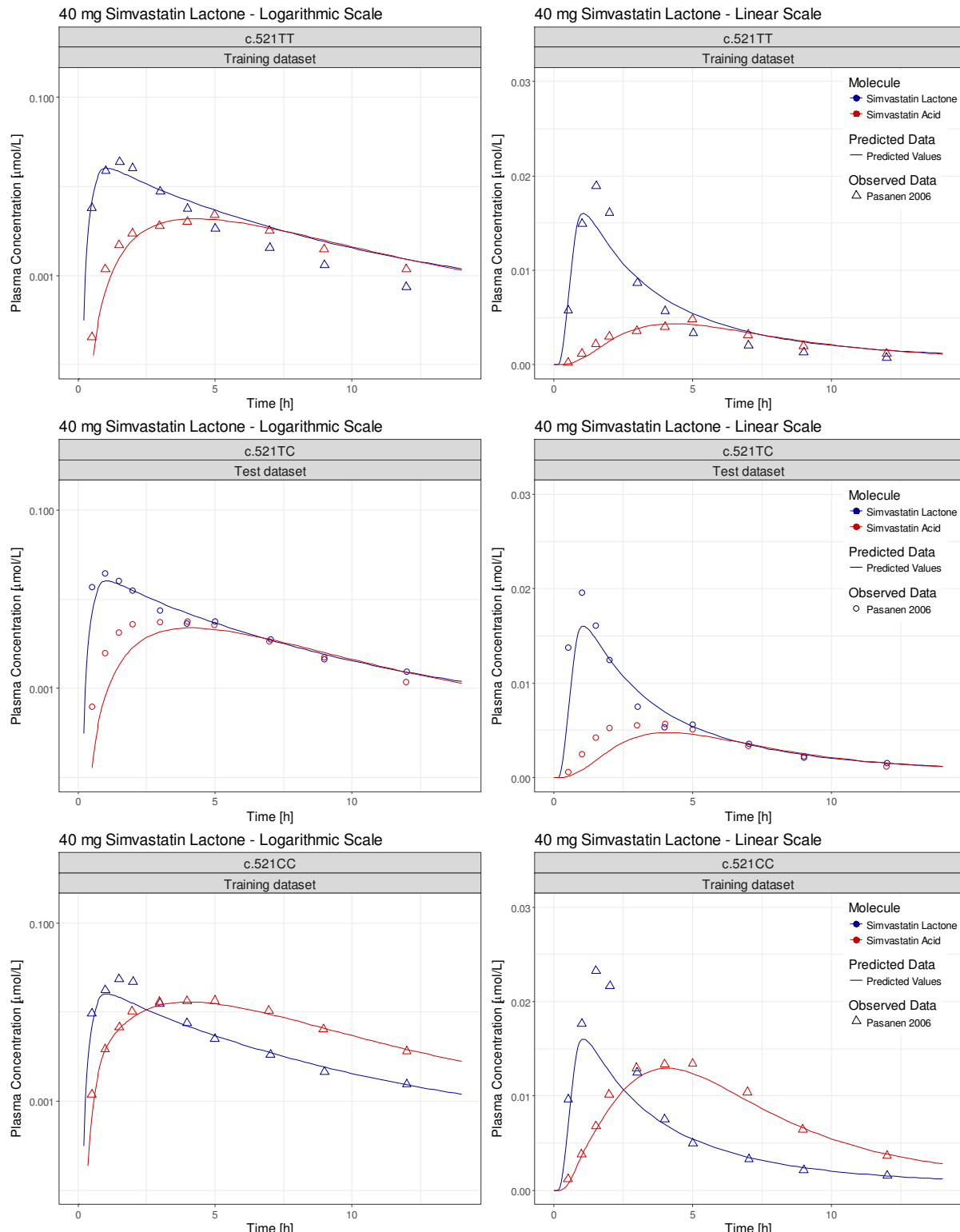
Suppl. Fig. 4 Training dataset: Population simulations compared to observed data of simvastatin lactone (upper panel) and simvastatin acid (lower panel) plasma concentrations on day 6 following once daily oral administration of 40 mg simvastatin lactone. Clinical data [18] are shown as triangles. Population simulation means are shown as lines; the shaded areas depict the 5th - 95th percentile population prediction intervals



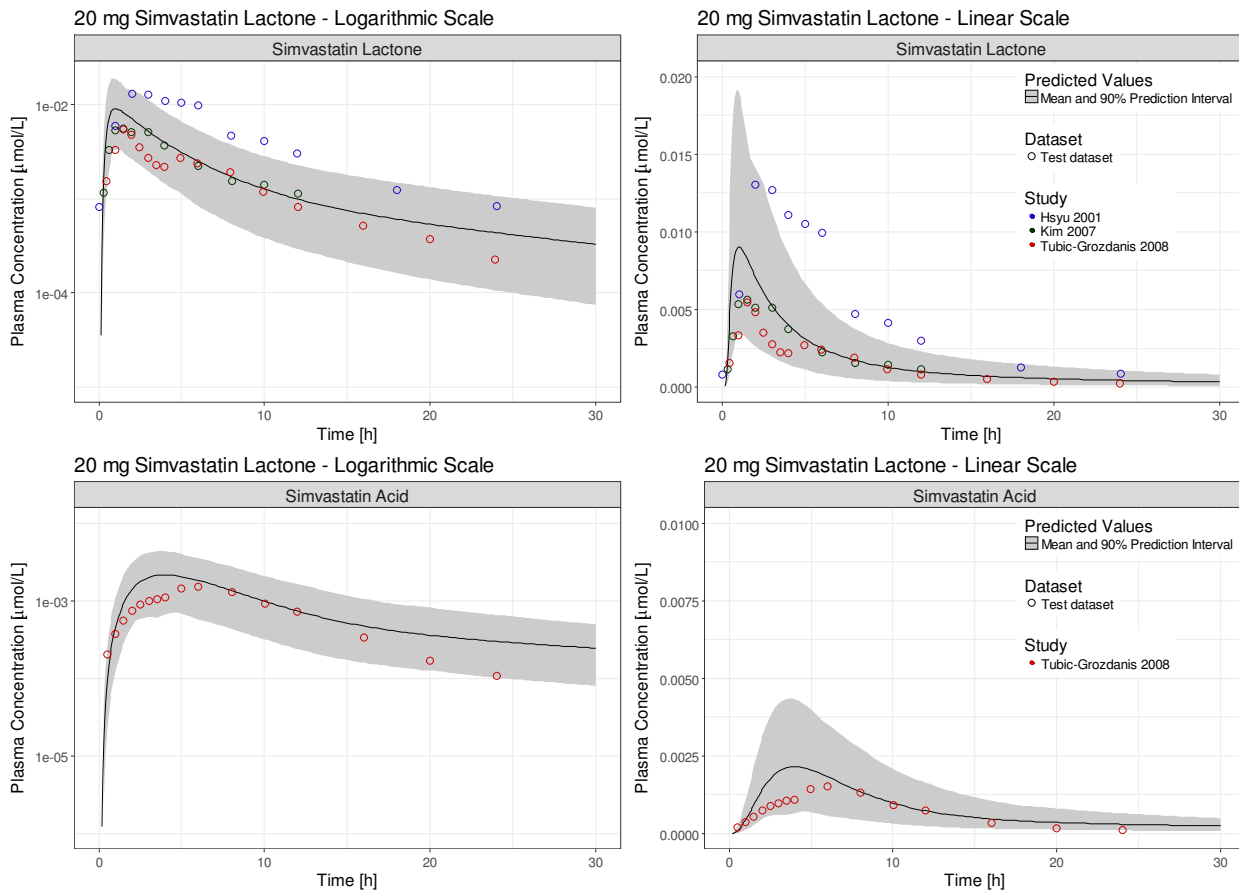
Suppl. Fig. 5 Training dataset: Population simulations compared to observed data of simvastatin lactone (upper panel) and simvastatin acid (lower panel) plasma concentrations following single oral administration of 60 mg simvastatin lactone. Clinical data [19] are shown as triangles. Population simulation means are shown as lines; the shaded areas depict the 5th - 95th percentile population prediction intervals



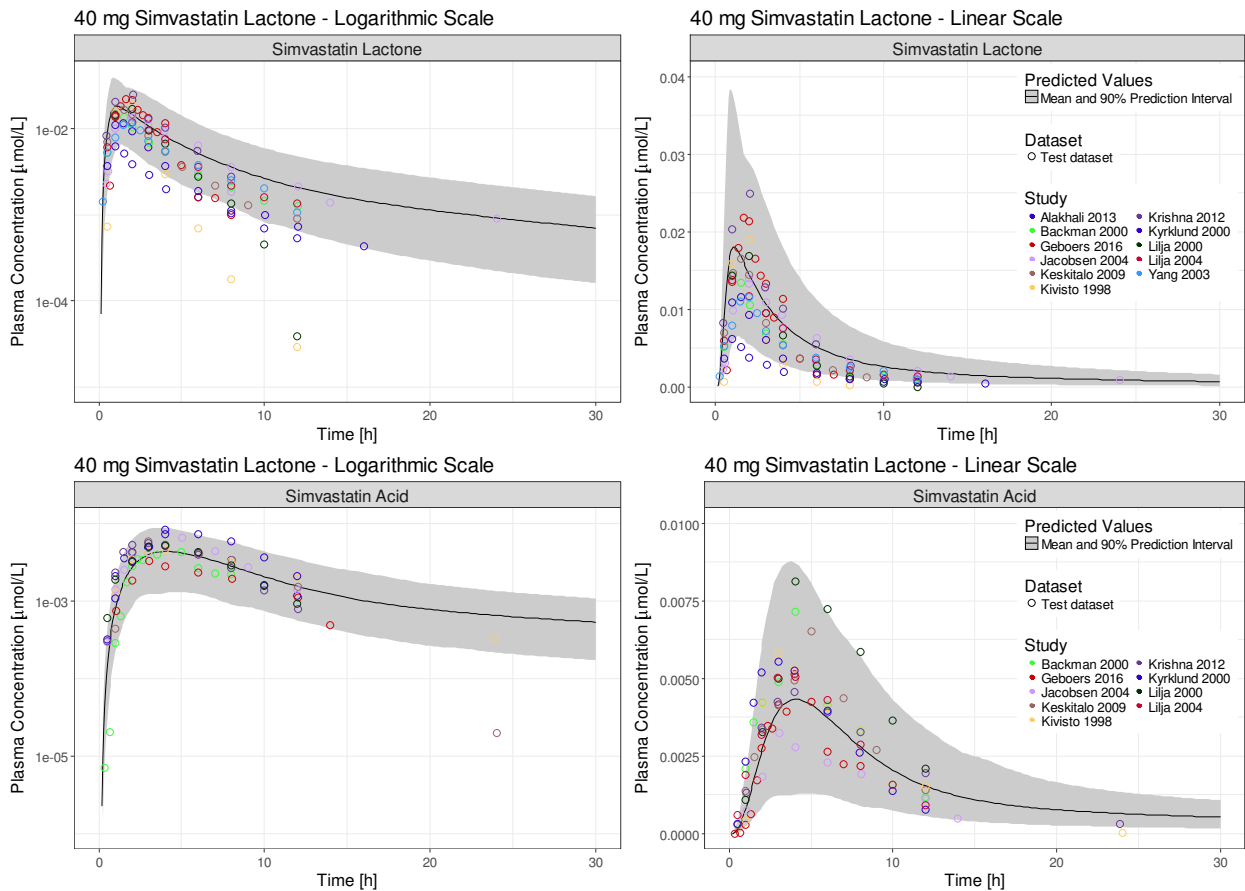
Suppl. Fig. 6 Training dataset: Population simulations compared to observed data of simvastatin lactone (upper panel) and simvastatin acid (lower panel) plasma concentrations following single oral administration of 80 mg simvastatin lactone. Clinical data [20] are shown as triangles. Population simulation means are shown as lines; the shaded areas depict the 5th - 95th percentile population prediction intervals



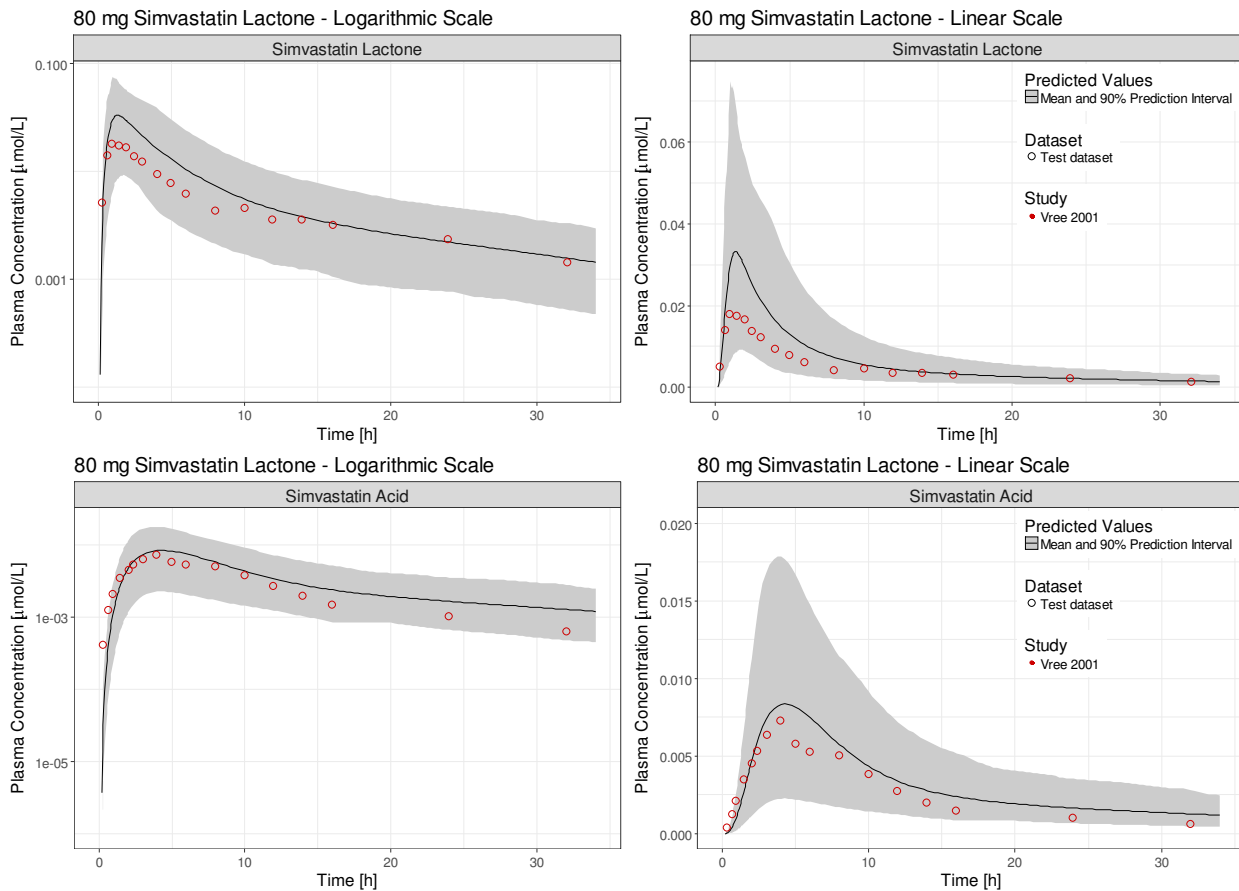
Suppl. Fig. 7 Simulated compared to observed plasma concentrations of simvastatin lactone (blue) and simvastatin acid (red) in typical individuals of the c.521TT (upper panel), the c.521TC (middle panel) and the c.521CC (lower panel) OATP1B1 genotype following single oral administration of 40 mg simvastatin lactone. Clinical data [8] are shown as triangles (training dataset) or circles (test dataset). Simulations are shown as lines



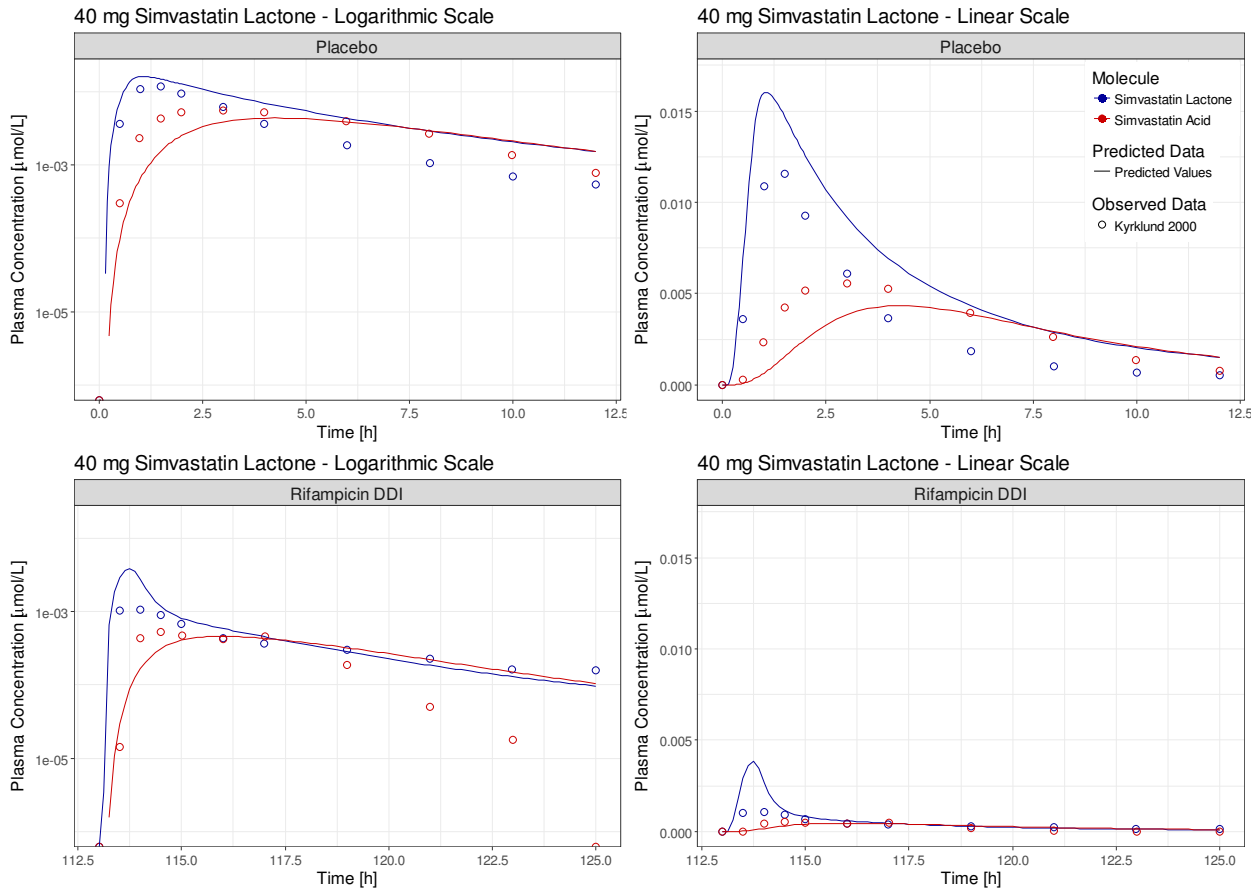
Suppl. Fig. 8 Test dataset: Population simulations compared to observed data of simvastatin lactone (upper panel) and simvastatin acid (lower panel) plasma concentrations following single oral administration of 20 mg simvastatin lactone. Clinical data [21–23] are shown as circles. Population simulation means are shown as lines; the shaded areas depict the 5th - 95th percentile population prediction intervals



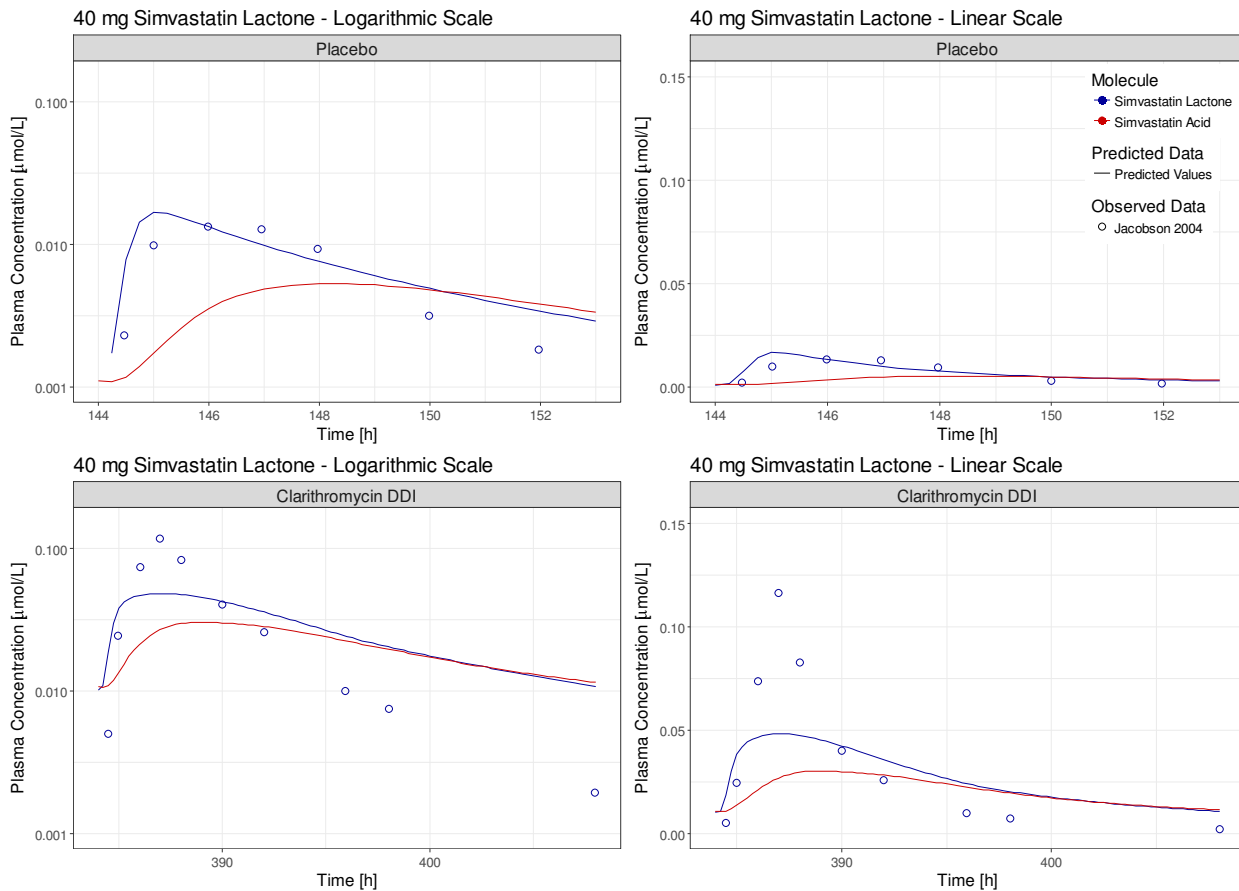
Suppl. Fig. 9 Test dataset: Population simulations compared to observed data of simvastatin lactone (upper panel) and simvastatin acid (lower panel) plasma concentrations following single oral administration of 40 mg simvastatin lactone. Clinical data [11, 12, 14, 24–31] are shown as circles. Population simulation means are shown as lines; the shaded areas depict the 5th - 95th percentile population prediction intervals



Suppl. Fig. 10 Test dataset: Population simulations compared to observed data of simvastatin lactone (upper panel) and simvastatin acid (lower panel) plasma concentrations following single oral administration of 80 mg simvastatin lactone. Clinical data [32] are shown as circles. Population simulation means are shown as lines; the shaded areas depict the 5th - 95th percentile population prediction intervals



Suppl. Fig. 11 Test dataset: Simulated compared to observed plasma concentrations of simvastatin lactone (blue) and simvastatin acid (red) in a typical individual without (upper panel) and following pre-treatment with once daily oral administration of 600 mg rifampicin for 5 days (lower panel). A single oral dose of 40 mg simvastatin lactone was administered 17 h after the last dose of rifampicin. Clinical data [11] are shown as circles. Simulations are shown as lines



Suppl. Fig. 12 Test dataset: Simulated compared to observed plasma concentrations of simvastatin lactone (blue) and simvastatin acid (red) in a typical individual without (upper panel) and during co-treatment with twice daily oral administration of 500 mg clarithromycin for 7 days (lower panel). 40 mg simvastatin lactone were administered orally once daily for 7 days. After a washout phase (3 days), 40 mg simvastatin lactone were administered orally once daily together with the morning dose of clarithromycin for further 7 days. PK samples were collected on day 7 and 17. Clinical data [12] are shown as circles. Simulations are shown as lines

Suppl. Tab. 1 Clinical studies used for simvastatin lactone and simvastatin acid model development and evaluation

Dose (mg)	Administration	n	Women (%)	Age (years)	Weight (kg)	Genotype	Dataset	Study reference
20	po (tab), SD	31	19	38	72	-	test	[21]
20	po (tab), SD	12	42	22	68	P-gp (TTT)	training	[15]
20	po (tab), SD	12	42	24	66	P-gp (CGC)	training	[15]
20	po (tab), SD	7	14	30	77	-	test	[23]
20	po (tab), SD	4	0	25	69	CYP3A5 (*3/*3)	test	[22]
40	po (tab), SD	10	50	22	62	-	test	[26]
40	po (tab), SD	9	0	31	68	-	test	[24]
40	po (tab), SD	5	60	30 ^a	64 ^a	-	test	[27]
40	po (tab), SD	30	50 ^a	30 ^a	64 ^a	-	test	[12]
40	po (tab), SD	23	52	22	68	BCRP (CC)	test	[14]
40	po (tab), SD	10	40	24	68	-	test	[31]
40	po (tab), SD	10	10	30 ^a	64 ^a	-	test	[28]
40	po (tab), SD	10	0	30 ^a	64 ^a	-	test	[29]
40	po (tab), SD	16	50	23	68	OATP1B1 (TT)	training	[8]
40	po (tab), SD	12	42	24	69	OATP1B1 (TC)	training	[8]
40	po (tab), SD	4	25	23	84	OATP1B1 (CC)	training	[8]
40	po (tab), SD	28	29	39	73	-	training	[17]
40	po (tab), SD	20	0	30 ^a	64 ^a	-	test	[30]
40	po (tab), SD	35	34	30 ^a	64 ^a	-	test	[25]
40	po (tab), MD	18	44	25	73	-	training	[18]
60	po (tab), SD	10	50	30 ^a	64 ^a	-	training	[19]
80	po (tab), SD	12	0	30 ^a	64 ^a	-	training	[20]
80	po (tab), SD	34	53	24	69	-	test	[32]
40	po (tab), SD/DDI	10	50	30 ^a	64 ^a	-	test	[11]
40	po (tab), MD/DDI	15	50 ^a	30 ^a	64 ^a	-	test	[12]

^a: assumed, BCRP: breast cancer resistance protein - included BCRP genotype: c.421CC (high activity), CYP3A5: included genotype: *3/*3 (nonexpressors), MD: multiple dosing, n: number of individuals studied, OATP1B1: organic anion-transporting polypeptide 1B1 - included OATP1B1 polymorphism: c.521TT (high activity), c.521TC (intermediate activity), c.521CC (low activity), P-gp: permeability glycoprotein - included P-gp polymorphisms: c.1236TT-c.2677TT-c.3435TT, c.1236CC-c.2677GG-c.3435CC, po: peroral, SD: single dose, test: test dataset (model evaluation), training: training dataset (model development and parameter optimization), -: no data available. Values given for age and weight are arithmetic means

Suppl. Tab. 2 Drug-dependent parameters of the final simvastatin lactone and simvastatin acid PBPK model

Parameter	Unit	Simvastatin lactone model	Simvastatin lactone reference	Simvastatin acid model	Simvastatin acid reference	Description
MW	g/mol	418.57	-	436.6	-	Molecular weight
pKa	-	-	-	4.18 (acid)	[33]	Acid dissociation constant
Solubility (pH)	mg/L	30.0 (water)	[34]	11.0 (7.0)	[34]	Solubility
logP	-	4.58	optimized	1.35	optimized	Lipophilicity
fu	%	1.09	[66]	5.66	[35]	Fraction unbound
PON3 K _M	μmol/L	31.7	optimized	-	-	Michaelis-Menten constant
PON3 k _{cat}	1/ min	429.0	optimized	-	-	Metabolization rate
CYP3A4 K _M	μmol/L	30.7	[38]	56.7	[7]	Michaelis-Menten constant
CYP3A4 k _{cat}	1/ min	879.0	optimized	276.0	optimized	Metabolization rate
OATP1B1 K _M c.521TT	μmol/L	-	-	2.09	[36]	Michaelis-Menten constant
OATP1B1 k _{cat} c.521TT	1/ min	-	-	331.6	optimized	Transportation rate
OATP1B1 K _M c.521CC	μmol/L	-	-	1.69	[36]	Michaelis-Menten constant
OATP1B1 k _{cat} c.521CC	1/ min	-	-	0.67	optimized	Transportation rate
GFR fraction	-	1	-	1	-	Fraction of glomerular filtration
EHC continuous fraction	-	1	-	1	-	Fraction of bile bypassing the gallbladder
Administration	-	tab	[37]	-	-	Route of administration
Partition coefficients	-	calculated	R + R	calculated	R + R	Organ-plasma partitioning
Cell permeabilities	-	calculated	PK-Sim	calculated	PK-Sim	Cell membrane permeation
Specific intest. perm.	cm/min	6.14E-05	optimized	1.49E-04	calculated	Normalized transcellular intest. perm.
Specific organ perm.	cm/min	0.205	calculated	0.029	calculated	Normalized to surface area

CYP3A4: cytochrome P450 3A4, intest.: intestinal, OATP1B1: organic anion-transporting polypeptide 1B1 with the genotypes c.521TT (high activity) and c.521CC (low activity), perm.: permeability, PK-Sim: PK-Sim standard calculation method, PON3: paraoxonase 3, R + R: Rodgers and Rowland calculation method [38, 39], tab: tablet – digitized dissolution profile from the literature used, trans.: transcellular

Suppl. Tab. 3 System-dependent parameters of the final simvastatin lactone and simvastatin acid PBPK model

Enzyme/ Transporter	Reference concentration, tissue of highest expression ($\mu\text{mol/L}$)	Geometric standard deviation in virtual populations	Tissue localization (relative expression, normalized to tissue with highest expression)
PON3	1.0 [38]	1.28 ($\pm 25\% \text{CV}$)	Liver 1.0, lung 0.18, gonads 0.15, skin 0.13, kidney 0.12, stomach 0.09, small intestine 0.09, bone 0.08, pancreas 0.07, spleen 0.06, large intestine 0.06, brain 0.06, heart 0.05, muscle 0.04 [39]
CYP3A4	4.32 [40]	PK-Sim ontogeny function	Liver 1.0, small intestine 0.07, kidney 0.01 [41]
OATP1B1	1.0 [38]	1.28 ($\pm 25\% \text{CV}$)	Liver 1.0, gonads 0.01 [42]

CYP3A4: cytochrome P450 3A4, OATP1B1: organic anion-transporting polypeptide 1B1, PON3: paraoxonase 3. If no information on reference concentration was available it was set to 1.0 $\mu\text{mol/L}$ and the reaction/transportation rate (k_{cat}) was optimized according to [38]

Suppl. Tab. 4 AUC ratio comparison for simvastatin lactone and simvastatin acid during the DDI with rifampicin

Simvastatin Lactone	Predicted AUC (h*ng/mL)	Observed AUC (h*ng/mL)	Ratio Predicted/Observed
DDI-Rifampicin	2.7	1.8	
	28.1	16.2	
	0.096	0.111	0.86
Simvastatin Acid			
DDI-Rifampicin	1.4	1.1	
	14.4	16.2	
	0.097	0.068	1.43

Suppl. Tab. 5 AUC ratio comparison for simvastatin lactone and simvastatin acid during the DDI with clarithromycin

Simvastatin Lactone	Predicted AUC (h*ng/mL)	Observed AUC (h*ng/mL)	Ratio Predicted/Observed
DDI-Clarithromycin	258.5	219.0	
	37.4	22.0	
	6.912	9.955	0.69
Simvastatin Acid			
DDI-Clarithromycin	204.0	73.0	
	26.9	6.0	
	7.584	12.167	0.62

Supplementary References

1. IMS Institute for Healthcare Informatics (2011) The Use of Medicines in the United States: Review of 2010.
2. Merck Canada Inc. (2006) Product Monograph: Zocor.
3. Elsby R, Hilgendorf C, Fenner K (2012) Understanding the critical disposition pathways of statins to assess drug-drug interaction risk during drug development: it's not just about OATP1B1. *Clin Pharmacol Ther* 92:584–98
4. Draganov DI, La Du BN (2004) Pharmacogenetics of paraoxonases: a brief review. *Naunyn Schmiedebergs Arch Pharmacol* 369:78–88
5. Wang X, Zhu H, Markowitz JS (2015) Carboxylesterase 1-mediated drug-drug interactions between clopidogrel and simvastatin. *Biol Pharm Bull* 38:292–7
6. Prueksaritanont T, Gorham LM, Ma B, Liu L, Yu X, Zhao JJ, Slaughter DE, Arison BH, Vyas KP (1997) In vitro metabolism of simvastatin in humans [SBT]identification of metabolizing enzymes and effect of the drug on hepatic P450s. *Drug Metab Dispos* 25:1191–9
7. Prueksaritanont T, Ma B, Yu N (2003) The human hepatic metabolism of simvastatin hydroxy acid is mediated primarily by CYP3A, and not CYP2D6. *Br J Clin Pharmacol* 56:120–4
8. Pasanen MK, Neuvonen M, Neuvonen PJ, Niemi M (2006) SLCO1B1 polymorphism markedly affects the pharmacokinetics of simvastatin acid. *Pharmacogenet Genomics* 16:873–9
9. Hanke N, Frechen S, Britz H, Moj D, Kanacher T, Eissing T, Wendl T, Lehr T (2016) Physiologically-based pharmacokinetic modeling of rifampin drug-drug interactions with midazolam and digoxin. *PAGE 25 Abstr* 5929
10. Moj D, Hanke N, Britz H, Frechen S, Kanacher T, Wendl T, Haefeli WE, Lehr T (2017) Clarithromycin, midazolam, and digoxin: application of PBPK modeling to gain new insights into drug-drug interactions and co-medication regimens. *AAPS J* 19:298–312
11. Kyrlund C, Backman JT, Kivistö KT, Neuvonen M, Laitila J, Neuvonen PJ (2000) Rifampin greatly reduces plasma simvastatin and simvastatin acid concentrations. *Clin Pharmacol Ther* 68:592–7
12. Jacobson TA (2004) Comparative pharmacokinetic interaction profiles of pravastatin, simvastatin, and atorvastatin when coadministered with cytochrome P450 inhibitors. *Am J Cardiol* 94:1140–6
13. U.S. Food and Drug Administration (2012) Drug Interaction Studies - Study Design, Data Analysis, Implications for Dosing, and Labeling Recommendations. Draft Guidance for Industry.
14. Keskitalo JE, Pasanen MK, Neuvonen PJ, Niemi M (2009) Different effects of the ABCG2 c.421C>A SNP on the pharmacokinetics of fluvastatin, pravastatin and simvastatin. *Pharmacogenomics* 10:1617–24
15. Keskitalo JE, Kurkinen KJ, Neuvonen PJ, Niemi M (2008) ABCB1 haplotypes differentially affect the pharmacokinetics of the acid and lactone forms of simvastatin and atorvastatin. *Clin Pharmacol Ther* 84:457–61
16. Prueksaritanont T, Subramanian R, Fang X, Ma B, Qiu Y, Lin JH, Pearson PG, Baillie TA (2002) Glucuronidation of statins in animals and humans: a novel mechanism of statin lactonization. *Drug Metab Dispos* 30:505–12
17. Polli JW, Hussey E, Bush M, Generaux G, Smith G, Collins D, McMullen S, Turner N, Nunez DJ (2013) Evaluation of drug interactions of GSK1292263 (a GPR119 agonist) with statins: from in vitro data to clinical study design. *Xenobiotica* 43:498–508
18. Bernsdorf A, Giessmann T, Modess C, Wegner D, Igelbrink S, Hecker U, Haenisch S, Cascorbi I, Terhaag B, Siegmund W (2006) Simvastatin does not influence the intestinal P-glycoprotein and MPR2, and the disposition of talinolol after chronic medication in healthy subjects genotyped for the ABCB1, ABCC2 and SLCO1B1 polymorphisms. *Br J Clin Pharmacol* 61:440–50
19. Lilja JJ, Kivistö KT, Neuvonen PJ (1998) Grapefruit juice-simvastatin interaction: effect on serum

- concentrations of simvastatin, simvastatin acid, and HMG-CoA reductase inhibitors. *Clin Pharmacol Ther* 64:477–83
- 20. Ucar M, Neuvonen M, Luurila H, Dahlqvist R, Neuvonen PJ, Mjörndal T (2004) Carbamazepine markedly reduces serum concentrations of simvastatin and simvastatin acid. *Eur J Clin Pharmacol* 59:879–82
 - 21. Hsyu PH, Schultz-Smith MD, Lillibridge JH, Lewis RH, Kerr BM (2001) Pharmacokinetic interactions between nelfinavir and 3-hydroxy-3-methylglutaryl coenzyme A reductase inhibitors atorvastatin and simvastatin. *Antimicrob Agents Chemother* 45:3445–50
 - 22. Kim K-A, Park P-W, Lee O-J, Kang D-K, Park J-Y (2007) Effect of polymorphic CYP3A5 genotype on the single-dose simvastatin pharmacokinetics in healthy subjects. *J Clin Pharmacol* 47:87–93
 - 23. Tubic-Grozdanis M, Hilfinger JM, Amidon GL, Kim JS, Kijek P, Staubach P, Langguth P (2008) Pharmacokinetics of the CYP 3A substrate simvastatin following administration of delayed versus immediate release oral dosage forms. *Pharm Res* 25:1591–600
 - 24. Alkhali K, Hassan Y, Mohamed N, Mordi MN (2013) Pharmacokinetic of simvastatin study in Malaysian. *IOSR J Pharm* 3:46–51
 - 25. Krishna G, Ma L, Prasad P, Moton A, Martinho M, O'Mara E (2012) Effect of posaconazole on the pharmacokinetics of simvastatin and midazolam in healthy volunteers. *Expert Opin Drug Metab Toxicol* 8:1–10
 - 26. Backman JT, Kyrklund C, Kivistö KT, Wang JS, Neuvonen PJ (2000) Plasma concentrations of active simvastatin acid are increased by gemfibrozil. *Clin Pharmacol Ther* 68:122–9
 - 27. Geboers S, Stappaerts J, Tack J, Annaert P, Augustijns P (2016) In vitro and in vivo investigation of the gastrointestinal behavior of simvastatin. *Int J Pharm* 510:296–303
 - 28. Lilja JJ, Kivistö KT, Neuvonen PJ (2000) Duration of effect of grapefruit juice on the pharmacokinetics of the CYP3A4 substrate simvastatin. *Clin Pharmacol Ther* 68:384–90
 - 29. Lilja JJ, Neuvonen M, Neuvonen PJ (2004) Effects of regular consumption of grapefruit juice on the pharmacokinetics of simvastatin. *Br J Clin Pharmacol* 58:56–60
 - 30. Yang H, Feng Y, Luan Y (2003) Determination of Simvastatin in human plasma by liquid chromatography–mass spectrometry. *J Chromatogr B* 785:369–375
 - 31. Kantola T, Kivistö KT, Neuvonen PJ (1998) Erythromycin and verapamil considerably increase serum simvastatin and simvastatin acid concentrations. *Clin Pharmacol Ther* 64:177–182
 - 32. Vree TB, Dammers E, Ulc I, Horkovics-Kovats S, Ryska M, Merkx I (2001) Variable plasma/liver and tissue esterase hydrolysis of simvastatin in healthy volunteers after a single oral dose. *Clin Drug Investig* 21:643–652
 - 33. Yoshinari M, Matsuzaka K, Hashimoto S, Ishihara K, Inoue T, Oda Y, Ide T, Tanaka T (2007) Controlled release of simvastatin acid using cyclodextrin inclusion system. *Dent Mater J* 26:451–6
 - 34. Lippert J, Brosch M, von Kampen O, Meyer M, Siegmund H-U, Schafmayer C, Becker T, Laffert B, Görlitz L, Schreiber S, Neuvonen PJ, Niemi M, Hampe J, Kuepfer L (2012) A mechanistic, model-based approach to safety assessment in clinical development. *CPT pharmacometrics Syst Pharmacol* 1:e13
 - 35. Vickers S, Duncan CA, Vyas KP, Kari PH, Arison B, Prakash SR, Ramjit HG, Pitzenberger SM, Stokker G, Duggan DE (1990) In vitro and in vivo biotransformation of simvastatin, an inhibitor of HMG CoA reductase. *Drug Metab Dispos* 18:476–483
 - 36. Huang H (2010) Characterization of in vitro systems for transporter studies Hua Huang.
 - 37. Guzik L, Mrozik W, Kamysz W (2010) Determination of simvastatin in pharmaceutical dosage forms by optimized and validated method using HPLC / UV. *Croat Chem Acta* 83:371–377
 - 38. Meyer M, Schneckener S, Ludewig B, Kuepfer L, Lippert J (2012) Using expression data for quantification of active processes in physiologically based pharmacokinetic modeling. *Drug Metab Dispos* 40:892–901

39. Kolesnikov N, Hastings E, Keays M, Melnichuk O, Tang YA, Williams E, Dylag M, Kurbatova N, Brandizi M, Burdett T, Megy K, Pilicheva E, Rustici G, Tikhonov A, Parkinson H, Petryszak R, Sarkans U, Brazma A (2015) ArrayExpress update-simplifying data submissions. *Nucleic Acids Res* 43:D1113–D1116
40. Rodrigues AD (1999) Integrated cytochrome P450 reaction phenotyping. Attempting to bridge the gap between cDNA-expressed cytochromes P450 and native human liver microsomes. *Biochem Pharmacol* 57:465–480
41. Nishimura M, Naito S (2006) Tissue-specific mRNA expression profiles of human phase I metabolizing enzymes except for cytochrome P450 and phase II metabolizing enzymes. *Drug Metab Pharmacokinet* 21:357–374
42. Nishimura M, Naito S (2005) Tissue-specific mRNA expression profiles of human ATP-binding cassette and solute carrier transporter superfamilies. *Drug Metab Pharmacokinet* 20:452–477

A physiologically-based pharmacokinetic (PBPK) parent-metabolite model of the chemotherapeutic zoptarelin doxorubicin - integration of in vitro results, Phase I and Phase II data and model application for drug-drug interaction potential analysis

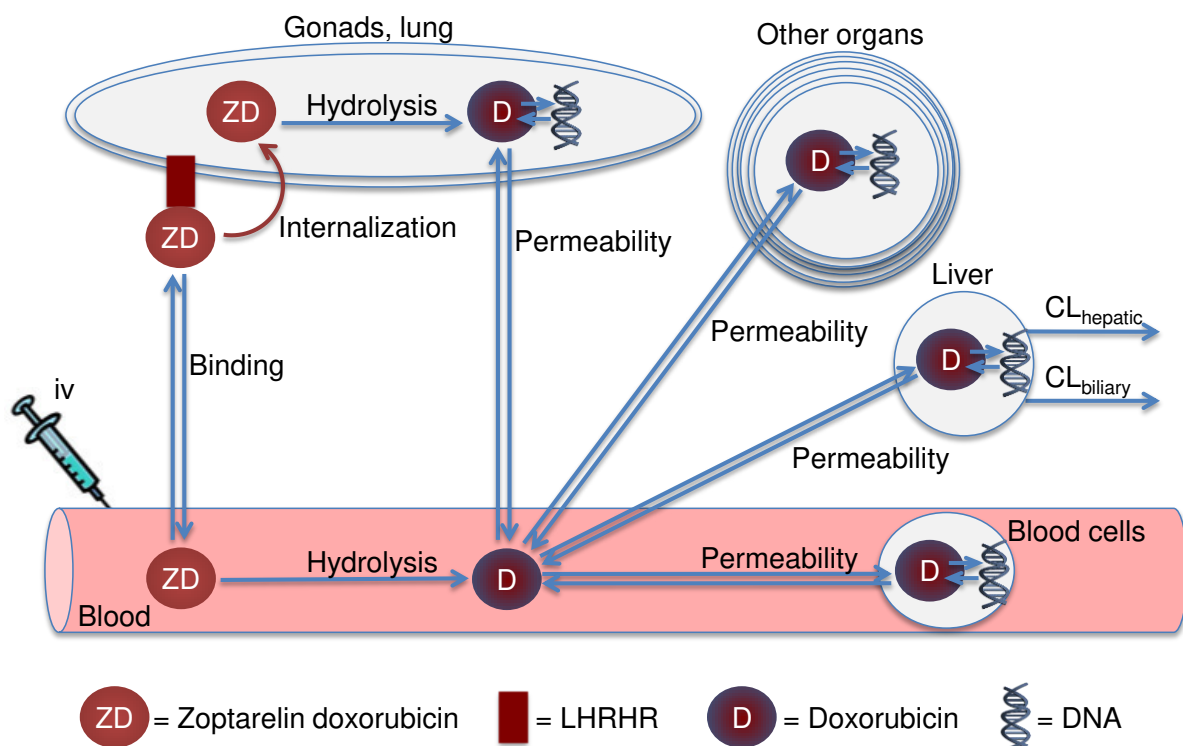
Zoptarelin Doxorubicin Supplementary

Nina Hanke ¹, Michael Teifel ², Daniel Moj ¹, Jan-Georg Wojtyniak ¹, Hannah Britz ¹, Babette Aicher ², Herbert Sindermann ², Nicola Ammer ², Thorsten Lehr ¹

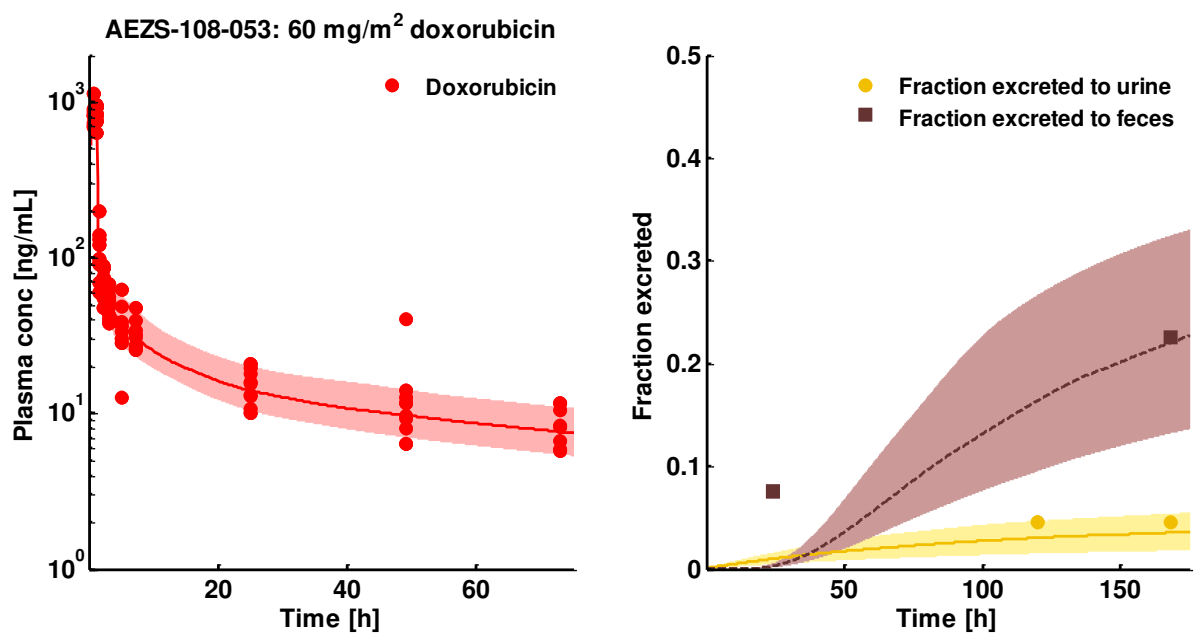
¹ Clinical Pharmacy, Saarland University, Saarbruecken, Germany

² Aeterna Zentaris GmbH, Weismuellerstr. 50, Frankfurt, Germany

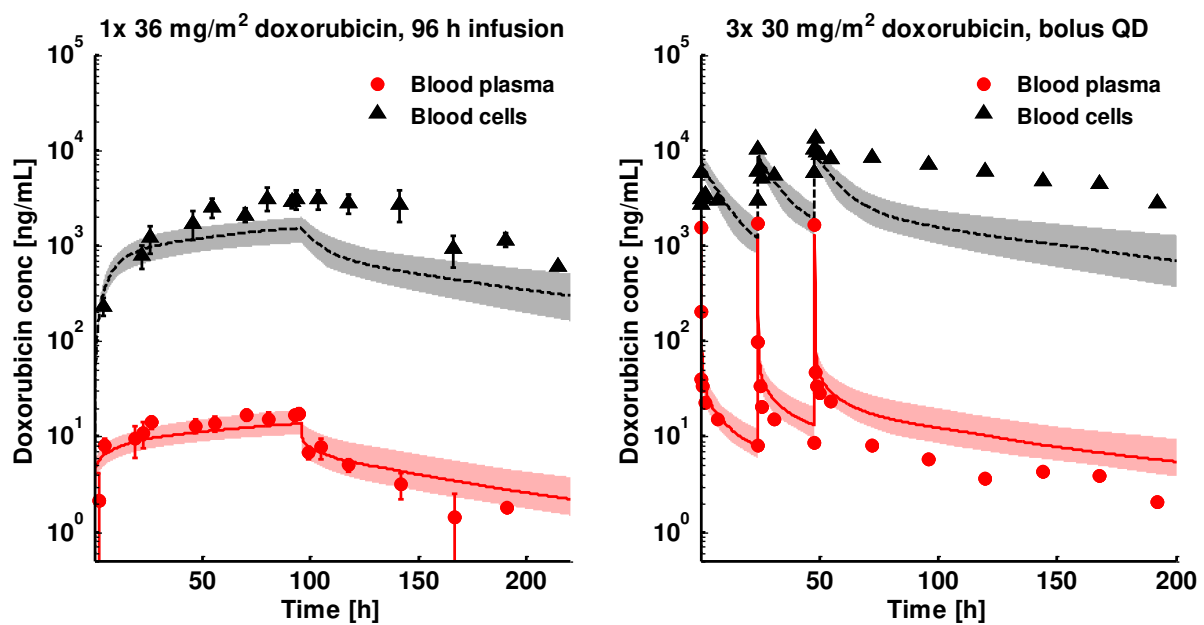
Corresponding Author: Thorsten Lehr, Clinical Pharmacy, Saarland University, Campus C2 2, 66123 Saarbruecken, +49 681 302 70255, thorsten.lehr@mx.uni-saarland.de



Suppl. Fig. 1 Zoptarelin doxorubicin parent-metabolite PBPK model structure. $CL_{biliary}$: biliary plasma clearance, $CL_{hepatic}$: hepatic metabolic plasma clearance, iv: intravenous administration, LHRHR: luteinizing hormone-releasing hormone receptor

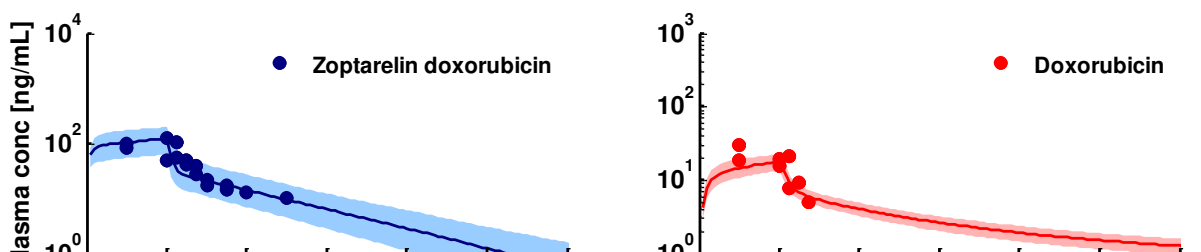


Suppl. Fig. 2 Training dataset: Population simulations compared to observed data of doxorubicin plasma concentrations (red, semilog scale) and fractions excreted to urine and feces (yellow and brown, linear scale) following intravenous administration of 60 mg/m² doxorubicin. Clinical data (Study 3, doxorubicin arm, n = 9 and [1]) are shown as dots and squares. Population simulation medians are shown as lines or dashed lines; the shaded areas depict the 5th - 95th percentile population prediction intervals

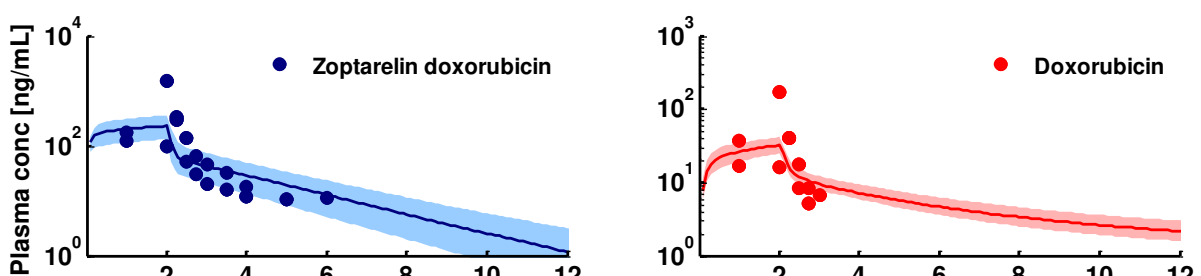


Suppl. Fig. 3 Training dataset: Population simulations (semilog scale) compared to observed data of doxorubicin concentrations in blood plasma (red) and in nucleated blood cells (black) following intravenous administration of 1x 36 mg/m² doxorubicin as 96 h long-term infusion (left) or 3x 30 mg/m² doxorubicin as daily bolus infusions (right). Simulated blood cell concentrations represent free plus DNA-bound doxorubicin in the blood cell compartment. Clinical data ([2], n = 7 and [3], n = 7) are shown as dots and triangles (\pm SD values). Population simulation medians are shown as lines or dashed lines; the shaded areas depict the 5th - 95th percentile population prediction intervals

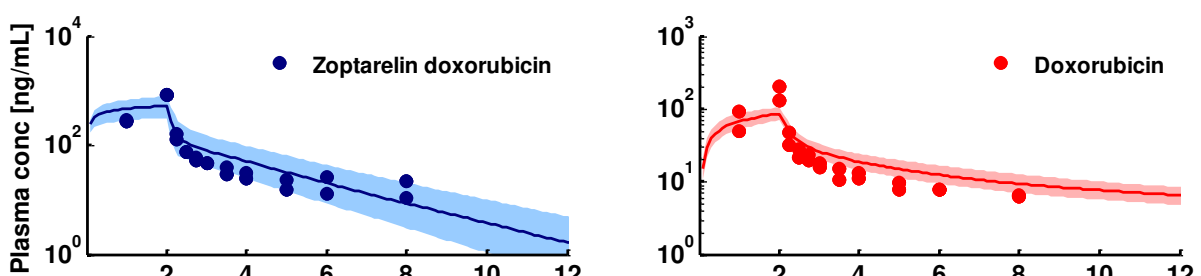
a ZEN-008-Z023: 10 mg/m² zoptarelin doxorubicin



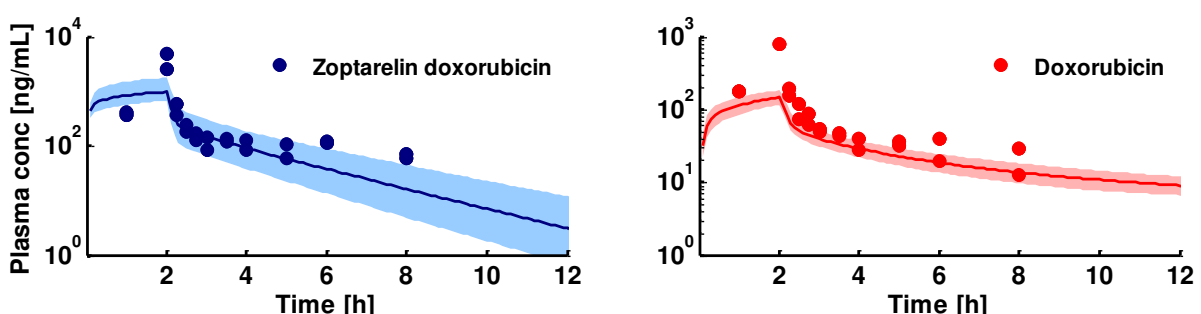
b ZEN-008-Z023: 20 mg/m² zoptarelin doxorubicin



c ZEN-008-Z023: 40 mg/m² zoptarelin doxorubicin

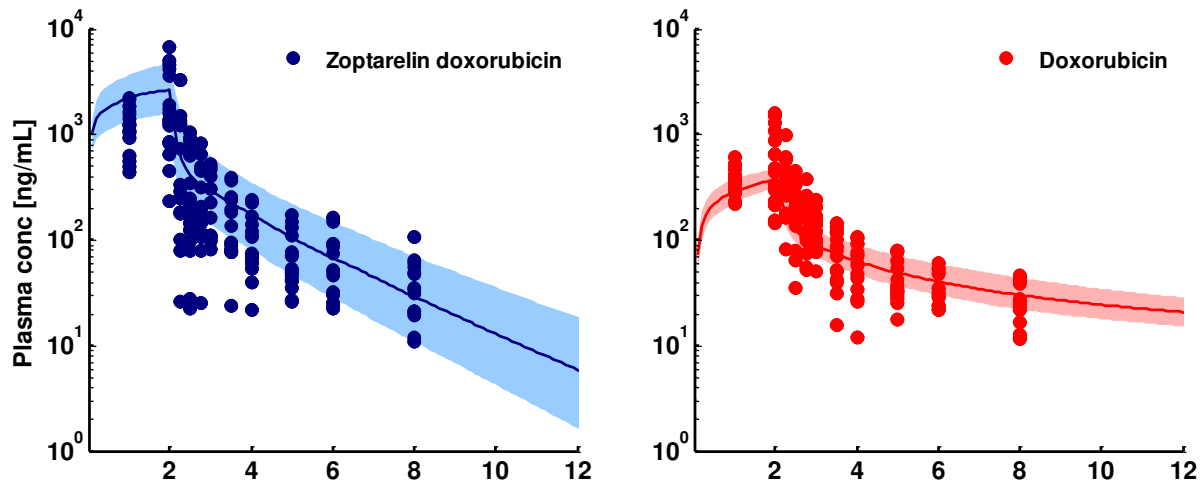


d ZEN-008-Z023: 80 mg/m² zoptarelin doxorubicin

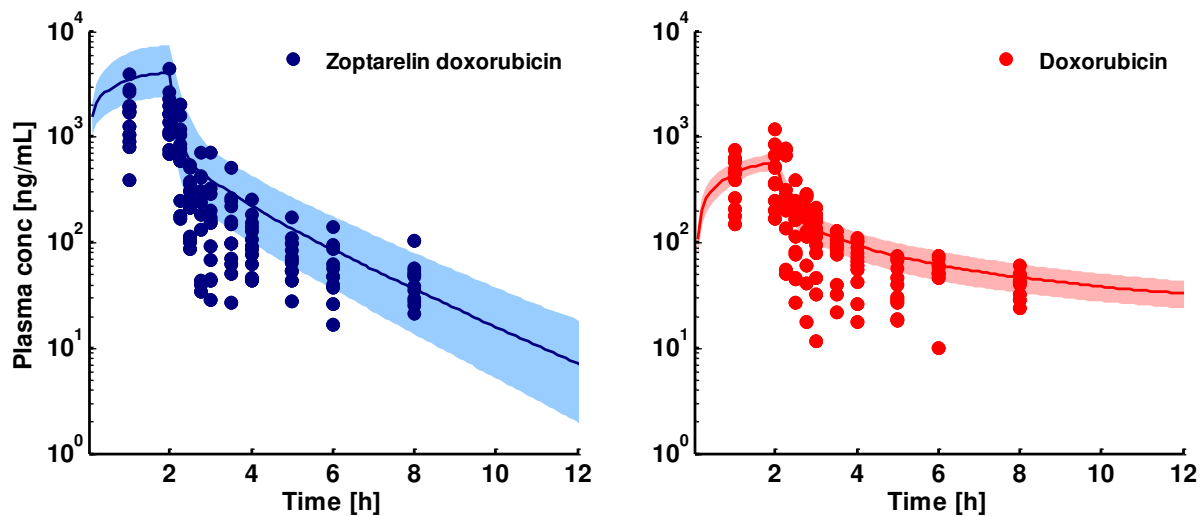


Suppl. Fig. 4 Training dataset: Population simulations (semilog scale) compared to observed data of zoptarelin doxorubicin (blue) and doxorubicin plasma concentrations (red) following intravenous administration of 10, 20, 40 or 80 mg/m² (a, b, c, d) zoptarelin doxorubicin. Clinical data (Study 1, n = 1 for each dose, 2 cycles per patient, one dose every 3 weeks) are shown as dots. Population simulation medians are shown as lines; the shaded areas depict the 5th - 95th percentile population prediction intervals

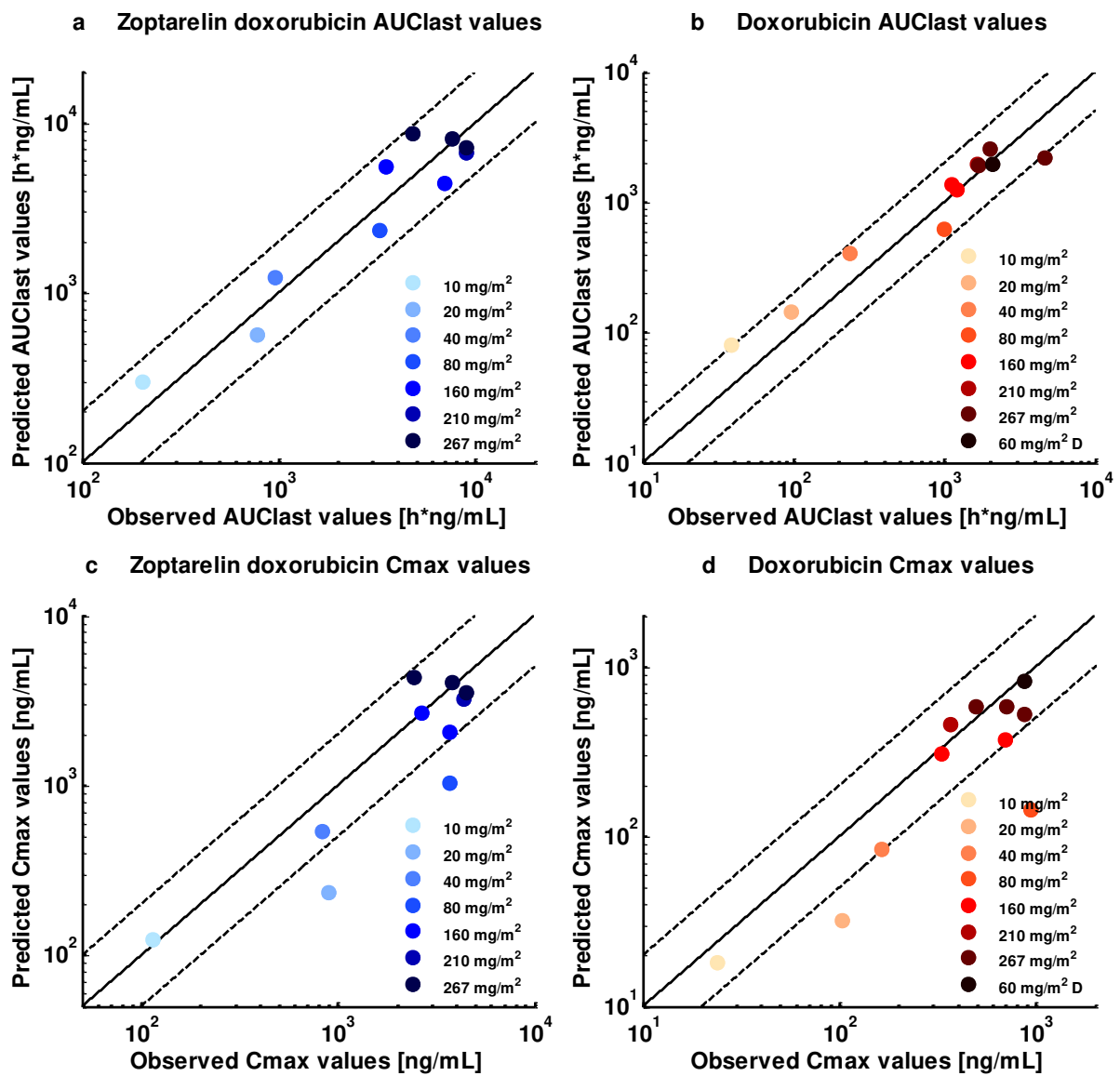
a ZEN-008-Z023: 160 mg/m² zoptarelin doxorubicin



b ZEN-008-Z023: 267 mg/m² zoptarelin doxorubicin



Suppl. Fig. 5 Test dataset: Population simulations (semilog scale) compared to observed data of zoptarelin doxorubicin (blue) and doxorubicin plasma concentrations (red) following intravenous administration of 160 or 267 mg/m² (a, b) zoptarelin doxorubicin. Clinical data (Study 1, n = 6 and n = 5, multiple cycles per patient, one dose every 3 weeks) are shown as dots. Population simulation medians are shown as lines; the shaded areas depict the 5th - 95th percentile population prediction intervals



Suppl. Fig. 6 Model performance: Mean AU_{last} (a, b) and C_{max} (c, d) values of population predictions compared to observed data (log scale) of zoptarelin doxorubicin (blue) and doxorubicin (red) plasma concentrations following intravenous administration of 10 to 267 mg/m² zoptarelin doxorubicin or of 60 mg/m² doxorubicin. Each dot represents a dosing group of one clinical study. Number of patients per dosing group and further details are listed in Zoptarelin Doxorubicin Supplementary Tables 1 and 2. The solid line marks the line of identity, the dashed lines show the 0.5 to 2.0-fold prediction success limits. AU_{last}: area under the plasma concentration-time curve from time 0 to the last measurement, C_{max}: peak plasma concentration, D: intravenous administration of doxorubicin

Suppl. Tab. 1 Model performance: Predicted and observed pharmacokinetic parameters of zoptarelin doxorubicin

Dose [mg/m ²]	n	AUC _{last} obs ± SD [h*ng/mL]	AUC _{last} pred ± SD [h*ng/mL]	Pred error [%]	C _{max} obs ± SD [ng/mL]	C _{max} pred ± SD [ng/mL]	Pred error [%]	Study reference
Zoptarelin doxorubicin								
10	1	202	297 ± 102	47	115	123 ± 43	7	Study 1 (ZEN-008-Z023)
20	1	783	570 ± 168	-27	895	236 ± 69	-74	Study 1 (ZEN-008-Z023)
40	1	965	1223 ± 360	27	828	535 ± 152	-35	Study 1 (ZEN-008-Z023)
80	1	3273	2323 ± 743	-29	3699	1039 ± 332	-72	Study 1 (ZEN-008-Z023)
160	6	3507 ± 2170	5570 ± 1887	59	2667 ± 1732	2688 ± 913	1	Study 1 (ZEN-008-Z023)
267	5	4812 ± 3201	8713 ± 3059	81	2436 ± 974	4329 ± 1532	78	Study 1 (ZEN-008-Z023)
160	3	6975 ± 2932	4421 ± 1552	-37	3722 ± 796	2055 ± 733	-45	Study 2 (AEZS-108-046)
210	7	9001 ± 3400	6685 ± 2614	-26	4379 ± 754	3225 ± 1284	-26	Study 2 (AEZS-108-046)
267	4	8995 ± 2910	7217 ± 2311	-20	4485 ± 1280	3534 ± 1149	-21	Study 2 (AEZS-108-046)
267	21	7647 ± 3109	8152 ± 2948	7	3829 ± 1229	4041 ± 1479	6	Study 3 (AEZS-108-053)

AUC_{last}: area under the plasma concentration-time curve from time 0 to the last measurement, C_{max}: peak plasma concentration, n: number of individuals studied, obs: observed, pred: predicted, pred error: prediction error, SD: standard deviation. Shown are mean ± SD values

Suppl. Tab. 2 Model performance: Predicted and observed pharmacokinetic parameters of doxorubicin

Dose [mg/m ²]	n	AUC _{last} obs ± SD [h*ng/mL]	AUC _{last} pred ± SD [h*ng/mL]	Pred error [%]	C _{max} obs ± SD [ng/mL]	C _{max} pred ± SD [ng/mL]	Pred error [%]	Study reference
Doxorubicin								
60	9	2079 ± 441	1958 ± 306	-6	874 ± 128	821 ± 96	-6	Study 3 (AEZS-108-053)
Zoptarelin doxorubicin								
10	1	39	81 ± 11	108	24	18 ± 3	-25	Study 1 (ZEN-008-Z023)
20	1	97	145 ± 22	49	104	32 ± 5	-69	Study 1 (ZEN-008-Z023)
40	1	238	401 ± 52	68	164	84 ± 11	-49	Study 1 (ZEN-008-Z023)
80	1	990	616 ± 86	-38	945	145 ± 21	-85	Study 1 (ZEN-008-Z023)
160	6	1201 ± 483	1249 ± 187	4	702 ± 425	374 ± 49	-47	Study 1 (ZEN-008-Z023)
267	5	1676 ± 1179	1894 ± 266	13	712 ± 294	581 ± 66	-18	Study 1 (ZEN-008-Z023)
160	3	1113 ± 155	1377 ± 196	24	333 ± 39	306 ± 38	-8	Study 2 (AEZS-108-046)
210	7	1639 ± 983	1947 ± 309	19	368 ± 41	456 ± 64	24	Study 2 (AEZS-108-046)
267	4	4678 ± 827	2177 ± 341	-53	872 ± 198	524 ± 66	-40	Study 2 (AEZS-108-046)
267	21	1990 ± 479	2549 ± 443	28	497 ± 114	582 ± 78	17	Study 3 (AEZS-108-053)

AUC_{last}: area under the plasma concentration-time curve from time 0 to the last measurement, C_{max}: peak plasma concentration, n: number of individuals studied, obs: observed, pred: predicted, pred error: prediction error, SD: standard deviation. Shown are mean ± SD values

Suppl. Tab. 3 Impact of zoptarelin doxorubicin administration time on victim drug exposure

Zoptarelin doxorubicin co-administration time	Victim drug AUC	% increase	Victim drug C_{max}	% increase
Simvastatin acid				
No zoptarelin doxorubicin	45.091		3.088	
Zoptarelin doxorubicin at 94 h	45.140	0.107	3.090	0.075
Zoptarelin doxorubicin at 96 h	45.139	0.105	3.090	0.070
Zoptarelin doxorubicin at 98 h	45.143	0.114	3.092	0.117
Zoptarelin doxorubicin at 100 h	45.143	0.114	3.090	0.078
Metformin				
No zoptarelin doxorubicin	20.719		4.702	
Zoptarelin doxorubicin at 94 h	20.722	0.014	4.701	-0.004
Zoptarelin doxorubicin at 95 h	20.739	0.096	4.708	0.143
Zoptarelin doxorubicin at 96 h	20.730	0.052	4.703	0.036

AUC₉₆₋₁₀₄: area under the plasma concentration-time curve from 96 h to 104 h, AUC₉₆₋₁₂₀: area under the plasma concentration-time curve from 96 h to 120 h, C_{max}: peak plasma concentration, co-administration time: start of the zoptarelin doxorubicin infusion (267 mg/m², infusion duration 2 h). Last administration of simvastatin (80 mg, every 24 h) and metformin (1000 mg, every 8 h) at 96 h

Suppl. Tab. 4 Drug-dependent parameters of the final zoptarelin doxorubicin parent-metabolite PBPK model

Parameter	Unit	Zoptarelin doxo-rubicin model (SE)	Zoptarelin doxo-rubicin reference	Doxorubicin model (SE)	Doxorubicin reference	Description
MW	g/mol	1893.06	-	543.525	-	Molecular weight
pKa	-	6.1 (base) 8.2 (base) 9.5 (acid) 10.1 (acid) 12.1 (base)	[4] [5] [5] [4] [4]	8.2 (base) 9.5 (acid)	[5] [5]	Acid dissociation constants
Solubility	g/L	25.0 (water)	AEZS	20.0 (water)	[6]	Solubility
logP	-	-3.60	[7] ^a	1.27	[8]	Lipophilicity
fu	%	2.1	AEZS	26.3	AEZS	Fraction unbound
LHRHR K _d	μmol/L	0.0182 (0.50%)	optimized	-	-	Dissociation constant
LHRHR k _{off}	1/min	0.0113 (0.0001%)	optimized	-	-	Dissociation rate constant
Internalization K _M	μmol/L	7.45E-03	[9]	-	-	Michaelis-Menten constant
Internalization k _{cat}	1/min	8.01E-04 (0.53%)	optimized	-	-	Internalization turnover
Hydrolysis	L/(μmol*min)	15.81 (0.59%)	optimized	-	-	Hydrolysis rate
DNA K _d	μmol/L	-	-	3.23	[10]	Dissociation constant
DNA k _{off}	1/min	-	-	509.4	[10]	Dissociation rate constant
CL _{hep}	1/min	-	-	2.31 (3.14%)	optimized	Normalized to liver volume
CL _{bil}	1/min	-	-	2.70 (1.64%)	optimized	Normalized to liver volume
GFR fraction	-	1	-	1	-	Fraction of glomerular filtration
EHC continuous fraction	-	1	-	1	-	Fraction of bile bypassing gallbladder
Administration	-	intravenous	-	intravenous	-	Route of administration
Partition coefficients	-	calculated	R + R	calculated	R + R	Organ-plasma partitioning
Cell permeabilities	-	calculated	PK-Sim	calculated	PK-Sim	Cell membrane permeation
Specific intest. perm.	cm/min	7.17E-15	calculated	1.46E-07	calculated	Normalized transcellular intest. perm.
Specific organ perm.	cm/min	1.57E-13	calculated	1.32E-04 (0.21%)	optimized	Normalized to surface area

^a: DrugBank entry for gonadorelin, AEZS: Aeterna Zentaris in vitro result, CL_{bil}: biliary plasma clearance, CL_{hep}: hepatic metabolic plasma clearance, EHC: enterohepatic circulation, intest.: intestinal, LHRHR: luteinizing hormone-releasing hormone receptor, perm.: permeability, PK-Sim: PK-Sim Standard calculation method, SE: standard error, R + R: Rodgers and Rowland calculation method [11, 12]

Suppl. Tab. 5 System-dependent parameters of the final zoptarelin doxorubicin parent-metabolite PBPK model

Protein/ Clearance	Reference concentration, tissue of highest expression [$\mu\text{mol/L}$] (SE)	Geometric standard deviation in virtual populations	Tissue localization (relative expression, normalized to tissue with highest expression)
Zoptarelin doxorubicin			
LHRHR1	470.77 (1.25%) optimized	1.28 (\pm 25 %CV)	Gonads 1.0, lung 0.5
Hydrolysis	1.0 [13]	1.28 (\pm 25 %CV)	Plasma 1.0, gonads 1.0, lung 0.5
Doxorubicin			
DNA	46050.0 (76.6%) optimized	1.28 (\pm 25 %CV)	Heart 1.0, kidney 1.0, liver 1.0, pancreas 1.0, spleen 1.0, intestinal mucosa 1.0, gonads 1.0, lung 1.0, blood cells 0.04
CL _{hep}	normalized to liver volume	1.28 (\pm 25 %CV)	Unspecific hepatic metabolic clearance
CL _{bil}	normalized to liver volume	1.28 (\pm 25 %CV)	Unspecific hepatic biliary clearance

CL_{bil}: biliary plasma clearance, CL_{hep}: hepatic metabolic plasma clearance, LHRHR1: luteinizing hormone-releasing hormone receptor 1. If no information on reference concentration was available it was set to 1.0 $\mu\text{mol/L}$ and the reaction rate constant (k_{cat}) was optimized according to [13]

Supplementary References

1. American Society of Health-System Pharmacists (2009) AHFS drug information. American Society of Health-System Pharmacists, Bethesda, MD
2. Speth PA, Linssen PC, Holdrinet RS, Haanen C (1987) Plasma and cellular adriamycin concentrations in patients with myeloma treated with ninety-six-hour continuous infusion. *Clin Pharmacol Ther* 41:661–665
3. Speth PA, Linssen PC, Boezeman JB, Wessels HM, Haanen C (1987) Cellular and plasma adriamycin concentrations in long-term infusion therapy of leukemia patients. *Cancer Chemother Pharmacol* 20:305–310
4. Haynes WM (2010) CRC Handbook of Chemistry and Physics. CRC Press, Taylor and Francis, Boca Raton, FL
5. Munnier E, Tewes F, Cohen-Jonathan S, Linassier C, Douziech-Eyrolles L, Marchais H, Soucé M, Hervé K, Dubois P, Chourpa I (2007) On the interaction of doxorubicin with oleate ions: fluorescence spectroscopy and liquid-liquid extraction study. *Chem Pharm Bull (Tokyo)* 55:1006–1010
6. International Agency for Research on Cancer (1976) Monographs on the Evaluation of the Carcinogenic Risk of Chemicals to Humans. 10:44
7. Wishart DS, Knox C, Guo AC, Shrivastava S, Hassanali M, Stothard P, Chang Z, Woolsey J (2006) DrugBank: a comprehensive resource for in silico drug discovery and exploration. *Nucleic Acids Res* 34:D668–D672
8. Hansch C, Leo A, Hoekman D (1995) Exploring QSAR: Hydrophobic, electronic, and steric constants. American Chemical Society, Washington, DC
9. Halmos G, Nagy A, Lamharzi N, Schally A (1999) Cytotoxic analogs of luteinizing hormone-releasing hormone bind with high affinity to human breast cancers. *Cancer Lett* 136:129–136
10. Yao F, Duan J, Wang Y, Zhang Y, Guo Y, Guo H, Kang X (2015) Nanopore single-molecule analysis of DNA-doxorubicin interactions. *Anal Chem* 87:338–342
11. Rodgers T, Leahy D, Rowland M (2005) Physiologically based pharmacokinetic modeling 1: Predicting the tissue distribution of moderate-to-strong bases. *J Pharm Sci* 94:1259–1276
12. Rodgers T, Rowland M (2006) Physiologically based pharmacokinetic modelling 2: Predicting the tissue distribution of acids, very weak bases, neutrals and zwitterions. *J Pharm Sci* 95:1238–1257
13. Meyer M, Schneckener S, Ludewig B, Kuepfer L, Lippert J (2012) Using expression data for quantification of active processes in physiologically based pharmacokinetic modeling. *Drug Metab Dispos* 40:892–901

9.2 Supporting Information of Project II

Supplemental Figures and Tables

Clarithromycin, Midazolam, and Digoxin: Application of PBPK Modeling to Gain New Insights into Drug-Drug interactions and Co-medication Regimens

Daniel Moj¹, Nina Hanke¹, Hannah Britz¹, Sebastian Frechen², Tobias Kanacher², Thomas Wendl², Walter Emil Haefeli³, and Thorsten Lehr¹

¹ Department of Pharmacy, Clinical Pharmacy, Saarland University, Saarbruecken, Germany

² Computational Systems Biology, Bayer Technology Services GmbH, Leverkusen, Germany

³ Department of Clinical Pharmacology and Pharmacoepidemiology, University of Heidelberg, Heidelberg, Germany

Corresponding Author:

Thorsten Lehr, Clinical Pharmacy, Saarland University, Campus C2 2, 66123 Saarbruecken, Tel: +49/681/302-70255, Fax: +49/681/302-70258, email: Thorsten.Lehr@mx.uni-saarland.de

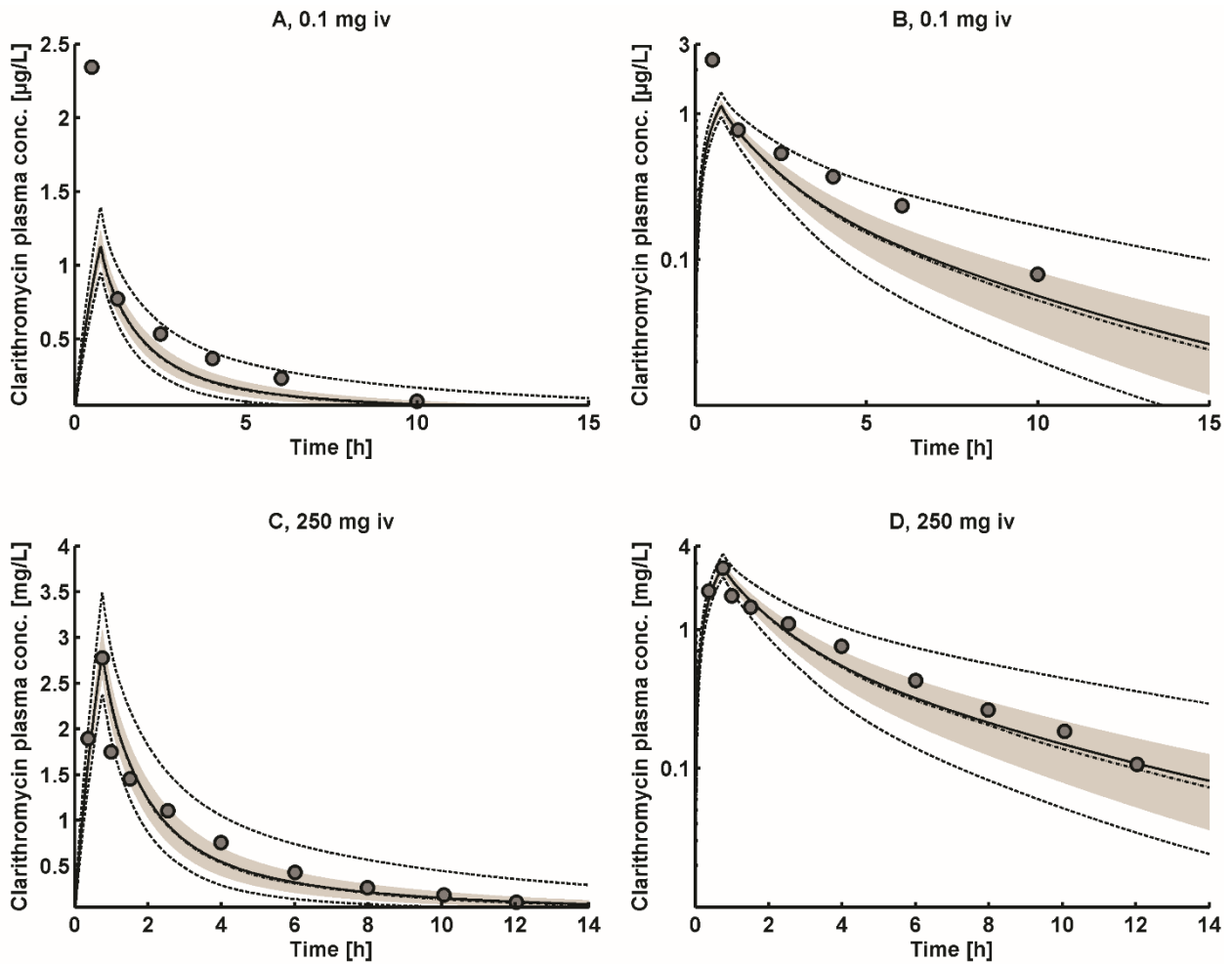


Fig. 1 Predicted concentration-time profiles of clarithromycin after intravenous application of clarithromycin (A,B: ref. (23), C,D: ref. (24)) in comparison with observed mean data. Solid line: predicted mean, dash-dotted line: predicted median, gray shaded area: predicted SD, dashed line: predicted minimum/maximum, gray circles: observed mean data.

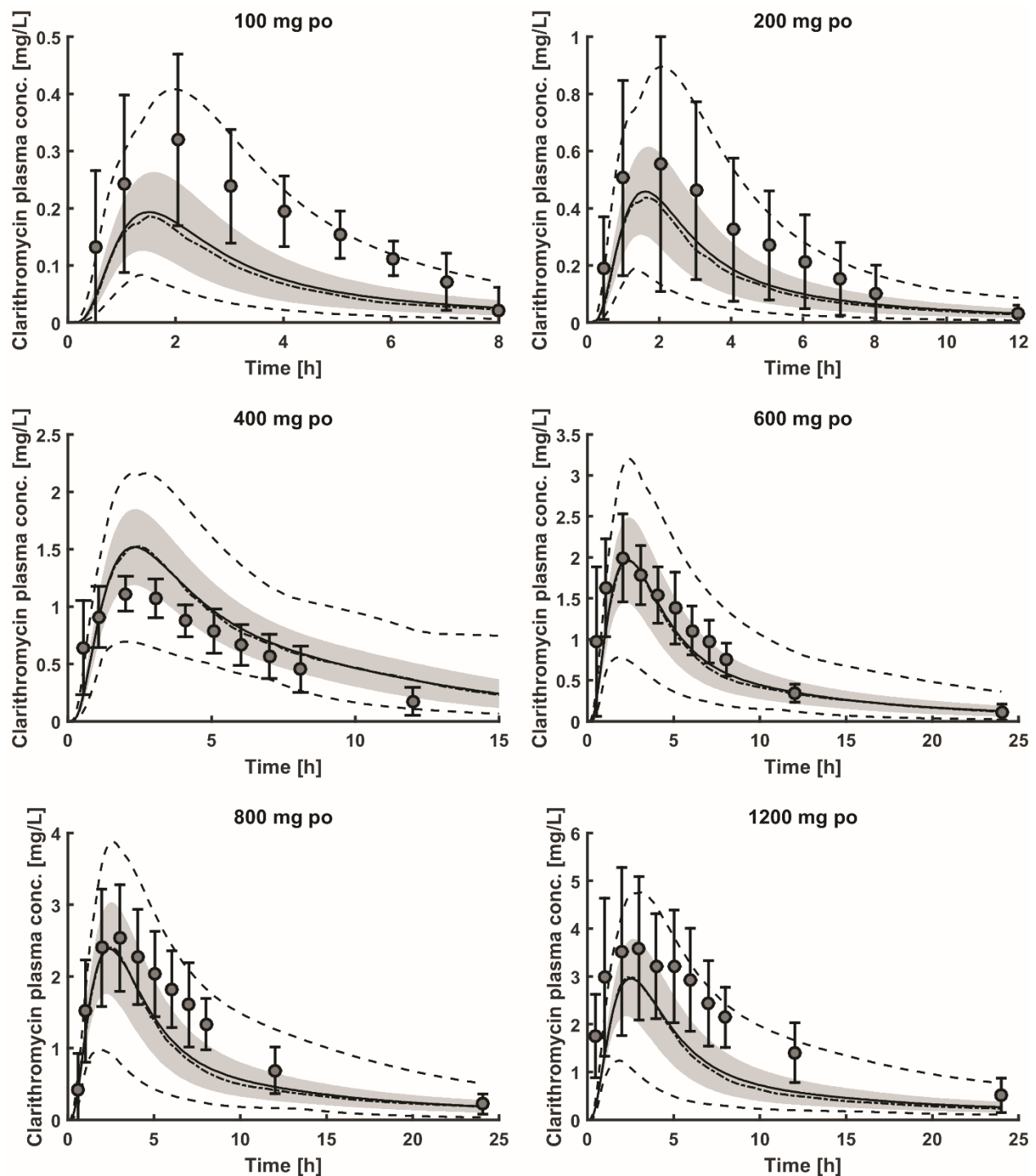


Fig. 2 Predicted concentration-time profiles of clarithromycin after oral rising doses of clarithromycin (13) in comparison with observed mean data (\pm standard deviation (SD)). Solid line: predicted mean, dash-dotted line: predicted median, gray shaded area: predicted SD, dashed line: predicted minimum/maximum, gray circles: observed mean data (\pm SD).

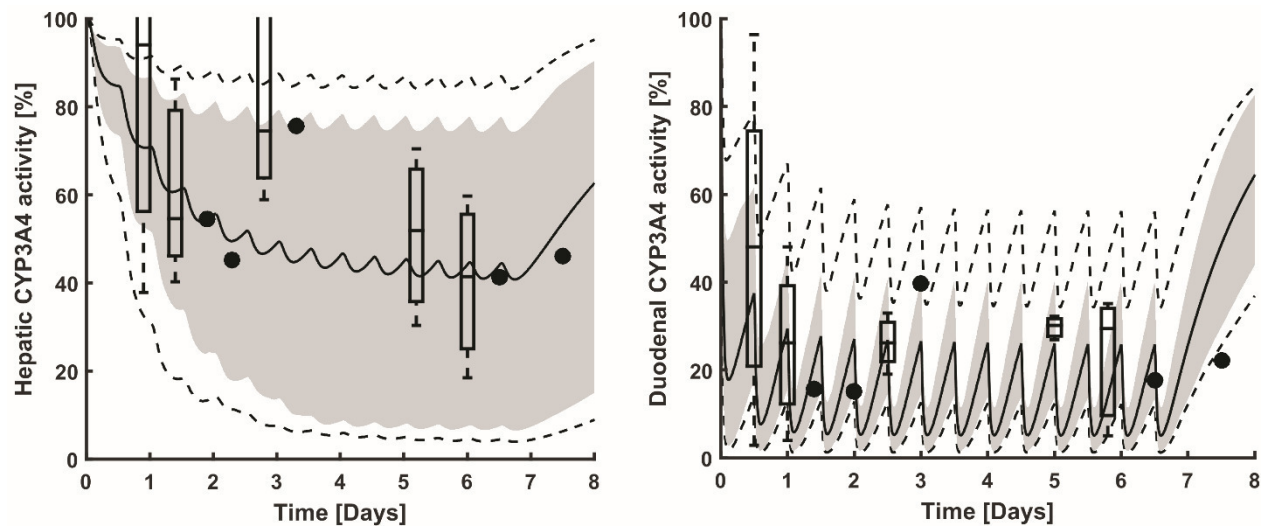


Fig. 3 Predicted CYP3A4 activity after multiple doses of clarithromycin in comparison with observed data. Left: CYP3A4 activity in the liver, right: CYP3A4 activity in the duodenum. Solid line: predicted median, gray shaded area: predicted 5th–95th percentile, dashed line: predicted minimum/maximum, boxplots/point estimates: observed data (94).

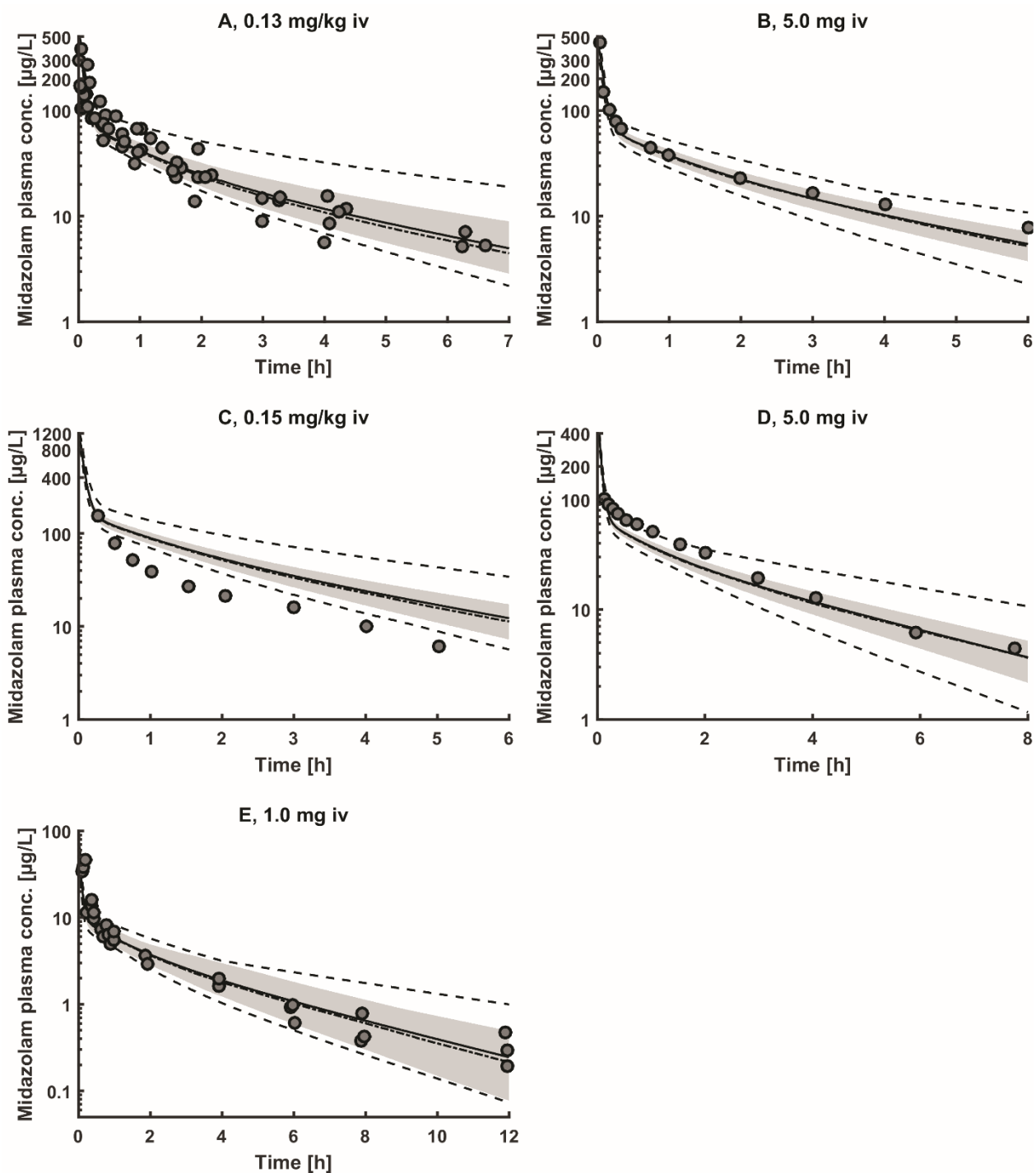


Fig. 4 Predicted concentration-time profiles of midazolam after single intravenous doses of midazolam in comparison with observed mean/individual data. Training dataset A,B: ref. (30,34) and evaluation dataset C–E: ref. (32,33,35). Solid line: predicted mean, dash-dotted line: predicted median, gray shaded area: predicted SD, dashed line: predicted minimum/maximum, gray circles: observed mean and individual data.

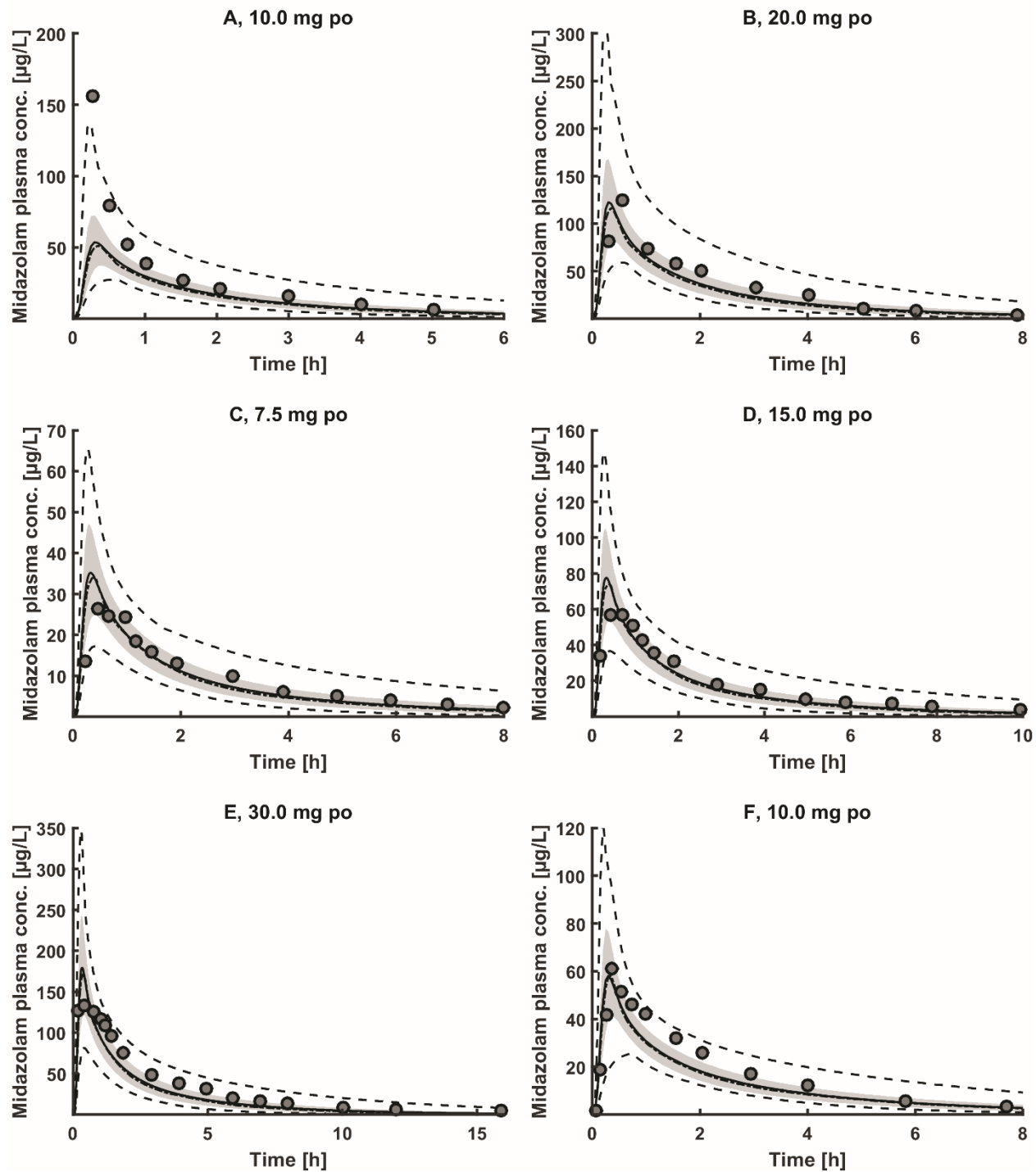


Fig. 5 Predicted concentration-time profiles of midazolam after single oral doses of midazolam in comparison with observed mean data. Training dataset A–C: ref. (35,38) and evaluation dataset D–F: ref. (33,38). Solid line: predicted mean, dash-dotted line: predicted median, gray shaded area: predicted SD, dashed line: predicted minimum/maximum, gray circles: observed mean data.

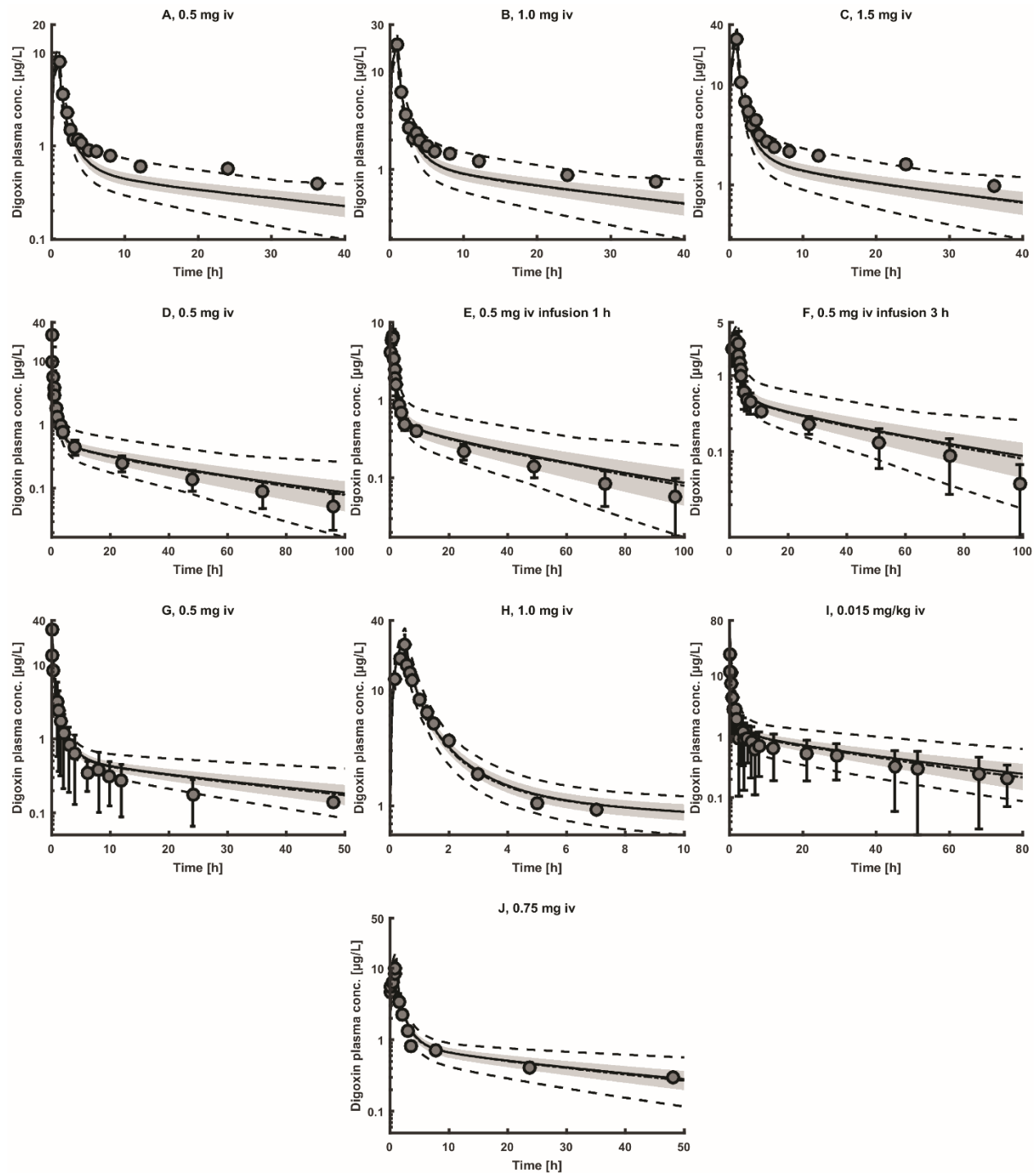


Fig. 6 Predicted concentration-time profiles of digoxin after single intravenous doses of digoxin in comparison with observed mean data. Training dataset A–F: ref. (41,46) and evaluation dataset G–J: ref. (20,42, 43, 44). Solid line: predicted mean, dash-dotted line: predicted median, gray shaded area: predicted SD, dashed line: predicted minimum/maximum, gray circles: observed mean data (\pm SD).

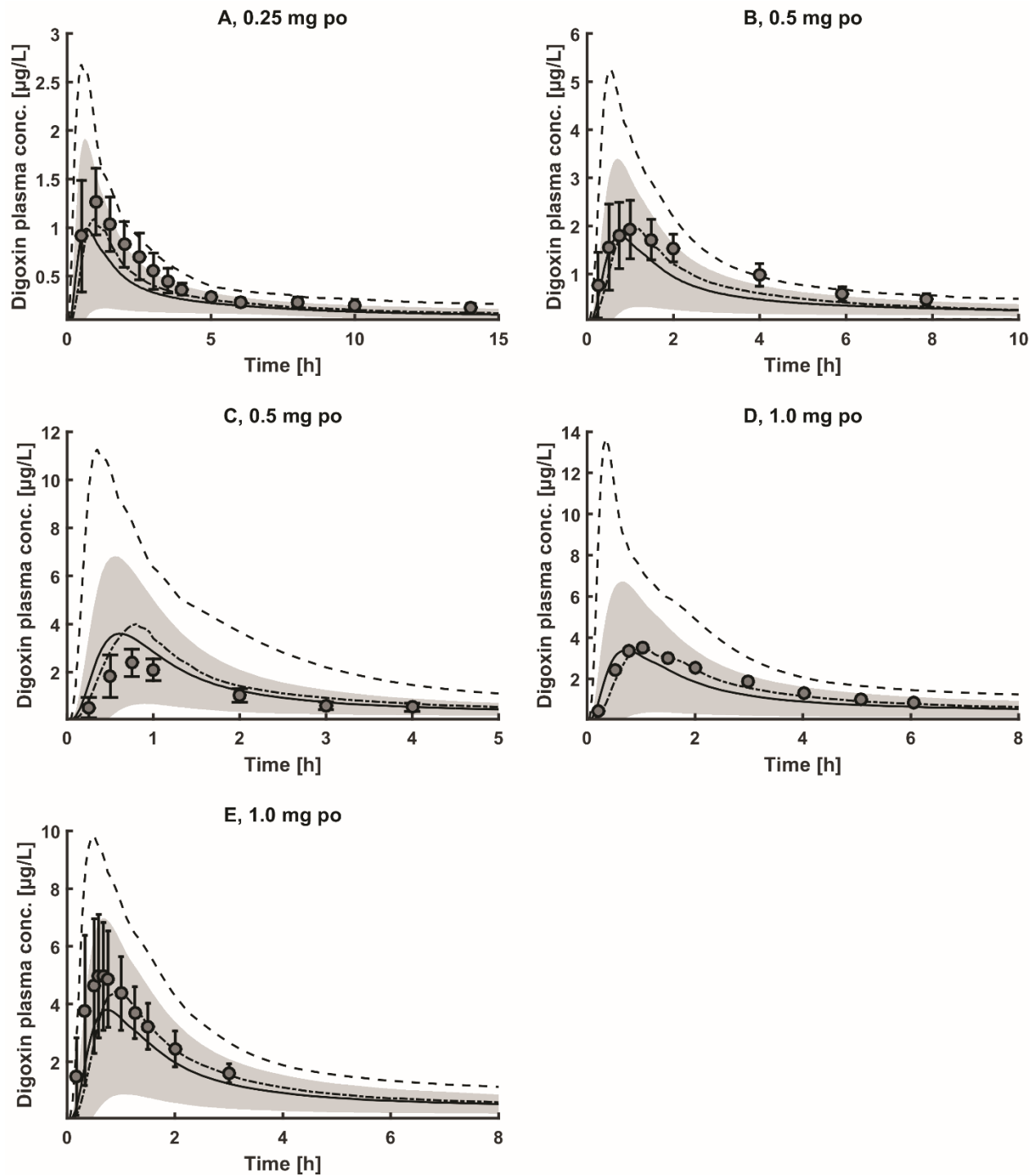


Fig. 7 Predicted concentration-time profiles of digoxin after single oral doses of digoxin in comparison with observed mean data. Training dataset A–C: ref. (44,47,49) and evaluation dataset D,E: ref. (41,50). Solid line: predicted mean, dash-dotted line: predicted median, gray shaded area: predicted SD, dashed line: predicted minimum/maximum, gray circles: observed mean data (\pm SD).

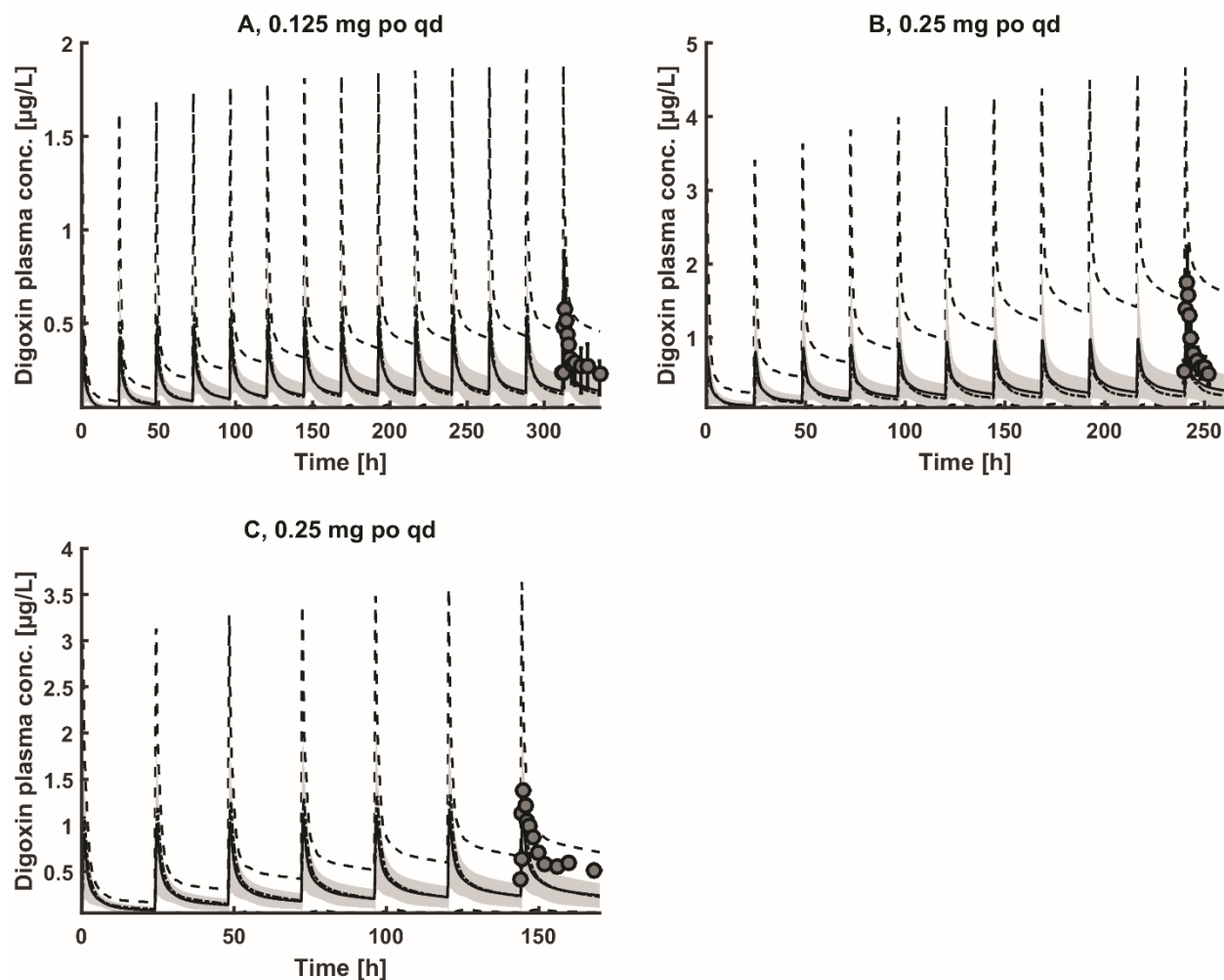


Fig. 8 Predicted concentration-time profiles of digoxin after multiple oral doses of digoxin in comparison with observed mean data. Training dataset A,B: ref. (52,53) and evaluation dataset C: ref. (54). Solid line: predicted mean, dash-dotted line: predicted median, gray shaded area: predicted SD, dashed line: predicted minimum/maximum, gray circles: observed mean data (\pm SD).

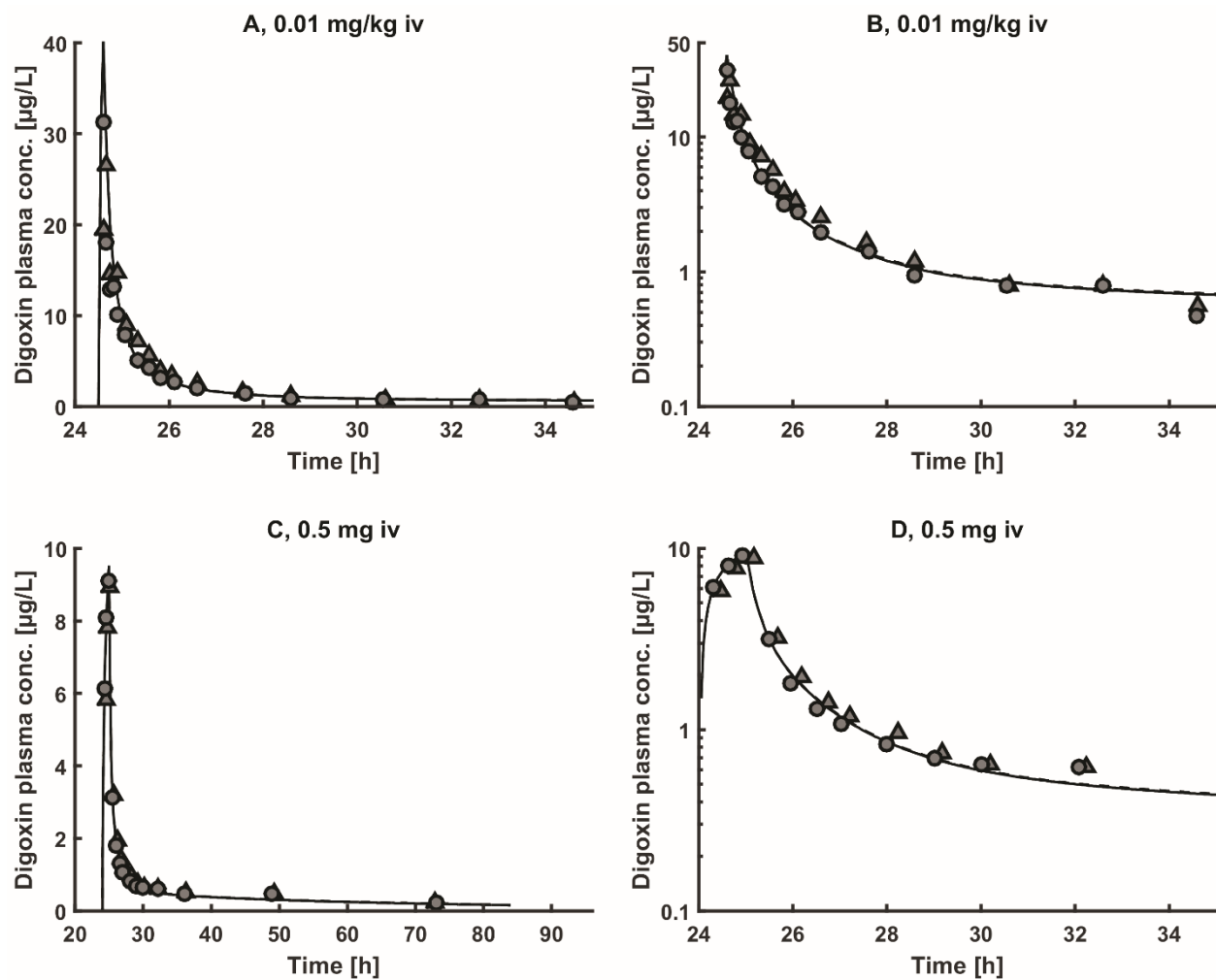


Fig. 9 Predicted concentration-time profiles of digoxin after single intravenous doses of digoxin (A,B: (26), C,D: (45)) with and without prior clarithromycin regimens in comparison with observed mean data. Solid line: predicted digoxin mean without prior clarithromycin, dashed line: predicted digoxin mean with prior clarithromycin, gray circles: observed mean digoxin without prior clarithromycin, gray triangles: observed mean digoxin with prior clarithromycin. Clarithromycin was administered orally (bid) with 250 mg (A,B) and 200 mg (C,D).

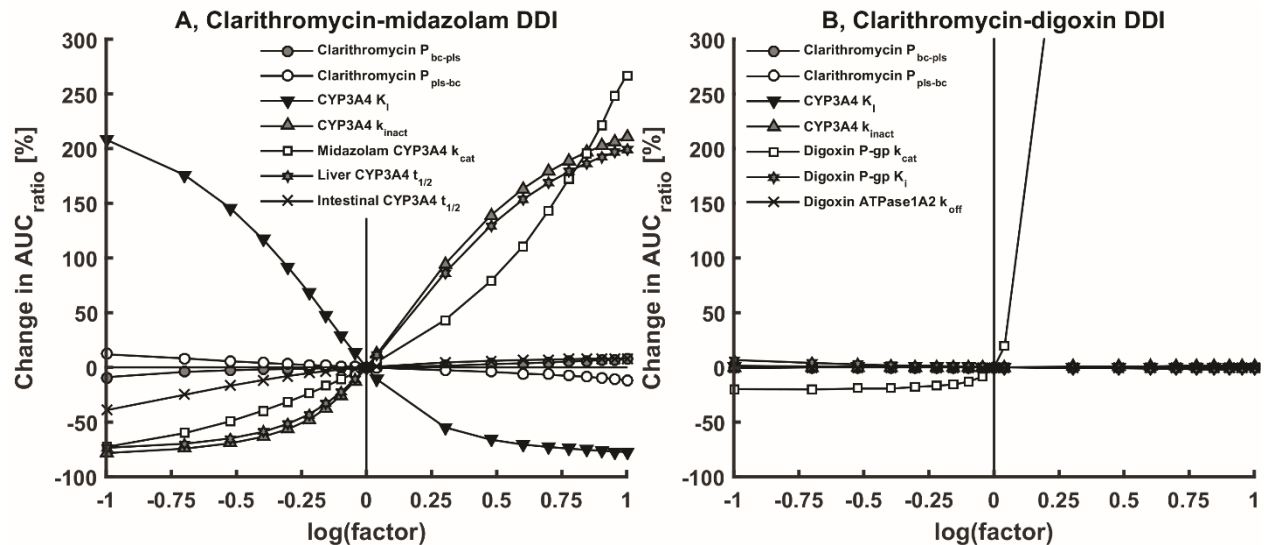


Fig. 10 Parameter sensitivity analysis. The x-axis represents the logarithm of the factor by which the parameters are multiplied in order to vary them over a range of 0.1 to 10-fold.

Table 1. Predicted count of DDI using adapted doses of midazolam and digoxin

Application and dose [mg] of clarithromycin	Application and dose [mg] of victim drug	DDI classification*	CSD [%]	RD [%]	Δ CSD	Ref.
<i>Midazolam</i>						
po (tab, MD), 500	iv (inf, 30 min, SD), 0.05 /kg	<i>No</i>	17.5	42.5	25.0	
		<i>Weak</i>	39.4	26.9	-12.5	
		<i>Moderate</i>	40.0	29.4	-10.6	(29)
		<i>Strong</i>	3.1	1.3	-1.9	
po (tab, MD), 500	po (tab, SD), 4	<i>No</i>	0.0	83.8	83.4	
		<i>Weak</i>	0.6	9.4	8.8	
		<i>Moderate</i>	58.1	6.9	-51.3	(29)
		<i>Strong</i>	41.3	0.0	-41.3	
po (tab, MD), 250	po (tab, SD), 15	<i>No</i>	0.0	66.9	66.9	
		<i>Weak</i>	16.7	6.9	-9.8	
		<i>Moderate</i>	74.2	1.3	-72.9	(39)
		<i>Strong</i>	9.2	0.0	-9.2	
<i>Digoxin</i>						
po (tab, MD), 500	po (tab, SD), 0.25	<i>No</i>	70.8	86.7	15.8	
		<i>Weak</i>	20.8	10.0	-10.8	
		<i>Moderate</i>	19.2	41.7	22.5	(48)
		<i>Strong</i>	39.2	11.7	-27.5	
po (tab, MD), 250	po (tab, SD), 0.75	<i>No</i>	51.7	54.2	2.5	
		<i>Weak</i>	7.5	8.3	0.8	
		<i>Moderate</i>	8.3	18.3	10	
		<i>Strong</i>	32.5	19.2	-13.3	

* DDI classification is based on FDA Drug Interaction Studies guidance (4): “no”, “weak”, “moderate” and “strong” are used according to $AUC_{ratio} < 1.25$, $1.25 \leq AUC_{ratio} < 2.0$, $2.0 \leq AUC_{ratio} < 5.0$ and $AUC_{ratio} \geq 5.0$, CSD (clinical study dose) % of individuals at clinical study dose, RD (reduced dose) % of individuals at adapted dose

9.3 Supporting Information of Project III

Supplemental Figures and Tables

A physiologically based pharmacokinetic and pharmacodynamic (PBPK/PD) model of the histone deacetylase (HDAC) inhibitor vorinostat for pediatric and adult patients and its application for dose specification

Daniel Moj¹, Hannah Britz¹, Jürgen Burhenne⁴, Clinton F. Stewart², Gerlinde Egerer³, Walter E. Haefeli⁴, Thorsten Lehr¹

¹ Department of Pharmacy, Clinical Pharmacy, Saarland University, Saarbruecken, Germany

² Department of Pharmaceutical Sciences, St. Jude Children's Research Hospital, Memphis, Tennessee, USA

³ Department of Hematology, Oncology, and Rheumatology, Heidelberg University Hospital, Heidelberg, Germany

⁴ Department of Clinical Pharmacology and Pharmacoepidemiology, University of Heidelberg, Heidelberg, Germany

Corresponding Author:

Thorsten Lehr, Clinical Pharmacy, Saarland University, Campus C2 2, 66123 Saarbruecken, Tel: +49/681/302-70255, Fax: +49/681/302-70258, email: Thorsten.Lehr@mx.uni-saarland.de

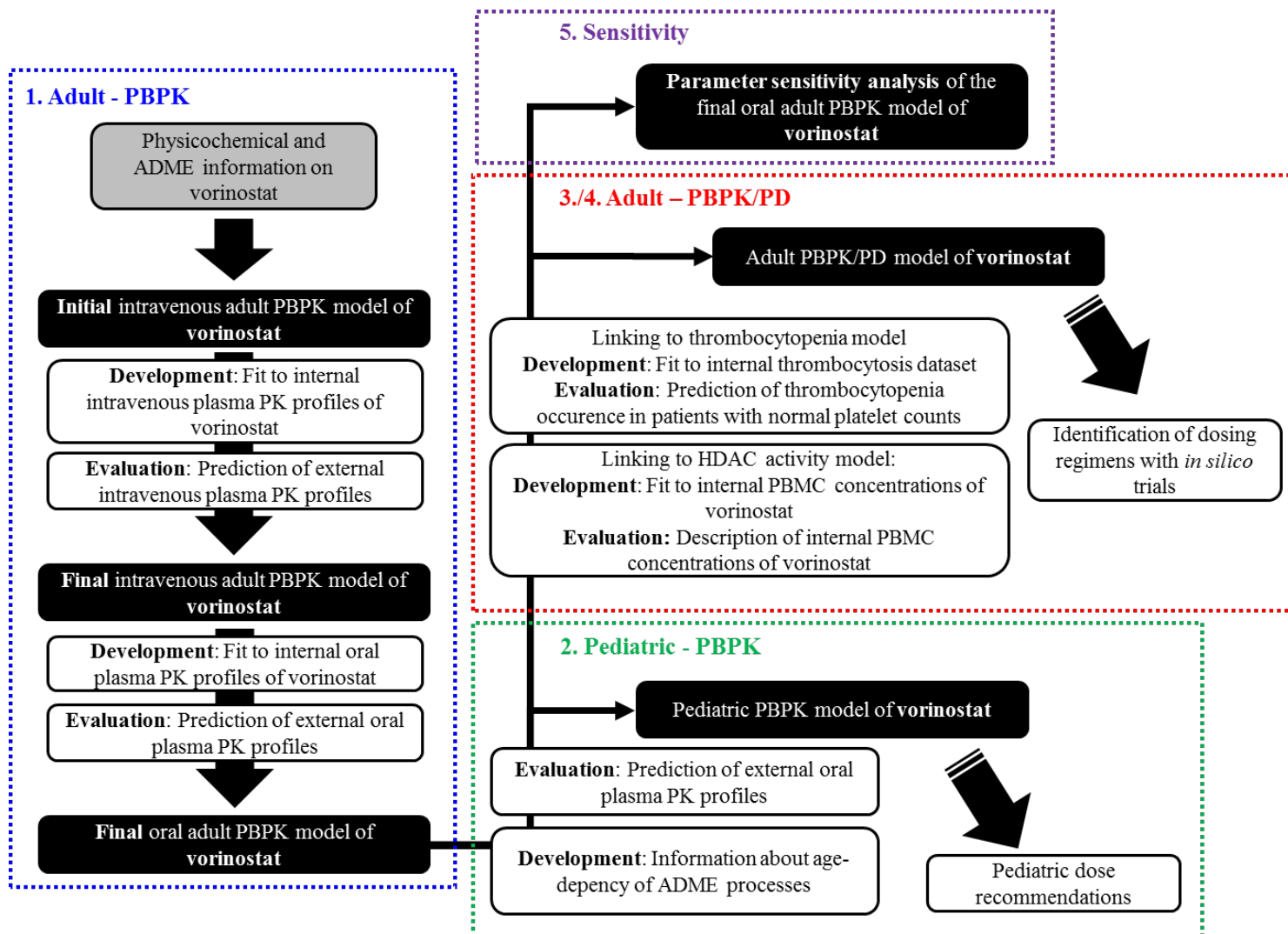


Fig. S1 Schematic overview of the PBPK/PD model development process. The sequence of model development is indicated by arrows starting with “1. Adult - PBPK”.

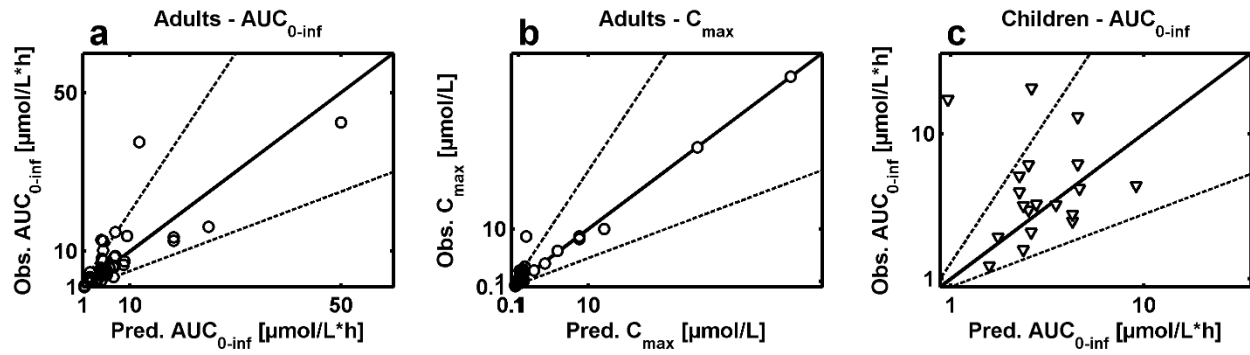


Fig. S2 Predicted versus observed PK parameters. **a** $AUC_{0-\infty}$ in adults ($n = 52$). **b** C_{\max} in adults ($n = 52$). **c** $AUC_{0-\infty}$ in children ($n = 19$). Circles indicate adults and triangles children. Dashed line: 2-fold acceptance limits.

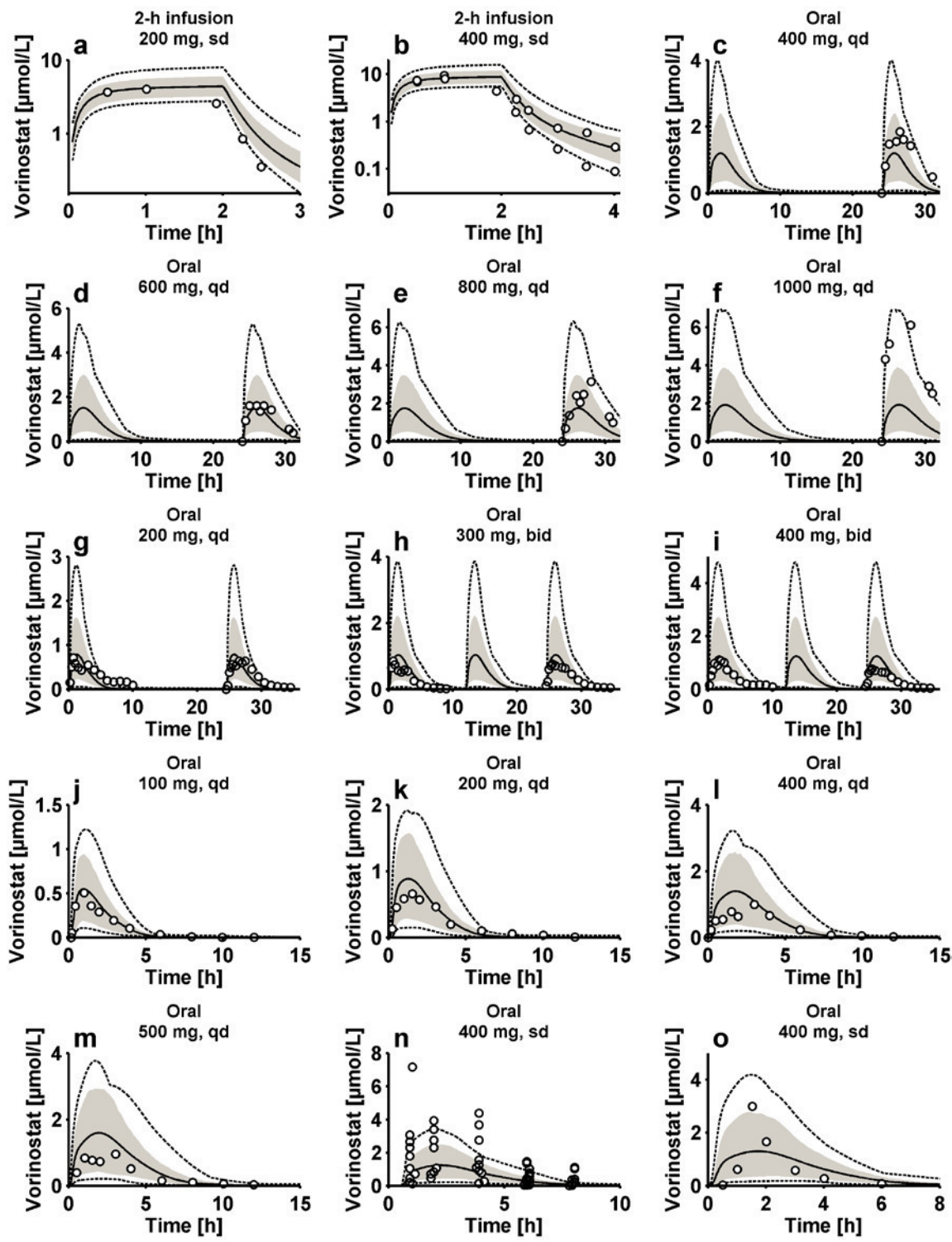
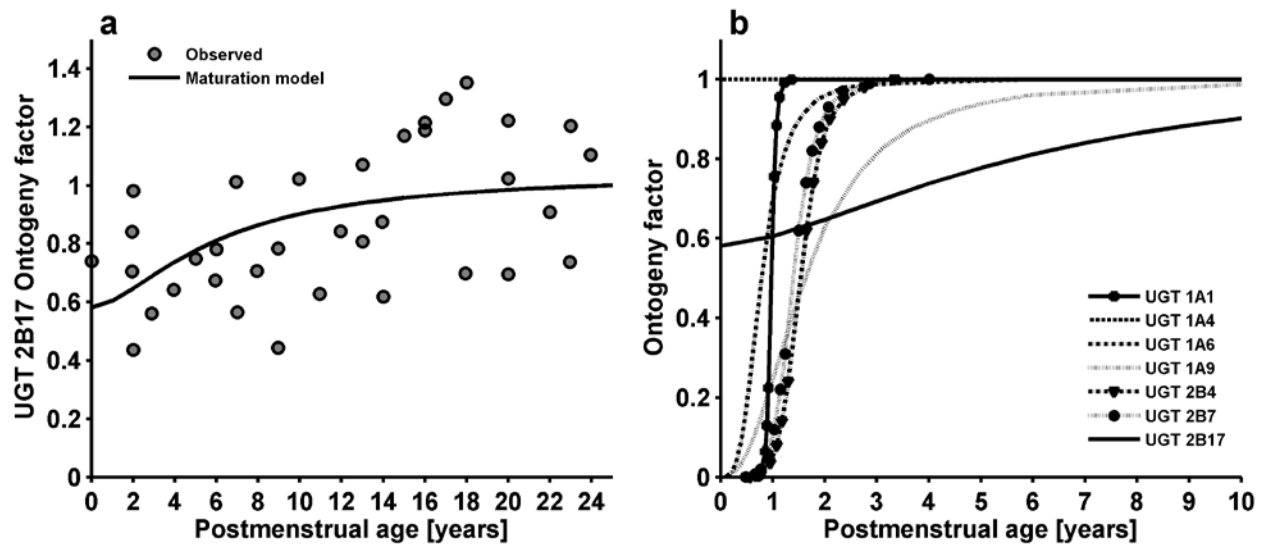


Fig. S3 External evaluation of the vorinostat PBPK model in plasma. Simulated data are represented as median (black line), 90% prediction interval (grey shaded area) and minimum and maximum values (dotted lines). Observed data are represented as white circles. **a,b** [1], **c-f** [2], **g-i** [1], **j-m** [3], **n** [4], and **o** [5]. Single doses: sd, repeated once daily doses: qd.



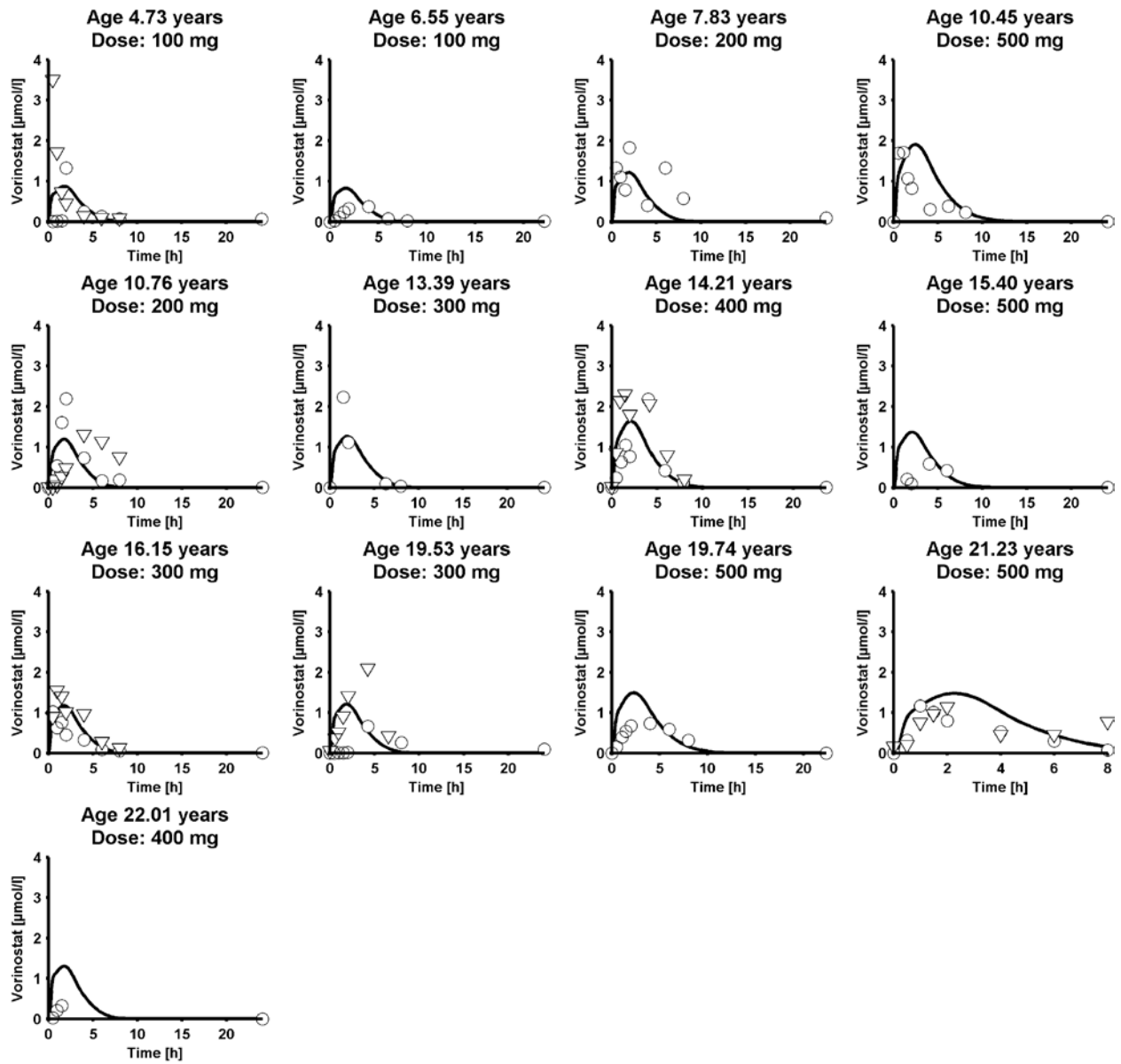


Fig. S5 Individual single oral vorinostat plasma predictions in pediatric and adult patients [12].

Circles and triangles indicate two occasions of vorinostat concentration-time measurements.

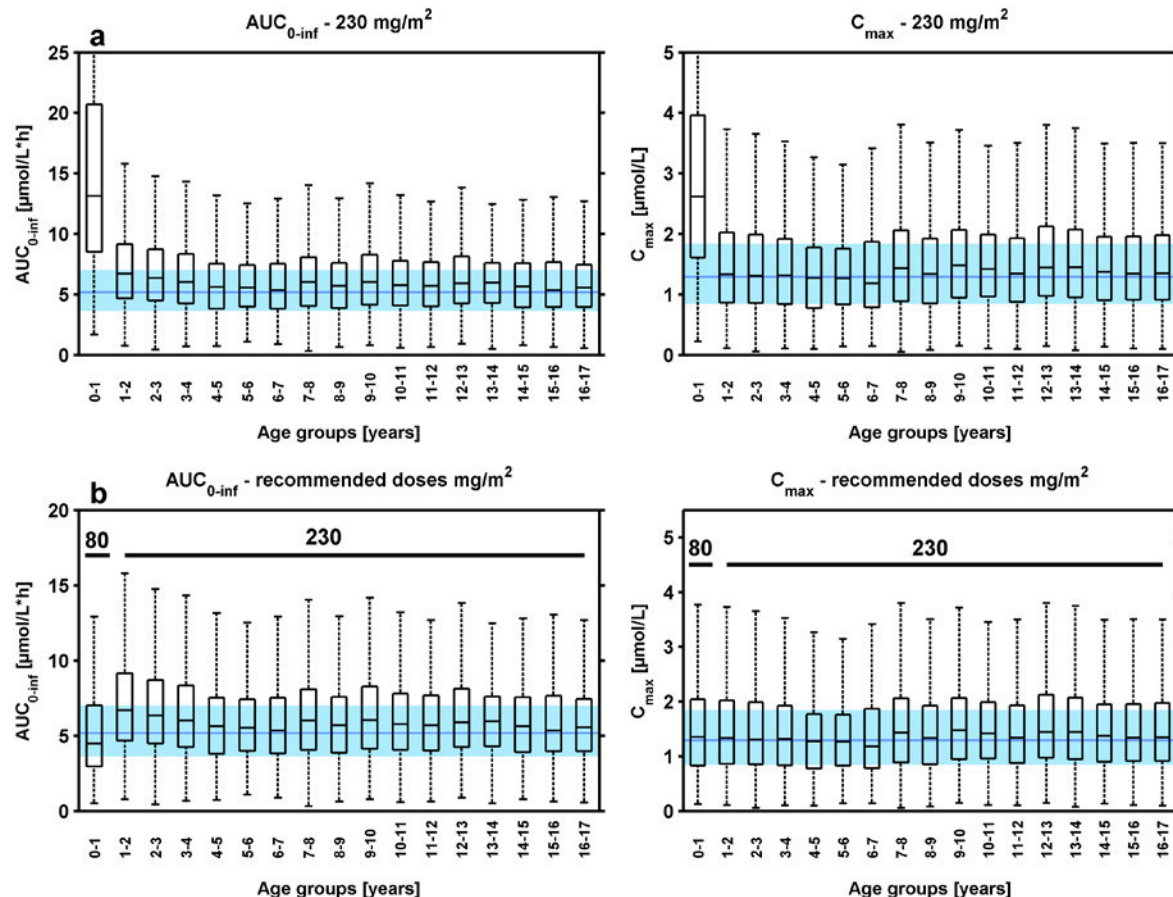


Fig. S6 Identification of pediatric vorinostat doses from 0 – 17 years. **a** $AUC_{0-\text{inf}}$ and C_{max} predictions for previously proposed 230 mg/m^2 . **b** $AUC_{0-\text{inf}}$ and C_{max} predictions for doses of 80 and 230 mg/m^2 . Boxes: 25th, 50th and 75th of predicted $AUC_{0-\text{inf}}$ and C_{max} values in the respective age groups. Box whiskers: defined as 1.0-times the interquartile range. Blue area: 25th to 75th percentile of the adult predictions following the approved adult standard dose of 400 mg. Blue solid line: median of the adult predictions.

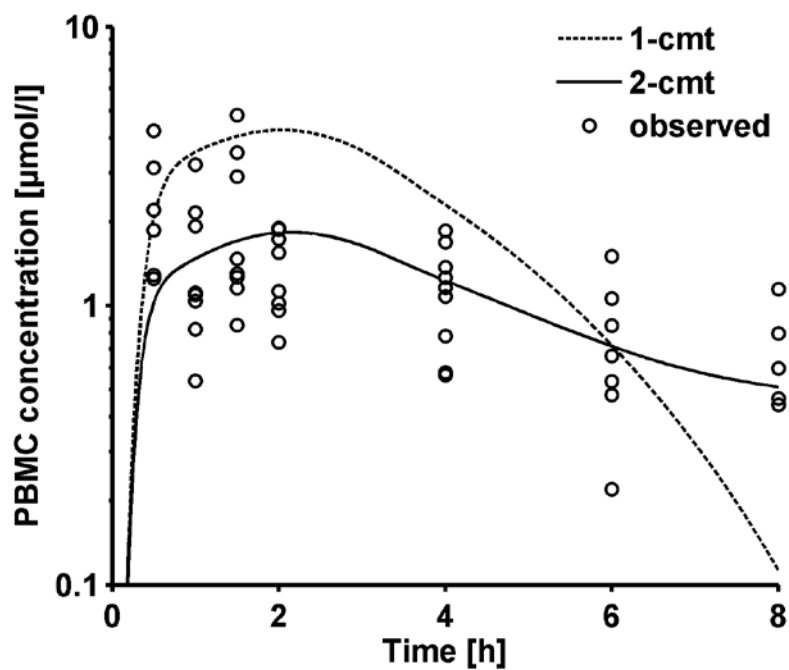


Fig. S7 Comparison of vorinostat PBMC concentration-time profiles simulated using a 1- or 2-compartmental (cmt) model following a single oral vorinostat dose of 400 mg. Simulated data are represented as dashed (1-cmt) and solid (2-cmt) lines. Observed data are represented as white circles.

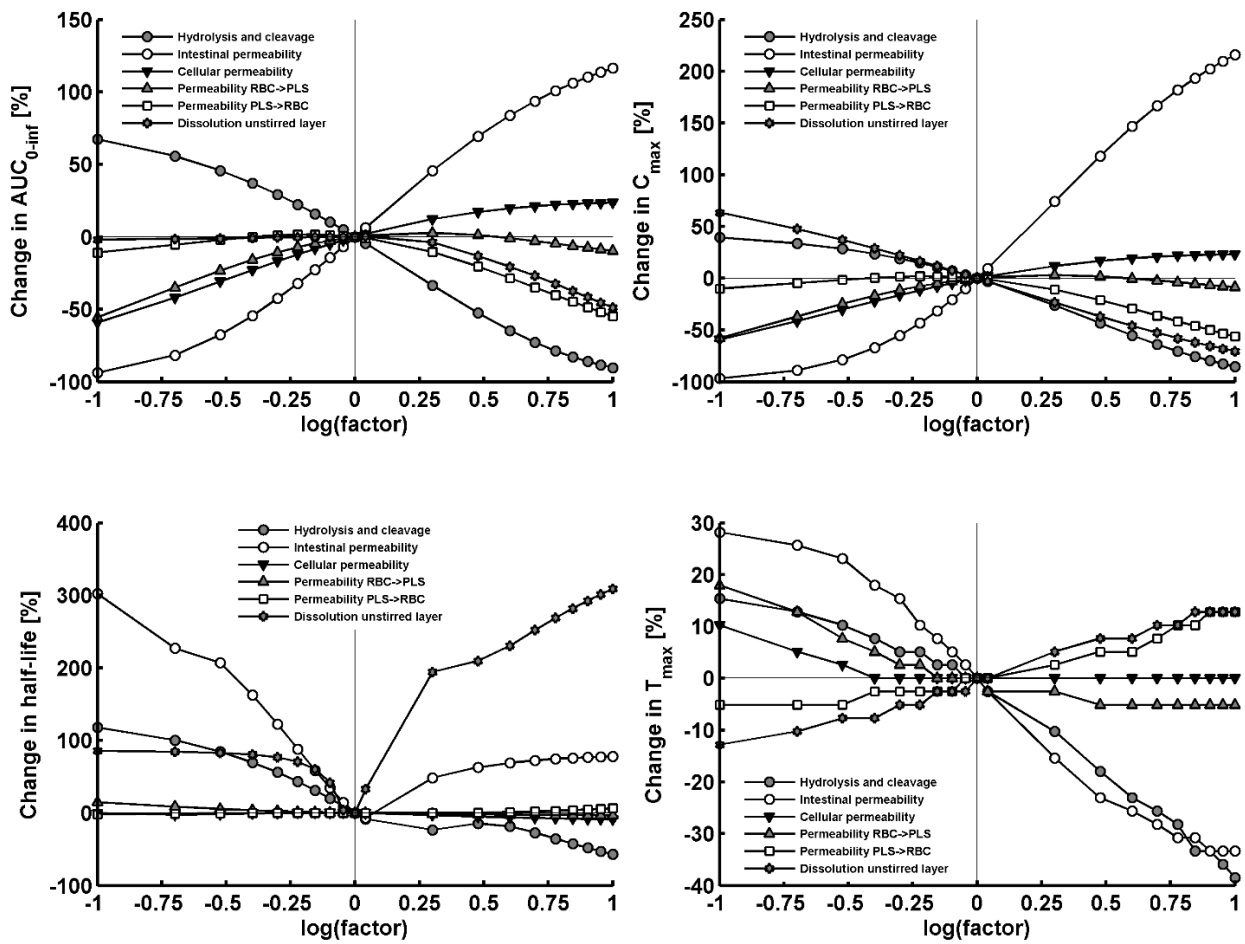


Fig. S8 Parameter sensitivity analysis of the vorinostat PBPK model.

Table S1 Overview of fitted parameters and applied optimization methods

Parameter	Optimization method	Parameter description
<i>Whole-body PBPK model of vorinostat</i>		
CL _{hydr.,β-ox.}	Nelder-Mead	Clearance via hydrolysis and β-oxidation
P _{intest}	Nelder-Mead	Intestinal permeability
P _{cell}	Nelder-Mead	Cellular permeability
P _{RBC->PLS}	Nelder-Mead	Plasma-blood permeability
P _{PLS->RBC}	Nelder-Mead	Blood-plasma permeability
Layer _{PD,unstirred,water}	Nelder-Mead	Particle dissolution unstirred water layer
<i>PBMC effect compartment model</i>		
k _{effect,1}	Monte-Carlo	Transfer rate constant Plasma→PBMC
k _{effect,2}	Monte-Carlo	Transfer rate constant PBMC→Plasma
k _{effect,deep,1}	Monte-Carlo	Transfer rate constant PBMC→PBMC _{deep}
k _{effect,deep,2}	Monte-Carlo	Transfer rate constant PBMC _{deep} →PBMC
<i>HDAC indirect response model</i>		
S _{max}	Monte-Carlo	Maximum inhibition
SC ₅₀	Monte-Carlo	Concentration at half maximum inhibition
k _{in}	Monte-Carlo	HDAC activity synthesis
k _{out}	Monte-Carlo	HDAC activity degradation

Monte-Carlo settings: Break condition for relative error improvement = 0.001, Scale of projection degree (alpha) = 30, Maximum number of iterations = 10000

Nelder Mead settings: Maximum number of iterations = 1000

Table S2 Overview of assumptions

	Assumption	New/established	Testable/ not-testable	Test/approach to assess impact	Justification	Impact on the results/recommendations
Pharmacology	HDAC inhibition turnover model can be used for dose identification in <i>in silico</i> trials with varying vorinostat doses although developed with HDAC activity measurements following a single 400 mg dose of vorinostat only	new	Not testable with the present dataset	Development of HDAC inhibition model with HDAC activity measurements following varying single and multiple vorinostat doses and compare dose identifications	Only HDAC activity measurements following a single 400 mg vorinostat dose was available	HDAC inhibition might be over- or under-predicted; doses identified for adults using the PBPK/PD approach could differ from the current ones; dose recommendations for children would not differ
	Vorinostat does not accumulate in organs and tumors	established; new	Not testable with the present dataset	Measurement of multiple dose vorinostat PK in organs and tumors	Unknown whether vorinostat accumulates in organs or tumors, but half-life of vorinostat is very short indicating no accumulation	In case of accumulation of vorinostat in organs or tumors: recommended vorinostat doses should be reduced for adults
	The only differences between patients with thrombocytosis and normal thrombocyte counts are the baseline cell counts of proliferating and circulating cells	new	Not testable with the present dataset/modeling approach	Combined analysis of the thrombocyte counts of both patient populations using the population approach	The only dataset available assessing the impact of multiple doses of vorinostat was the presented one in a thrombocytosis patient population; vorinostat impact on platelet count in patient with normal cell counts could be successfully predicted	Platelet counts might be over- or under-predicted in the patient population with normal platelet counts. Doses identified for adults using the PBPK/PD approach could differ from the current ones; dose recommendations for children would not differ
	PK/PD (HDAC activity, platelet count) relationship is similar in adults and children	new/established	Not testable with the present dataset	Combined analysis of PK/PD relationships in adults and children	Comparable vorinostat doses of 230 mg/m ² for children and 400 mg for adults lead to significant accumulation of acetylated H3 histones in both populations and to similar dose-limiting toxicities; no time-biomarker data available for children; PK data in children shows no clear relationship between dose and exposure	Different PK/PD relationships in adults and children might change interpretation of dose recommendations for children
Physiology	Maturation of UGT 2B17 protein abundance can be described by mRNA expression profile as surrogate	established	Not testable with the present dataset	Combined analysis of UGT 2B17 protein abundance over time and available mRNA data over time	In general mRNA correlates adequately with respective protein abundance; no age-dependent UGT 2B17 protein abundance measurements available	Dose recommendation for children might change as maturation might change using protein data
	The unidentified hydrolytic and oxidative enzyme is fully developed from birth on	new	Not testable with the present dataset	Identification of hydrolytic and oxidative enzyme responsible for vorinostat metabolism; identification of maturation profiles; Assessment of dose recommendations for children with and without maturation profile	Unidentified enzyme; unknown maturation profile; assuming full development from birth on, dose recommendations for children can be interpreted as maximum doses	Potential maturation would decrease vorinostat clearance at ages with immature enzyme; recommended doses would decrease
Disease	In patients with hematologic cancer or solid tumors, vorinostat has similar PK	established	Testable	Combined PK analysis of patients with hematologic or solid tumors	No differences in PK found in clinical studies	Differences in vorinostat PK in different patient groups could lead to disease-dependent PBPK model parameterization
	In patients with hematologic cancer or solid tumors, vorinostat has similar impact on HDAC inhibition	new	Not testable with the present dataset	Combined HDAC inhibition analysis of patients with hematologic or solid tumors	HDAC inhibition data only available for patients with soft tissue sarcoma only	Differences in HDAC inhibition in different patient groups could lead to disease-dependent dosing regimens
Data	Data BLQ have no impact on analysis results	new	Not testable with the present dataset	Model development with and without BLQ data followed by comparison of model simulations	No BLQ data were available	Vorinostat has a short half-life of 1-2 h, BLQ should have negligible impact on dose recommendations
Statistics	PD parameters are distributed with a CV of 20%	established	Not testable with the present modeling approach	Development of PD models using the population approach	PD parameters are known to differ between individuals	Dose recommendations for adults based on the PBPK/PD approach were carried out using a typical individual; assumption has no impact on dose recommendations

BLQ below limit of quantification, CV coefficient of variation, HDAC histone deacetylase, mRNA messenger ribonucleic acid, PBMC peripheral blood mononuclear cells, PD pharmacodynamics, PK pharmacokinetics, UGT Uridine 5'-diphospho-glucuronosyltransferase

Table S3 System-related thrombocytopenia model parameters

Reference	Circ ₀ [10 ⁹ cells/l]	MTT [h]	k _{tr} [1/h]	γ [-]	δ [-]
[13]	267	97	0.0412	0.288	NA
[14]	NA	60	0.0663	0.118	NA
[15]	277	104	0.0385	0.239	NA
[16]	255	37	0.1070	0.135	NA
[17]	253	110	0.0364	0.203	NA
[18]	195	95	0.0421	0.498	0.177
[18]	273	95 ^a	0.0421 ^a	0.498 ^a	0.177 ^a
[19]	NA	142	0.0282	0.176	NA
[20]	185	112	0.0357	NA	NA
Mean	244	95	0.0486	0.269	0.177

Circ₀ circulating thrombocytes baseline

MTT mean transit time

k_{tr} transit rate constant

γ and *δ* feedback exponents

^a only counted once for the calculation of the mean

NA not available

Table S4 Overall precision and accuracy of the simulated and predicted adult and pediatric pharmacokinetic profiles

Ref.	Route of administration	Dose [mg]	Dosing schedule	Internal (in) or external (ex) dataset	MPE [%]
[21]	iv (inf. 2 h)	75 - 900 /m ²	sd	in	47
[1]	iv (inf. 2 h)	200, 400	sd	ex	35
[2]	po	400 - 1000	qd	ex	-40
[3]	po	100 - 500	qd	in	15
[22]	po	200 - 400	qd	ex	-7
[23,24] ^a	po	400	sd	in	-8
[4]	po	400	qd	ex	48
[5]	po	400	qd	ex	62
[12] ^a	po	100 - 500	sd	ex	248
Mean:					44

^a unpublished

iv intravenous

inf infusion

MPE mean prediction error

po per oral

qd once daily

sd single dose

Table S5 PBPK/PD model parameter values for the PBMC effect compartment model and the HDAC indirect response model

Parameter	Unit	Value	Parameter description
<i>PBMC effect compartment model</i>			
$k_{effect,1}$	1/min	1.58	Transfer rate constant Plasma → PBMC
$k_{effect,2}$	1/min	4.00E-3	Transfer rate constant PBMC → Plasma
$k_{effect,deep,1}$	1/min	1.19	Transfer rate constant PBMC → PBMC _{deep}
$k_{effect,deep,2}$	1/min	1.26E-3	Transfer rate constant PBMC _{deep} → PBMC
<i>HDAC indirect response model</i>			
S_{max}	-	8.35	Maximum inhibition
SC_{50}	μmol/l	2.38	Concentration at half maximum inhibition
k_{in}	1/min	0.043	HDAC activity synthesis
k_{out}	1/min	0.043	HDAC activity degradation

Table S6 Overview of *in silico* trials (part 1)

<i>In silico</i> trial	Admin. route	Dose [mg]	Infusion time [h]	Dosing regimen	Δ HDAC activity [% APV]	Δ Acc. time HDAC activity < 50 % [% APV]	Δ Thrombocyte count [% APV] ^a
F1	infusion	900 /m ²	2	qd	-68	+50	-97
APV	oral	400		qd	0	0	0
J1	oral	400		bid (every 2 nd week)	0	0	-6
O1	infusion	400		bid (every 2 nd week)	-54	0	-54
D	oral	800		single dose, every 2 nd day	-14	-10	-1
N1	oral	400		bid; 3 cons. days a week	0	-14	+2
N2	oral	436.56		bid; 3 cons. days a week	-3	-14	0
M2	oral	641.74		bid; 2 cons. days a week	-14	-15	0
L2	oral	860.32		qd; 3 cons. days a week	-19	-16	0
J2	oral	324.23		bid (every 2 nd week)	5	-17	0
E	oral	1600		single dose, every 4 th day	-24	-22	0
G	infusion	900 /m ²	2	qd (every 2 nd week)	-68	-26	-87
I2	oral	631.09		qd (every 2 nd week)	-14	-26	0
K2	oral	1284.41		qd; 2 cons. days a week	-22	-27	0
F2	infusion	120	2	qd	-24	-33	0
O2	infusion	97.11		bid (every 2 nd week)	-14	-33	0
H1	infusion	600 /m ²	2	qd (every 2 nd week)	-65	-34	-71
M1	oral	400		bid; 2 cons. days a week	0	-43	+9
I1	oral	400		qd (every 2 nd week)	0	-51	+9
L1	oral	400		qd; 3 cons. days a week	0	-58	+14
H2	infusion	194.3	2	qd (every 2 nd week)	-38	-59	0
H3	infusion	194.3	2.47	qd (every 2 nd week)	-35	-59	0
B	oral	200		bid	+27	-66	+1
K1	oral	400		qd; 2 cons. days a week	0	-72	+18
C	oral	150		tid	+38	-100	-2

Acc. accumulated

Admin. administration

APV approved standard treatment

^a -74% is equal to the lower thrombocyte constraint of 50*10⁹ cells/l

qd dosing once daily

bid dosing twice daily

tid dosing thrice daily

cons consecutive

Table S7 Overview of *in silico* trials (part 2)

<i>In silico</i> trial	Admin. route	Dose [mg]	Infusion time [h]	Dosing regimen	Δ HDAC activity [% APV]	Δ Acc. time HDAC activity < 50 % [% APV]	Δ Thrombocyte count [% APV] ^a
C	oral	3000		tid	-16	+509	-72
B	oral	3000		bid	-24	+471	-74
A	oral	3000		qd	-27	+283	-62
J1	oral	3000		bid (every 2 nd week)	-27	+224	-69
N1	oral	3000		bid; 3 cons. days a week	-27	+211	-55
D	oral	3000		single dose, every 2 nd day	-27	+89	-30
I1	oral	3000		qd (every 2 nd week)	-27	+89	-40
L1	oral	3000		qd; 3 cons. days a week	-27	+61	-27
F1	infusion	773	2	qd	-62	+33	-74
O1	infusion	614		bid (every 2 nd week)	-59	+17	-74
K1	oral	3000		qd; 2 cons. days a week	-27	+6	-12
APV	oral	400		qd	0	0	0
E	oral	3000		single dose, every 4 th day	-27	-6	-7
G	infusion	1230	2	qd (every 2 nd week)	-65	-34	-74
M1	oral	3000		bid; 2 cons. days a week	-27	-43	-37

Acc. accumulated

Admin. administration

APV approved standard treatment

^a -74% is equal to the lower thrombocyte constraint of 50×10^9 cells/l

qd dosing once daily

bid dosing twice daily

tid dosing thrice daily

cons consecutive

References

1. U.S. Food and Drug Administration. Center for Drug Evaluation and Research. Vorinostat NDA 021991 Clinical Pharmacology and Biopharmaceutics Review. (2006)
http://www.accessdata.fda.gov/drugsatfda_docs/nda/2006/021991s000_Zolinza_ClinPharmR.pdf. Accessed November 11, 2016
2. Dickson MA, Rathkopf DE, Carvajal RD, Grant S, Roberts JD, Reid JM, Ames MM, McGovern RM, Lefkowitz RA, Gonen M, Cane LM, Dials HJ, Schwartz GK (2011) A phase I pharmacokinetic study of pulse-dose vorinostat with flavopiridol in solid tumors. *Invest New Drugs* 29 (5):1004-1012. doi:10.1007/s10637-010-9447-x
3. Fujiwara Y, Yamamoto N, Yamada Y, Yamada K, Otsuki T, Kanazu S, Iwasa T, Hardwick JS, Tamura T (2009) Phase I and pharmacokinetic study of vorinostat (suberoylanilide hydroxamic acid) in Japanese patients with solid tumors. *Cancer Sci* 100 (9):1728-1734. doi:10.1111/j.1349-7006.2009.01237.x
4. Mahalingam D, Mita M, Sarantopoulos J, Wood L, Amaravadi RK, Davis LE, Mita AC, Curiel TJ, Espitia CM, Nawrocki ST, Giles FJ, Carew JS (2014) Combined autophagy and HDAC inhibition. *Autophagy* 10 (8):1403-1414. doi:10.4161/auto.29231
5. Ramalingam SS, Parise RA, Ramanathan RK, Lagattuta TF, Musguire LA, Stoller RG, Potter DM, Argiris AE, Zwiebel JA, Egorin MJ, Belani CP (2007) Phase I and pharmacokinetic study of vorinostat, a histone deacetylase inhibitor, in combination with carboplatin and paclitaxel for advanced solid malignancies. *Clin Cancer Res* 13 (12):3605-3610. doi:10.1158/1078-0432.CCR-07-0162
6. Strassburg CP, Strassburg A, Kneip S, Barut A, Tukey RH, Rodeck B, Manns MP (2002) Developmental aspects of human hepatic drug glucuronidation in young children and adults. *Gut* 50 (2):259-265
7. Zaya MJ, Hines RN, Stevens JC (2006) Epirubicin glucuronidation and UGT2B7 developmental expression. *Drug Metab Dispos* 34 (12):2097-2101. doi:10.1124/dmd.106.011387
8. Pacifici GM, Sawe J, Kager L, Rane A (1982) Morphine glucuronidation in human fetal and adult liver. *Eur J Clin Pharmacol* 22 (6):553-558
9. McRorie TI, Lynn AM, Nespeca MK, Opheim KE, Slattery JT (1992) The maturation of morphine clearance and metabolism. *American journal of diseases of children* (1960) 146 (8):972-976
10. Edginton AN, Schmitt W, Willmann S (2006) Development and evaluation of a generic physiologically based pharmacokinetic model for children. *Clin Pharmacokinet* 45 (10):1013-1034. doi:10.2165/00003088-200645100-00005
11. Neumann E, Mehboob H, Ramirez J, Mirkov S, Zhang M, Liu W (2016) Age-dependent hepatic UDP-glucuronosyltransferase gene expression and activity in children. *Front Pharmacol* 7:437. doi:10.3389/fphar.2016.00437
12. Fouladi M, Park JR, Stewart CF, Gilbertson RJ, Schaiquevich P, Sun J, Reid JM, Ames MM, Speights R, Ingle AM, Zwiebel J, Blaney SM, Adamson PC (2010) Pediatric phase I trial and pharmacokinetic study of vorinostat: a Children's Oncology Group phase I consortium report. *J Clin Oncol* 28 (22):3623-3629. doi:10.1200/JCO.2009.25.9119
13. Fouliard S, Robert R, Jacquet-Bescond A, du Rieu QC, Balasubramanian S, Loury D, Loriot Y, Hollebecque A, Kloos I, Soria JC, Chenel M, Depil S (2013) Pharmacokinetic/pharmacodynamic modelling-based optimisation of administration schedule for the histone deacetylase inhibitor abexinostat (S78454/PCI-24781) in phase I. *European journal of cancer (Oxford, England : 1990)* 49 (13):2791-2797. doi:10.1016/j.ejca.2013.05.009
14. Nagata M, Ishiwata Y, Takahashi Y, Takahashi H, Saito K, Fujii Y, Kihara K, Yasuhara M (2015) Pharmacokinetic-pharmacodynamic analysis of sunitinib-induced thrombocytopenia in Japanese patients with renal cell carcinoma. *Biological & pharmaceutical bulletin* 38 (3):402-410. doi:10.1248/bpb.b14-00636
15. Vong C, Chalret du Rieu Q, Fouliard S, Roger E, Kloos I, Depil S, Chenel M, Friberg LE Semi-mechanistic PKPD model of thrombocytopenia characterizing the effect of a new histone deacetylase

- inhibitor (HDACi) in development, in co-administration with doxorubicin. PAGE 22 (2013) Abstr 2915. Available at: www.page-meeting.org/?abstract=2915. [Last accessed 21 February 2017].
16. Bender BC, Schaedeli-Stark F, Koch R, Joshi A, Chu YW, Rugo H, Krop IE, Girish S, Friberg LE, Gupta M (2012) A population pharmacokinetic/pharmacodynamic model of thrombocytopenia characterizing the effect of trastuzumab emtansine (T-DM1) on platelet counts in patients with HER2-positive metastatic breast cancer. *Cancer Chemother Pharmacol* 70 (4):591-601. doi:10.1007/s00280-012-1934-7
17. Sasaki T, Takane H, Ogawa K, Isagawa S, Hirota T, Higuchi S, Horii T, Otsubo K, Ieiri I (2011) Population pharmacokinetic and pharmacodynamic analysis of linezolid and a hematologic side effect, thrombocytopenia, in Japanese patients. *Antimicrob Agents Chemother* 55 (5):1867-1873. doi:10.1128/aac.01185-10
18. Chalret du Rieu Q, Fouliard S, White-Koning M, Kloos I, Chatelut E, Chenel M (2014) Pharmacokinetic/Pharmacodynamic modeling of abexinostat-induced thrombocytopenia across different patient populations: application for the determination of the maximum tolerated doses in both lymphoma and solid tumour patients. *Invest New Drugs* 32 (5):985-994. doi:10.1007/s10637-014-0118-1
19. Zandvliet AS, Schellens JHM, Dittrich C, Wanders J, Beijnen JH, Huitema ADR (2008) Population pharmacokinetic and pharmacodynamic analysis to support treatment optimization of combination chemotherapy with indisulam and carboplatin. *British Journal of Clinical Pharmacology* 66 (4):485-497. doi:10.1111/j.1365-2125.2008.03230.x
20. Minichmayr I, Nock V, Jaehde U, Kloft C (2013) Thrombocytopenia following high-dose chemotherapy with carboplatin, etoposide and thiopeta in patients with testicular germ cell cancer. *International journal of clinical pharmacology and therapeutics* 51 (1):74-76
21. Kelly WK, Richon VM, O'Connor O, Curley T, MacGregor-Curtelli B, Tong W, Klang M, Schwartz L, Richardson S, Rosa E, Drobniak M, Cordon-Cordozo C, Chiao JH, Rifkind R, Marks PA, Scher H (2003) Phase I clinical trial of histone deacetylase inhibitor suberoylanilide hydroxamic acid administered intravenously. 9 (10):3578-3588
22. Kelly WK (2005) Phase I study of an oral histone deacetylase inhibitor, suberoylanilide hydroxamic acid, in patients with advanced cancer. *Journal of Clinical Oncology* 23 (17):3923-3931. doi:10.1200/jco.2005.14.167
23. Schmitt T, Mayer-Steinacker R, Mayer F, Grunwald V, Schutte J, Hartmann JT, Kasper B, Husing J, Hajda J, Ottawa G, Mechtersheimer G, Mikus G, Burhenne J, Lehmann L, Heilig CE, Ho AD, Egerer G (2016) Vorinostat in refractory soft tissue sarcomas - Results of a multi-centre phase II trial of the German Soft Tissue Sarcoma and Bone Tumour Working Group (AIO). *European journal of cancer (Oxford, England : 1990)* 64:74-82. doi:10.1016/j.ejca.2016.05.018
24. Liu L, Detering JC, Milde T, Haefeli WE, Witt O, Burhenne J (2014) Quantification of vorinostat and its main metabolites in plasma and intracellular vorinostat in PBMCs by liquid chromatography coupled to tandem mass spectrometry and its relation to histone deacetylase activity in human blood. *J Chromatogr B Analyt Technol Biomed Life Sci* 964:212-221. doi:10.1016/j.jchromb.2014.02.014

10 Appendix

10.1 Original Publications

1. Hanke N, Teifel M, Moj D, Wojtyniak JG, Britz H, Aicher B, Sindermann H, Ammer N, Lehr T. A physiologically based pharmacokinetic (PBPK) parent-metabolite model of the chemotherapeutic zoxtarelin doxorubicin-integration of in vitro results, Phase I and Phase II data and model application for drug-drug interaction potential analysis. *Cancer Chemother and Pharmacol*, 81(2): 291-304 (2018).
2. Moj D, Hanke N, Britz H, Frechen S, Kanacher T, Wendl T, Haefeli WE, Lehr T. Clarithromycin, midazolam, and digoxin: Application of PBPK modeling to gain new insights into drug-drug interactions and co-medication regimens. *AAPS J*, 19(1): 298-312 (2017).
3. Moj D, Britz H, Burhenne J, Stewart CF, Egerer G, Haefeli WE, Lehr T. A physiologically based pharmacokinetic and pharmacodynamic (PBPK/PD) model of the histone deacetylase (HDAC) inhibitor vorinostat for pediatric and adult patients and its application for dose specification. *Cancer Chemother and Pharmacol*, 80(5): 1013-1026 (2017).
4. Schäfer N, Moj D, Lehr T, Schmidt PH, Ramsthaler F. The feasibility of physiologically based pharmacokinetic modeling in forensic medicine illustrated by the example of morphine. *Int J Legal Med*, 132(2): 415-424 (2018).

10.2 Conference Abstracts

1. Hanke N, Teifel M, Moj D, Wojtyniak JG, Britz H, Aicher B, Sindermann H, Ammer N, Lehr T. Physiologically-based pharmacokinetic (PBPK) modeling of the chemotherapeutic zoxtarelin doxorubicin and model application for drug-drug interaction (DDI) potential analysis. *Central European Society for Anti-cancer Drug Research (CESAR)* meeting 2018, Berlin, Germany
2. Moj D, Britz H, Egerer G, Haefeli WE, Lehr T. A PBPK-PD modeling approach to improve vorinostat dosing regimens in adult patients accounting for histone deacetylase activity and thrombocyte counts. *Population Approach Group Europe (PAGE)* meeting 2017, Budapest, Hungary

3. Titze M, Moj D. Pharmacometric Modeling in Clinical Pharmacy – Population Pharmacokinetic Modeling. *GradUS Global Meeting 2016*, Saarbrücken, Germany
4. Moj D, Titze M. Pharmacometric Modeling in Clinical Pharmacy - Physiologically-based Pharmacokinetic (PBPK) Modeling. *GradUS Global Meeting 2016*, Saarbrücken, Germany
5. Britz H, Moj D, Hanke N, Lehr T. Physiologically-Based Pharmacokinetic (PBPK) Modeling of the Dronedarone Drug-Drug Interaction with Digoxin. *Population Approach Group Europe (PAGE) meeting 2016*, Lisbon, Portugal
6. Hanke N, Frechen S, Britz H, Moj D, Kanacher, Eissing T, Wendl T, Lehr T. Physiologically-based Pharmacokinetic Modeling of Rifampin Drug-Drug Interactions with Midazolam and Digoxin. *Population Approach Group Europe (PAGE) meeting 2016*, Lisbon, Portugal
7. Moj D, Haefeli WE, Lehr T. Application of Physiologically Based Pharmacokinetic (PBPK) Modeling to Support Midazolam Dose Selection during Clarithromycin Treatment. *5th HIPS Symposium 2015*, Saarbrücken, Germany
8. Moj D, Schäftlein A, Hanke N, Braun W, Müller MJ, Lehr T. Is the reference man still suitable for physiologically-based pharmacokinetic (PBPK) modeling? *Population Approach Group Europe (PAGE) meeting 2015*, Crete, Greece
9. Moj D, T. Kanacher, T. Wendl, S. Willmann, T. Lehr. Physiologically-based Pharmacokinetic (PBPK) modeling of the time-dependent drug-drug interaction (DDI) of clarithromycin and midazolam. *Population Approach Group Europe (PAGE) meeting 2014*, Alicante, Spain
10. Moj D, K. Thelen, S. Willman, T. Lehr. Physiologically-based pharmacokinetic (PBPK) model of clarithromycin. *Annual meeting of the German Pharmaceutical Society (DPhG) 2013*, Freiburg, Germany

10.3 Oral Presentation

Moj D.

Introduction to Physiologically-based pharmacokinetic modeling.
2nd MOSIPS meeting 2013, Saarbrücken, Germany

10.4 Book Chapter

Moj D, Titze M, Scherer N, Lehr T.

Pharmakogenetik in der Onkologie. In: Klein HG and Haen E, editors.

Pharmakogenetik und Therapeutisches Drug Monitoring: Diagnostische Bausteine für die individualisierte Therapie [Pharmacogenetics: Ancillary Diagnosis and Genetic Pre-disposition]. Berlin: De Gruyter; 2017.

11 Acknowledgments

First and foremost, I would like to express my special thanks and my gratitude to my supervisor Professor Thorsten Lehr for the exciting and challenging topic, for his support and patience throughout my work at the university and beyond and for the inspiring and creative discussions.

I want to thank Professor Claus-Michael Lehr for his contributions as my scientific co-advisor.

A very special gratitude goes out to all of my cooperation partners at the Saarland University, in Germany and the United States of America: Michael Teifel, Babette Aicher, Herbert Sindermann, Nicola Ammer, Sebastian Frechen, Tobias Kanacher, Thomas Wendl, Professor Walter Emil Haefeli, Jürgen Burhenne, Professor Gerlinde Egerer, Clinton Fields Stewart, Nadine Schäfer, Professor Peter Harald Schmidt and Professor Frank Ramsthaler - Without them, none of the presented work would have been possible!

I want to thank my colleagues who started this wonderful journey with me, Melanie Titze and André Schäftlein: Thank you for your thoughts, humor and brilliant coffees. I want to thank further Nina Hanke, Hannah Britz, Jan-Georg Wojtyniak and all the rest of the Clinical Pharmacy working group.

With a special mention to Professor Charlotte Kloft and Professor Wilhelm Huiszinga for giving me the opportunity to participate in the “Graduate Research Training Program PharMetrX - Pharmacometrics and computational disease modeling”.

And finally, last but by no means least, to my family, my friends and all the other people who positively influenced and supported me over the last five years, thank you so much!